ActaNaturae

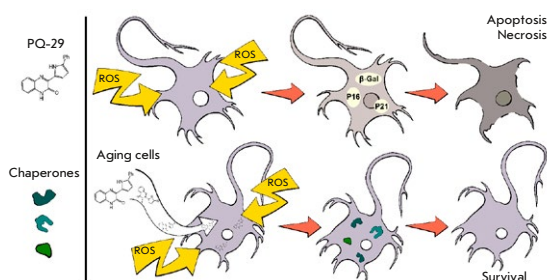# Induction of Chaperone Synthesis in Human Neuronal Cells Blocks Oxidative Stress-Induced Aging

Illustration of the principle of action of low-molecular-weight chaperone inducers to protect neuronal cells from oxidative stress

E. A. Dutysheva, L. S. Kuznetcova, I. A. Utepova, B. A. Margulis, I. V. Guzhova, V. F. Lazarev

Oxidative stress accompanies many pathologies characterized by neuronal degradation, leading to a deterioration of the disease. The main causes are the disruption of protein homeostasis and activation of irreversible processes of cell cycle disruption and deterioration of cellular physiology, leading to senescence. In this paper, authors propose a new approach to combating senescence caused by oxidative stress. This approach is based on the use of a low-molecular inducer of chaperone synthesis, one of the cell protective systems regulating proteostasis and apoptosis.

Combination with a Low Dose of Doxorubicin Further Boosts the Antitumor Effect of SLURP-1 *In Vivo* and Associates with EGFR Down-Regulation

O. V. Shlepova, M. L. Bychkov, V. O. Shipunova, E. I. Shramova, M. A. Shulepko, T. Y. Gornostaeva, E. A. Kiseleva, I. D. Kukushkin, V. A. Kazakov, E. A. Tukhovskaya, I. A. Dyachenko, A. N. Murashev, Z. O. Shenkarev, S. M. Deyev, M. P. Kirpichnikov, E. N. Lyukmanova

Skin cancers such as squamous cell carcinoma (SCC) are among the most aggressive types of tumors. They come with a high rate of growth, metastasis, and frequently occurring chemoresistance. Cytotoxic antibiotic doxorubicin has been proposed for the SCC therapy; however, its use is limited due to the high toxicity. In this study we investigated the usage of enhanced SLURP-1 dose and of combination of SLURP-1 with low-dozen doxorubicin for SCC treatment of mice xenografted with squamous cell carcinoma A431 cells. The combination with doxorubicin further en-

Scheme of drugs administration and tumor growth measurements

hanced the anti-tumor activity of SLURP-1 and dramatically suppressed metastasis. The effect from the combined therapy was accompanied by down-regulation of EGFR expression in tumors. Direct inhibition of EGFR activation by SLURP-1 was shown. No toxicity of the combined therapy was encountered. The data obtained indicate that the combination of SLURP-1 with chemo-therapy in lower doses is a promising approach in SCC treatment and should be further studied.
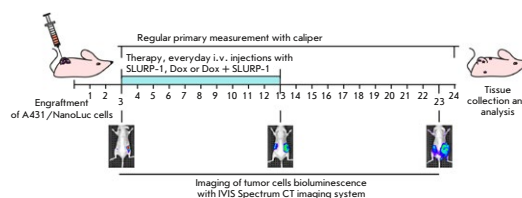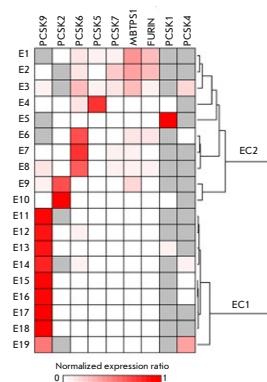
Alterations in the Expression of Proprotein Convertase Genes in Human Esophagus Squamous Cell Carcinomas

A. A. Komissarov, M. V. Zinovyeva, A. V. Sass, T. V. Vinogradova, S. I. Koshechkin, V. V. Demkin, I. B. Zborovskaya, S. V. Kostrov, I. V. Demidyuk

Proprotein convertases (PCs) are an enzyme family that includes nine highly specific human subtilisin-like serine proteases. Authors used quantitative real-time PCR to evaluate the expression levels of PC genes in the paired samples of tumor and adjacent normal tissues derived from 19 patients with esophageal squamous cell carcinomas. Authors observed a significant enrichment of *PCSK6*, *PCSK9*, *MBTPS1*, and *FURIN* mRNAs in the tumor tissue, which may be indication of the involvement of these PCs in the development and progression of esophageal cancers. The findings indicate that PC genes may be important markers of human cancers.

Cluster analysis of PC expression patterns in esophageal samples

ActaNaturae

*Founder and Chairman
of the Editorial Board (from 2009 to 2023)
of the journal Acta Naturae
Academician Grigoriev Anatoly Ivanovich*

CONTENTS

CONTENTS

SHORT REPORTS

IMAGE ON THE COVER PAGE
(see the article by Pipiya et al.)

Pro-inflammatory Cytokines, Ferroptosis, and Cancer

A. A. Vartanian[*], V. S. Kosorukov

N.N. Blokhin National Medical Research Center of Oncology of the Ministry of Health of Russia, Moscow, 115478 Russian Federation

[*]E-mail: zhivotov57@mail.ru

ABSTRACT Ferroptosis, iron-dependent regulated cell death, is induced by the polyunsaturated fatty acid peroxidation of membrane phospholipids and is controlled by glutathione peroxidase 4. In recent years, convincing evidence has emerged, demonstrating a close relationship between chemo-, radio-, immuno-, and targeted therapy resistance and ferroptosis resistance. In this review, we discuss the basic principles of ferroptosis in cancer. Considerable attention is paid to the formation of an immunosuppressive tumor microenvironment. The main focus is centered on the involvement of the excessive, chronic production of pro-inflammatory cytokines in ferroptosis resistance development in tumors.

KEYWORDS ferroptosis, intratumoral immunosuppression, pro-inflamatory cytokines, cancer.

ABBREVIATIONS Tf – transferrin; TfR1 – transferrin receptor 1; FPN – ferroportin; GPX4 – glutathione peroxidase 4; DAMP – damage-associated molecular pattern; PARP – poly(ADP-ribose) polymerase; CAF – cancer-activated fibroblast; MDSC – myeloid-derived suppressor cell; FDA – Food and Drug Administration; IFN – interferon; Treg – regulatory T cell; TNF – tumor necrosis factor; IL-6 – interleukin 6; GSH – glutathione; xC-system – cysteine/glutamate antiporter system; PUFA – polyunsaturated fatty acid.

INTRODUCTION

The concept holding that changes in the tumor cell genome contribute little to the progression of malignancy is now generally accepted [1]. The behavior of a tumor cell — survival, proliferation, and transition to the metastatic growth phase – is controlled by its microenvironment (extracellular matrix, neighboring non-transformed cells, immune system cells, blood). The tumor microenvironment also regulates resistance to therapy [2].

Ferroptosis, an iron-dependent form of cell death, was first reported in 2012 [3]. In ferroptosis, excess Fe^{2+} ions, which are not bound to proteins, trigger the Fenton reaction:

$$Fe^{2+} + H_2O_2 \rightarrow Fe^{3+} + OH^- + \cdot OH.$$
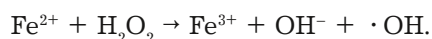
The Fenton reaction-generated hydroxyl radical is highly reactive and capable of oxidizing virtually any cellular component. The central mediator in ferroptosis is the accumulation of polyunsaturated fatty acid peroxidation products in the cell [4]. It should be noted that ferroptosis activation does not require the processing of cell death effectors, such as caspases or gasdermins: ferroptosis is an energetically less expensive cell death process. Data on the sensitivity of chemotherapy-, radiotherapy-, and targeted therapy-resistant tumor cells to ferroptosis have considerably heightened interest in the phenomenon [5].

The transition of a tumor to the aggressive growth phase occurs when control by the immune system is incomplete. Dysfunction of both tumor-infiltrating and circulating T cells has been reported (see review [6]). Also, the tumor induces significant changes in macrophages: polarization of macrophages to the M2 phenotype is observed [7]. Tumor cell secreted cytokines recruit Tregs to the tumor. The number of Tregs in the tumor increases at all stages of the disease; they suppress the proliferation and functional

activity of CD4+ and CD8+ T cells [8]. MDSCs also play an important role in suppressing the immune response [9]. Reprogramming of antitumor immunity, which results in the stimulation of primary tumor growth by immunocompetent cells of the microenvironment, as well as instability of the tumor cell genome, is now considered a factor that confers protection from the immune system to the tumor and facilitates its progression.

This review briefly discusses the features of iron metabolism in cancers, the main characteristics of ferroptosis, and the involvement of the chronic production of pro-inflammatory cytokines in tumor progression. Particular attention is paid to the development of tumor resistance to ferroptosis.

IRON IN THE TUMOR MICROENVIRONMENT

Until recently, tumor progression was studied in terms of the dependence of tumor cell survival on important metabolites, such as glucose and glutamine. But today, there is probably no doubt that the iron in the tumor microenvironment is also an important component of tumor cell survival. This is now quite obvious, since iron performs a number of metabolically important functions in the cell, delivering oxygen to tissues (heme) or acting as a cofactor for several enzymes; e.g., the ribonucleotide reductase that is involved in the biosynthesis of DNA or Krebs cycle enzymes [10]. The proliferation of tumor cells can be controlled through the regulation of iron reserves in the tumor. Also, iron is used not only by tumor cells, but also by the cells of the tumor microenvironment.

Cells take up iron mainly through receptor-mediated endocytosis of the Tf/iron complex. Binding of the Tf/iron complex to its receptor, TfR1 (CD71), results in ingestion of the Tf/iron/CD71 complex into the cell. In the cell, iron dissociates from the complex in endosomes and is incorporated into iron-dependent proteins, whereas the receptor and Tf return to the cell surface [11]. Non-protein-bound iron is stored in the cell as a complex with ferritin [12]. Free iron, not bound to proteins and ferritin, is excreted from the cell via a membrane-bound protein, FPN, or becomes part of the labile iron pool [13]. Iron levels in the body are regulated by the peptide hormone hepcidin. In response to increased iron concentrations in the blood, hepatocytes activate hepcidin expression and secretion into the blood stream. Binding of hepcidin to FPN promotes ingestion of both proteins into the cell and their degradation in lysosomes. This blocks the release of iron from depot cells, which reduces the plasma iron level. In the case of iron deficiency, hepcidin tran-

scription is suppressed [14]. Iron binding by proteins not only maintains cell viability, but also protects cells from the highly reactive hydroxyl radical generated in the Fenton reaction. It should be noted that our body has developed fairly strict control mechanisms for self-protection against changes in the iron metabolism. This means that our cells fail to control iron reserves only in extreme cases; in particular, cancers.

Tumor cells require significantly more iron to maintain a high proliferation index; so, TfR1 expression in tumor cells is increased to compensate for iron deficiency. Tumor cells also accumulate ferritin, depositing iron. The expression of FPN that exports iron from the cell also changes. A decreased FPN expression is observed in most malignancies (see review [15]). These successive processes lead to decreased blood iron levels and, thereby, to extremely low hemoglobin levels in cancer patients. Intravenous iron infusions, which normalize hemoglobin levels in anemia, usually do not increase hemoglobin levels in cancer patients. An autopsy reveals that most of the iron is deposited in the liver [16]. Reprogramming of the iron metabolism, which promotes iron accumulation in the tumor cell, is typical of all tumor types.

Today, an aggressive course of the disease is also believed to be associated with mutations in the tumor cell. It is important to note that mutations in many oncogenes (*c-myc*, *KRAS*, *BRAF*, *PI3K*) and deletion in *PTEN* promote an increase in iron levels inside the cell, and that mutations in tumor suppressor genes (*p53*) shrink the labile iron pool [17, 18]. An aggressive course of the tumor process is also associated with the accumulation of iron-secreting M2 macrophages in the tumor. Therefore, to increase the uptake of iron and reduce its loss, it is not enough to initiate changes in the expression of the proteins that control iron levels in tumor cells. Cross-talk between tumor cells and microenvironment cells is also nessesary. It should also be noted that the tumor microenvironment constantly changes.

FERROPTOSIS IS IRON-DEPENDENT REGULATED CELL DEATH

In 2018, the Nomenclature Committee on Cell Death officially defined ferroptosis as regulated cell death caused by abnormal oxidation of the polyunsaturated fatty acids of membrane phospholipids and controlled by GPX4.

This form of cell death is associated with hydroxyl radical generation in the Fenton reaction. In ferroptosis, HO· attacks the PUFAs of membrane phos-

pholipids. Phosphatidylethanolamine, which contains arachidonic ($C_{20}H_{32}O_2$) or adrenic ($C_{22}H_{36}O_2$) acids as a polyunsaturated fatty acid, is the substance that most often undergoes peroxidation. The products of membrane phospholipid peroxidation in a tumor cell accumulate not only due to the activation of the Fenton reaction, but also due to a reduced activity of the antioxidant defense system of the cell. The antioxidant defense system includes the selenoproteins GPX4 and GSH [19]. GPX4 uses GSH as an electron donor to reduce potentially harmful lipid hydroperoxides to non-toxic alcohols. Oxidized glutathione is reduced by the glutathione reductase that is constitutively activated in the cell [20]. Detoxification of lipid peroxides by GPX4 is limited by the presence of cystine, a GSH precursor, in the cell, which is transported via the xC-system [21]. In the cell, glutamate is exchanged for cystine in a 1:1 ratio. Cystine is reduced to cysteine by various reductases, in particular thioredoxin reductase 1, and is used as a building block for GSH biosynthesis. That the xC-system plays a key role in disease progression is confirmed by the results of clinical observations: the relapse rate of xC-positive tumors is significantly higher than that of xC-negative ones. GPX4 and the xC-system are considered potential targets for altering the redox status of the cell. Erastin, which blocks transport of cystine into the cell, remains the "gold standard" for ferroptosis induction. The second group of ferroptosis inducers includes GPX4 inhibitors (mainly RAS-selective lethal 3 (RSL3) and RAS-selective lethal 5 (RSL5)).

Phospholipid peroxidation disrupts protein–lipid interactions, alters the activity of membrane-bound enzymes, and affects membrane permeability. Continuous, intensive oxidation of membrane phospholipid PUFAs induces plasma membrane rupture and cell contents leakage into the intercellular environment. DAMPs in the tumor microenvironment (they may be divided into two subgroups, adjuvant and antigen) promote enhanced tumor infiltration by CD8+ T cells, maturation of dendritic cells, and increased phagocytic activity by macrophages [22, 23]. Therefore, ferroptosis in tumor cells is involved not only in the direct induction of cell death, but also in the reprogramming of the immune system, generating a specific immune response to tumor antigens, which should lead to the destruction of more tumor cells.

The oncosuppressive role of ferroptosis was first shown in triple-negative breast cancer [24]. The pronounced dependence of tumor growth on glutamine was indicative of a decrease in xC-system activity in the uptake of cystine. Further, sorafenib, a tyrosine kinase inhibitor, was found to deplete glutathione reserves in the cell, by blocking the xC-system, and trigger ferroptosis [25]. PARP inhibitors have exhibited similar action [26]. Ferroptosis in tumor cells is also induced by compounds that block GPX4 activity (e.g., altretamine, an FDA-approved alkylating agent) [27]. It is interesting to note that resistance to PD-1/PD-L1 immunotherapy is also believed to be associated with resistance to ferroptosis [28]. Even the clinical data mentioned in this brief review indicate that ferroptosis most likely contributes to the effects of antitumor drugs.

MICROENVIRONMENT IN TUMOR PROGRESSION

Continuous growth of the tumor mass, when the tumor's blood supply is inadequate, is accompanied by partial cell death. Dying cells induce the production of pro-inflammatory cytokines (TNF-α and -β, IL-1, IL-6, IFN-γ, etc.) [29]. The role of the cytokines is to regulate the body's immune response to the inflammation caused by tissue damage. In response to the immunostimulatory signals released by dying cells, immunocompetent cells migrate to the tumor microenvironment and secrete pro-inflammatory cytokines. High concentrations of pro-inflammatory cytokines bring the tumor to a more aggressive growth phase [30]. As the tumor mass grows, the amount of dying tumor cells and the number of antigens in the tumor microenvironment increase: the inflammation becomes chronic. Chronic overexpression of pro-inflammatory mediators is observed at all stages of cancer development: inflammation severity is significantly higher in metastatic tumors than it is in the early stages of the disease [31].

Molecular changes initiated by tumor adaptation to a lack of nutrition, oxygen, and energy activate resident resting fibroblasts. Cancer-associated fibroblasts (CAFs) virtually rebuild the extracellular matrix by secreting vimentin, laminin, fibronectin, and collagen, the major scaffold protein of the extracellular matrix. Compaction of the extracellular matrix stimulates malignant tumor growth. The rigidity of the extracellular matrix acts as a barrier preventing drug penetration into the tumor (see review [32]).

Malnutrition during rapid tumor growth is accompanied by the formation of necrotic foci. DAMPs are released into the intercellular space, which leads to dendritic cell-mediated antigen uptake and presentation, as well as induction of a cytotoxic T cell response. As the tumor progresses, the reactive capabilities of T cells decreases. T cells switch to an anergy state that is characterized by decreased cytolytic activity and a reduced T cell proliferation index (see review [33]).

The immune response to DAMPs also involves macrophages (see review [34]). The cytotoxic activity of macrophages at the initial stages of tumor infiltration by macrophages retards tumor progression, but it is not enough to control tumor growth. The anti-tumor immune response is suppressed by the polarization of macrophages to the M2 phenotype. By secreting growth factors, cytokines, and extracellular matrix components, M2 macrophages enhance the malignant potential of tumor cells.

Tregs are the central link in the regulation of the immune response to both self- and tumor antigens. Normally, Tregs prevent the development of autoimmune diseases. The main function of Tregs in the tumor is to inhibit the proliferation of CD4+ and CD8+ T cells (see review [35]). It is very important that Tregs create an immunodeficient space in the tumor, which is suitable for bacterial growth. An increase in the number of Tregs in the tumor was shown to significantly raise prostate cancer mortality rates, regardless of other clinical factors [36].

The tumor recruits MDSCs from the blood to maintain immunosuppression. In malignancies, myeloid suppressors suppress the response of T and NK cells. MDSCs also express the CD40 that induces the accumulation of Tregs in the tumor microenvironment (see review [37]). It is interesting to note that Tregs, MDSCs, and M2 macrophages are resistant to ferroptosis, and that CD8+ T cells are sensitive to Fe-dependent death [38].

PRO-INFLAMMATORY INTERLEUKINS IN THE TUMOR MICROENVIRONMENT

Interleukins, low-molecular weight proteins, are synthesized primarily by immune system cells and are divided into pro-inflammatory (IL-1, -6, -12, TNF-α, interferons, chemokines, IL-8, etc.) and anti-inflammatory (IL-4, -10, -13, and -17) (see review [39]).

IL-6 expression dominates in the tumor microenvironment (see review [40]). IL-6 levels are elevated in breast, cervical, colon, esophageal, head and neck, ovarian, pancreatic, and prostate cancers, as well as in patients with non-small cell lung cancer and multiple myeloma [41]. Abundant clinical data have been accumulated, confirming a correlation of IL-6 with resistance to therapy [42] and activation of metastasis (see review [43]). IL-6 binding to its receptor (IL-6Ra, gp80) and co-receptor, gp130, activates the JAK2/STAT3 signaling pathway [44]. STAT3 belongs to the family of pro-oncogenic transcription factors that are closely associated with inhibition of apoptosis, proliferation of tumor cells, and activation of metastasis and angiogenesis [45]. Hyperactivation of the IL-6/IL-6R/JAK2/STAT3 signaling pathway is observed in almost all types of tumors [46]. It is important to note that the level of IL-6 circulating in the blood of patients is a prognostic marker for both the disease course and the tumor response to therapy [47].

High concentrations of both IL-1α and IL-1β are found in the tumor microenvironment [48]. IL-1α and IL-1β levels are significantly increased in melanoma, colon, lung, and breast cancers, head and neck tumors and are associated with a tumor's transition to the aggressive growth phase [49]. In genotoxic stress, increased production of IL-1α and IL-1β and their secretion activate tumor blood supply (see review [50]). There also exist data on a correlation between IL-1β expression and the formation of distant metastases [51]. Binding of IL-1α to its receptor activates expression of the pro-oncogenic transcription factor NF-kB that blocks Fas-dependent apoptosis and provides conditions for tumor survival and progression [52]. It is becoming evident that high concentrations of pro-inflammatory cytokines in the tumor microenvironment are organic components of malignant tumor growth. Many recent studies have bolstered the idea that progression of malignancies is driven by smoldering inflammation.

PRO-INFLAMMATORY CYTOKINES IN FERROPTOSIS IN CANCER

As noted above, the tumor reprograms the metabolism of iron and promotes its accumulation in the cell. It would seem that high iron concentrations inside the tumor cell should activate ferroptosis. However, ferroptosis is blocked in the tumor. In head and neck squamous cell carcinoma, IL-6 was shown to stimulate the expression of xC-system proteins [53]. Inhibition of the xC-system in these cells restored ferroptosis. Genetic knockdown of xC-system proteins reduced cell proliferation *in vitro*. Thus, it has been experimentally confirmed that the pro-inflammatory cytokine IL-6 blocks ferroptosis by activating the xC-system. Involvement of intratumoral immunosuppression in the blocking of ferroptosis has also been confirmed in subcutaneous tumor xenograft mouse models. RSL3, an inhibitor of GPX4, suppressed tumor growth in athymic nude mice [54]. Another study demonstrated the antitumor effect of imidazole ketonerastine (IKE), a ferroptosis inducer, in an immunodeficient mouse lymphoma model [55].

The induction of ferroptosis in tumor cells also involves other pro-inflammatory cytokines. IFN-γ in hepatocellular carcinoma cells was shown to block transcription of the *SLC7A11* gene that encodes a subunit

of the xC-system [56]. Under conditions of GSH deficiency, accumulation of phospholipid peroxidation products triggers ferroptosis. SLC7A11 and SLC3A2 expression in tumor cells was also suppressed by TNF-α: decreased cystine uptake led to cell death due to oxidative stress development [57]. It is important to note that IFN-γ- or TNF-α-induced ferroptosis can develop only at the initial stages of the disease; when the tumor switches to the aggressive growth phase, a shift towards IL-6 secretion occurs. In the aggressive growth phase, intratumoral IL-6 levels are many-fold higher than those of other cytokines: ferroptosis in cells with a highly malignant phenotype is blocked [58].

The next regulator of oncogenesis-associated inflammation is the transcription factor NF-kB that is activated in response to pro-inflammatory cytokines, the insulin-like growth factor, and the tumor necrosis factor. NF-kB is involved in the regulation of the cell cycle, proliferation, adhesion, and migration control, as well as in angiogenesis and invasion (see review [59]). There exists experimental evidence that NF-kB is also involved in ferroptosis. In U87 glioblastoma cells, RSL3, an inhibitor of GPX4, was shown to activate the NF-kB signaling pathway. Active NF-kB triggers ferroptosis by reducing the expression of SLC7A11, a subunit of the xC-system, and GPX4 [60]. As a result, lipid hydroperoxide concentrations increase and ferroptosis is triggered. In subcutaneous xenografts, inhibition of NF-kB by BAY 11-7082 abolished the antitumor effect of RSL3. Therefore, during tumor progression, the tumor develops mechanisms to avoid ferroptosis. Apparently, resistance to ferroptosis in a setting of high intracellular iron concentrations is another determinant that allows the tumor to escape antitumor therapy. The revealed resistance to ferroptosis, which is induced by the pro-inflammatory tumor microenvironment, not only expands our knowledge of the mechanisms underlying malignant disease progression, but also shifts the emphasis in interpreting the significance of intratumoral immunosuppression in carcinogenesis. Given the constitutive activity of the IL-6/JAK2/STAT3 signaling pathway in malignant diseases [61], resistance to ferroptosis may be considered a necessary condition for tumor progression.

CONCLUSION

Although programs for the early detection of malignancies have significantly improved the chances of survival for cancer patients, drug resistance remains a serious impediment in cancer treatment. The realization that cells that survive chemo-, radio-, and targeted therapy are sensitive to ferroptosis has significantly increased interest in ferroptosis. The death of a therapy-resistant cell is induced by additional oxidative stress by Fenton reaction-generated hydroxyl radicals: the antioxidant defense system of the cell is almost completely destroyed. Strategies for using ferroptosis in the treatment of metastases open up new opportunities in cancer therapy. In preclinical models, ferroptosis inducers have caused relatively limited toxic effects in normal cells and demonstrated good tolerability. The randomized study Functional Assessment of Cancer Therapy–Lung Cancer in non-small cell lung cancer patients revealed that the humanized anti-IL-6 antibody (ALD518) delayed cachexia by reducing weight loss from 1.5 kg/month to 0.19 kg/month and increased the relapse-free survival time patients by 2.2 months [62]. ALD518 did not significantly affect tumor growth. Apparently, the use of anti-IL-6 antibodies is not enough to block tumor growth, although monotherapy improves the quality of life of patients. Of significant interest are the preliminary results of clinical studies on the combined use of ferroptosis inducers and antitumor drugs in ovarian cancer, triple-negative breast cancer, prostate cancer, colorectal cancer, and hepatocellular carcinoma (see review [63]). In addition, it may be hoped that the potential ability of ferroptosis to induce a specific immune response which enhances the therapeutic effect of other treatments (see review [64]) will prolong remission in cancer patients. ●

REFERENCES

1. de Visser K.E., Joyce J.A. // Cancer Cell. 2023. V. 41. № 3. P. 374–403.
2. Al-Akra L., Bae D.H., Leck L.Y.W., Richardson D.R., Jansson P.J. // Biochim. Biophys. Acta Gen. Subj. 2019. V. 1863. № 9. P. 1390–1397.
3. Dixon S.J., Stockwell B.R. // Cell. 2012. V. 49. P. 1060–1072.
4. Mou Y., Wang J., Wu J., He D., Zhang C., Duan C., Li B. // J. Hematol. Oncol. 2019. V. 12. № 1. P. 34.
5. Friedmann Angeli J.P., Krysko D.V., Conrad M. // Nat. Rev. Cancer. 2019. V. 19. № 7. P. 405–414.
6. Martínez-Lostao L., Anel A., Pardo J. // Clin. Cancer Res. 2015. V. 21. № 22. P. 5047–5056.
7. Li M., Yang Y., Xiong L., Jiang P., Wang J., Li C. // J. Hematol. Oncol. 2023. V. 16. № 1. P. 80.
8. Ohue Y., Nishikawa H. // Cancer Sci. 2019. V. 110. № 7. P. 2080–2089.
9. Gabrilovich D.I. // Cancer Immunol. Res. 2017. V. 5. № 1. P. 3–8.
10. Zhang D.L., Ghosh M.C., Rouault T.A. // Front. Pharmacol. 2014. V. 5. P. 124–129.
11. Wallace D.F. // Clin. Biochem. Rev. 2016. V. 37. № 2. P. 51–62.
12. Plays M., Müller S., Rodriguez R. // Metallomics. 2021. V. 13. № 5. P. mfab021.
13. Drakesmith H., Nemeth E., Ganz T. // Cell Metabolism. 2015. V. 22. № 5. P. 777–787.
14. Vela D., Vela-Gaxha Z. // Exp. Mol. Med. 2018. V. 50. № 2. P. e436.
15. Ludwig H., Evstatiev R., Kornek G., Aapro M., Bauernhofer T., Buxhofer-Ausch V., Fridrik M., Geissler D., Geissler K., Gisslinger H., et al. // Wien Klin. Wochenschr. 2015. V. 127. № 23–24. P. 907–919.
16. Kew M.C. // Liver Cancer. 2014. V. 3. № 1. P. 31–40.
17. Horniblow R.D., Bedford M., Hollingworth R., Evans S., Sutton E., Lal N., Beggs A., Iqbal T., Tselepis C. // Cancer Sci. 2017. V. 108. P. 1135–1143.
18. Zhang F., Wang W., Tsuji Y., Torti S.V., Torti F.M. // J. Biol. Chem. 2008. V. 283. P. 33911–33918.
19. Brigelius-Flohe R., Maiorino M. // Biochim. Biophys. Acta. 2013. V. 1830. P. 3289–3303.
20. Meister A. // Meth. Enzymol. 1995. V. 251. P. 3–7.
21. Liu J., Xia X., Huang P. // Mol. Ther. 2020. V. 28. № 11. P. 2358–2366.
22. Murao A., Aziz M., Wang H., Brenner M., Wang P. // Apoptosis. 2021. V. 26. № 3–4. P. 152–162.
23. Roussot N., Ghiringhelli F., Rébé C. // Cells. 2022. V. 11. № 22. P. 3672.
24. Liu Y., Hu Y., Jiang Y., Bu J., Gu X. // Front. Pharmacol. 2022. V. 13. P. 1036140.
25. Li Q., Chen K., Zhang T., Jiang D., Chen L., Jiang J., Zhang C., Li S. // Eur. J. Pharmacol. 2023. V. 955. P. 175913.
26. Hong T., Lei G., Chen X., Li H., Zhang X., Wu N., Zhao Y., Zhang Y., Wang J. // Redox Biol. 2021. V. 42. P. 101928.
27. Morcos C.A., Khattab S.N., Haiba N.S., Bassily R.W., Abu-Serie M.M., Teleb M. // Bioorg. Chem. 2023. V. 141. P. 106839.
28. Yin J., Meng X., Peng L., Xie W., Liu X., He W., Li S. // Curr. Mol. Med. 2023. V. 23. № 5. P. 401–409.
29. Dinarello C.A. // Cancer Metastasis Rev. 2006. V. 25. № 3. P. 307–313.
30. Goenka A., Khan F., Verma B., Sinha P., Dmello C.C., Jogalekar M.P., Gangadaran P., Ahn B.C. // Cancer Commun. (London). 2023. V. 43. № 5. P. 525–561.
31. Inácio Pinto N., Carnier J., Oyama L.M., Otoch J.P., Alcântara P.S., Tokeshi F., Nascimento C.M. // Mediators Inflamm. 2015. V. 2015. P. 791060.
32. Lavie D., Ben-Shmuel A., Erez N., Scherz-Shouval R. // Nat. Cancer. 2022. V. 3. № 7. P. 793–807.
33. Farhood B., Najafi M., Mortezaee K. // J. Cell Physiol. 2019. V. 234. № 6. P. 8509–8521.
34. Pan Y., Yu Y., Wang X., Zhang T. // Front. Immunol. 2020. V. 11. P. 583084.
35. Ohue Y., Nishikawa H. // Cancer Sci. 2019. V. 110. № 7. P. 2080–2089.
36. Karpisheh V., Mousavi S.M., Sheykholeslami N., Fathi M., Saray M., Aghebati-Maleki L., Jafari R., Zolbanin N., Jadidi-Niaragh F. // Life Sci. 2021. V. 284. P. 119132.
37. Hegde S., Leader A.M., Merad M. // Immunity. 2021. V. 54. № 5. P. 875–884.
38. Kim R., Taylor D., Vonderheide R.H., Gabrilovich D.I. // Trends Pharmacol. Sci. 2023. V. 44. № 8. P. 542–552.
39. Briukhovetska D., Dörr J., Endres S., Libby P., Dinarello C.A., Kobold S. // Nat. Rev. Cancer. 2021. V. 21. № 8. P. 481–499.
40. Uciechowski P., Dempke W.C.M. // Oncology. 2020. V. 98. № 3. P. 131–137.
41. Heikkilä K., Ebrahim S., Lawlor D.A. // Eur. J. Cancer. 2008. V. 44. № 7. P. 937–945.
42. Kumari N., Dwarakanath B.S., Das A., Bhatt A.N. // Tumour Biol. 2016. V. 37. № 9. P. 11553–11572.
43. Goulet C.R., Champagne A., Bernard G., Vandal D., Chabaud S., Pouliot F., Bolduc S. // BMC Cancer. 2019. V. 19. № 1. P. 137.
44. Taher M.Y., Davies D.M., Maher J. // Biochem. Soc. Trans. 2018. V. 46. № 6. P. 1449–1462.
45. Li Y.J., Zhang C., Martincuks A., Herrmann A., Yu H. // Nat. Rev. Cancer. 2023. V. 23. № 3. P. 115–134.
46. El-Tanani M., Al Khatib A.O., Aladwan S.M., Abuelhana A., McCarron P.A., Tambuwala M.M. // Cell Signal. 2022. V. 92. P. 110275.
47. Łukaszewicz M., Mroczko B., Szmitkowski M. // Pol. Arch. Med. Wewn. 2007. V. 117. № 5–6. P. 247–251.
48. Baker K.J., Houston A., Brint E. // Front Immunol. 2019. V. 10. P. 1197–1205.
49. Gelfo V., Romaniello D., Mazzeschi M., Sgarzi M., Grilli G., Morselli A., Manzan B., Rihawi K., Lauriola M. // Int. J. Mol. Sci. 2020. V. 21. № 17. P. 6009.
50. Voronov E., Shouval D.S., Krelin Y., Cagnano E., Benharroch D., Iwakura Y., Dinarello C.A., Apte R.N. // Proc. Natl. Acad. Sci. USA. 2003. V. 100. № 5. P. 2645–2650.
51. Apte R.N., Dotan S., Elkabets M., White M.R., Reich E., Carmi Y., Song X., Dvozkin T., Krelin Y., Voronov E. // Cancer Metastasis Rev. 2006. V. 25. № 3. P. 387–408.
52. Diep S., Maddukuri M., Yamauchi S., Geshow G., Delk N.A. // Cells. 2022. V. 11. № 8. P. 1673.
53. Li M., Jin S., Zhang Z., Ma H., Yang X. // Cancer Lett. 2022. V. 527. P. 28–40.
54. Yang J., Mo J., Dai J., Ye C., Cen W., Zheng X., Jiang L., Ye L. // Cell Death Dis. 2021. V. 12. № 11. P. 1079.
55. Zhang Y., Tan H., Daniels J.D., Zandkarimi F., Liu H., Brown L.M. // Cell Chem. Biol. 2019. V. 26. № 5. P. 623–633.
56. Li L., Xing T., Chen Y., Xu W., Fan B., Ju G., Zhao J., Lin L., Yan C., Liang J., Ren X. // Cell Death Discov. 2023. V. 9. № 1. P. 331.

57. Yin J., Meng X., Peng L., Xie W., Liu X., He W., Li S. // Curr. Mol. Med. 2023. V. 23. № 5. P. 401–409.

58. Rašková M., Lacina L., Kejík Z., Venhauerová A., Skaličková M., Kolář M., Jakubek M., Rosel D., Smetana K., Brábek J. // Cells. 2022. V. 22. P. 3698.

59. Taniguchi K., Karin M. // Nat. Rev. Immunol. 2018. V. 18. № 5. P. 309–324.

60. Li S., He Y., Chen K., Sun J., Zhang L., He Y., Yu H., Li Q. // Oxid. Med. Cell Longev. 2021. P. 2915019.

61. Huang B., Lang X., Li X. // Front. Oncol. 2022. V. 12. P. 1023177.

62. Bayliss T.J., Smith J.T., Schuster M., Dragnev K.H., Rigas J.R. // Expert. Opin. Biol. Ther. 2011. V. 11. № 12. P. 1663–1668.

63. Liu X., Zhang Y., Wu X., Xu F., Ma H., Wu M., Xia Y. // Front. Pharmacol. 2022. V. 13. P. 909821.

64. Qi D., Peng M. // Front. Immunol. 2023. V. 14. P. 1188365.

Immunoregulatory Enzymes

S. V. Kupriyanov*, K. M. Kirilenko, D. N. Starkov
Tomsk State University, Laboratory of Evolutionary Cytogenetics, Tomsk, 634050 Russian Federation
*E-mail: pfft@mail.ru

ABSTRACT Immunoregulatory enzymes, which function both as biological catalysts and regulatory elements, play a crucial role in controlling immune responses. Dysfunction of these proteins can contribute to various pathological conditions, such as the suppression of antitumor immunity or impairment of anti-infectious immune responses. This review discusses the most extensively studied immunoregulatory enzymes, including indoleamine 2,3-dioxygenase 1, arginase 1, inducible nitric oxide synthase, glyceraldehyde-3-phosphate dehydrogenase, and ectonucleoside triphosphate diphosphohydrolase 1. Their classification is provided, along with an analysis of the distinctive characteristics inherent to this group of enzymes. Additionally, new directions for the medical application of immunoregulatory enzymes are explored.

KEYWORDS Immunometabolism, immune response regulation, enzymatic regulation.

ABBREVIATIONS IDO1 – indoleamine 2,3-dioxygenase 1; ARG1 – arginase 1; GAPDH – glyceraldehyde-3-phosphate dehydrogenase; IFN-γ – interferon-gamma; Th1 – T helper type 1; AhR – aryl hydrocarbon receptor; Th2 – T helper type 2; PBMC – peripheral blood mononuclear cells; iNOS – inducible nitric oxide synthase; NO – nitric oxide; IL-12 – interleukin 12; Th17 – T helper type 17; ENTPD1 – ectonucleoside triphosphohydrolase 1; PAMPs – pathogen-associated molecular patterns.

INTRODUCTION

The primary function of the immune system is to maintain homeostasis by eliminating foreign agents, such as pathogens, as well as aberrant self-cells [1]. This applies not only to tumor cells, but also to immune cells, whose uncontrolled activity can be detrimental to the host, leading to autoimmune or allergic disorders. Therefore, regulation of the immune system can be regarded as a central mechanism that ensures its proper function.

The metabolism of immune cells differs significantly from that of other systems in the body. Many specialized immune functions, such as proliferation in response to antigen stimulation or the synthesis and release of cytotoxic agents for pathogen defense, necessitate metabolic reprogramming [2]. A key example is the Warburg effect, which is a prerequisite for the activation of many lymphocyte types. This phenomenon is characterized by the diversion of pyruvate, generated through glycolysis, away from the pyruvate dehydrogenase complex toward lactate production, despite the absence of hypoxia, distinguishing it from anaerobic glycolysis [3]. The field of immunometabolism investigates the metabolic processes involved in immune responses [4], with one of its key aspects being the regulation of immune function via metabolic pathways. A crucial role in this regulation is played by immunoregulatory enzymes. However, there is currently no universally accepted definition of what constitutes an immunoregulatory enzyme. Instead, several representative enzymes have been identified, including indoleamine 2,3-dioxygenase 1 (IDO1) [5], arginase 1 (ARG1) [6], and glyceraldehyde-3-phosphate dehydrogenase (GAPDH) [7], among others. The aim of this review is to systematize current knowledge on immunoregulatory enzymes.

It is important to emphasize that metabolic regulation of immune processes occurs not only at the level of individual enzymes, but also at the level of entire metabolic pathways [8, 9]. Glycolysis is a crucial process governing T-lymphocyte activation; however, its execution requires the coordinated activity of multiple enzymes. In this review, we do not classify such enzymes as immunoregulatory, since they function as components of a regulatory metabolic pathway. In contrast, expression of a single enzyme, such

as IDO1, is sufficient to alter how the immune system functions [5], and this enzyme acts as an independent regulatory element. The review focuses on the enzymes that function in such a manner. Since research into immunoregulatory enzymes is still in its early stages, it is necessary to first identify the enzymes with known immunoregulatory properties and subsequently establish a definition for this class of enzymes as a whole. This work examines indoleamine 2,3-dioxygenase 1, arginase 1, inducible nitric oxide synthase, glyceraldehyde-3-phosphate dehydrogenase, and ectonucleoside triphosphate diphosphohydrolase 1, since these enzymes represent the most extensively studied members of the immunoregulatory enzyme group and exemplify key regulatory mechanisms. Based on the properties of these proteins, we propose a classification of immunoregulatory enzymes according to their mechanism of action and site of activity.

IDO1

Indoleamine 2,3-dioxygenase 1 (IDO1) is an enzyme involved in tryptophan catabolism [10], although its substrate specificity is not strictly confined to tryptophan. The immunosuppressive effect of IDO1 is primarily associated with the conversion of tryptophan to kynurenines. IDO1 is expressed by antigen-presenting cells [11] and is strongly induced by interferon-gamma (IFN-γ) [12]. Notably, the immunosuppressive activity of IDO1 is most prominent against T helper type 1 (Th1) cells [13], which *per se* produce IFN-γ [14]. This creates a potential negative feedback loop limiting excessive proliferation of Th1 cells, thereby maintaining immune homeostasis.

The immunoregulatory effects of IDO1 are mediated through the following mechanisms:

– tryptophan depletion [15];

– production of kynurenines, which act through the aryl hydrocarbon receptor (AhR) [16];

– the non-enzymatic function as a signaling protein [17].

IDO1-mediated immunosuppression supports immunological tolerance in immune-privileged organs, such as the placenta [18] and the cornea [19].

A number of pathological conditions are associated with the dysfunction of the IDO1 system. For instance, the expression of this enzyme in tumors enables immune evasion, thereby promoting disease progression [20]. Certain pathogens have also evolved mechanisms to exploit IDO1 for host immune suppression. For example, *Leishmania major* and *L. donovani* can induce IDO1 expression in human dendritic cells, leading to the inhibition of lymphocyte proliferation and disruption of the immune response [21]. On the other hand, IDO1 has been shown to exert antibacterial effects against certain pathogens by depleting an essential substrate, tryptophan [22]. IDO1 inhibitors have been extensively studied as antitumor agents; however, their clinical efficacy remains limited despite promising preclinical results. This limitation may be due to the activation of alternative immunosuppressive mechanisms [23].

ARG1

Arginase 1 (ARG1) catalyzes the conversion of arginine to ornithine and urea [24]. This enzyme prforms a regulatory activity through arginine depletion, since arginine is an essential amino acid for immune cells [25]. T-cell activation and differentiation are suppressed in an environment with active arginase and arginine deficiency; however, this mechanism is ineffective when arginine is abundant [26]. Murine models have demonstrated that in response to cytokine production by Th2 cells, macrophages express arginase, which regulates Th2 cell numbers and the inflammation induced by this cell population [27]. In humans, ARG1 expression by immune cells is also implicated in immune response regulation. Neutrophils isolated from the blood of septic patients were shown to suppress CD8+ T-lymphocyte proliferation in co-culture experiments due to ARG1 expression [28]. Similarly, neutrophils circulating in the blood of glioblastoma patients can degranulate arginase, thereby suppressing the activity of adaptive immune cells [29]. Notably, under normal conditions, neutrophils contain a high quantity of arginase-rich granules. Yet the enzyme does not interact with cytoplasmic arginine. As a result, neutrophil circulation does not lead to increased arginine consumption by the blood [30]. This suggests that degranulation may be necessary for activating the regulatory function of arginase. Other leukocytes within the peripheral blood mononuclear cell (PBMC) fraction have also been shown to express ARG1 in response to damaging factors [31], although it remains unclear whether this represents a regulatory mechanism. Notably, ARG1 also exhibits an antimicrobial activity. In human neutrophils, the enzyme is localized within specific granules and is released into the phagolysosome upon pathogen phagocytosis, leading to localized arginine depletion and subsequent microbial death [30]. The activity of macrophage arginase at the sites of specific inflammation may also help curb the spread of a pathogen, as demonstrated in murine models of the tuberculosis infection [32]. This mechanism is most likely to be associated with arginine depletion, since no direct effect of ARG1 metabolites on mycobacterial growth has been identified.

iNOS

Unlike arginase and IDO1, inducible nitric oxide synthase (iNOS) functions as an immunoregulatory enzyme primarily within the innate immune system. Specifically, nitric oxide (NO) can suppress interleukin-12 (IL-12) production in macrophages and dendritic cells, as demonstrated in animal models [33]. Additionally, NO acts as an antimicrobial agent [34], targeting intracellular pathogens. Its bactericidal effect is attributed to the formation of peroxynitrite, a potent oxidant that damages various cellular structures of the pathogen. Due to its short half-life, nitric oxide exerts its primary regulatory effects within NO-producing cells, where it nitrosylates functional amino acid residues such as tyrosine, in signaling proteins. Through nitrosylation, NO was shown to inhibit Th17 cell differentiation in mice [35], as well as M1 macrophage differentiation [36]. Since these studies were conducted in murine models, further investigation is required to assess their applicability to human cells. The expression of iNOS in innate immune cells regulates the production of proinflammatory cytokines, which contrasts with its role as a bactericidal agent. By analogy with ARG1, a hypothesis can be put forward that the subcellular localization of iNOS can be linked to the dual functionality of this enzyme.

GADPH

Glyceraldehyde-3-phosphate dehydrogenase (GAPDH) is a key enzyme in glycolysis, the central pathway of glucose metabolism in immune cells [37]. Recently, a mechanism for immune response regulation in T-lymphocytes involving GAPDH has been described [38]. Under glucose-sufficient conditions, this enzyme facilitates glycolysis, which is essential for energy production and the supply of substrates for anabolic processes. However, under glucose-limiting conditions, GAPDH shifts to a regulatory function by recognizing specific motifs in certain mRNAs and promoting their degradation. This leads to a decrease in the expression of several proteins, including IFN-γ, the key cytokine of Th1 cells. As a result, T-lymphocytes are unable to synthesize IFN-γ in a glucose-deficient environment. This phenomenon may partially explain the reduced Th1 immune response activity observed in some tumor tissues, which also exhibit high glucose consumption. Indeed, glucose deprivation has been identified as an immunosuppressive factor within the tumor microenvironment [39]. Notably, cytokine production regulated by GAPDH can be subject to negative feedback, designed to limit excessive IFN-γ production during uncontrolled T-lymphocyte expansion. This mechanism prevents excessive glucose consumption by proliferating lymphocytes and helps maintain a metabolic balance in the immune response [40].

ENTPD1

The enzyme ectonucleoside triphosphate diphosphohydrolase 1 (ENTPD1) is an exonucleotide phosphatase that hydrolyzes nucleotides to nucleosides [41]. ENTPD1, also known as CD39, is expressed on the surface of immune cells. The immunoregulatory function of CD39 is based on the breakdown of extracellular ATP into adenosine, which suppresses the activation of various immune cells, particularly macrophages and T-lymphocytes, through A2A receptors and their associated intracellular signaling pathways [42, 43]. This mechanism has been studied both in murine models and in human cells [44]. A substantial body of research, conducted in both animal models and patient-derived samples, indicates the involvement of ENTPD1 in immunosuppression across various oncological diseases [45]. Additionally, the hydrolysis of ATP in plasma by ENTPD1 localized on the surface of plasma cells is considered one of the mechanisms contributing to immunosuppression in patients who have experienced sepsis [46].

CLASSIFICATION AND GENERAL CHARACTERISTICS OF IMMUNOREGULATORY ENZYMES

A classification can be established based on the available data on the described members of the immunoregulatory enzyme group (*Fig. 1*). Additionally, several common features of these enzymes can be identified, which may aid in the discovery of new members of this group.

Classification

Based on their mechanism of action, these enzymes can be classified into the following groups:
– enzymes mediating the deprivation of essential and conditionally essential compounds (*Fig. 2*);
– enzymes synthesizing a regulatory metabolite (*Fig. 3*); and
– enzymes exhibiting a non-enzymatic activity (*Fig. 4*).

The deprivation of essential compounds restricts the proliferative activity of cells; therefore, this strategy is primarily utilized in the regulation of the adaptive immune response, given the high proliferative activity of lymphocytes. This effect has a lesser impact on the populations of resting cells, whose metabolism is less intensive. Additionally, its effectiveness depends on the concentration of the essential compound, the tissue's ability to synthesize or transport it, and external supplementation. For example, in a murine model of a *L. major* infection, the inhibitory
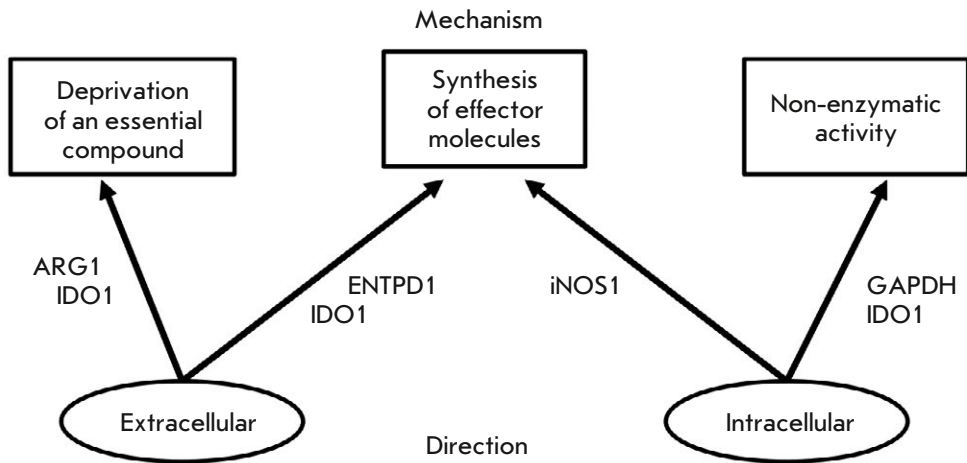
effect of arginase on T-lymphocytes was neutralized by arginine administration [26]. Among the enzymes discussed, IDO1 (when functioning enzymatically) and ARG1 operate via this mechanism.

Regulation through the synthesis of regulatory metabolites, in contrast, does not affect all cells with a specific metabolic level in the microenvironment but rather targets specific populations expressing the corresponding receptors. This regulation can be either external or internal, depending on the localization of the enzymes and receptors for the regulatory metabolites. This mechanism is characteristic of IDO1, ENTPD1, and iNOS, with the action of NO being primarily confined to the producing cell, due to its rapid degradation.

Non-enzymatic activity implies that an enzyme possesses additional properties, such as the ability to influence intracellular signaling proteins or regulate mRNA levels. IDO1 and GAPDH exhibit this type of mechanism. The example of IDO1 highlights the fact that enzymes can simultaneously employ multiple regulatory mechanisms. For instance, iNOS has a potential to deplete arginine, an essential substrate for immune cells. However, there is currently no direct evidence confirming arginine deprivation by iNOS. In contrast, arginase, which also depletes the same substrate, is more efficient than iNOS, because its catalytic activity does not require oxygen, whose levels are often reduced in inflammatory foci [47].

Based on their direction, enzymes can be classified into the following groups:
– enzymes with an extracellular direction, and
– enzymes with an intracellular direction.

GAPDH, iNOS, and IDO1 (when IDO1 functions as a signaling protein) fall into intracellular direction, since they reside within cells and primarily influence gene expression in the cells where they are present. Notably, the intracellular activity of these proteins depends on the substrate levels in the cellular microenvironment, allowing for fine-tuned regulation of enzyme activity. This principle is best illustrated by GAPDH, which functions as a regulatory molecule only under conditions where its enzymatic activity is inhibited, such as in glucose deficiency.

Enzymes with extracellular direction, such as ARG1, ENTPD1, and IDO1 (when IDO1 functions enzymatically), influence not only the cells expressing them, but also surrounding cell populations. In some cases, these enzymes may not affect the cells in which they are expressed. For example, ENTPD1 expression appears to have no impact on plasmablasts, despite being localized on their surface [46].

General characteristics of the function of immunoregulatory enzymes

Enzymes involved in immune regulation share several characteristics; the most fundamental ones are their activation in response to immune system stimulation. The expression of these enzymes is dependent on immune response activators, such as pathogen-associated molecular patterns (PAMPs) and pro- or anti-inflammatory cytokines, as observed for IDO1 [12], ARG1 and iNOS [6], and ENTPD1 [48]. One exception to this pattern may be GAPDH; however, its regulatory activity is linked to the degradation of IFN-γ mRNA, whose expression is upregulated in response to PAMPs and cytokines [49]. As a consequence of this property, immunoregulatory enzymes are subject to negative feedback regulation. Upon activation by immune response stimuli (such as PAMPs and cytokines), they contribute to immune suppression and the maintenance of homeostasis. This mechanism prevents immune overactivation, which could otherwise lead to tissue damage and self-destruction [50].

The second key feature is the dependence of enzyme activity on the metabolic context in which it op-

erates. The effects of deprivation-based enzymes can be neutralized if a sufficient substrate concentration is maintained. Conversely, the activity of enzymes producing regulatory metabolites is enhanced under conditions of substrate abundance, and diminished when substrate availability declines. While deprivation enzymes also lose their level of activity when substrate levels decrease, their regulatory effect is actually amplified, as their primary function — substrate depletion — is achieved. IDO1 represents a distinct case, since it functions under both substrate excess and deficiency. A hypothesis suggests that IDO1 preferentially suppresses Th1 cells over Th2 cells, as kynurenines exert a pro-apoptotic effect on Th1 cells, whereas tryptophan depletion merely arrests Th2 cell proliferation [13]. Hence, the action of IDO1 may also be context-dependent: an excess of tryptophan suppresses Th1 cells via kynurenine production, while tryptophan depletion leads to broader suppression, affecting Th2 cells through enhanced deprivation. Given that Th1 and Th2 cells exert mutually inhibitory effects [51], it can be hypothesized that under normal tryptophan concentrations, IDO1 supports a Th2-mediated immune response, whereas the overall T-cell activity is suppressed under conditions of tryptophan deficiency.

Antimicrobial activity is another characteristic feature of some immunoregulatory enzymes (although not all of them are being discussed in this review). IDO1 [22], ARG1 [30], and iNOS [34] exhibit antimicrobial properties and are utilized by the immune system to combat specific pathogens. The mechanisms underlying the antimicrobial activity of these enzymes are analogous to their immunoregulatory functions: either through deprivation of essential compounds, thereby restricting the proliferative activity of the pathogen [22], or through the synthesis of antimicrobial metabolites [34]. It can be hypothesized that the original function of these enzymes was primarily to combat infectious agents, but they have also acquired a regulatory role over the course of evolution. This adaptation was likely to occur, because the metabolism of highly active immune cells, such as proliferating lymphocytes, resembles that of rapidly dividing pathogen cells (e.g., bacteria, fungi, and protozoa). It has been suggested that certain immunoregulatory mechanisms may have evolved from effector mechanisms originally designed for pathogen elimination.

POTENTIAL IMMUNOREGULATORY ENZYMES AND STRATEGIES FOR THEIR IDENTIFICATION

Based on the characteristics of immunoregulatory enzymes, it is possible to propose strategies for identifying new members of the group. A fundamental criterion for potential candidates is that enzymes involved
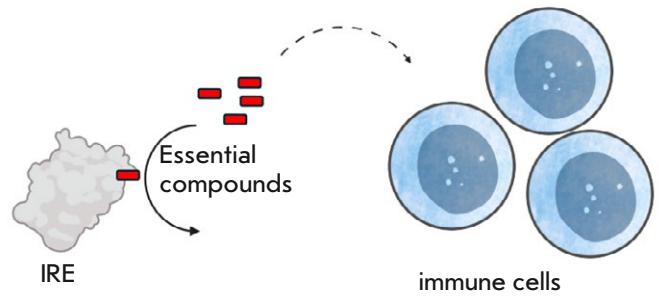
Fig. 2. The regulation mechanism through the deprivation of essential and conditionally essential compounds
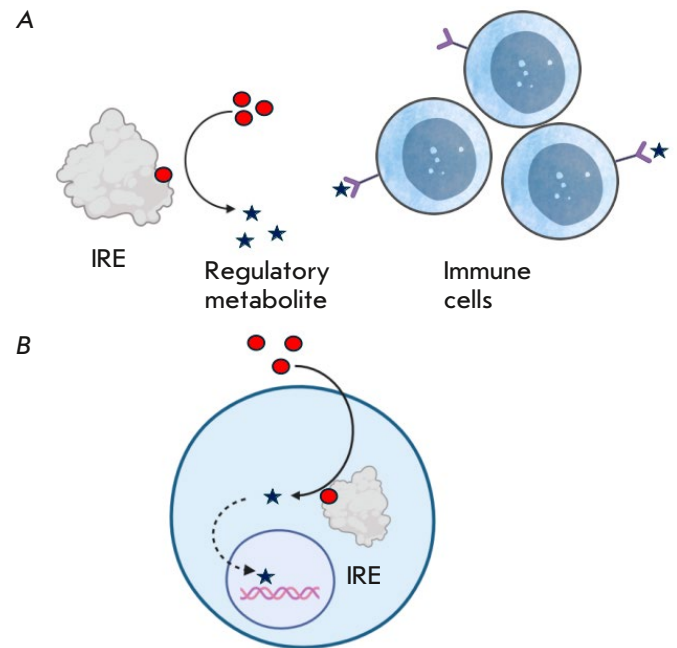

Fig. 3. The mechanism of immune cell regulation through the synthesis of a regulatory metabolite. (*A*) Synthesis of a regulatory metabolite outside the cell (external regulation); (*B*) synthesis of a regulatory metabolite inside the cell (internal regulation)
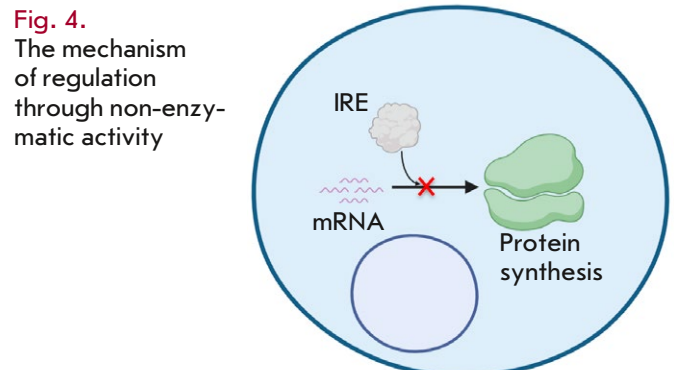

Fig. 4. The mechanism of regulation through non-enzymatic activity

in immune regulation must be responsive to immune activation. This feature can be assessed using bioinformatics approaches, such as analyzing the promoter sequence of the gene encoding the protein to identify binding sites for the proteins involved in pro- or anti-inflammatory signaling pathways [52], such as NF-kB [53]. If a protein lacks binding sites for known signaling factors, it may still play a role in immune regulation by being indirectly activated through alternative signaling pathways not yet directly linked to the inflammatory response. In such cases, differential gene expression analysis [54] upon immune activation can be used to identify potential candidates. The most promising candidates should yield positive results in both of these approaches. Once an enzyme's activation during the immune response is confirmed, its regulatory mechanism is then determined.

Deprivation of an essential or conditionally essential compound

A distinctive feature of this mechanism is that suitable properties may be found in enzymes involved in the catabolism of essential compounds. These enzymes may either be the first in the cascade of metabolic reactions (as seen with IDO1 and ARG1) or act as rate-limiting enzymes within the metabolic pathways of the respective substrates. A critical aspect is the identification of essential compounds, since it has been demonstrated that in activated immune cells exhibiting a significantly increased anabolic activity, certain substrates become essential even if they can be synthesized by the body. For instance, glutamine is required for the proliferative response of T-lymphocytes, as shown in human and animal cell cultures [55]. This suggests that glutaminase 1 is a potential immunoregulatory enzyme. In human cell cultures, inhibition of glutaminase 1 was shown to suppress the proliferation of CD4+ T-lymphocytes [56], which is consistent with the role of glutaminolysis in supporting lymphocyte proliferation. *Mycobacterium tuberculosis* has recently been found to inhibit glutaminase 1 in murine macrophage cultures, promoting pathogen survival [57]. Tumor cells (as actively proliferating cells) or tumor microenvironment components may also leverage glutaminase to enhance glutamine metabolism, which is associated with a reduced antitumor immune response [58]. However, it remains unknown whether the immune system *per se* employs regulatory mechanisms mediated by glutaminase 1. Specifically, it is unclear whether certain immune cells, by consuming glutamine, can deplete this amino acid and thereby regulate the function of other immune cells, analogous to the mechanism of IDO1.

Vitamins are essential compounds required for the proliferation and differentiation of all cells, including those of the immune system [59]. Therefore, enzymes involved in vitamin metabolism may potentially possess immunoregulatory functions and could be classified as immunoregulatory enzymes. A notable example is dihydrofolate reductase, which is involved in folic acid metabolism. Folic acid deficiency was shown to affect the activity of immune cells in mice [60]. Moreover, experimental studies in mice have demonstrated that targeted depletion of T-lymphocyte populations expressing high levels of the folate receptor can be used to modulate immune responses [61]. In this context, folic acid deficiency within this specific subpopulation of immune cells may lead to functional impairments. However, it remains unknown whether immune cell populations can be regulated through folate depletion *in vivo*.

Synthesis of a regulatory metabolite

Many metabolites with signaling functions, such as hormones and neurotransmitters, are potential regulators of immune activity. For example, serotonin was shown to influence the proliferation and cytokine release of various immune cell types [62], making tryptophan hydroxylase a potential immunoregulatory enzyme. Another enzyme with an immunosuppressive function is L-amino acid oxidase (IL4I1), which mediates the synthesis of the tryptophan metabolites that activate AhR, similar to IDO1. This leads to immunosuppression and tumor progression in murine models, although further research is needed to confirm whether IL4I1 is actively utilized by immune cells *per se* [63]. A key feature of the enzyme triad — IDO1, IL4I1, and tryptophan hydroxylase — is their shared substrate, tryptophan. This suggests that a rational approach to identifying potential immunoregulatory enzymes involved in the synthesis of regulatory metabolites is to focus on enzymes that metabolize substrates already utilized by known immunoregulatory enzymes, or those involved in the synthesis of low-molecular-weight hormones and neurotransmitters. For instance, the neurotransmitter gamma-aminobutyric acid (GABA) is synthesized by immune cells and influences their function, making glutamate decarboxylase a potential immunoregulatory enzyme [64].

Non-enzymatic activity

A significant number of proteins with multiple biological activities have been identified [65]. The enzymes within this category represent potential immunoregulatory enzymes. Non-enzymatic regulatory activity is not confined to GAPDH but is also observed in

another glycolytic enzyme, hexokinase. Hexokinase was shown to bind to the mitochondrial ion channel VDAC, allowing tumor cells to inhibit one of the apoptotic pathways under experimental conditions [66]. Hexokinase may also play a role in immune response regulation, potentially enhancing the survival of specific immune cell populations by reducing apoptosis. The most promising strategy for identifying non-enzymatic activity involves analyzing the protein structure and searching for RNA-binding motifs or interaction sites for signaling and structural proteins using modern bioinformatics approaches [67].

PROSPECTS FOR THE RESEARCH INTO IMMUNOREGULATORY ENZYMES

The research into immunoregulatory enzymes is not only of fundamental significance, but also holds great potential for medical applications. Technologies leveraging the functions of immunoregulatory enzymes have promising prospects in clinical practice. One of the best studied approaches is the use of immunoregulatory enzyme inhibitors. IDO1 inhibitors have been investigated as immunotherapeutic antitumor agents. Although their efficacy as monotherapy has been limited, these drugs exhibit synergistic capabilities when combined with immune checkpoint inhibitors [68]. Arginase inhibitors are also being explored as potential immunotherapeutic agents for cancer treatment [69]. Another strategy involves direct application of immunoregulatory enzymes. For example, recombinant human arginase has been used as an antitumor agent against arginine-auxotrophic tumors [70]. In murine experiments, the enzyme was injected into tumor tissue alongside standard therapy, utilizing the same essential substrate deprivation principle that underlies the regulation of rapidly proliferating cells. This strategy may be further enhanced by using scaffolds incorporating enzymes or their inhibitors for a localized modulation of the immune function. This approach, which is currently being actively developed for various immunomodulators [71], may have potential applications in cancer immunology, transplantation medicine, and the treatment of infectious and autoimmune diseases.

CONCLUSIONS

Immunoregulatory enzymes represent a relatively new field of research, and further studies are required for their identification, classification, and mechanistic characterization. By considering the features outlined in this review, the discovery of new members of this group may be made easier, as substantial knowledge already exists about metabolic reactions involving essential compounds and the enzymes induced by pro- or anti-inflammatory cytokines. Such proteins are the most promising candidates in terms of potential immunoregulatory properties. Regulation of immune responses through metabolism enriches our understanding of immune system biology and provides opportunities for the development of novel targeted interventions. The formation of feedback mechanisms through metabolic pathways may be leveraged for therapeutic purposes, allowing immune modulation through the administration of substrates, inhibitors, or enzymes *per se*, depending on the specific context of the disease. ●

REFERENCES
1. Villani A.C., Sarkizova S., Hacohen N. // Annu. Rev. Immunol. 2018. V. 36. № 1. P. 813–842. https://doi.org/10.1146/annurev-immunol-042617-053035.
2. O'Neill L.A.J., Kishton R.J., Rathmell J. // Nat. Rev. Immunol. 2016. V. 16. № 9. P. 553–565. https://doi.org/10.1038/nri.2016.70.
3. Maciolek J.A., Pasternak J.A., Wilson H.L. // Curr. Opin. Immunol. 2014. V. 27. P. 60–74. https://doi.org/10.1016/j.coi.2014.01.006.
4. Jung J., Zeng H., Horng T. // Nat. Cell Biol. 2019. V. 21. P. 85–93. https://doi.org/10.1038/s41556-018-0217-x.
5. Wu H., Gong J., Liu Y. // Mol. Med. Rep. 2018. V. 17. № 4. P. 4867–4873. https://doi.org/10.3892/mmr.2018.8537.
6. Munder M. // Br. J. Pharmacol. 2009. V. 158. № 3. P. 638–651. https://doi.org/10.1111/j.1476-5381.2009.00291.x.
7. Nakano T., Goto S., Takaoka Y., Tseng H.P., Fujimura T., Kawamoto S., Ono K., Chen C.L. // Biofactors. 2018. V. 44. № 6. P. 597–608. https://doi.org/10.1002/biof.1379.
8. Li Y., Jia A., Wang Y., Dong L., Wang Y., He Y., Wang S., Cao Y., Yang H., Bi Y., Liu G.J. // Cell. Physiol. 2019. V. 234. № 11. P. 20298–20309. https://doi.org/10.1002/jcp.28300.
9. Elebo N., Fru P., Omoshoro-Jones J., Candy G.P., Nweke E.E. // Mol. Med. Rep. 2020. V. 22. № 6. P. 4981–4991. https://doi.org/10.3892/mmr.2020.11622.
10. Xue C., Li G., Zheng Q., Gu X., Shi Q., Su Y., Chu Q., Yuan X., Bao Z., Lu J. // Cell Metab. 2023. V. 35. № 8. P. 1304–1326. https://doi.org/10.1016/j.cmet.2023.06.004.
11. Trabanelli S., Ocadlikova D., Evangelisti C., Parisi S., Curti A. // Curr. Med. Chem. 2011. V. 18. № 15. P. 2234–2239. https://doi.org/10.2174/092986711795656054.
12. Taylor M.W., Feng G. // FASEB J. 1991. V. 5. № 11. P. 2516–2522. https://doi.org/10.1096/fasebj.5.11.1907934.
13. Xu H., Zhang G.-X., Ciric B., Rostami A. // Immunol. Lett. 2008. V. 121. P. 1–6. https://doi.org/10.1016/j.imlet.2008.08.008.
14. Romagnani S. // Immunol. Today. 1991. V. 12. № 8.

P. 256–257. https://doi.org/10.1016/0167-5699(91)90120-I.

15. Munn D.H., Sharma M.D., Baban B., Harding H.P., Zhang Y., Ron D., Mellor A.L. // Immunity. 2005. V. 22. № 5. P. 633–642. https://doi.org/10.1016/j.immuni.2005.03.013.

16. Mezrich J.D., Fechner J.H., Zhang X., Johnson B.P., Burlingham W.J., Bradfield C.A. // J. Immunol. 2010. V. 185. № 6. P. 3190–3198. https://doi.org/10.4049/jimmunol.0903670.

17. Pallotta M.T., Orabona C., Volpi C., Vacca C., Belladonna M.L., Bianchi R., Servillo G., Brunacci C., Calvitti M., Bicciato S. // Nat. Immunol. 2011. V. 12. № 9. P. 870–878. https://doi.org/10.1038/ni.2077.

18. Munn D.H., Zhou M., Attwood J.T., Bondarev I., Conway S.J., Marshall B., Brown C., Mellor A.L. // Science. 1998. V. 281. № 5380. P. 1191–1193. https://doi.org/10.1126/science.281.5380.1191.

19. Zaher S.S., Germain C., Fu H., Larkin D.F.P., George A.J.T. // Invest. Ophthalmol. Vis. Sci. 2011. V. 52. № 5. P. 2640–2648. https://doi.org/10.1167/iovs.10-5793.

20. Ferns D.M., Kema I.P., Buist M.R., Nijman H.W., Kenter G.G., Jordanova E.S. // Oncoimmunology. 2015. V. 4. № 2. P. e981457. https://doi.org/10.4161/2162402X.2014.981457.

21. Donovan M.J., Tripathi V., Favila M.A., Geraci N.S., Lange M.C., Ballhorn W., McDowell M.A. // Parasite Immunol. 2012. V. 34. № 10. P. 464–472. https://doi.org/10.1111/j.1365-3024.2012.01380.x.

22. Njau F., Geffers R., Thalmann J., Haller H., Wagner A.D. // Microbes Infect. 2009. V. 11. № 13. P. 1002–1010. https://doi.org/10.1016/j.micinf.2009.07.006.

23. Fujiwara Y., Kato S., Nesline M.K., Conroy J.M., DePietro P., Pabla S., Kurzrock R. // Cancer Treat. Rev. 2022. V. 110. P. 102461. https://doi.org/10.1016/j.ctrv.2022.102461.

24. Jenkinson C.P., Grody W.W., Cederbaum S.D. // Comp. Biochem. Physiol. B Biochem. Mol. Biol. 1996. V. 114. № 1. P. 107–132. https://doi.org/10.1016/0305-0491(95)02138-8.

25. Popovic P.J., Zeh H.J. III, Ochoa J.B. // J. Nutr. 2007. V. 137. № 6. P. 1681S–1686S. https://doi.org/10.1093/jn/137.6.1681S.

26. Modolell M., Choi B.S., Ryan R.O., Hancock M., Titus R.G., Abebe T., Hailu A., Müller I., Rogers M.E., Bangham C.R.M., et al. // PLoS Negl. Trop. Dis. 2009. V. 3. № 7. P. e480. https://doi.org/10.1371/journal.pntd.0000480.

27. Pesce J.T., Ramalingam T.R., Mentink-Kane M.M., Wilson M.S., El Kasmi K.C., Smith A.M., Thompson R.W., Cheever A.W., Murray P.J., Wynn T.A. // PLoS Pathog. 2009. V. 5. № 4. P. e1000371. https://doi.org/10.1371/journal.ppat.1000371.

28. Dai X.K., Ding Z.X., Tan Y.Y., Bao H.R., Wang D.Y., Zhang H. // World J. Emerg. Med. 2022. V. 13. № 4. P. 266. https://doi.org/10.5847/wjem.j.1920-8642.2022.068.

29. Sippel T.R., White J., Nag K., Tsvankin V., Klaassen M., Kleinschmidt-DeMasters B.K., Waziri A. // Clin. Cancer Res. 2011. V. 17. № 22. P. 6992–7002. https://doi.org/10.1158/1078-0432.CCR-11-1107.

30. Munder M., Mollinedo F., Calafat J., Canchado J., Gil-Lamaignere C., Fuentes J.M., Luckner C., Doschko G., Soler G., Eichmann K. // Blood. 2005. V. 105. № 6. P. 2549–2556. https://doi.org/10.1182/blood-2004-07-2521.

31. Ochoa J.B., Bernard A.C., O'Brien W.E., Griffen M.M., Maley M.E., Rockich A.K., Tsuei B.J., Boulanger B.R., Kearney P.A., Morris S.M. // Jr. Ann. Surg. 2001. V. 233. № 3. P. 393–399. https://doi.org/10.1097/00000658-200103000-00014.

32. Duque-Correa M.A., Kühl A.A., Rodriguez P.C., Zedler U., Schommer-Leitner S., Rao M., Weiner J. III, Hurwitz R., Qualls J.E., Kosmiadi G.A. // Proc. Natl. Acad. Sci. USA. 2014. V. 111. № 38. P. E4024–E4032. https://doi.org/10.1073/pnas.1408839111.

33. Xiong H., Zhu C., Li F., Hegazi R., He K., Babyatsky M., Bauer A.J., Plevy S.E. // J. Biol. Chem. 2004. V. 279. № 11. P. 10776–10783. https://doi.org/10.1074/jbc.M313416200.

34. De Groote M.A., Fang F.C. // Clin. Infect. Dis. 1995. V. 21. Suppl. 2. P. S162–S165. https://doi.org/10.1093/clinids/21.Supplement_2.S162.

35. Yang J., Zhang R., Lu G., Shen Y., Peng L., Zhu C., Cui M., Wang W., Arnaboldi P., Tang M., Gupta M. // J. Exp. Med. 2013. V. 210. № 7. P. 1447–1462. https://doi.org/10.1084/jem.20122494.

36. Lu G., Zhang R., Geng S., Peng L., Jayaraman P., Chen C., Xu F., Yang J., Li Q., Zheng H. // Nat. Commun. 2015. V. 6. P. 6676. https://doi.org/10.1038/ncomms7676.

37. Soto-Heredero G., Gómez de Las Heras M.M., Gabandé-Rodríguez E., Oller J., Mittelbrunn M. // FEBS J. 2020. V. 287. № 16. P. 3350–3369. https://doi.org/10.1111/febs.15327.

38. Chang C.H., Curtis J.D., Maggi L.B., Faubert B., Villarino A.V., O'Sullivan D., Huang S.C.C., van der Windt G.J., Blagih J., Qiu J. // Cell. 2013. V. 153. № 6. P. 1239–1251. https://doi.org/10.1016/j.cell.2013.05.016.

39. Marijt K.A., Sluijter M., Blijleven L., Tolmeijer S.H., Scheeren F.A., van der Burg S.H., van Hall T. // J. Immunother. Cancer. 2019. V. 7. P. 152. https://doi.org/10.1186/s40425-019-0627-8.

40. Palmer C.S., Ostrowski M., Balderson B., Christian N., Crowe S.M. // Front. Immunol. 2015. V. 6. P. 1. https://doi.org/10.3389/fimmu.2015.00001.

41. Kukulski F., Lévesque S.A., Lavoie E.G., Lecka J., Bigonnesse F., Knowles A.F., Robson S.C., Kirley T.L., Sévigny J. // Purinergic Signal. 2005. V. 1. P. 193–204. https://doi.org/10.1007/s11302-005-6217-x.

42. Deaglio S., Dwyer K.M., Gao W., Friedman D., Usheva A., Erat A., Chen J.F., Enjyoji K., Linden J., Oukka M. // J. Exp. Med. 2007. V. 204. № 6. P. 1257–1265. https://doi.org/10.1084/jem.20062512.

43. Haskó G., Pacher P. // Arterioscler. Thromb. Vasc. Biol. 2012. V. 32. № 4. P. 865–869. https://doi.org/10.1161/ATVBAHA.111.226852.

44. Borsellino G., Kleinewietfeld M., Di Mitri D., Sternjak A., Diamantini A., Giometto R., Höpner S., Centonze D., Bernardi G., Dell'Acqua M.L. // Blood. 2007. V. 110. № 4. P. 1225–1232. https://doi.org/10.1182/blood-2006-12-064527.

45. Bastid J., Cottalorda-Regairaz A., Alberici G., Bonnefoy N., Eliaou J.F., Bensussan A. // Oncogene. 2013. V. 32. № 14. P. 1743–1751. https://doi.org/10.1038/onc.2012.269

46. Nascimento D.C., Viacava P.R., Ferreira R.G., Damaceno M.A., Piñeros A.R., Melo P.H., Donate P.B., Toller-Kawahisa J.E., Zoppi D., Veras F.P. // Immunity. 2021. V. 54. № 9. P. 2024–2041. https://doi.org/10.1016/j.immuni.2021.08.005.

47. El Kasmi K.C., Qualls J.E., Pesce J.T., Smith A.M., Thompson R.W., Henao-Tamayo M., Basaraba R.J., König T., Schleicher U., Koo M.S., Kaplan G. // Nat. Immunol. 2008. V. 9. № 12. P. 1399–1406. https://doi.org/10.1038/ni.1671.

48. Mascanfroni I.D., Yeste A., Vieira S.M., Burns E.J., Patel B., Sloma I., Wu Y., Mayo L., Ben-Hamo R., Efroni S. // Nat. Immunol. 2013. V. 14. № 10. P. 1054–1063. https://doi.org/10.1038/ni.2695.

49. Young H.A., Ghosh P. // Prog. Nucl. Acid Res. Mol. Biol. 1997. V. 56. P. 109–128. https://doi.org/10.1016/s0079-6603(08)61004-1.

50. Rosenblum M.D., Remedios K.A., Abbas A.K. // J. Clin. Invest. 2015. V. 125. № 6. P. 2228–2233. https://doi.org/10.1172/JCI78088.

51. Morel P.A., Oriss T.B. // Crit. Rev. Immunol. 1998. V. 18. № 4. P. 275–303. https://doi.org/10.1615/CritRevImmunol.v18.i4.10.

52. Bortoluzzi S., Coppe A., Bisognin A., Pizzi C., Danieli G.A. // BMC Bioinformatics. 2005. V. 6. № 1. P. 1–15. https://doi.org/10.1186/1471-2105-6-121.

53. Moynagh P.N.J. // Cell Sci. 2005. V. 118. № 20. P. 4589–4592. https://doi.org/10.1242/jcs.02579.

54. Costa-Silva J., Domingues D., Lopes F.M. // PLoS One. 2017. V. 12. № 12. P. e0190152. https://doi.org/10.1371/journal.pone.0190152.

55. Calder P.C., Yaqoob P. // Amino Acids. 1999. V. 17. P. 227–241. https://doi.org/10.1007/BF01366922.

56. Sener Z., Cederkvist F.H., Volchenkov R., Holen H.L., Skålhegg B.S. // PLoS One. 2016. V. 11. № 7. P. e0160291. https://doi.org/10.1371/journal.pone.0160291.

57. Yu J., Yan N., Gong Z., Ma Q., Liu J., Wu X., Deng G. // Cell. Signal. 2024. V. 124. P. 111422. https://doi.org/10.1016/j.cellsig.2024.111422.

58. Wang B., Pei., Xu S., Liu J., Yu J. // J. Exp. Clin. Cancer Res. 2024. V. 43. № 1. P. 74. https://doi.org/10.1186/s13046-024-02994-0.

59. Peterson C.T., Rodionov D.A., Osterman A.L., Peterson S.N. // Nutrients. 2020. V. 12. № 11. P. 3380. https://doi.org/10.3390/nu12113380.

60. Wu C.H., Huang T.C., Lin B.F. // J. Nutr. Biochem. 2017. V. 41. P. 65–72. https://doi.org/10.1016/j.jnutbio.2016.11.008.

61. Yamaguchi T., Hirota K., Nagahama K., Ohkawa K., Takahashi T., Nomura T., Sakaguchi S. // Immunity. 2007. V. 27. № 1. P. 145–159. https://doi.org/10.1016/j.immuni.2007.04.017.

62. Roumier A., Béchade C., Maroteaux L. // Serotonin. Acad. Press. 2019. P. 181–196. https://doi.org/10.1016/B978-0-12-800050-2.00010-3.

63. Sadik A., Patterson L.F.S., Öztürk S., Mohapatra S.R., Panitz V., Secker P.F., Pfänder P., Loth S., Salem H., Prentzell M.T., et al. // Cell. 2020. V. 182. № 5. P. 1252–1270. https://doi.org/10.1016/j.cell.2020.07.038.

64. Jin Z., Mendu S.K., Birnir B. // Amino Acids. 2013. V. 45. P. 87–94. https://doi.org/10.1007/s00726-011-1193-7.

65. Werelusz P., Galiniak S., Mołoń M. // Biochim. Biophys. Acta Mol. Cell Res. 2024. V. 1871. № 1. P. 119598. https://doi.org/10.1016/j.bbamcr.2023.119598.

66. Rodríguez-Saavedra C., Morgado-Martínez L.E., Burgos-Palacios A., King-Díaz B., López-Coria M., Sánchez-Nieto S. // Front. Mol. Biosci. 2021. V. 8. P. 701975. https://doi.org/10.3389/fmolb.2021.701975.

67. Zhang Y., Yan J., Chen S., Gong M., Gao D., Zhu M., Gan W. // Curr. Bioinform. 2020. V. 15. № 8. P. 898–911. https://doi.org/10.2174/1574893615999200711165743.

68. Le Naour J., Galluzzi L., Zitvogel L., Kroemer G., Vacchelli E. // Oncoimmunology. 2020. V. 9. № 1. P. 1777625. https://doi.org/10.1080/2162402X.2020.1777625.

69. Borek B., Gajda T., Golebiowski A., Blaszczyk R. // Bioorg. Med. Chem. 2020. V. 28. № 18. P. 115658. https://doi.org/10.1016/j.bmc.2020.115658.

70. Badeaux M.D., Rolig A.S., Agnello G., Enzler D., Kasiewicz M.J., Priddy L., Wiggins J.F., Muir A., Sullivan M.R., van Cleef J. // Cancer Immunol. Res. 2021. V. 9. № 4. P. 415–429. https://doi.org/10.1158/2326-6066.CIR-20-0317.

71. Adu-Berchie K., Mooney D.J. // Acc. Chem. Res. 2020. V. 53. № 9. P. 1749–1760. https://doi.org/10.1021/acs.accounts.0c00341.

The Toxin-Producing Ability of *Fusarium Proliferatum* Strains Isolated from Grain

O. P. Gavrilova[1*], A. S. Orina[1], T. Yu. Gagkaeva[1], N. N. Gogina[2]

[1]All-Russian Institute of Plant Protection, St. Petersburg, 196608 Russian Federation
[2]All-Russian Scientific Research and Technological Institute of Poultry, Sergiev Posad, 141311 Russian Federation
*E-mail: olgavrilova1@yandex.ru

ABSTRACT The widespread fungus *Fusarium proliferatum* can infect numerous plant species and produce a range of mycotoxins, the amount of which can vary significantly. Twelve *F. proliferatum* sensu lato strains isolated from six wheat, four oat, and two maize grain samples were analyzed. The strains were identified through a phylogenetic analysis of nucleotide sequences derived from gene fragments of the translation elongation factor EF-1α, β-tubulin, and RNA polymerase II second subunit. The mating types of the strain were determined by allele-specific PCR. Secondary toxic metabolite production by the strains was quantified using high-performance liquid chromatography-tandem mass spectrometry (HPLC-MS/MS). All twelve *Fusarium* strains formed a distinct clade alongside the *F. proliferatum* reference strains, thereby confirming the taxonomic identification. Only one idiomorph at the MAT locus in each *F. proliferatum* strain was found, indicative of heterothallic mating. The frequency of the MAT1-1 idiomorph was double that of the MAT1-2 idiomorph. The active biosynthesis of fumonisins B_1 (71–6175 mg/kg), B_2 (12–2661 mg/kg), and B_3 (6–588 mg/kg), significant beauvericin (64–455 mg/kg), and trace amounts of moniliformin (12–6565 µg/kg) were identified across all examined *F. proliferatum* strains.

KEYWORDS *Fusarium*, phylogenetic analysis, mycotoxins, HPLC-MS/MS.

ABBREVIATIONS FF – *Fusarium fujikuroi*; *tef* – the translation elongation factor 1-α gene; *tub* – β-tubilin gene; *rpb2* – second subunit gene of RNA polymerase II; ML (maximum likelihood) – maximum likelihood method; BP (Bayesian probability) – Bayesian posterior probability scores; MAT locus – mating type locus; HPLC-MS/MS – high-performance liquid chromatography coupled with a tandem mass spectrometry; FUM – group B fumonisins; FB_1 – fumonisin B_1; FB_2 – fumonisin B_2; FB_3 – fumonisin B_3; BEA – beauvericin; MON – moniliformin.

INTRODUCTION

Among the *Fusarium* genus, the *Fusarium fujikuroi* (FF) species complex is particularly large and serves as a prime illustration of the considerable evolution undergone by species concepts. A dataset of both morphological and molecular studies reveals the FF species complex to contain more than 60 identified species, though this figure is probably an underestimate [1]. Taxonomic resolution within the FF species complex is achieved through the integration of physiological and biochemical characteristics due to the ambiguity, instability, and limited utility of morphological traits for species delimitation. Molecular technologies have revealed the paraphyletic nature of previously characterized FF species, demonstrating morphological convergence among phylogenetically disparate taxa [2–4].

Species within the FF complex include plant pathogens, endophytes, and pathogens of humans and animals [5]. The secondary metabolites produced by these fungi exhibit structural diversity and include mycotoxins and phytohormones such as gibberellins, auxins, and cytokinins [6, 7]. A comprehensive understanding of secondary metabolite diversity within various members of the FF species complex remains elusive, with potential discrepancies even between closely related species. Distinguishing between *Fusarium* species with clarity and thoroughly characterizing their properties improves the accuracy of strain identification and expands our understanding of their biological features.

One of the most actively studied members of the FF species complex is *F. proliferatum* (Matsush.) Nirenberg ex Gerlach & Nirenberg. This is due to its ubiquitous distribution and ability to infect a wide range of plants [11], including cereals, legumes [12, 13], vegetables [14], and fruit crops [15–17]. The mani-
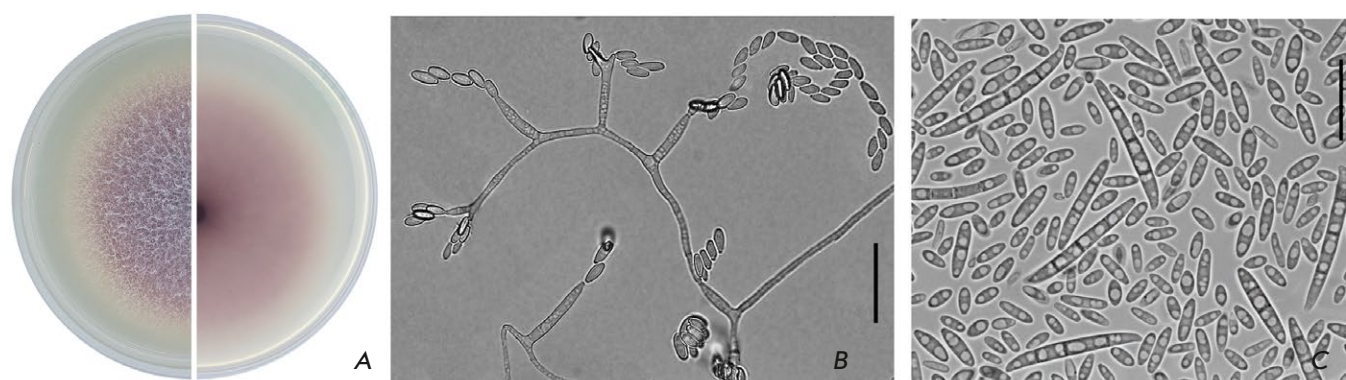
Fig. 1. (A) – culture of *F. proliferatum* MFG 58486 (potato-sucrose agar, 7 days, 25°C, in the dark); (B) – microconidia on mono- and polyphyalides; (C) – microconidia and macroconidia (synthetic Nirenberg agar, 14 days, 25°C, in the dark). Scale bars = 20 μm

festations of diseases caused by *F. proliferatum* include wilting and rot [13, 18, 19], with asymptomatic infection also frequently observed. Similar to the closely related species *F. verticillioides* (Sacc.) Nirenberg, *F. proliferatum* is one of the most harmful pathogens for maize, causing cob and stem rots [20]. Under optimal fungal growth conditions in cereal crops, infected wheat grains may exhibit stunted growth and black germ [21], while infected oats may display discoloration, necrotic lesions on spikelet scales, and grain browning [22].

Due to the abundant formation of microconidia in false heads, short chains on mono- and polyphyalides, and macroconidia (*Fig. 1*), *F. proliferatum* is easily spread through the air and transferred by insects to new uninfected plants [23]. Like many other pathogens, it persists in seeds [14] and on plant debris in soil [24].

F. proliferatum has a teleomorphic stage characterized by the formation of perithecia containing ascospores on the substrate surface [25]. Sexual reproduction in heterothallic members of the FF species complex requires different sets of opposite mating-type genes, this characteristic determined by the MAT locus and its two idiomorphs, MAT1-1 and MAT1-2 [26]. A balanced effective population size, with roughly equal proportions of each mating type, is necessary for sexual reproduction in heterothallic species. A skewed distribution of mating types, however, can impair sexual sporulation and diminish intraspecific diversity [27].

Similar to other fungi of the FF species complex, *F. proliferatum* produces toxic secondary metabolites: FUM, BEA, MON, fusaproliferin, fusarins, fusaric acid, and others, which can accumulate in grain and pose a health hazard to its consumers [28]. A reliable relationship between *F. proliferatum* infection of wheat grain and the amount of FUM detected in it

has been established [29, 30]. A summary of the current data on mycotoxin contamination in various cereal grains reveals that wheat and barley exhibit lower levels of fumonisin accumulation [31–33] compared to maize, which frequently displays significantly higher amounts [34, 35]. The mycotoxin amounts produced by *F. proliferatum* strains of different substrate origin can vary significantly, and both active producers and non-toxigenic strains can be found among them [8, 28, 29, 36–38].

The objective of this research was the phylogenetic identification of *F. proliferatum* strains isolated from cereal crops and the subsequent *in vitro* determination of their ability for mycotoxin production.

EXPERIMENTAL

Fusarium strains
A choice of twelve fungal strains, identified morphologically as belonging to the FF species complex, was made from the pure culture collection maintained in the laboratory of mycology and phytopathology of VIZR (*Table 1*). All the strains were isolated from grain samples collected from different regions of the Russian Federation: six from wheat (*Triticum aestivum* L.), four from oats (*Avena sativa* L.), and two from maize (*Zea mays* L.).

Molecular and genetic analysis
Potato-sucrose agar (PSA) was used as the growth medium for all fungal strains. Cultivation occurred within a KBW 400 thermostat (Binder, Germany) at 25°C for 7 days. Fungal DNA was isolated from the mycelium via a standard protocol employing a 2% cetyltrimethylammonium bromide/chloroform solution.

The *tef*, *tub*, and *rpb2* gene fragments were amplified using the primers EF1/EF2, T1/T2, and

Table 1. *F. proliferatum* strains included in the study

Strain number	Origin	Host plant	Year	GenBank accsession number		
				tef	*tub*	*rpb2*
MFG* 58227	Krasnodarskiy kray	wheat	2009	MW811114	OK000500	OK000527
MFG 58471	Krasnodarskiy kray	wheat	2012	MW811115	OK000501	OK000528
MFG 58486	Krasnodarskiy kray	wheat	2012	MW811117	OK000503	OK000530
MFG 59046	Krasnodarskiy kray	wheat	2016	MW811122	OK000508	OK000535
MFG 60309	Krasnodarskiy kray	wheat	2017	MW811125	OK000513	OK000540
MFG 60803	Amur region	wheat	2019	MW811134	OK000522	OK000549
MFG 58589	Leningrad region	oats	2013	MW811118	OK000504	OK000531
MFG 58590	Primorsky Krai	oats	2013	MW811119	OK000505	OK000532
MFG 92501	Leningrad region	oats	2007	MW811135	OK000524	OK000551
MFG 58667	Nizhny Novgorod region	oats	2014	MW811121	OK000507	OK000534
MFG 58484	Voronezh region	maize	2012	MW811116	OK000502	OK000529
MFG 58603	Lipetsk region	maize	2012	MW811120	OK000506	OK000533

*Note. MFG – the culture collection of the laboratory of mycology and phytopathology of VIZR, St. Petersburg, Russia.

fRPB2-5F/fRPB2-7Cr [39]. The resulting fragments were sequenced by the Sanger sequencing method on an ABIPrism 3500 sequencer (Applied Biosystems – Hitachi, Japan) using the BigDye Terminator v3.1 Cycle Sequencing Kit (ABI, USA). The consensus nucleotide sequences were aligned in the Vector NTI Advance 10 program (Thermo Fisher Scientific, USA) and deposited in the NCBI GenBank database (*Table 1*).

The phylogenetic analysis involved nucleotide sequences from representative *Fusarium* strains from the collections of the Agricultural Research Service Cultural Collection (NRRL, USA), Westerdijk Institute for Fungal Biodiversity (CBS, The Netherlands), and other collections (*Table 2*). The phylogenetic relationships among taxa were evaluated by the ML method using the program IQ-TREE 2 v.2.1.3. Optimal nucleotide substitution modeling for maximum likelihood (ML) tree inference was achieved using TIM2e+R2, as determined by IQ-TREE 2 v.2.1.3. A bootstrap analysis (1 000 replicates) was conducted to evaluate the robustness of the phylogenetic tree topology. The BP values were calculated using MrBayes version 3.2.1, implemented on the Armadillo 1.1 platform.

The mating type of the strains was identified by allele-specific PCR. The primers Gfmat1a/Gfmat1b (MAT1-1) and Gfmat1c/Gfmat1d (MAT1-2), designed for the FF species complex, were employed in accordance with the protocol in [40], but the annealing temperature was changed to 55°C. The fragment sizes corresponding to the MAT1-1 and MAT1-2 alleles were 200 and 800 bp, respectively.

Mycotoxin analysis

A mixture of twenty grams of rice grains and twelve milliliters of water contained within 250 mL glass vessels underwent autoclaving at 121°C for forty minutes. Following the autoclaving, the rice grains were cooled and inoculated with two 5 mm diameter disks cut from fungal cultures grown on PSA. Uninoculated grains served as the control. A two-week incubation period in the dark at 25°C was implemented, with daily shaking of the flasks. The samples were dried at 55°C for 24 h, then ground using a laboratory mill (IKA, Germany) at 25 000 rpm for one minute, and subsequently stored at -20°C.

HPLC-MS/MS analysis was used to determine the profile of secondary toxic metabolites [41]. Five grams of rice flour were combined with 20 milliliters of extraction solvent (acetonitrile/water/acetic acid, 79 : 20 : 1). Secondary metabolites detection and quantification were conducted using an AB SCIEX Triple Quad™ 5500 MS/MS system (Applied Biosystems, USA), incorporating a TurboV electrospray ionization source (SCIEX, USA) and an Agilent Infinity 1290 series microwave analysis system (Agilent, USA). Chromatographic separation was achieved using a Phenomenex (USA) Gemini C18 column (150 × 4.6 mm) at a temperature of 25°C.

The content of FB_1, FB_2, FB_3, BEA, and MON were analyzed in the extracts. Mycotoxin recovery rates ranged from 79% to 105%. Mycotoxin quantification was achieved through a comparative analysis of peak areas against the calibration curves generated from standard solutions (Romer Labs Diagnostic GmbH,

Table 2. Reference strains of *Fusarium* spp. included in the phylogenetic analysis

Species	Strain number in the collection*	Origin	Substrate	Year	GenBank accsession number		
					tef	*tub*	*rpb2*
F. acutatum	CBS 402.97 T	India		1995	MW402125	MW402323	MW402768
F. acutatum	NRRL 13308	India		1985	AF160276	MW402348	MN193883
F. agapanthi	NRRL 54463 T	Australia	*Agapanthus* sp.	2010	KU900630	KU900635	KU900625
F. agapanthi	NRRL 54464	Australia	*Agapanthus* sp.	2010	MN193856	KU900637	KU900627
F. aglaonematis	ZHKUCC 22-0077 T	China	*Aglaonema modestum*, stem	2020	ON330437	ON330440	ON330443
F. aglaonematis	ZHKUCC 22-0078	China	*Aglaonema modestum*, stem	2020	ON330438	ON330441	ON330444
F. anthophilum	CBS 119859	New Zealand	*Cymbidium* sp., leaves		MN533991	MN534092	MN534233
F. anthophilum	CBS 222.76 T	Germany	*Euphorbia pulcherrima*, stem		MW402114	MW402312	MW402811
F. concentricum	CBS 450.97 T	Costa Rica	*Musa sapientum*, fruit	1983	AF160282	MW402334	JF741086
F. concentricum	CBS 453.97	Guatemala	*Musa sapientum*	1996	MN533998	MN534123	MN534264
F. elaeagni	LC 13627 T	China	*Elaeagnus pungens*	2017	MW580466	MW533748	MW474412
F. elaeagni	LC 13629	China	*Elaeagnus pungens*	2017	MW580468	MW533750	MW474414
F. erosum	LC 15877 T	China	maize, stem	2021	OQ126066	OQ126321	OQ126518
F. erosum	LC 18581	China	maize, cob	2021	OQ126067	OQ126320	OQ126519
F. fujikuroi	CBS 221.76 T	Taiwan	*Oryza sativa*, stem	1973	MN534010	MN534130	KU604255
F. fujikuroi	CBS 257.52	Japan	*Oryza sativa*, seedling	1947	MW402119	MW402317	MW402812
F. globosum	CBS 428.97 T	South Africa	*Zea mays*, seed	1992	KF466417	MN534124	KF466406
F. globosum	CBS 120992	South Africa	*Zea mays*, seed	1992	MW401998	MW402198	MW402788
F. hechiense	LC 13644 T	China	*Musa nana*	2017	MW580494	MW533773	MW474440
F. hechiense	LC 13646	China	*Musa nana*	2017	MW580496	MW533775	MW474442
F. lumajangense	InaCCF 872 T	Indonesia	*Musa acuminata*, stem	2014	LS479441	LS479433	LS479850
F. lumajangense	InaCCF 993	Indonesia	*Musa acuminata*, stem	2014	LS479442	LS479434	LS479851
F. mangiferae	CBS 120994 T	Israel	*Mangifera indica*	1993	MN534017	MN534128	MN534271
F. mangiferae	NRRL 25226	India	*Mangifera indica*		AF160281	U61561	HM068353
F. nirenbergiae	CBS 744.97	USA	*Pseudotsuga menziesii*	1994	AF160312	U34424	LT575065
F. nygamai	NRRL 13448 T	Australia	*Sorghum bicolor*	1980	AF160273	U34426	EF470114
F. nygamai	CBS 834.85	India	*Cajanus cajan*		MW402154	MW402355	MW402821
F. panlongense	LC 13656 T	China	*Musa nana*	2017	MW580510	MW533789	MW474456
F. panlongense	MUCL 55950	China	*Musa* sp.	2012	LT574905	LT575070	LT574986

Table 2 (continued).

Species	Strain number in the collection[*]	Origin	Substrate	Year	GenBank accsession number		
					tef	*tub*	*rpb2*
F. proliferatum	NRRL 22944	Germany	*Cymbidium* sp.	1994	AF160280	U34416	JX171617
F. proliferatum	ITEM 2287	Italy			LT841245	LT841243	LT841252
F. proliferatum	NRRL 31071	USA	wheat	2001	AF291058	AF291055	
F. proliferatum	NRRL 32155	India	*Cicer arietinum*		FJ538242		
F. proliferatum	CBS 131570	Iran	wheat		JX118976		JX162521
F. sacchari	CBS 223.76 T	India	*Saccharum officinarum*	1975	MW402115	MW402313	JX171580
F. sacchari	CBS 131372	Australia	*Oryzae australiensis*, stem	2009	MN534033	MN534134	MN534293
F. sanyaense	LC 15882 T	China	maize, stem	2021	OQ126093	OQ126322	OQ126547
F. sanyaense	LC 18540	China	maize, stem	2021	OQ126095	OQ126308	OQ126549
F. siculi	CBS 142222 T	Italy	*Citrus sinensis*	2015	LT746214	LT746346	LT746327
F. siculi	CPC 27189	Italy	*Citrus sinensis*		LT746215	LT746347	LT746328
F. sterilihyposum	NRRL 53991	Brazil	*Mangifera indica*	2009	GU737413	GU737305	
F. sterilihyposum	NRRL 53997	Brazil	*Mangifera indica*	2009	GU737414	GU737306	
F. subglutinans	CBS 536.95				MW402139	MW402339	
F. subglutinans	CBS 136481	Italy	human blood		MW402059	MW402258	MW402748
F. verticillioides	NRRL 22172	Germany	maize	1992	AF160262	U34413	EF470122
F. verticillioides	CBS 531.95		*Zea mays*		MW402136	MW402336	MW402771
F. xylaroides	NRRL 25486 T	Côte d'Ivoire	*Coffea* sp., stem	1951	AY707136	AY707118	JX171630
F. xylaroides	CBS 749.79	Guinea	*Coffea robusta*	1963	MN534049	MN534143	MN534259

[*]Note. Acronyms of the culture collections: CBS – the Westerdijk Institute for Fungal Biodiversity (Utrecht, The Netherlands); InaCCF – the Indonesian Biology Research Center (Cibinong, Indonesia); ITEM – the Institute of Science of Food Production (Bari, Italy); LC – the laboratory of Dr. Lei Cai, Institute of Microbiology, Chinese Academy of Sciences (Beijing, China); MUCL – the Laboratory of Mycology, Université Catholique de Louvain (Ottigny-Louvain-la-Neuve, Belgium); NRRL – the Agricultural Research Service Cultural Collection (Peoria, USA); ZHKUCC – the Zhongkai University of Agriculture and Engineering (Guangzhou, China); T – type strain.

Austria). The limits of quantification for BEA and MON were 1.9 and 3.1 µg/kg, respectively; FB_1, FB_2, and FB_3 displayed limits of 8.7, 3.2, and 3.2 µg/kg, respectively.

Statistical analysis
Statistical computations were performed with the aid of Microsoft Excel 2010 and Minitab 17.0.

RESULTS AND DISCUSSION

Molecular and genetic characterization of the strains
The phylogenetic analysis included the combined sequences (1 913 bp) of three loci: *tef* – 615 bp, *tub* – 473 bp, and *rpb2* – 825 bp, with 154 bp (25.0%), 70 bp (14.8%), and 141 bp (17.1%) informative sites, respectively. All the twelve strains were clustered to a sep-
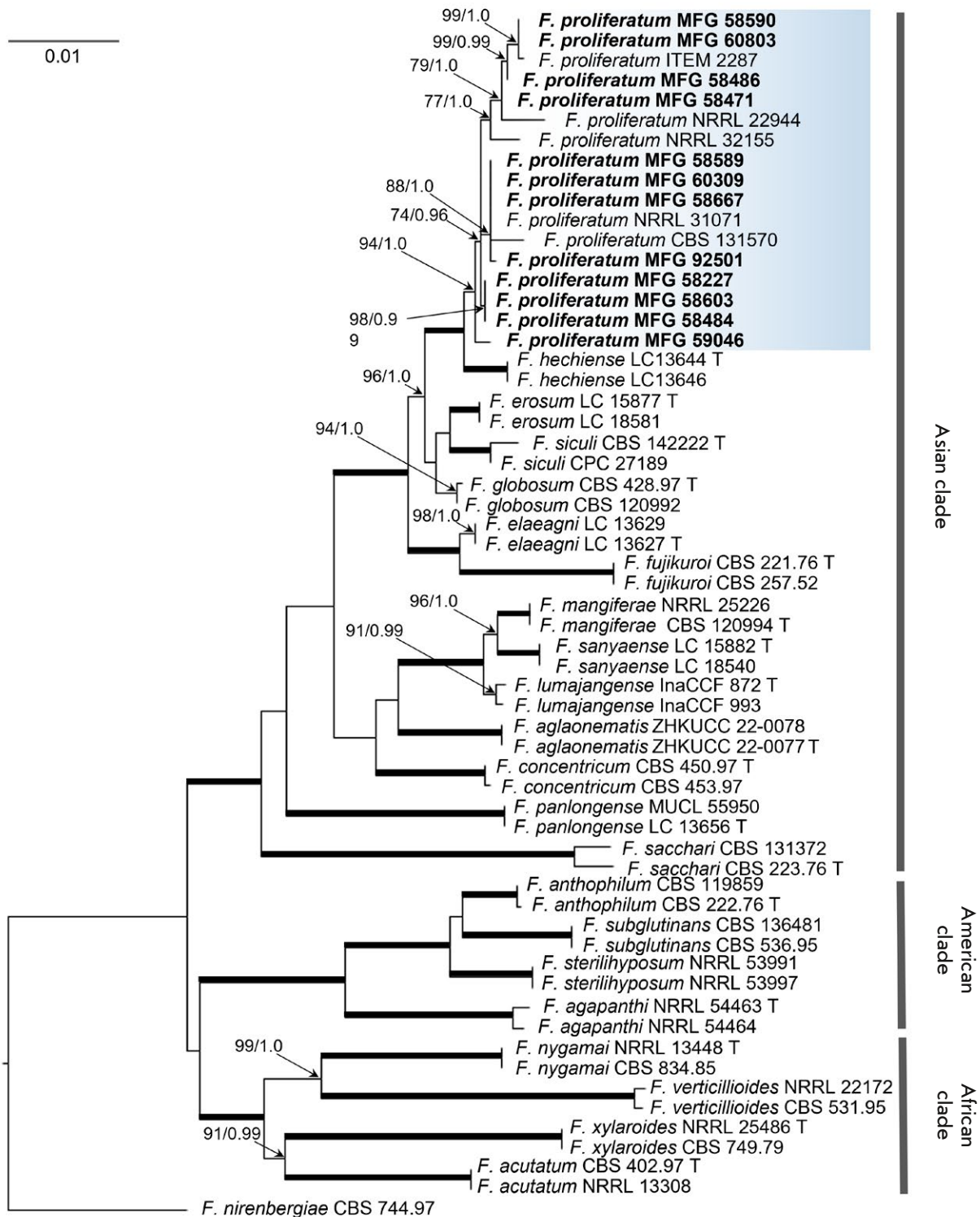
Fig. 2. Dendrogram of phylogenetic similarity of *Fusarium* spp. based on combined nucleotide sequences of the *tef*, *tub*, and *rpb2* gene fragments by the ML method. Nodes show bootstrap support values (> 70%) in the ML analysis, as well as BP values (> 0.95). The thickening of lines signifies support at the 100/1.0 ML/BP level. Strains within the study, obtained from the MFG collection, are denoted in bold. *F. nirenbergiae* strain CBS 744.97 was designated as the outgroup

Table 3. Toxin-producing ability of *F. proliferatum* strains isolated from different cereal crops

Host plant (number of strains)	Mycotoxins[*]		
	FUM, mg/kg	BEA, mg/kg	MON, µg/kg
Wheat (6)	3470 ± 1008	307 ± 67	1690 ± 764
Oat (4)	4024 ± 1930	385 ± 43	260 ± 158
Maize (2)	3538; 5578	363; 158	1041; 6565

[*]Presented are the mean values and the confidence intervals at a significance level of $p < 0.05$.

arate bootstrap-supported clade, ML/BP 94/1.0, also including five reference strains of *F. proliferatum* (*Fig. 2*). The *F. proliferatum* clade was distributed among the Asian group of FF species complex, and the topology of phylogenetic trees constructed by different methods was similar and consistent with the one reconstructed previously [1]. The resulting phylogenetic tree demonstrates significant genetic diversity within the *F. proliferatum* strains. The clades contained both the analyzed and reference strains, exhibiting no correlation between grouping and geographic or substrate source. Previous studies [8, 42, 43] have also observed a comparable categorization of *F. proliferatum* due to the substantial intraspecific variability of the species, irrespective of strain origin.

Specific PCR analysis demonstrated the presence of only one idiomorph at the MAT locus per *F. proliferatum* strain genotype, yielding an 8 : 4 ratio of MAT1-1 to MAT1-2 idiomorphs among the strains examined. The MAT locus is represented exclusively by the MAT1-2 idiomorph in the strains from maize and exclusively by the MAT1-1 idiomorph in the strains

from oat. The MAT locus in the strains from wheat exhibited a 4 : 2 ratio of MAT1-1 to MAT1-2 alleles.

The disproportionate prevalence of alternative mating types within the *F. proliferatum* populations appears to correlate with a decreased frequency of sexual reproduction in the wild, consequently limiting genetic diversity. Furthermore, this impacts the pathogen's capacity to adapt to fluctuating environmental conditions. The ratio of *F. proliferatum* strains isolated from cultivated plants with different idiomorphs at the MAT locus has been previously shown to vary [8, 42]. However, the *F. proliferatum* strains isolated from durum wheat grain in Argentina were characterized by an equal frequency of alternative alleles of the MAT locus, which allowed researchers to predict a high probability of detecting the sexual stage of the fungus in wheat fields [42].

Profile of the mycotoxins produced by *F. proliferatum*

All five mycotoxins (BEA, MON, FB_1, FB_2, and FB_3) were detected in extracts from rice grains inoculated by *F. proliferatum* strains. However, these were absent in the control.

All strains exhibited significant FUM production ranging from 100 to 9 424 mg/kg. FB_1 proved to be the predominant mycotoxin, amounting to 53–82% of total FUM. The mycotoxins FB_2 and FB_3 were found to be present in lower quantities, amounting to 9–28% and 2–39%, respectively. Among all the strains tested, MFG 58590 — isolated from oat grain originating in Primorsky Krai , Russia — produced the maximum amount of FUM. A marked reduction in total FB_1, FB_2, and FB_3 was observed in the strains MFG 92501 and MFG 60803 (100 and 135 mg/kg, respectively), compared to the other strains (1 077–7 077 mg/kg) (*Fig. 3*).

The BEA production in all the *F. proliferatum* strains was similarly high, ranging between 64 and 455 mg/kg. The MON production proved substantially less than that of the four other mycotoxins, displaying variability from 12 to 6 565 µg/kg. The analysis of strain MFG 92501 indicated no presence of MON within its mycotoxin profile.
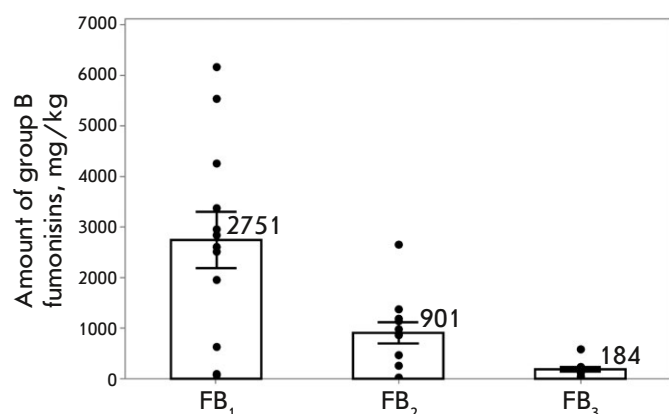

Fig. 3. Fumonisins production by *F. proliferatum* strains (autoclaved rice, 25°C, 14 days, in the dark). Presented are the mean values and the confidence intervals at a significance level of $p < 0.05$. The dots indicate the values for individual strains

The predominant FUM in the mycotoxin profile of *F. proliferatum* is FB_1, a characteristic independent of strain substrate origin [12, 37, 38, 44]. Our study has not revealed any statistically significant correlation between strain substrate origin and mycotoxin production (*Table 3*). The growth and fumonisin production of *F. proliferatum* are known to be affected by a multitude of abiotic and biotic factors [45–47]. The extensive host range of *F. proliferatum* demonstrates its considerable adaptive capacity, partly attributable to the synthesis of secondary metabolites. The ability to produce mycotoxins was found to be unrelated to the host plant from which *F. proliferatum* was isolated [23]. Infection of wheat with strains of this fungus isolated from different hosts resulted in the accumulation of FB_1 and BEA in the grain [23], despite the fact that the strains initially differed in toxin-producing ability, but the detected amount of FB_1 in infected wheat was much lower than that usually found in maize. The *F. proliferatum* strains isolated from maize grain were previously shown to possess a more variable FB_1 production ability than strains isolated from wheat grain [36]. The function of FUM, specifically FB_1, as a pathogenicity factor in *F. proliferatum* remains a subject of debate [48]. A cluster of genes (*FUM*) responsible for the biosynthesis of these mycotoxins has been identified in FUM producing *Fusarium* fungi [1, 11]. In contrast to *FUM19*, the genes *FUM1*, *FUM6*, *FUM8*, and *FUM21* were demonstrated to be essential for FUM synthesis in the *F. proliferatum* strains. The deletion of these genes leads not only to the loss of the ability of fungus to synthesize these mycotoxins, but also to a decrease in its aggressiveness against the host plant [49]. At the same time, it was recently discovered that *F. proliferatum* strains isolated from garlic could produce FUM *in vitro* but did not necessarily produce them *in planta* [38]. Furthermore, fungal exposure to host plant metabolites during colonization may influence mycotoxin production and concentration [50]. Although *F. proliferatum* inhabits the mycobiota of Eurasian wheat, barley, and oat, elevated fumonisin amounts in their grains are atypical, contrasting with the common detection of beauvericin and the less frequent detection of moniliformin [30, 51, 52]. Presumably, wheat grain is a less suitable substrate for FUM accumulation than maize [23, 44].

CONCLUSION

The phylogenetic study of *F. proliferatum* strains isolated from three cereal crops grown on the territory of the Russian Federation demonstrated significant intraspecific heterogeneity, independent of the geographical and substrate strain origin. Such an uneven distribution of *F. proliferatum* strains with differing mating types is likely to diminish the significance of sexual reproduction in the life cycle of this heterothallic fungus. In conjunction with environmental factors, the considerable mycotoxin production potential of *F. proliferatum* suggests a high risk of grain contamination, thus necessitating systematic monitoring. ●

REFERENCES

1. Yilmaz N., Sandoval-Denis M., Lombard L., Visagie C.M., Wingfield B.D., Crous P.W. // Persoonia. 2021. V. 46. P. 129–162.
2. Leslie J.F. // Canadian J. Botany. 1995. V. 7. P. 282–291.
3. O'Donnell K., Nirenberg H.I., Aoki T., Cigelnik E. // Mycoscience. 2000. V. 41. P. 61–78.
4. Kvas M., Marasas W.F.O., Wingfield B.D., Wingfield M.J., Steenkamp E.T // Fungal Diversity. 2009. V. 34. P. 1–21.
5. Wigmann E.F., Behr J., Vogel R.F., Niessen L. // Appl. Microbiol. Biotechnol. 2019. V. 103. P. 5323–5337.
6. Brown D.W., Proctor R.H. // Fungal Genetics Biol. 2016. V. 89. P. 37–51.
7. Niehaus E.-M., Münsterkötter M., Proctor R.H., Brown D.W., Sharon A., Idan Y., Oren-Young L., Sieber C. M., Novák O., Pěnčík A., et al. // Genome Biol. Evol. 2016. V. 8. № 11. P. 3574–3599.
8. Jurado M., Marín P., Callejas C., Moretti A., Vázquez C., González-Jaén M.T. // Food Microbiol. 2010. V. 27. № 1. P. 50–57.
9. Proctor R.H., van Hove F., Susca A., Stea G., Busman M., van der Lee T., Waalwijk C., Moretti A., Ward T.J. // Mol. Microbiol. 2013. V. 90. № 2. P. 290–306.
10. Stępień L., Koczyk G., Waśkiewicz A. // Fungal Biol. 2011. V. 115. № 2. P. 112–123.
11. Proctor R.H., Desjardins A.E., Moretti A. The role of plant pathology in food safety and food security / Eds Strange R., Gullino M. Dordrecht: Springer, 2010. V. 3. P. 97–111.
12. Qiu J., Lu Y., He D., Lee Y.W., Ji F., Xu J., Shi J. // Plant Disease. 2020. V. 104. № 8. P. 2193–2201.
13. Yu H., Hwang S.F., Strelkov S.E. // Pathogens. 2024. V. 13. № 5. P. 407.
14. Mondani L., Chiusa G., Pietri A., Battilani P. // Postharvest Biol. Technol. 2021. V. 173. Art. 111407.
15. Xie L., Wu Y., Duan X., Li T., Jiang Y. // Microbiol. Res. 2022. V. 256. Art. 126952.
16. Duan Y.N., Jiang W.T., Zhang R., Chen R., Chen X.S., Yin C.M., Mao Z.Q. // Plant Dis. 2022. V. 106. № 11. P. 2958–2966.
17. López-Moral A., Antón-Domínguez B.I., Lovera M., Arquero O., Trapero A., Agustí-Brisach C. // Sci. Repts. 2024. V. 14. Art. 5720.
18. Gaige A.R., Todd T., Stack J.P. // Plant Dis. 2020. V. 104. № 8. P. 2102–2110.
19. Koo Y.M., Ahsan S.M., Choi H.W. // Mycobiology. 2023.

V. 51. № 3. P. 186–194.

20. Munkvold G.P. // Eur. J. Plant Pathol. 2003. V. 109. P. 705–713.

21. Desjardins A.E., Busman M., Proctor R.H., Stessman R. // Food Addit. Contam. Part A. 2007. V. 24. № 10. P. 1131–1137.

22. Molnár O. // Eur. J. Plant Pathol. 2016. V. 146. P. 699–703.

23. Guo Z., Pfohl K., Karlovsky P., Dehne H.W., Altincicek B. // PLoS One. 2018. V. 13. № 9. Art. e0204602.

24. Gaige A.R., Giraldo M., Todd T., Stack J.P. // Canadian J. Plant Pathol. 2019. V. 41. № 2. P. 242–250.

25. Booth C. The genus *Fusarium*. Kew: Commonwealth Mycological Institute, 1971. 237 p.

26. Martin S.H., Wingfield B.D., Wingfield M.J., Steenkamp E.T. // Fungal Genet. Biol. 2011. V. 48. P. 731–740.

27. Leslie J.F., Klein K.K. // Genetics. 1996. V. 144. P. 557–567.

28. Stankovic S., Levic J., Petrovic T., Logrieco A., Moretti A. // Eur. J. Plant Pathol. 2007. V. 118. P. 165–172.

29. Guo Z., Pfohl K., Karlovsky P., Dehne H.-W., Altincicek B. // Agricult. Food Sci. 2016. V. 25. P. 138–145.

30. Senatore M.T., Prodi A., Tini F., Balmas V., Infantino A., Onofri A., Cappelletti E., Oufensou S., Sulyok M., Covarelli L. // J. Sci. Food Agriculture. 2023. V. 103. № 9. P. 4503–4521.

31. Stanković S., Lević J., Krnjaja V. // Biotechnol. Animal Husbandry. 2011. V. 27. № 3. P. 631–641.

32. Cendoya E., Chiotta M.L., Zachetti V., Chulze S.N., Ramirez M.L. // J. Cereal Sci. 2018. V. 80. P. 158–166.

33. Kononenko G.P., Burkin A.A., Zotova Ye.V. // Veterinary Sci. Today. 2020. V. 2. P. 139–145.

34. Kamle M., Mahato D.K., Devi S., Lee K.E., Kang S.G., Kumar P. // Toxins. 2019. V. 11. № 6. Art. 328.

35. Kononenko G.P., Burkin A.A., Zotova Ye.V., Smirnov A.M. // Rossiyskaya sel'skokhozyaystvennaya nauka. 2019. V. 3. P. 28–31. (In Russian)

36. Tancic S., Stankovic S., Levic J., Krnjaja V., Vukojevi J. // Genetika. 2012. V. 44. № 1. P. 163–176.

37. Gálvez L., Urbaniak M., Waśkiewicz A., Stępień Ł., Palmero D. // Food Microbiol. 2017. V. 67. P. 41–48.

38. Gasser K., Sulyok M., Spangl B., Krska R., Steinkellner S., Hage-Ahmed K. // Postharvest Biol. Technol. 2023. V. 200. Art. 112312.

39. O'Donnell K., Laraba I., Geiser D.M. Fusarium wilt. Methods in molecular biology. New York: Humana, 2022. P. 1–20.

40. Steenkamp E.T., Wingfield B.D., Coutinho T.A., Zeller K.A., Wingfield M.J., Marasas W.F.O., Leslie J.F. // Appl. Environ. Microbiol. 2000. V. 66. P. 4378–4382.

41. Malachová A., Sulyok M., Beltrán E., Berthillera F., Krska R. // J. Chromatography A. 2014. V. 1362. P. 145–156.

42. Palacios S.A., Susca A., Haidukowski M., Stea G., Cendoya E., Ramírez M.L., Chulze S.N., Farnochi M.C., Moretti A., Torres A.M. // Internat. J. Food Microbiol. 2015. V. 201. P. 35–41.

43. Wang L., Liu Q., Ge S., Liang W., Liao W., Li W., Jiao G., Wei X., Shao G., Xie L., et al. // Front. Microbiol. 2022. V. 13. Art. 1004454.

44. Busman M., Desjardins A.E., Proctor R.H. // Food Addit. Contam. Part A. 2012. V. 29. № 7. P. 1092–1100.

45. Cendoya E., Pinson-Gadais L., Farnochi M.C., Ramirez M.L., Chéreau S., Marcheguay G., Ducos C., Barreau C., Richard-Forget F. // Internat. J. Food Microbiol. 2017. V. 253. P. 12–19.

46. Vismer H.F., Shephard G.S., van der Westhuizen L., Mngqawa P., Bushula-Njah V., Leslie J.F. // Internat. J. Food Microbiol. 2019. V. 296. P. 31–36.

47. Dong T., Qiao S., Xu J., Shi J., Qiu J., Ma G. // Toxins. 2023. V. 15. № 4. Art. 260.

48. Xie L., Wu Y., Wang Y., Jiang Y., Yang B., Duan X., Li T. // Environ. Poll. 2021. V. 288. Art. 117793.

49. Sun L., Chen X., Gao J., Zhao Y., Liu L., Hou Y., Wang L., Huang S. // Toxins. 2019. V. 11. № 6. Art. 327.

50. Lalak-Kańczugowska J., Witaszak N., Waśkiewicz A., Bocianowski J., Stępień Ł. // Internat. J. Mol. Sci. 2023. V. 24. № 3. Art. 3002.

51. Fraeyman S., Croubels S., Devreese M., Antonissen G. // Toxins. 2017. V. 9. № 7. Art. 228.

52. Gavrilova O.P., Gagkaeva T.Yu., Orina A.S., Gogina N.N. // Dokl. Biol. Sci. 2023. V. 508. № 1. P. 9–19.

Induction of Chaperone Synthesis in Human Neuronal Cells Blocks Oxidative Stress-Induced Aging

E. A. Dutysheva[1], L. S. Kuznetcova[1], I. A. Utepova[2,3], B. A. Margulis[1], I. V. Guzhova[1], V. F. Lazarev[1*]

[1]Institute of Cytology RAS, St. Petersburg, 194064 Russian Federation
[2]Ural Federal University named after the first President of Russia B. N. Yeltsin, Yekaterinburg, 620002 Russian Federation
[3]I. Ya. Postovsky Institute of Organic Synthesis, Ural Branch of the Russian Academy of Sciences, Yekaterinburg, 620108 Russian Federation
*Email: lazarev@incras.ru

ABSTRACT Oxidative stress accompanies many pathologies that are characterized by neuronal degradation leading to a deterioration of the disease. The main causes are the disruption of protein homeostasis and activation of irreversible processes of cell cycle disruption and deterioration of cellular physiology, leading to senescence. In this paper, we propose a new approach to combating senescence caused by oxidative stress. This approach is based on the use of a low-molecular inducer of chaperone synthesis, one of the cell protective systems regulating proteostasis and apoptosis. We present data demonstrating the ability of the pyrrolylazine derivative PQ-29 to induce chaperone accumulation in human neuronal cells and prevent oxidative stress-induced aging.
KEYWORDS oxidative stress, senescence, chaperones, pyrrolylazines, apoptosis, neuroprotection.
ABBREVIATIONS ROS – reactive oxygen species; HSP – heat shock protein; ATP – adenosine triphosphate; AIF – apoptosis inducing factor; HRP – horseradish peroxidase; PBS – phosphate-buffered saline; FBS – fetal bovine serum; SYP – synaptophysin.

INTRODUCTION

Oxidative stress accompanies the majority of disorders characterized by neuronal degradation, including neurodegenerative diseases, traumatic brain injury, stroke, etc. In these disorders, the production of reactive oxygen species (ROS) in neuronal cells causes damage to proteins, lipids, and DNA and thus provokes cell senescence, which increases the risk of concomitant diseases.

Mitochondria are the main ROS source and target in the cell. ROS can cause the collapse of the mitochondrial membrane potential, the disruption of mitochondrial ultrastructure, and ATP depletion [1]. Damage to mitochondria can lead to necrosis and apoptosis. In addition, oxidative stress and mitochondrial malfunction can activate the p53/p21 and Rb/p16 pathways [2]. Both pathways increase the expression and activity of senescence-associated β-galactosidase. Therefore, combating the effects of cell-damaging oxidative stress is an important part of treating the majority of neurodegenerative diseases.

Heat shock proteins (HSP, chaperones) are important neuroprotective factors. These proteins play a significant role in preventing many types of cell death by targeting and destroying damaged proteins in the cell. For example, chaperone Hsp70 can prevent apoptosome formation, interact with the apoptosis-inducing factor (AIF) and pro-apoptotic protein Bim, and deactivate caspases 3 and 7 [3–5].

Another chaperone, Hsp90, also suppresses the activation of cell death signaling pathways. Hsp90 was shown to prevent apoptosome formation by binding to Apaf-1 and further inhibiting the oligomerization of the latter and its recruitment of caspase-9 [6]. It is important to note that both Hsp70 and Hsp90 bind denatured, misfolded proteins – including those misfolded due to excessive oxidation – and prevent their assembly into oligomers and aggregates [7].

Other important proteins required for the proper functioning of the chaperone machinery are co-chaperones. They are polypeptides containing the J domain, such as the Hsp40 protein. Co-chaperones regu-

late the formation of complexes between Hsp70 and client proteins, thus recognizing and degrading denatured and oxidized proteins [8].

In this context, it becomes interesting to study the potential chemical compounds might possess to stimulate the production of heat shock proteins for the protection of the nervous system. Compounds that are capable of inducing chaperone accumulation in cells have demonstrated their effectiveness in such disease models as Parkinson's [9], Alzheimer's [10], secondary damage after traumatic brain injury [11], and many others [12]. We have previously established that some pyrrolylazine derivatives can activate chaperone synthesis and accumulation, exerting a therapeutic effect in an *in vitro* model of Alzheimer's disease [13]. The PQ-29 derivative (3-(5-phenyl-1H-pyrrol-2-yl) quinoxalin-2(1H)-one) proved the most effective in this regard. In this work, we studied the ability of this compound to stave off oxidative stress-induced senescence in human neuronal cells.

EXPERIMENTAL

Neuronal cells

To confirm the chaperone-inducing and neuroprotective effects of pyrrolylazines, we used human dental pulp-derived mesenchymal stem cells (MSC-DP) as previously described [14]. MSC-DP cells were obtained from the "Vertebrate Cell Culture Collection" supported by the Ministry of Education and Science of the Russian Federation (Agreement No. 075-15-2021-683). The cells were cultured in a DMEM/F12 medium (Gibco, USA) supplemented with 10% fetal bovine serum (FBS; Gibco), 100 U/ml penicillin, and 0.1 mg/ml streptomycin (BioloT Ltd., Russia) at 37℃ and 5% CO_2.

The cells were reprogrammed into neuronal-phenotype cells (MSC-Neu) by incubation in a Neurobasal medium (BioinnLabs, Russia) supplemented with Neuromax (PanEco, Russia), 3% FBS, 100 U/ml penicillin, and 0.1 mg/ml streptomycin (PanEco) for 5 days. The neuronal phenotype was verified by analyzing the expression of a panel of mature neuron markers [15, 16], including β3-tubulin, NeuN, MAP2, synaptophysin (SYP), PSD95, and NeuroD1 by real-time RT-PCR.

RNA isolation and real-time PCR

RNA was isolated using an ExtractRNA kit (JSC Evrogen, Russia). Reverse transcription was conducted using a MMLV RT kit (JSC Evrogen) according to the manufacturer's instructions. RT-PCR was performed using the CFX96 real-time PCR detection system (BioRad, USA) and qPCRmix-HS SYBR

Table 1. The primers used in the study

Gene	Primer, nucleotide sequence
Actin	F – 5'-TCAATGTCCCAGCCATGTATGT-3'
	R – 5'-GTGACACCATCTCCAGAGTCC-3'
NeuN	F – 5'-CAAGGACGGTCCAGAAGGAG-3'
	R – 5'-GGTAGTGGGAGGTGAGGTCT-3'
MAP2	F – 5'-GGAGGGCGCTAAGTCCG-3'
	R – 5'-AAAATCTGGGCGCAGAAACTG-3'
NeuroD1	F – 5'-TCTTCCACGTTAAGCCTCCG-3'
	R – 5'- CCATCAAAGGAAGGGCTGGT-3'
β3-tubulin	F – 5'-CCATGAAGGAGGTGGACGAG-3'
	R – 5'-ACGTTGTTGGGGATCCACTC-3'
Syp	F – 5'-CTTCGCCATCTTGCCTTTG-3'
	R – 5'-TCACTCTCGGTCTTGTTGGC-3'
PSD95	F – 5'-GGATATGTGAACGGGACCGA-3'
	R – 5'-AAGCCCAGACCTGAGTTACC-3'
p16	F – 5'-ATAGTTACGGTCGGAGGCCG-3'
	R – 5'-CACGGGTCGGGTGAGAGTG-3'
p21	F – 5'-CTCAGAGGAGGCGCCATGT-3'
	R – 5'-CGCCATTAGCGCATCACAG-3'

kit (JSC Evrogen) according to the manufacturer's protocol. PCR amplicon specificity was confirmed by melting curve analysis. Primer sequences are presented in *Table 1*. All primers were synthesized by JSC Evrogen. PCR parameters were as follows: 5 min pre-denaturation at 95℃ followed by 40 cycles of 30 s at 95℃, 30 s at 65℃, and 30 s at 70℃. The fold change was analyzed using the BioRadCFX software.

Aging analysis

The activity of β-galactosidase in MSC-DP and MSC-Neu cells was assessed using a Beta-Glo assay system (Promega, UK) according to the manufacturer's instructions. Luminescence was measured on a Varioskan LUX microplate reader (Thermo Fisher Scientific, USA).

Electrophoresis and western blot analysis

MSC-Neu cells were treated with 100 μM hydrogen peroxide for 2 h and incubated with PQ-29 at concentrations of 0.5, 2, 8, and 300 μM for 1 and 2 h. The cells were lysed; lysates were used for electrophoresis and blotting analysis according to the previously described protocol [17]. Antibodies against Hsp40 (clone J32), Hsp70 (clone 3C5) [18], and Hsp90 (Thermo Fisher Scientific) were used for the analysis. Anti-tubulin antibodies (Thermo Fisher Scientific) were used as a loading control. Horseradish peroxidase (HRP)-conjugated goat anti-mouse and anti-rab-

bit antibodies (Repertoire, Russia) were used as secondary antibodies. Band intensities were calculated in arbitrary units (A.U.) using the TotalLab Quant 1.0 software (TotalLab, Gosforth, UK). The data were normalized to the mean intensity of tubulin staining.

Cytotoxicity analysis

The cytotoxic effects of PQ-29 were evaluated using the Mosmann dehydrogenase activity MTT assay [19]. LC_{50} was determined for PQ-29 in MSC-Neu cells. The cells were incubated with PQ-29 at a concentration range of 0.05 to 1 000 μM. The MTT test was conducted 48 h after incubation. Each experiment was performed in quadruplicate.

To confirm necrosis and apoptosis, the cells were placed in a 96-well plate and treated with 5 mg/ml ethidium bromide and 5 mg/ml acridine orange in phosphate-buffered saline (PBS). The stained cells were then examined on a Zeiss Axioscope (Carl Zeiss, Germany).

Statistical analysis

The mean ± standard deviation was calculated. Data were processed using the non-parametric Mann–Whitney test and the GraphPad Prism 8 software. Each experiment was conducted in at least a triplicate. Differences were considered statistically significant at $p < 0.05$.

RESULTS

At the first stage of the study, we tested the human model of oxidative stress-induced neuronal aging. For this, we used dental pulp-derived mesenchymal stem cells (MSC-DP) reprogrammed into the neuronal phenotype (MSC-Neu). To confirm the MSC-Neu neuronal phenotype after cell differentiation, we analyzed the following neuronal markers by RT-PCR: β3-tubulin, MAP2, SYP, NeuroD1, PSD95, and NeuN. The RT-PCR showed a significant increase in the mRNA levels of the studied genes after differentiation. The expression of mature neuron markers (namely, SYP, NeuroD1, PSD95, and NeuN) increased approximately threefold (*Fig. 1A*). The expression of early neuronal markers (β3-tubulin and MAP2) also increased, although insignificantly compared to that of mature neuron markers: approximately 1.4- to 1.5-fold.

We analyzed the ability of hydrogen peroxide to induce senescence in human neuronal cells. For this, MSC-Neu cells were cultured in either 100 or 300 μM hydrogen peroxide for 1 and 2 h. Next, the activity of β-galactosidase, a common senescence marker, was determined using a Beta-Glo assay system (*Fig. 1B*). Incubation of MSC-Neu cells with 100 and 300 μM
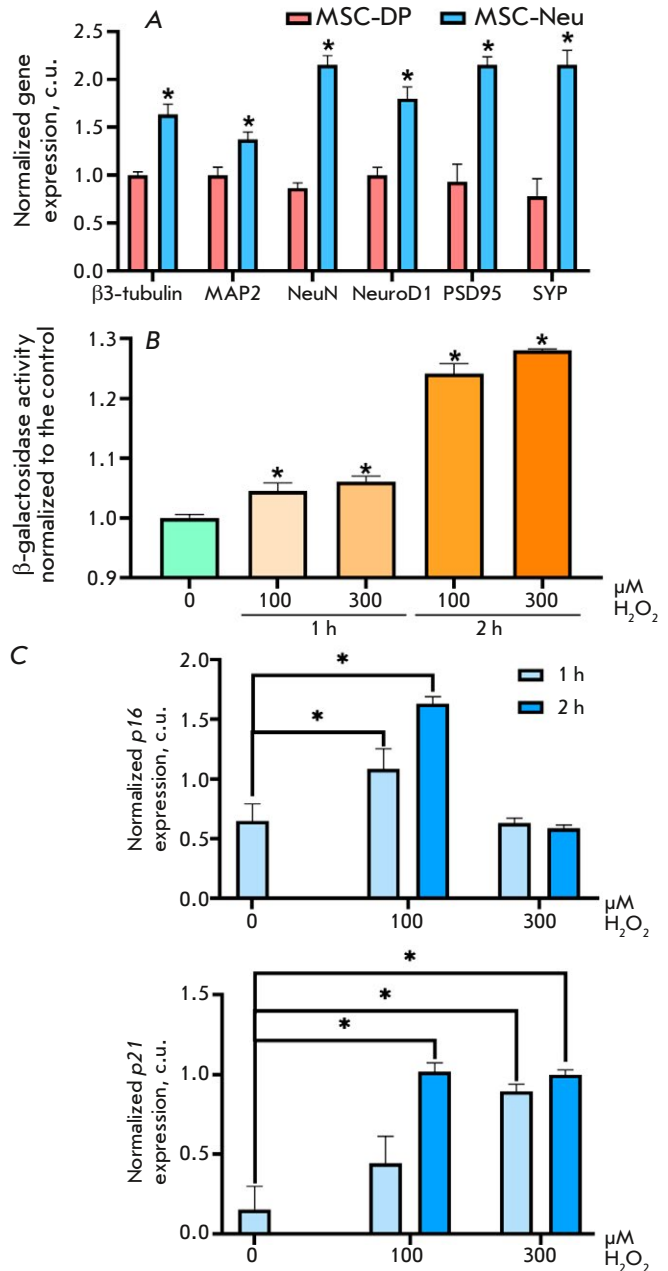
Fig. 1. Hydrogen peroxide induces senescence in reprogrammed human MSC-Neu neurons. (*A*) Expression of neuronal markers in MSC-DP (before differentiation) and MSC-Neu (after differentiation) cells. Actin mRNA was used as a control. (*B*) Incubation of MSC-Neu cells with 100 and 300 μM hydrogen peroxide for 1 and 2 h increases β-galactosidase activity. (*C*) Incubation of MSC-Neu cells in the presence of 100 and 300 μM hydrogen peroxide for 1 and 2 h increases the p16 and p21 mRNA levels. Data represent the mean ± standard deviation of three separate experiments; differences are significant at $^*p < 0.05$ (determined using the Mann–Whitney test)
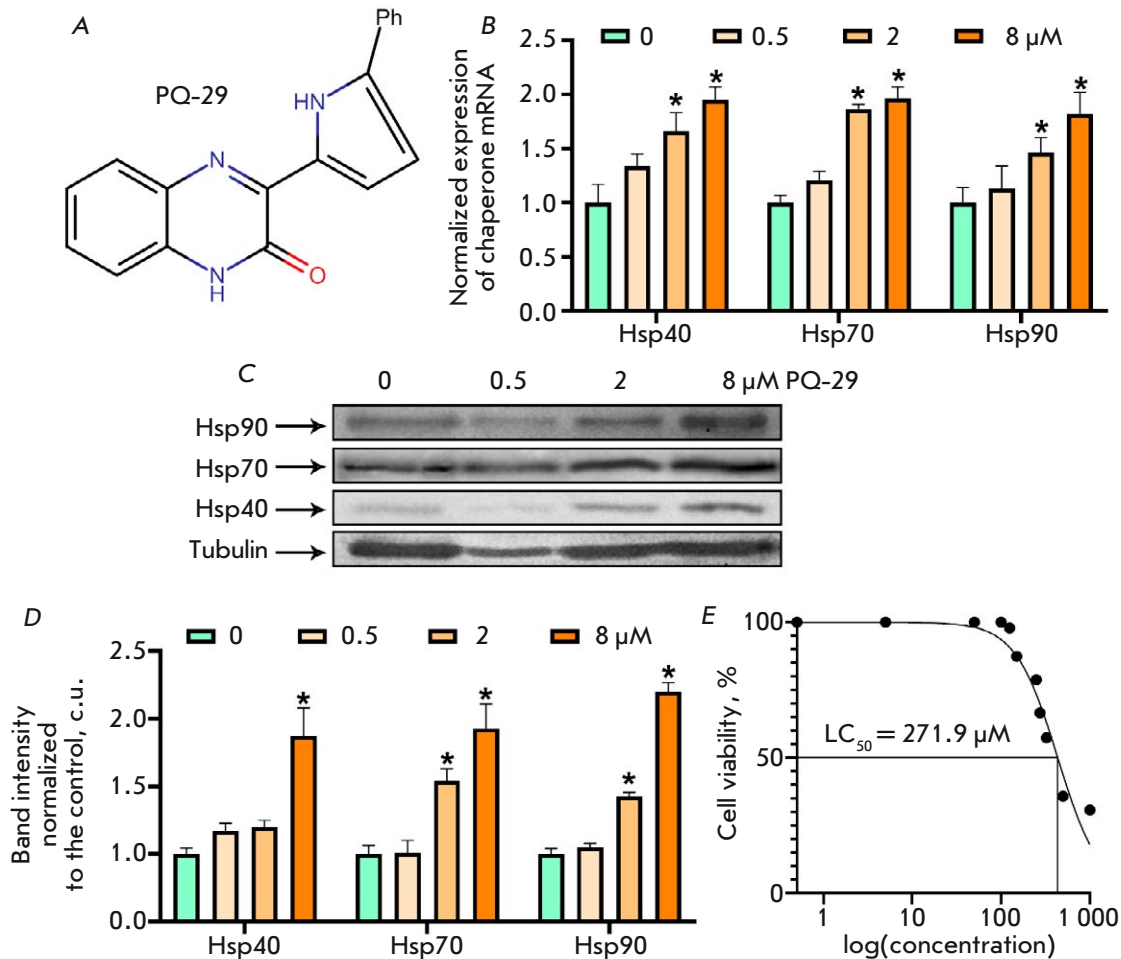
Fig. 2. PQ-29 at non-toxic doses increases chaperone levels in MSC-Neu under oxidative stress. (A) PQ-29 structural formula. (B) Chaperone expression in MSC-Neu cells after 6-h incubation with PQ-29. (C) Western blot analysis of the Hsp90, Hsp70, and Hsp40 levels in MSC-Neu cell lysates incubated with PQ-29 at the indicated concentrations for 24 h. Tubulin was used as a loading control. Representative images are provided. (D) Band intensity ratios of Hsp90, Hsp70, Hsp40, and tubulin normalized to the control cells. (E) PQ-29 LC_{50} in MSC-Neu cells under oxidative stress. Data represent the mean ± standard deviation of three separate experiments; the observed differences are statistically significant at $^*p < 0.05$ (determined using the Mann–Whitney test)

hydrogen peroxide for 1 h resulted in an increase in β-galactosidase activity by 4.4 and 6.2%, respectively. Incubation of MSC-Neu cells in the presence of 100 and 300 μM hydrogen peroxide for 2 h led to an increase in β-galactosidase activity by 24.2 and 28.1%, respectively.

To confirm that the change in β-galactosidase activity is relevant, p16 and p21 expressions were analyzed. These proteins play an important role in two key senescence-initiating pathways. A RT-PCR analysis demonstrated that cell incubation with 100 μM hydrogen peroxide for 1 h resulted in a 1.68- and 2.93-fold increase in the p16 and p21 mRNA levels,

respectively. Cell incubation under the same conditions for 2 h resulted in a 2.55- and 6.78-fold increase in the p16 and p21 mRNA levels, respectively (Fig. 1C). The use of higher hydrogen peroxide concentrations did not enhance p16 and p21 mRNA expression, which is, apparently, due to high toxicity. In further experiments on modeling oxidative stress-induced senescence, we incubated MSC-Neu cells in the presence of 100 μM hydrogen peroxide for 2 h.

The next stage of our study was to investigate the ability of PQ-29 (the structural formula is shown in Fig. 2A) to activate chaperone synthesis and accumulation in neuronal cells aged under oxidative stress

A

B

C
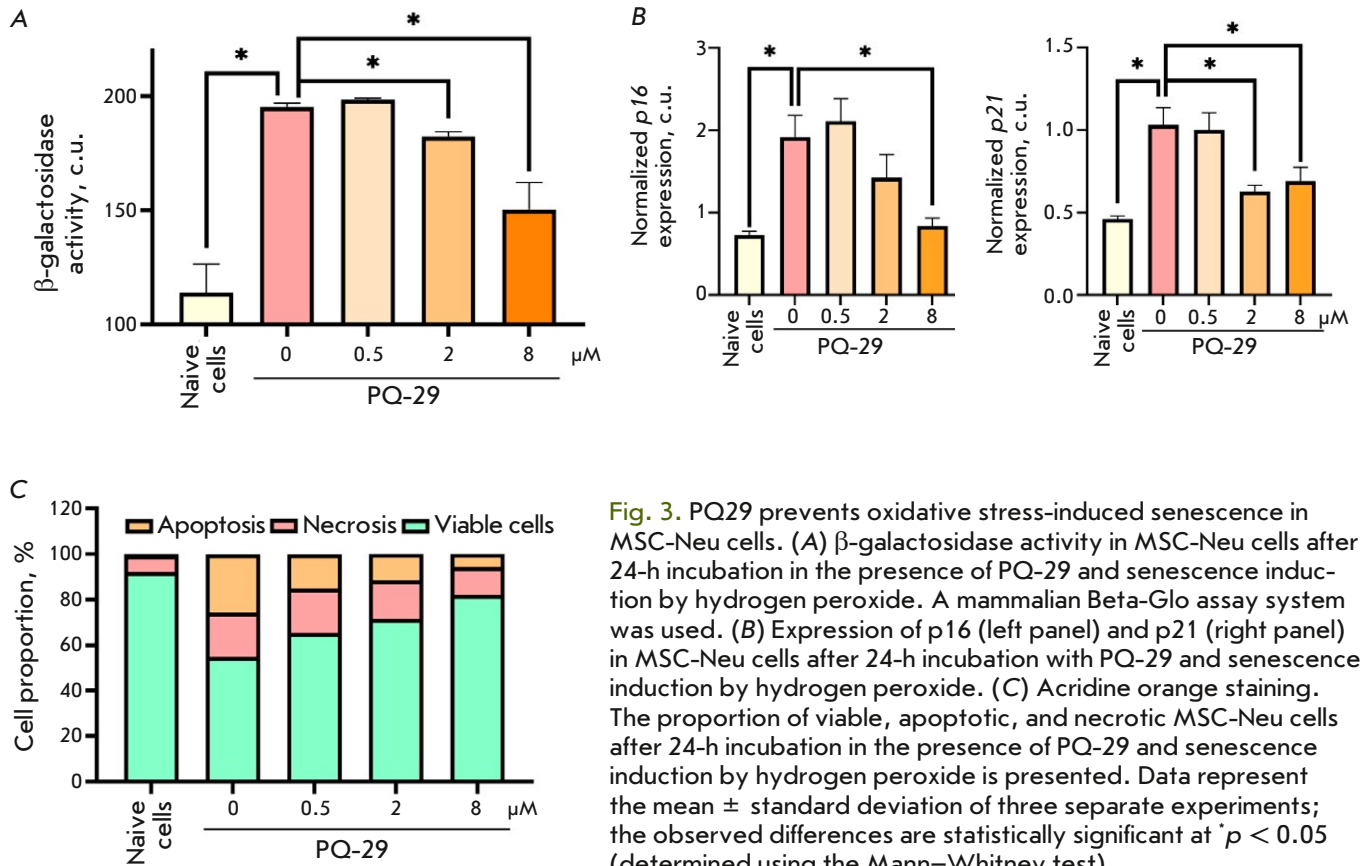
Fig. 3. PQ29 prevents oxidative stress-induced senescence in MSC-Neu cells. (*A*) β-galactosidase activity in MSC-Neu cells after 24-h incubation in the presence of PQ-29 and senescence induction by hydrogen peroxide. A mammalian Beta-Glo assay system was used. (*B*) Expression of p16 (left panel) and p21 (right panel) in MSC-Neu cells after 24-h incubation with PQ-29 and senescence induction by hydrogen peroxide. (*C*) Acridine orange staining. The proportion of viable, apoptotic, and necrotic MSC-Neu cells after 24-h incubation in the presence of PQ-29 and senescence induction by hydrogen peroxide is presented. Data represent the mean ± standard deviation of three separate experiments; the observed differences are statistically significant at $^*p < 0.05$ (determined using the Mann–Whitney test)

conditions. We had previously established the ability of PQ-29 to induce chaperone production in neuronal cells. However, it was necessary to confirm that PQ-29 can also affect aging cells. We conducted RT-PCR to evaluate the chaperone mRNA level in MSC-Neu cells aged under oxidative stress by incubation with PQ-29 for 6 h. The expression of major inducible chaperones, i.e., Hsp40, Hsp70, and Hsp90, was found to increase after PQ-29 treatment of cells aged under oxidative stress. The use of 8 μM PQ-29 resulted in 1.95-, 1.97-, and 1.82-fold increases in the Hsp40, Hsp70, and Hsp90 mRNA levels, respectively (*Fig. 2B*). Further, the chaperone level was assessed by western blot analysis in MSC-Neu cells incubated in the presence of PQ-29 for 4 h. The addition of 8 μM PQ-29 to the cells resulted in a 1.87-, 1.93-, and 2.2-fold increase in Hsp40, Hsp70, and Hsp90 mRNAs, respectively (*Fig. 2C,D*).

We had previously established that PQ-29 has low cytotoxicity [13]; however, we had to also confirm that the cytotoxicity effect would not rise in oxidative stress-aged cells. For this, we determined LC_{50} of PQ-29 in MSC-Neu cells aged under oxidative stress

by MTT analysis (*Fig. 2E*). The LC_{50} was found to be 271.9 μM. Thus, the PQ-29 concentrations used did not have a significant cytotoxic effect on the aged cells.

At the final stage of the study, we investigated the ability of PQ-29 to prevent oxidative stress-induced aging and the degradation of neurons. MSC-Neu cells subjected to oxidative stress-induced aging were cultured at different PQ-29 concentrations for further evaluation of β-galactosidase activity (using a Beta-Glo assay system) and cell viability (by staining with acridine orange). PQ-29 at concentrations of 2 and 8 μM reduced the increase in the β-galactosidase activity due to oxidative stress by 9.4 and 24.3%, respectively (*Fig. 3A*). We next analyzed the gene expression of the common senescence markers p16 and p21 in aging MSC-Neu cells in the presence of PQ-29. PQ-29 at a concentration of 8 μM was found to reduce the increase in p16 expression induced by oxidative stress by 78.3% (*Fig. 3B*, left panel). Both 2 and 8 μM PQ-29 supressed growth in p21 expression: by 54.7 and 47.8%, respectively (*Fig. 3B*, left panel). Finally, using acridine orange staining, we determined the proportion of cells subjected to oxidative stress-induced aging
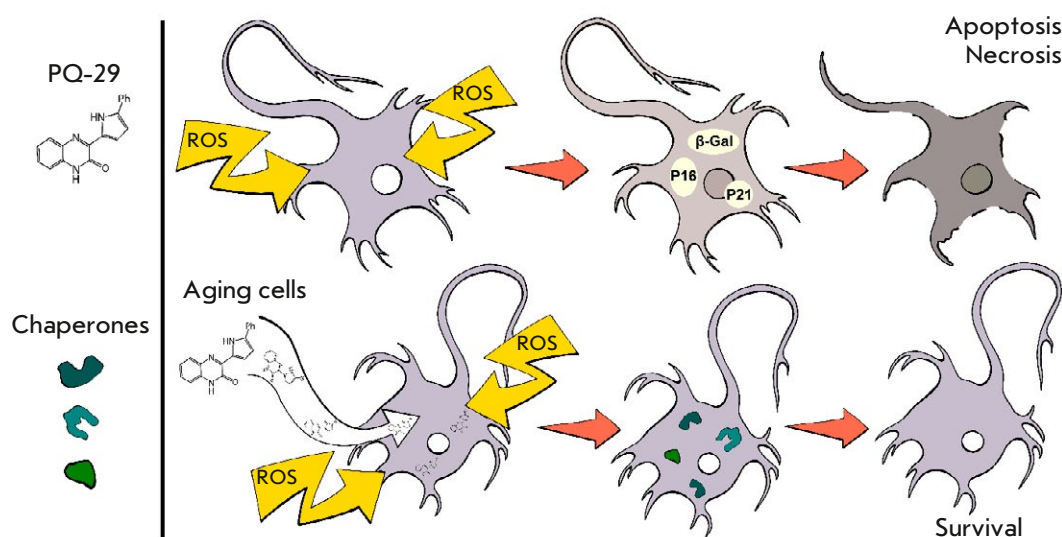
Fig. 4. Illustration of the principle of action of low-molecular-weight chaperone inducers to protect neuronal cells from oxidative stress

that underwent either apoptosis or necrosis, and we confirmed the ability of PQ-29 to prevent cell death. PQ-29 at concentrations of 2 and 8 µM prevented the development of both necrosis and apoptosis in neuronal cells. The proportion of necrotic cells decreased from 19.6 to 17.1 and 12.2% (in the presence of 2 and 8 µM PQ-29, respectively), while the proportion of apoptotic cells decreased from 25.6 to 11.4 and 5.8% (when using 2 and 8 µM PQ-29, respectively). Thus, the use of 2 and 8 µM PQ-29 resulted in an increase in the proportion of naive cells from 54.7 to 71.5 and 82%, respectively (*Fig. 3C*). These data indicate that PQ-29 can prevent oxidative stress-induced cell aging.

DISCUSSION
The lack of an effective response from the antioxidant cell system to oxidative stress is known to result in various pathologies. This is partially due to the inability of protein homeostasis systems to cope with the increasing number of damaged and mutated proteins [20]. Another negative effect of oxidative stress is the triggering of irreversible processes that disrupt the cell cycle and affect cellular physiology, leading to senescence. One of the mechanisms that protect cells, including neurons subjected to oxidative stress, involves, apart from antioxidants, chaperone synthesis inducers, which can enhance neuronal resistance to oxidative stress (*Fig. 4*). Such studies have already been conducted. For instance, the chaperone synthesis inducer U133 was shown to increase the resistance of C6 rat glioblastoma cells to ROS [17]. In addition, activation of chaperone synthesis reduces the proteotoxic load on cells associated with oxidative stress [21].

At the same time, delayed negative processes, including activation of senescence mechanisms, repre-

sents another important risk affecting neuronal function, in addition to a decrease in acute toxicity due to oxidative stress; namely, the oxidation of proteins and lipids and activation of apoptosis. Chaperones are known to prevent senescence activation through the p53/p21 and Rb/p16 signaling pathways [2]. However, the studies that have reported this regulation were conducted in cancer cells and cannot be considered relevant to neurodegenerative processes. Furthermore, chaperone expression in neuronal cells usually decreases with pathology progression; in particular, this phenomenon is found in traumatic brain injury, stroke, and Alzheimer's disease.

Chaperone synthesis inducers have been studied as promising neuroprotective drugs for a long time; the chaperone inducer arimoclomol is currently undergoing clinical trials [22]. However, there are no data on the effect of inducers on senescence. In this work, we propose PQ-29 as an agent capable of activating the production of the key chaperones Hsp70 and Hsp90 and co-chaperone Hsp40. The use of PQ-29 made it possible to not only inhibit the delayed cytotoxic effect of oxidative stress, but also to prevent neuronal cell senescence initiation in the presence of ROS. We would also like to note that LC_{50} of PQ-29 in old neurons was lower than that in neurons that had not undergone oxidative stress: 271 and 494 µM, respectively [10]. This indicates that the resistance of cells subjected to oxidative stress-induced aging decreases due to the effect of chemical agents.

We previously synthesized some pyrrolylazine compounds (including PQ-29) and established their ability to induce heat shock protein synthesis and exert a neuroprotective effect in Alzheimer's disease and traumatic brain injury [11, 13, 23]. In addition, the

ability of pyrrolylazine derivatives to induce Hsp70 production was confirmed in both young and old reprogrammed human MSCWJ-Neu neurons. In the present study, we have established the ability of the pyrrolylazine derivative PQ-29 to prevent oxidative stress-induced aging (*Fig. 4*). Taken together, these data allow us to conclude that these compounds possess a pronounced neuroprotective activity. ●

REFERENCES

1. Hu Y., Shao Z., Cai X., Liu Y., Shen M., Yao Y., Yuan T., Wang W., Ding F., Xiong L. // Spine (Phila. Pa. 1976). 2019. V. 44. P. 585–595.
2. Zhang S., Liu W., Wang P., Hu B., Lv X., Chen S., Wang B., Shao Z. // Mol. Cell. Biochem. 2021. V. 476. P. 1979–1994.
3. Guo Z., Song T., Wang Z., Lin D., Cao K., Liu P., Feng Y., Zhang X., Wang P., Yin F., et al. // J. Biol. Chem. 2020. V. 295. P. 12900–12909.
4. Kroemer G. // Sci. World J. 2001. V. 1. P. 590.
5. Komarova E.Y., Afanasyeva E.A., Bulatova M.M., Cheetham M.E., Margulis B.A., Guzhova I.V. // Cell Stress Chaperones. 2004. V. 9. P. 265–275.
6. Pandey P., Saleh A., Nakazawa A., Kumar S., Srinivasula S.M., Kumar V., Weichselbaum R., Nalin C., Alnemri E.S., Kufe D., Kharbanda S. // EMBO J. 2000. V. 19. № 16. P. 4310–4322. doi: 10.1093/emboj/19.16.4310.
7. Paul S., Mahanta S. // Mol. Cell. Biochem. 2014. V. 386. P. 45–61.
8. Fan C.Y., Lee S., Cyr D.M. // Cell Stress Chaperones. 2003. V. 8. P. 309.
9. Ekimova I.V., Plaksina D.V., Pastukhov Y.F., Lapshina K.V., Lazarev V.F., Mikhaylova E.R., Polonik S.G., Pani B., Margulis B.A., Guzhova I.V., et al. // Exp. Neurol. 2018. V. 306. P. 199–208.
10. Zhao Y., Zhao H., Lobo N., Guo X., Gentleman S.M., Ma D. // J. Alzheimers. Dis. 2014. V. 41. P. 835–844.
11. Dutysheva E.A., Mikeladze M.A., Trestsova M.A., Aksenov N.D., Utepova I.A., Mikhaylova E.R., Suezov R.V., Charushin V.N., Chupakhin O.N., Guzhova I.V., et al. // Pharmaceutics. 2020. V. 12. № 5. P. 414.
12. Adachi H., Katsuno M., Waza M., Minamiyama M., Tanaka F., Sobue G. // Int. J. Hyperthermia. 2009. V. 25. № 8. P. 647–654.
13. Dutysheva E.A., Utepova I.A., Trestsova M.A., Anisimov A.S., Charushin V.N., Chupakhin O.N., Margulis B.A., Guzhova I.V., Lazarev V.F. // Eur. J. Med. Chem. 2021. V. 222. P. 113577.
14. Koltsova A.M., Zenin V.V., Turilova V.I., Yakovleva T.K., Poljanskaya G.G. // Tsitologiia. 2018. V. 60. № 12. P. 955–968.
15. Gingras M., Champigny M.F., Berthod F. // J. Cell. Physiol. 2007. V. 210. № 2. P. 498–506.
16. Mature neuron markers. Abcam. https://www.abcam.com/neuroscience/mature-neurons-markers-and-their-functions.
17. Lazarev V.F., Nikotina A.D., Mikhaylova E.R., Nudler E., Polonik S.G., Guzhova I.V., Margulis B.A. // Biochem. Biophys. Res. Commun. 2016. V. 470. № 3. P. 766–771.
18. Meshalkina D.A., Shevtsov M.A., Dobrodumov A.V., Komarova E.Y., Voronkina I.V., Lazarev V.F., Margulis B.A., Guzhova I.V. // Oncotarget. 2016. V. 7. P. 7872.
19. Mosmann T. // J. Immunol. Methods. 1983. V. 65. № 1–2. P. 55–63.
20. Balchin D., Hayer-Hartl M., Hartl F.U. // Science. 2016. V. 353. № 6294. P. 42–54.
21. Ulrich K. // Biochem. Soc. Trans. 2023. V. 51. № 3. P. 1169–1177.
22. Kirkegaard T., Gray J., Priestman D.A., Wallom K.L., Atkins J., Olsen O.D., Klein A., Drndarski S., Petersen N.H.T., Ingemann L., et al. // Sci. Transl. Med. 2016. V. 8. № 355. P. 355.
23. Lazarev V.F., Dutysheva E.A., Mikhaylova E.R., Trestsova M.A., Utepova I.A., Chupakhin O.N., Margulis B.A., Guzhova I.V. // Molecules. 2022. V. 27. P. 8950.

Activation of the ERK1/2 Molecular Pathways and Its Relation to the Pathogenicity of Human Malignant Tumors

A. G. Emelyanova[1,2*], M. A. Zolotovskaia[1,2], E. V. Poddubskaya[2], A. A. Modestov[1,2], V. S. Prassolov[3], D. V. Kuzmin[1], A. A. Buzdin[1,2,4,5]

[1]Moscow Institute of Physics and Technology, Dolgoprudny, 141701 Russian Federation
[2]I.M. Sechenov First Moscow State Medical University, Moscow, 119991 Russian Federation
[3]Engelhardt Institute of Molecular Biology, Moscow, 119991 Russian Federation
[4]Shemyakin–Ovchinnikov Institute of Bioorganic Chemistry, Moscow, 117997 Russian Federation
[5]PathoBiology Group, European Organization for Research and Treatment of Cancer (EORTC), 1200 Brussels, Belgium
*E-mail: emelianova-a.g@yandex.ru

ABSTRACT Mitogen-activated protein kinases, ERK1/2 (MAPK3/1), play a key role in the regulation of cell growth, differentiation, and apoptosis. We have previously presented evidence proving that activation of the ERK1/2 axis in cancer cells following the administration of therapeutics leads to the overexpression of growth factor receptors and drug resistance. Recently, we have proposed a new bioinformatic technique that enables direct construction of interactome network-based molecular pathways for gene products of interest, as well as quantitation of their activation levels using high-throughput gene expression data. In this study, we, for the first time, algorithmically constructed ERK1/2 molecular pathways and investigated how their activation levels (PALs) affect survival and responsiveness to targeted drugs at the pan-cancer level based on transcriptomic data. We examined a total of 11 287 human tumor profiles from 31 types of cancer, drawn from 53 of our previously published and other literature datasets, looking at patient survival and clinical response to 29 chemo- and targeted therapy regimens. We found that activation of the ERK1/2 pathways has different prognostic significance depending on cancer type. In glioblastoma, sarcoma, lung, kidney, bladder, gastric, colon, and several other cancer types, ERK pathway activation was associated with worse survival. In contrast, the same phenomenon was associated with a better chance of survival in HER2+, luminal A and luminal B breast cancer, and uterine corpus cancer. These trends were consistent with treatment response analysis. At the same time, we found significantly worse associations with the expression levels of individual *MAPK1* and *MAPK3* genes: hence, ERK1/2 pathway activation levels can be considered putative biomarkers for predicting clinical outcomes and selecting new personalized treatment strategies, such as the use of MAPK inhibitors.
KEYWORDS ERK1 (MAPK3), ERK2 (MAPK1), gene expression in cancer, ERK molecular pathway activation in oncogenesis, cancer survival biomarkers.
ABBREVIATIONS MAPK – mitogen-activated protein kinase; PAL – pathway activation level; CNR – case-to-normal ratio; ARR – activation/repressor role; OS – overall survival; PFS – progression-free survival; HR – hazard ratio.

INTRODUCTION

Cancer is the second most common cause of death in the world after cardiovascular diseases. According to the World Health Organization (WHO), there were 19.3 million new cases of cancer and 10 million deaths from cancer in 2020, accounting for about 16% of all deaths worldwide [1]. Cancer incidence statistics have been steadily increasing over the past two decades, and cases are projected to rise to 28.4 million in 2040, a 47% increase from 2020 [2]. These trends emphasize the need for increased prevention, early diagnosis, and effective cancer treatment strategies.

Notwithstanding the medical advances in cancer diagnosis and treatment and the availability of targeted therapies, cancer treatment efficacy remains insufficient. It is not uncommon for individual cases of advanced tumors or even entire cancer types to respond poorly to clinically approved chemotherapies and targeted therapies, and, conversely, many cases of individual responses to unlisted drugs or combinations of drugs have been reported [3]. One of the reasons for this is the complexity of the molecular mechanisms of cancer, which makes the development of effective universal treatment strategies a challenge. Therefore, particular attention is being focused on research into the key molecular pathways that regulate the key cellular processes in oncogenesis. In particular, we know that signaling axes such as EGFR, PI3K/AKT/mTOR, RAS/RAF/MEK/ERK, and JAK/STAT play a key role in the regulation of cell growth and division. However, their complex interactions and the presence of parallel signaling pathways make it difficult to develop long-term effective targeted therapeutic regimens. In addition, abnormal regulation of these pathways is often associated with treatment resistance and tumor progression [4–6].

Of particular interest are the mitogen-activated protein kinases (MAPK) ERK1 and ERK2 (encoded by the *MAPK3* and *MAPK1* genes, respectively), which are activated in response to the activation of the RAS-RAF-MEK-ERK signaling axis that plays a key role in tumor cell survival, growth, and proliferation. This axis is closely related to the progression and metastasis of various types of human cancers. Activating mutations in the genes of upstream receptor tyrosine kinases or in the genes encoding the RAS, RAF, MEK and ERK proteins can lead to aberrant activation of ERK1/2 in tumors and, taken together, constitute the most frequent group of mutations in human cancer cells. In general, it is believed that 30–96% of all tumors are characterized by hyperactivation of the RAS/RAF/MEK/ERK signaling axis [7]. ERK1/2, as its downstream component, can be hyperactivated due to uncontrolled activation of receptor tyrosine kinase genes or mutations in the *RAS*, *RAF* and *MEK* genes [8]. Specific inhibitors of the EGFR, BRAF, KRAS, and MEK proteins are included in many standards of anticancer therapy and have proved effective in the therapy of cancers carrying oncogenic mutations in this axis. However, cancer cells often grow resistance to such inhibitors and ERK reactivation is believed to be one of the reasons for such resistance [8, 9].

ERK1/2 proteins play their oncogenic role through abnormal phosphorylation of a wide range of substrates, thereby regulating a variety of tumor-related biological processes, including cell proliferation, differentiation, migration, and angiogenesis [10]. ERK1/2 kinases localize at the crossroads of various signaling pathways, since they are a key node in activating the emergency survival program of tumor cells after the application of receptor tyrosine kinase inhibitors and standard chemotherapy [9].

Hence, these kinases appear to be promising targets for antitumor therapy, in combination with existing antitumor drugs to enhance their efficacy. Therefore, the search for groups of patients in whom the corresponding signaling is elevated may be promising in terms of using specific inhibitors of these MAPK kinases. One approach to identifying such patient groups involves assessing the expression levels of these genes. Variability in gene expression among tumors from different patients has facilitated the adoption of personalized treatment strategies [11]. However, the advent of omics technologies makes it possible to simultaneously examine thousands of genes and other biomarkers [12]. Additionally, various analytical tools allow researchers to summarize results and identify signaling or the biochemical pathways in which the products of these genes are involved, based on data in the literature (functional enrichment). Functional enrichment tools (e.g., over-representation analysis and functional class scoring (FCS), commonly used in the analysis of differential gene expression) do not account for the fact that genes operate within complex molecular networks, and their dysregulation in cancer can simultaneously disrupt the regulation of multiple pathways. Different components of a molecular pathway can have distinct functional roles. For example, increased expression of an inhibitory component may suppress the pathway, while activation of a stimulatory component may enhance it. Furthermore, the pathways are often regulated by positive and negative feedback loops, which significantly influence the biological outcomes resulting from pathway activation or inhibition [13, 14]. To address these challenges, a method was proposed to quantitatively assess the activation level of an entire molecular pathway, rather than individual genes, considering the pathway's architecture and the roles of its constituent components in its activation or suppression. An algorithm was developed for its automatic calculation [14]. The classical algorithm for calculating the molecular pathway activation level (PAL) involves recursive annotation of each node in a given pathway as an activator or repressor, based on the molecular architecture and the nature of each interaction [14]. PAL effectively smooths biases arising from data obtained on different platforms and reduces batch effects [15]. Its values have been used to tell

apart normal tissues from tumor ones [16] and predict therapeutic responses in colorectal, renal, and gastric cancer [17–20]. In addition to the classical PAL calculation, a recently proposed approach constructs the architecture of a molecular pathway as a network of interacting molecules centered around a key node: the central gene. These pathways, referred to as genecentric pathways, are constructed based on the human interactome model and include the maximum number of interactions starting from the central node and leading to every other node in the pathway. PAL of genecentric pathways has demonstrated prognostic and diagnostic value, making it a reliable biomarker for screening, prognosis, and therapy prediction [21, 22].

In this study, we for the first time algorithmically constructed the ERK1 and ERK2 genecentric molecular pathways based on the interactome model previously developed by our group [21]. We sought to investigate the associations of their PALs with survival and responsiveness to targeted drugs at a cancerwide level.

We found that activation of the ERK1/2 pathway has different prognostic values depending on the type of cancer. In glioblastoma, sarcoma, lung, kidney, bladder, gastric, colorectal, and several other cancer types, ERK pathway activation was associated with a worse survival chance. In contrast, it was associated with a better chance of survival in the HER2+, luminal A and luminal B breast cancer, and uterine corpus cancer. These results are consistent with those from the treatment response analysis. In contrast, we found significantly weaker associations with the expression levels of the individual *MAPK1* and *MAPK3* genes. Hence, the levels of ERK1/2 pathway activation can be considered putative biomarkers for predicting clinical outcomes and selecting new personalized treatment strategies such as the use of MAPK inhibitors.

EXPERIMENTAL

RNA expression datasets

The Cancer Genome Atlas (TCGA) project dataset. The RNA sequencing data of solid tumors (STAR counts) and matching normal tissues from the TCGA project were downloaded from the NCI Genomic Data Commons portal [23, 24], along with associated metadata with information on survival, progression, the therapy used, and response to therapy. Only primary tumor samples of cancer types with 100 or more samples were evaluated. In addition, data from the TCGA READ (rectal adenocarcinoma) and COAD

(colon adenocarcinoma) projects were combined into the Colorectal Cancer group; similarly, data from the KIRC (renal clear cell cancer) and KIRP (renal papillary cancer) projects were combined into the Renal Cell Carcinoma group. In addition, gliomas and glioblastomas from the TCGA-GBM and TCGA-LGG projects were pooled and reclassified according to the updated WHO classification as shown by Zakharova et al. [25]. The TCGA-BRCA breast cancer dataset was divided into subgroups according to the PAM50 signature [26] due to the high heterogeneity of tumors in this localization. Five molecular subtypes were derived: basal, HER2+, luminal A, luminal B, and normal breast cancer. In the end, a total of 24 cancer types with a total of 8 427 tumor samples were included in the analysis (*Table 1*).

Overall survival (OS) and progression-free survival (PFS) data were assessed in parallel in our analysis. Wherever possible, datasets from the TCGA project were also tapped to analyze the response to therapy according to the RECIST criteria [27] (*Table 1*). For reasons of uniformity and compatibility, the following selection criteria were applied to the TCGA data. First, groups of patients with the same type of therapy, at least 20 patients for each cancer type, were included in the analysis. Second, if the same patient received multiple lines of the same therapy, the best response according to the RECIST criteria was selected for further analysis. Some patients received up to eight lines of therapy, but only the responses to lines 1–3 were included in the analysis, because by the time the later lines of therapy were administered a significant change in the molecular profile of the tumor may have occurred and, therefore, the use of transcriptomic data obtained earlier may be questionable. Finally, only RECIST-defined response groups consisting of at least three patients were considered, for statistical reasons. As a result, data on the response to therapy by patients with 10 cancer types were included (*Table 2*).

Gene Expression Omnibus (GEO) and Tumor Alterations Relevant for GEnomics-driven Therapy (TARGET) repository datasets. The datasets included were selected from the previous collection of clinically annotated gene expression datasets with a validated quality of the expression profiles [28]. The solid tumor RNA sequencing data (STAR-counts) from the TARGET project were downloaded from the NCI Genomic Data Commons portal [29]. Microarray gene expression datasets were extracted from the GEO portal [30, 31]. The TARGET-AML dataset (for acute myeloid leukemia) was divided into two sub-datasets based on the presence or absence of busul-

Table 1. Statistics for the TCGA RNA expression samples included in the analysis

Cancer type	TCGA project ID	Total number of samples	Number of samples with survival data (OS/PFS)	Number of samples with response to therapy data
Astrocytoma, *IDH*-mutant. Grade 2	Part of *LGG + GBM*	110	110/110	22
Basal breast cancer	Part of *BRCA*	198	198/198	0
Colorectal cancer	*COAD + READ*	624	619/624	120
Glioblastoma, *IDH*-wildtype	Part of *LGG + GBM*	206	204/206	24
HER2+ breast cancer	Part of *BRCA*	124	124/124	0
Luminal A breast cancer	Part of *BRCA*	230	229/230	0
Luminal B breast cancer	Part of *BRCA*	515	514/515	0
Renal cell carcinoma	*KIRP + KIRC*	823	822/823	15
Urothelial bladder carcinoma	*BLCA*	406	403/406	92
Cervical squamous cell carcinoma and endocervical adenocarcinoma	*CESC*	304	304/304	77
Esophageal carcinoma	*ESCA*	184	184/184	32
Head and neck squamous cell carcinoma	*HNSC*	520	518/520	77
Hepatocellular carcinoma	*LIHC*	368	367/368	24
Lung adenocarcinoma	*LUAD*	516	507/516	98
Lung squamous cell carcinoma	*LUSC*	501	495/501	61
Pancreatic adenocarcinoma	*PAAD*	178	178/178	74
Pheochromocytoma and paraganglioma	*PCPG*	179	179/179	4
Prostate adenocarcinoma	*PRAD*	497	495/497	40
Sarcoma	*SARC*	259	259/259	58
Cutaneous melanoma	*SKCM*	103	103/105	14
Stomach adenocarcinoma	*STAD*	412	403/412	115
Thyroid cancer	*THCA*	505	505/505	12
Thymoma	*THYM*	120	119/120	3
Uterine corpus endometrial carcinoma	*UCEC*	545	544/545	60

fan and cyclophosphamide in the treatment regimen. Additionally, the analysis included data from the TCGA project for LGG and UCEC and the combined dataset for lung cancer (LUSC + LUAD) where the information was extracted from the collection by Borisov et al. [28]. A total of 26 additional datasets of nine cancer types, with a total of 2 736 tumor samples, were included (*Table 3*).

Original clinical datasets. We also included proprietary clinically annotated RNA sequencing datasets previously obtained in our laboratory and published elsewhere. When available, the treatment outcomes were assigned according to the RECIST criteria [27].

The following original datasets were included:
1) patients with glioblastoma treated with temozolomide, annotated with progression-free survival data (n = 49) [32, 33];
2) patients with gastric cancer from a previously published clinical investigation [18] who received ramucirumab as monotherapy (n = 7), or in combination with paclitaxel (n = 6) or the FOLFIRI regimen (n = 2). Response to therapy as well as progression-free survival was assessed;
3) patients with multiple myeloma (n = 60) who received complex chemotherapy in several regimens, each including bortezomib. The response to therapy was registered [34].

Table 2. Sufficient TCGA tumor groups with available data on RECIST treatment outcomes

Cancer type	Chemotherapy[1]	Number of patients in the response group[2]
Astrocytoma, *IDH*-mutant. Grade 2	Temozolomide	SD (n = 12); R (n = 3)
Colorectal cancer	5-Fluorouracil, leucovorin, oxaliplatin	NR (n = 6); R (n = 39)
Glioblastoma, *IDH*-wildtype	Temozolomide	SD (n = 12); R (n = 4)
Urothelial bladder carcinoma	Cisplatin, gemcitabine	SD (n = 4); R (n = 33); NR (n = 12)
Cervical squamous cell carcinoma and endocervical adenocarcinoma	Cisplatin	R (n = 49); NR (n = 6)
Head and neck squamous cell carcinoma	Cisplatin	R (n = 35); NR (n = 3)
Thyroid cancer	Gemcitabine	SD (n = 4); R (n = 23); NR (n = 25)
Sarcomas	Docetaxel, gemcitabine	R (n = 12); NR (n = 9)
Stomach adenocarcinoma	5-Fluorouracil	R (n = 17); NR (n = 16)
Uterine corpus endometrial carcinoma	Paclitaxel, carboplatin	R (n = 35); NR (n = 5)

[1]Type of chemotherapy used in a patient cohort;
[2]R – responders (total number of patients with RECIST v1.1 Complete Response and Partial Response outcomes);
NR – non-responders (number of patients with RECIST v1.1 Progressive Disease outcome);
SD – patients with Stable Disease outcome according to RECIST v1.1 classification.

Construction of ERK1/2 molecular pathways and assessment of pathway activation level (PAL) values
The ERK1 (MAPK3) and ERK2 (MAPK1) molecular pathways were algorithmically reconstructed as previously reported in [21]. The human interactome model was constructed using the OncoboxPD collection of published molecular pathways [35] as a molecular interaction database. In total, the architecture of 50 178 distinct molecular pathways was used to build the interactome model. All pathway graphs were merged based on overlapping gene products. The included genes form a connected network, meaning that at least one undirected edge exists between any pair of gene products. As a result, a directed graph was obtained, where nodes represent genes or metabolites, and edges correspond to the known pairwise molecular interactions included in the OncoboxPD collection. The interactome model was visualized using the Gephi software and the ForceAtlas2 algorithm.

For each ERK1 and ERK2 protein, genecentric algorithmic molecular pathways were constructed, including central nodes (ERK1 and ERK2, respectively) and gene products with first-order interactions with the corresponding central nodes. The following types of interactions were considered: "activation", "coupling", "inhibition", "phosphorylation", "dissociation", "repression", "dephosphorylation", "binding/association", and "ubiquitination".

The pathway activation level (PAL) is an aggregate quantitative and qualitative characterization of the changes in the expression level of the genes involved in a particular molecular pathway [36]. The PAL values were calculated as follows:

$$PAL_p = 100 \times \Sigma_n(ARR_{n,p} \times lg(CNR_n))/\Sigma_n|ARR_{n,p}|,$$

where PAL_p is the level of activation of the pathway p; CNR_n is the ratio of the expression of gene n in the tested sample to its average level in the control group; and ARR is the role (activator/repressor) played by the given gene product in the p pathway. ARR can take on the following values:
-1: when the n gene product is a repressor of the p pathway;
-0.5: when the n gene product is mainly a repressor;
0: when the role of the n gene product in the p pathway is neutral, uncertain or ambiguous;
0.5: when the n gene product is predominantly an activator;
1: when the gene product n is an activator.

The ARR values were assigned algorithmically based on the pathway architecture and central node position [14], and PAL calculations were performed using the Python library "oncoboxlib" [14].

If data were downloaded in non-normalized form, normalization of gene expression was performed us-

Table 3. Datasets added from the collection of clinically annotated tumor expression profiles

Cancer type	Dataset ID	Therapy[1]	Number of samples	Number of responder and non-responder patients according to [28][2]
Breast cancer with different hormonal and HER2 statuses	GSE18728	Docetaxel, capecitabine	61	23R, 38NR
Breast cancer with different hormonal and HER2 statuses	GSE20181	Letrozole	52	37R, 15NR
Breast cancer with different hormonal and HER2 statuses	GSE20194	Paclitaxel, 5-fluorouracil, cyclophosphamide, doxorubicin	52	11R, 41NR
Breast cancer with different hormonal and HER2 statuses	GSE20271	Paclitaxel, 5-fluorouracil, adriamycin, cyclophosphamide	84	18R, 66NR
Breast cancer	GSE22358	Docetaxel, capecitabine	122	116R, 6NR
Breast cancer	GSE23988	Docetaxel, capecitabine	61	20R, 41NR
Breast cancer with different hormonal and HER2 statuses	GSE25066	Neoadjuvant therapy with taxanes and anthracyclines	508	118R, 389NR
Breast cancer	GSE32646	Paclitaxel, 5-fluorouracil, epirubicin cyclophosphamide	115	27R, 88NR
Breast cancer	GSE37946	Trastuzumab	50	27R, 23NR
Multiple myeloma	GSE39754	Vincristine, adriamycin, dexamethasone followed by autologous stem cell transplantation	136	74R, 62NR
Breast cancer with different hormonal and HER2 statuses	GSE41998	Neoadjuvant therapy with doxorubicin, cyclophosphamide, paclitaxel	124	90R, 34NR
Breast cancer	GSE42822	Docetaxel, 5-fluorouracil, epirubicin, cyclophosphamide, capecitabine	91	38R, 53NR
Breast cancer with different hormonal and HER2 statuses	GSE50948	Paclitaxel, doxorubicin, cyclophosphamide, methotrexate, trastuzumab	156	53R, 103NR
Acute myeloid leukemia	GSE5122	Tipifarnib	57	13R, 44NR
Breast cancer	GSE59515	Letrozole	75	51R, 24NR
Multiple myeloma	GSE68871	Bortezomib, thalidomide, dexamethasone.	118	69R, 49NR
Breast cancer	GSE76360	Trastuzumab	48	42R, 6NR
Multiple myeloma	GSE9782	Bortezomib	169	85R, 84NR
Non-small cell lung cancer (lung adenocarcinoma + squamous cell lung cancer + other types)	GSE207422*	Anti-PD-1 immunotherapy	24 (8 + 12 + 4)	9R, 15NR
B-cell acute lymphoblastic leukemia	TARGET10	Vincristine sulfate, carboplatin, cyclophosphamide, doxorubicin	98	30R, 68NR
Pediatric acute myeloid leukemia	TARGET20 _Busulfan	Polychemotherapy** + Busulfan, cyclophosphamide	54	31R, 23NR
Pediatric acute myeloid leukemia	TARGET20_ NoBusulfan	Polychemotherapy**	142	62R, 80NR
Williams tumor (nephroblastoma)	TARGET50	Vincristine sulfate, cyclosporine, cytarabine, daunorubicin	122	36R, 86NR
Lung cancer	TCGA_LC	Paclitaxel, optional: cisplatin/carboplatin, rheolysin	35	22R, 13NR
Low-grade glioma	TCGA_LGG	Temozolomide, optionally: mibefradil	131	100R, 31NR
Endometrioid adenocarcinoma	TCGA_ UCEC	Paclitaxel, optional: cisplatin/cisplatin, doxorubicin	52	45R, 7NR

[1] Type of chemotherapy, targeted therapy, immunotherapy, or hormone therapy used in a patient cohort.

[2] "R" stands for treatment responders; "NR", for non-responders.

*This dataset was not annotated in [28]. It includes information about patients' response to immunotherapy according to the RECIST criteria and, therefore, was added to the analysis.

**Polychemotherapy regimen included: asparaginase, cytarabine, daunorubicin hydrochloride, etoposide, gemtuzumab ozogamicin, and mitoxantrone hydrochloride.

ing DeSeq2 [37]. An artificial gene expression profile obtained by averaging all gene expression data in the study cohort was used as a reference (control) gene expression profile for each individual dataset.

Statistical tests

Statistical analyses were performed in R, version 3.4.2 [38]. The PAL or central gene expression level values were divided into groups with a high and low PAL score/gene expression level, depending on whether the score was above or below the optimal value corresponding to the minimum p-value of the log-rank test calculated using the "surv_cutpoint" function of the R package "surviminer" [39].

Survival associations were assessed using the Kaplan–Meier method and log-rank test to determine the statistical significance of the difference between the two groups; the hazard ratio (HR, 95% CI) was calculated using the Cox regression model to assess the differences in survival chances between the compared groups using the R packages "survival" [40] and "survminer" [39]. Overall survival (OS) was calculated to the date of death or to the date of the last follow-up; patients who were alive at the time of last follow-up were censored. Progression-free survival (PFS) was calculated up to the date of progression, death, or last follow-up. Surviving patients, as well as patients without progression at the date of the last follow-up, were censored. Hazard ratios with $p < 0.05$ and 95% CI not including 1 were considered statistically significant.

In the analysis of the responsiveness to the therapy, when no "responder" nor "non-responder" marks were available in the dataset, the patients with the RECIST *Complete Response* and *Partial Response* outcomes were considered *responders*, and patients with the *Progressive Disease* label were considered *non-responders*, whereas patients with the *Stable Disease* outcome were considered separately.

Normality of distribution was assessed using the Shapiro–Wilk test; homogeneity of variance, using the Levene's test. If the number of compared groups exceeded 2, ANOVA or the Kruskal–Wallis test was used depending on whether the distribution met the criteria of normal distribution or not, followed by post-hoc comparison by the Student's or Dunn's test, respectively, with correction for multiple comparisons by Benjamini–Hochberg or Holm, respectively. If the number of groups compared was 2, the analyses were performed using the Student's or Wilcoxon's test, depending on the normality of distribution. Intergroup comparisons were performed using the R packages "FSA" [41] and "car" [42].

Data visualization was performed using the R packages "ggplot2" [43] and "ComplexHeatmap" [44].

Differences were considered statistically significant at $p < 0.05$.

RESULTS

Algorithmic reconstruction of the ERK1 and ERK2 genecentric molecular pathways

Both pathways were reconstructed based on a previously developed human interactome model represented as a graph comprising 361 654 interactions among 64 095 molecular players. The pathways included members directly interacting with the central node (ERK1/MAPK3 or ERK2/MAPK1, respectively). Annotation of the functional roles of the pathway components was performed algorithmically according to [14]. The resulting pathways (*Fig. 1*) contained 447 and 443 molecular players, respectively. The functionally annotated list of pathway members is provided in *Supplementary Table 1*. A total of 428 members of these pathways (95.7 and 96.6%, respectively) were shared, evidence of their close structural similarity.

Prognostic significance of the activation of the ERK1/2 pathway and gene expression in relation to cancer patient survival in TCGA data

RNA sequencing data from the TCGA repository were analyzed to assess the degree of association between patient survival and the expression of the *MAPK3* and *MAPK1* genes, as well as the PAL values of the newly reconstructed ERK1 and ERK2 pathways. Our analysis revealed that the PAL values for the ERK1 and ERK2 pathways generally exhibit similar distributions across various tumor types. At that stage, the genecentric KRAS pathway was additionally included in the analysis. this justified by the key role played by RAS family gene products in the activation of the RAS-RAF-MEK-ERK cascade (*Supplementary Fig. 1A*). The KRAS pathway was found to generally display a broader distribution and lower PAL values (except in pheochromocytoma and paraganglioma, where its median value is higher) compared to the ERK1/2 pathways. However, the overall trends in PAL variability across these molecular pathways are consistent (*Supplementary Fig. 1B*). The activation of the KRAS pathway is directly linked to the activation of ERK1/2, providing a means to assess the interplay between these signaling pathways and identify differences in their activity across tumor types. In this case, despite similar trends in PAL values within various tumor types for all three pathways, the lower PAL values observed for the KRAS pathway suggest that ERK pathway activation in these tumors may occur via alternative mechanisms that are independent of KRAS activity.
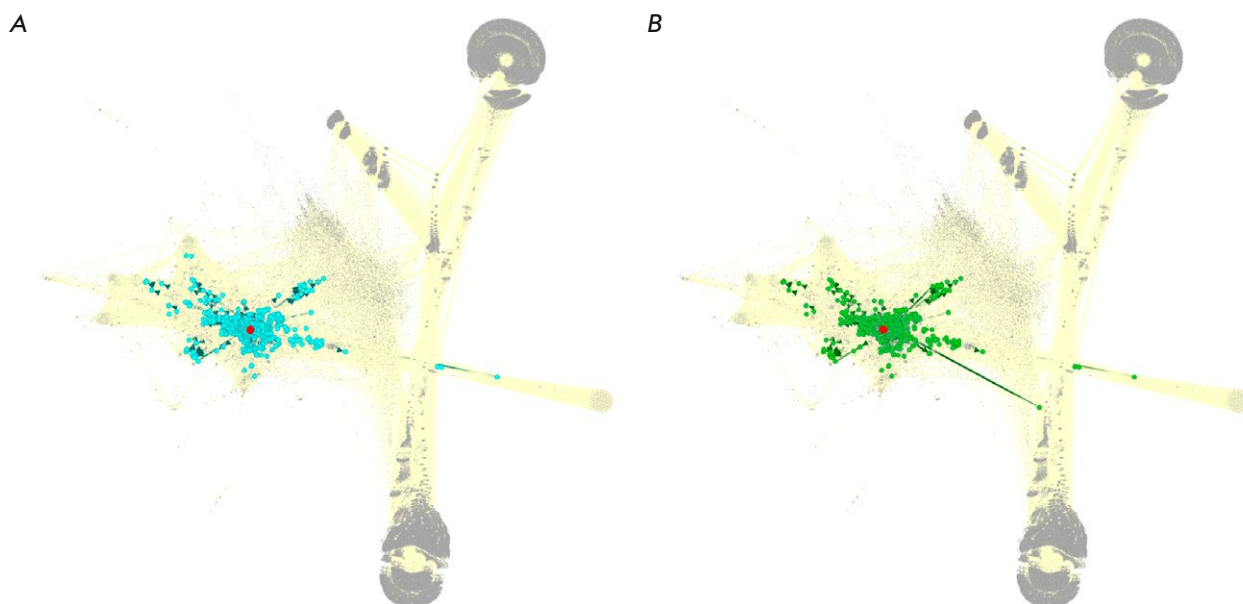
Fig. 1. Schematic representation of the composition of algorithmically built molecular pathways centered around the ERK1 (*A*) and ERK2 (*B*) proteins. The gene products participating in the ERK1 and ERK2 signaling pathways are highlighted in the context of the model of human interactome encompassing 361 654 protein–protein interactions across 64 095 molecular players [35]. Red dots represent the central nodes of the pathways (ERK1 or ERK2); projections of pathway members are shown in blue and green for the ERK1 and ERK2 molecular pathways, respectively. Other nodes are shown in grey, with the rest of the interactome graph shown as a background. Visualized using the Gephi software and ForceAtlas2 algorithm [35]

At the next stage, for each cancer type and each putative biomarker, patients were divided into two groups based on whether the PAL or gene expression value was above or below the optimal cut-off point. The Kaplan–Meier method was employed to estimate the chances of survival. The log-rank test was used to assess the statistical significance of the differences between the two groups. In addition, the hazard ratio (HR) and its 95% confidence interval (CI) were calculated. The data were grouped according to the HR value and its statistical significance, and the results were presented as a heatmap with hierarchical clustering (*Fig. 2*).

For the overall survival (OS) data, different cancer types showed differential clustering when grouped according to HR values for the ERK1/2 pathways (*Fig. 2A*). Both pathways generally showed consistent patterns. Specifically, for glioblastoma, kidney, pancreatic, gastric, bladder, lung adenocarcinoma and lung squamous cell carcinoma, activation of both of the ERK1/2 molecular pathways was associated with significantly lower patient OS numbers. Conversely, for the group of gender-associated female tumors (subtypes of breast cancer and endometrioid carcinoma of the uterine corpus),

activation of both pathways was a positive prognostic biomarker of OS (*Fig. 2A*). Interestingly, conflicting trends were observed in the prognostic significance of ERK1 and ERK2 pathway activation for sarcoma and thyroid cancer. Given the high similarity between these pathways, differences in prognosis may be attributed to variations in the ARR value, which is also considered when calculating PAL and reflects the functional role of the gene product in the pathway under study (*Supplementary Fig. 2, Supplementary Table 1*).

The data obtained for progression-free survival (PFS) generally confirmed the observations obtained for overall survival (*Fig. 2B*). Again, activation of the ERK1/2 pathway was a negative biomarker for glioblastoma, renal, pancreatic, gastric, bladder, lung adenocarcinoma, and squamous cell carcinoma of the lung. In addition, for PFS (not so for OS) it was also a negative biomarker for sarcomas, thyroid cancer, and colorectal cancer. As with OS, activation of the ERK1/2 pathways was a positive biomarker for several subtypes of breast cancer and for endometrioid carcinoma of the uterine corpus. In addition (unlike in OS), it was a positive biomarker for the head and neck, liver, and prostate cancers (*Fig. 2B*).
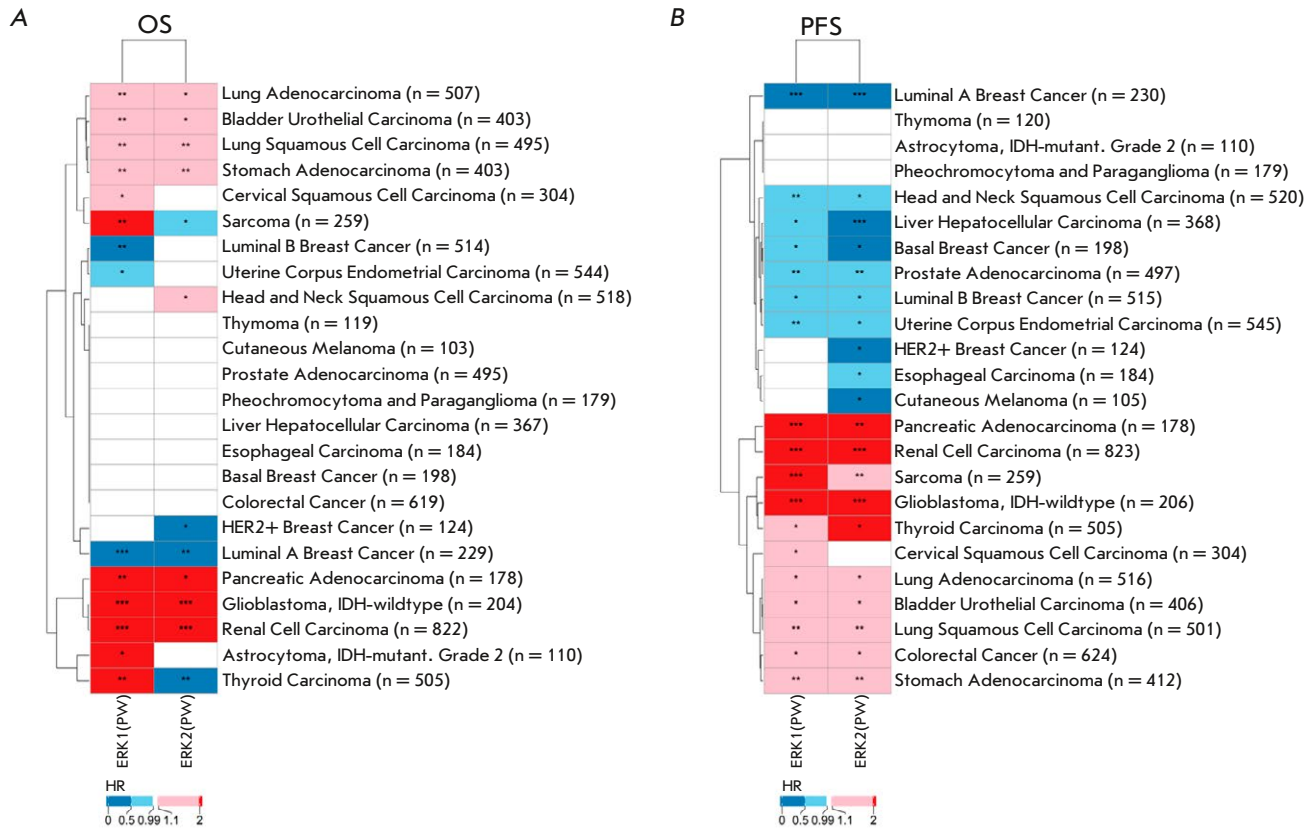
Fig. 2. The heatmap of hazard ratio values calculated for the activation of the ERK1 and ERK2 molecular pathways for the (*A*) TCGA overall survival (OS) and (*B*) progression-free survival (PFS) data. HR − hazard ratio; PW − pathway; $^*p < 0.05$; $^{**}p < 0.01$; $^{***}p < 0.001$

In parallel, a similar analysis was performed for the expression levels of the respective central genes of these pathways: *MAPK3* and *MAPK1* (*Fig. 3*). For the individual gene level, only for bladder carcinoma did both genes show a consistent trend (were negative biomarkers) for both OS and PFS data.

We then averaged the HR values for both OS and PFS data for the PAL and single gene expression types of analyses (*Fig. 4*). For the average HR of PAL, a clear separation of cancer types into two clusters was observed (*Fig. 4A*), whereas the analyses of single gene expression levels showed no definitive clustering (*Fig. 4B*). Hence, the pathway activation analysis returned more consistent and stable results than the assessment of single gene expression levels did. This phenomenon is most probably related to the more stable nature of the pathway-based, aggregated gene expression data, as has been theoretically and experimentally confirmed in previous works [3, 15, 22].

We also calculated the percentage of cancer types where the individual *MAPK3* and *MAPK1* genes and respective genecentric molecular pathways could be statistically significant potential prognostic biomarkers according to the TCGA data (*Table 4*). Overall, the activation of molecular pathways was a putative prognostic biomarker more frequently than the expression of the central genes of the respective pathways.

A dendrogram was then constructed showing the structure of the resulting clusters of cancer types in relation to the HR values calculated for the molecular pathway activation data (*Fig. 5*).

The dendrogram clearly shows two clusters including 10 and 12 cancer types, respectively; within each of those, activation of the ERK1 and ERK2 molecular pathways has similar prognostic value. Thus, the first cluster of 10 cancer types includes the gastric, pancreatic, lung, kidney, bladder, thyroid, cervical, sarcoma, and glioblastoma cancers,
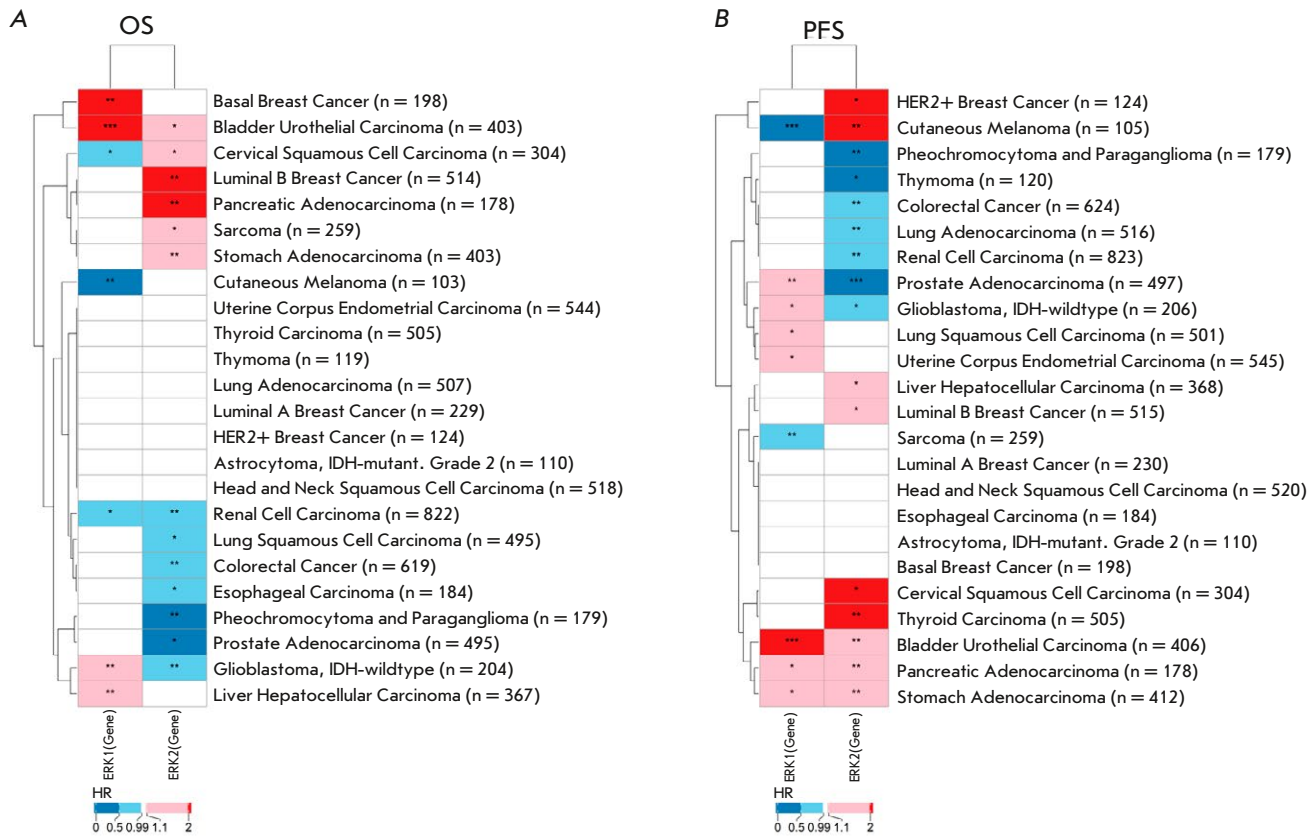
Fig. 3. The heatmap of hazard ratio values calculated for the expression levels of the ERK 1 and ERK 2 individual genes for the (*A*) TCGA overall survival (OS) and (*B*) progression-free survival (PFS) data. HR − hazard ratio; * *p* < 0.05; ** *p* < 0.01; *** *p* < 0.001

where ERK1/2 pathway activation is a rather negative prognostic biomarker (for 90–100% of cluster 1 cancer types). The second cluster includes 12 other tumor types for which activation of these pathways is either a positive prognostic biomarker (HER2+, luminal A and luminal B breast cancer, uterine corpus cancer; a total of 17–25% of cluster 2 cancer types) or has no prognostic value (basal breast cancer, hepatocellular carcinoma, melanoma, etc.; a total of ~75% of cluster 2 cancer types).

Prognostic significance of ERK1/2 pathway activation according to RNA expression datasets in the literature

In this study, we assessed the prognostic values of ERK1/2 pathway activation levels and individual genes using an additional set of previously published clinically annotated gene expression profiles collected by Borisov et al. [28]. Based on the data in the litera-

Table 4. The percentage of cancer types where the ERK1/2 genes or ERK1/2-centric molecular pathways can be potential prognostic biomarkers in the TCGA data

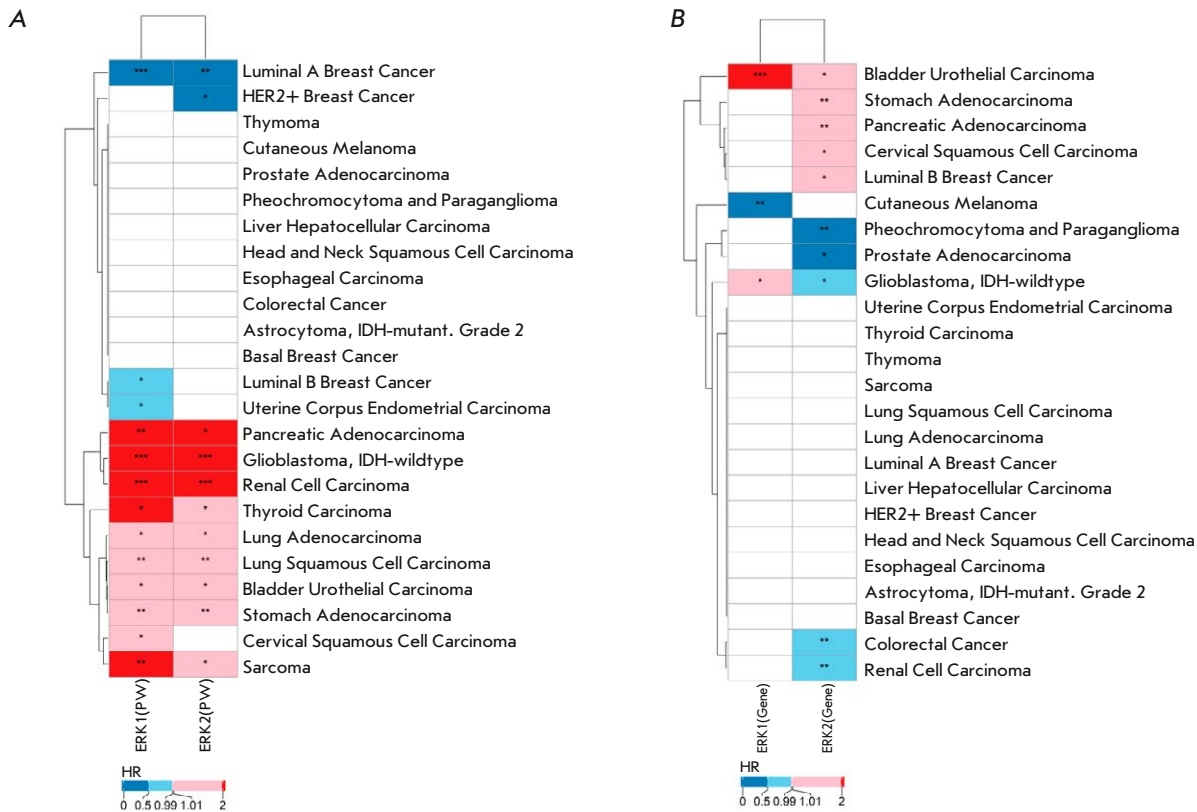| Type of analysis	Type of biomarker	ERK1, %	ERK2, %
Molecular pathway	Negative	42	42
	Positive	12.5	8
Individual gene	Negative	8	21
	Positive	4	21

Fig. 4. The heatmap of averaged overall survival (OS) and progression-free survival (PFS) hazard ratio values calculated for (*A*) the expression levels of the ERK1 and ERK2 molecular pathways and (*B*) ERK1 and ERK2 individual genes for the TCGA data. HR – hazard ratio; PW – pathway; * $p < 0.05$; ** $p < 0.01$; *** $p < 0.001$. If the orders of significance level of *p*-values differed for the OS and PFS data, the lower significance level was shown

ture, patient responses to therapy were evaluated according to the RECIST criteria [27].

Our analysis yielded statistically significant differences in the PAL values between response groups for patients with the following cancers: colorectal cancer, sarcomas, breast cancer, lung adenocarcinoma, and multiple myeloma.

Interestingly, the results of the analysis of the response to therapy for patients with colorectal cancer (*Fig. 6A*) and sarcomas (*Fig. 6B*) from the TCGA project are consistent with the results of the HR analysis and the prognostic value of the molecular pathways studied for the survival of patients from the same TCGA datasets in the larger sample. In both cancer types, patients with lower activation of one or both of the studied molecular pathways responded better to therapy.

In turn, the previously reported positive prognostic significance of ERK1/2 pathway activation in breast cancer was confirmed in two gene expression datas-

ets for patients receiving combination treatment with taxanes and anthracyclines: GSE25066 (paclitaxel, 5-fluorouracil, cyclophosphamide, doxorubicin or epirubicin in adjuvant and neoadjuvant regimens) and GSE20194 (paclitaxel, 5-fluorouracil, cyclophosphamide, doxorubicin in combination in neoadjuvant regimen), (*Fig. 6C,D*).

In addition, in this study, we evaluated the association between PAL and the response to therapy in blood tumors. Statistically significant relationships were identified for the multiple myeloma dataset in patients receiving bortezomib monotherapy (GSE9782). Although this cancer type was not included in the previous TCGA analysis, the results suggest that activation of the ERK1/2 pathway may point to a positive survival prognosis (*Fig. 6E*).

Furthermore, the association between the ERK1/2 pathway PAL and the response to anti-PD1 immunotherapy was evaluated in patients with lung cancer using the GSE207422 dataset. This dataset included
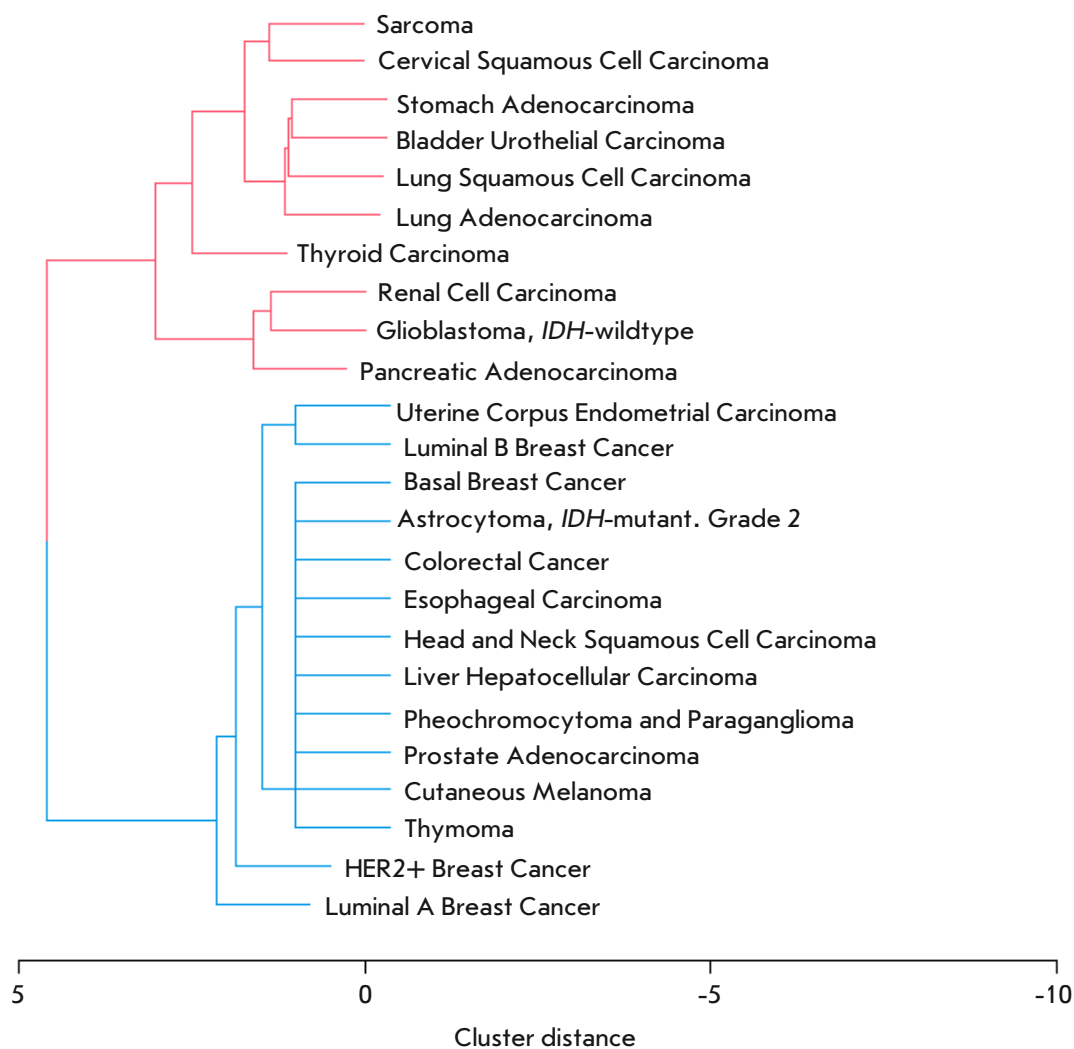
Fig. 5. Dendrogram based on clustering tumors by hazard ratio calculated for the ERK1- and ERK2-centric pathway activation data using TCGA gene expression profiles

RNA expression data from 24 lung cancer patients, of whom twelve were diagnosed with squamous cell lung cancer, eight, with lung adenocarcinoma, and the remaining patients had other diagnoses. For both the entire sample and the individual squamous cell lung cancer and lung adenocarcinoma groups, there was a trend for patients who responded to immunotherapy to demonstrate higher ERK1/2 activation in tumor samples (*Fig. 6F–H*). However, because the sample was small and the observed difference did not reach the level of statistical significance, this finding needs to be revisited in an independent analysis using a larger cohort of patients.

In summary, an analysis of clinical datasets confirmed that activation of ERK1/2 molecular pathways

may be closely associated with the response to several anticancer therapies, such as in breast cancer, colorectal cancer, and sarcomas.

Prognostic significance of ERK1/2 pathway activation according to the original experimental RNA expression datasets

The previous findings were supplemented with the results obtained using our proprietary gene expression datasets previously published by our team for cancer patients annotated with the therapy response. Three of our previous clinical datasets were considered here: glioblastoma ($n = 49$), stomach cancer ($n = 15$), and multiple myeloma ($n = 60$) patients receiving anticancer therapy. The response to the ther-
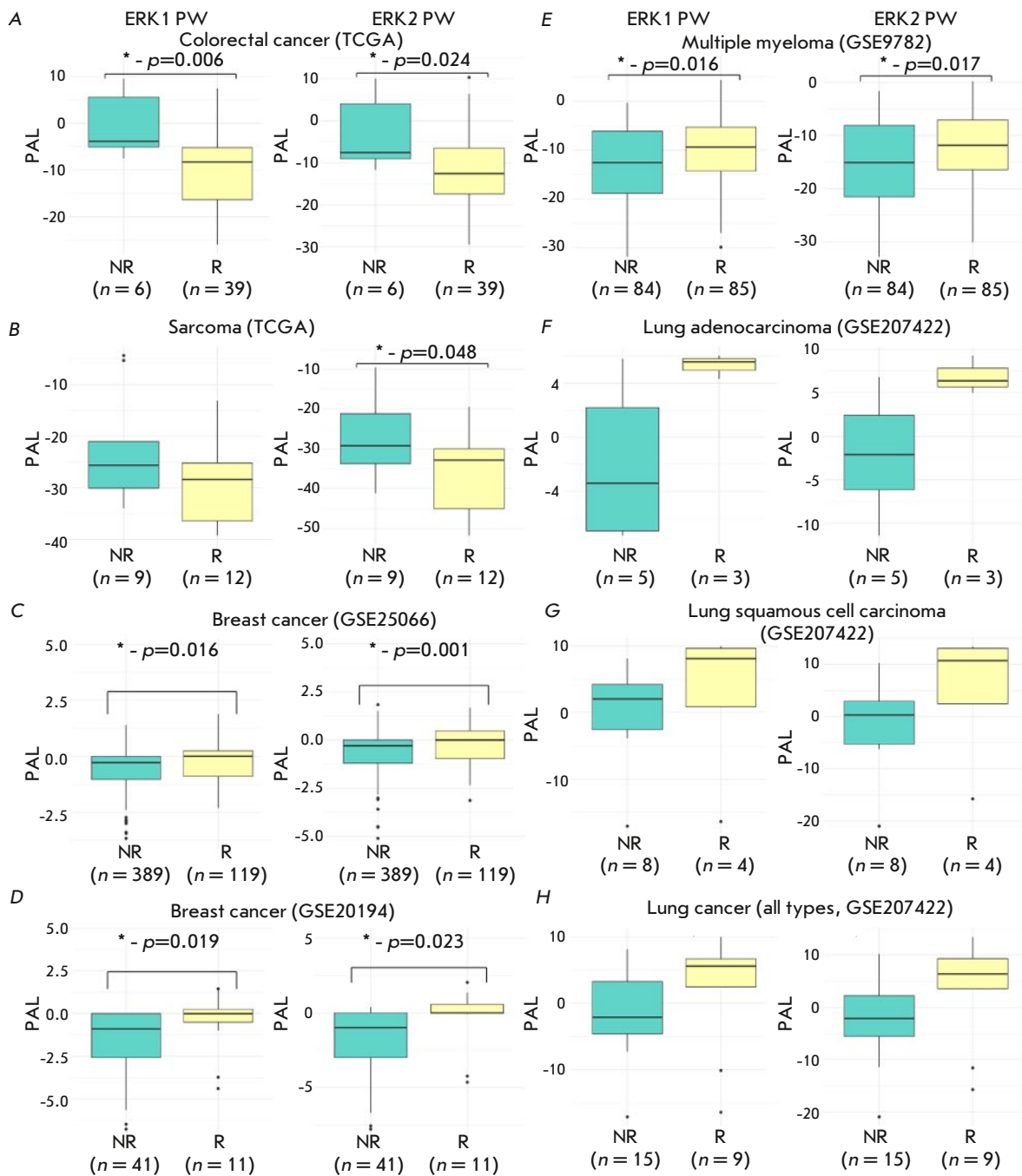
Fig. 6. Differences in PAL of the studied molecular pathways according to the response to therapy (*A*) with a combination of 5-fluorouracil, leucovorin, and oxaliplatin in patients with colorectal cancer from the TCGA project; (*B*) with a combination of docetaxel and gemcitabine in sarcoma patients from the TCGA project; (*C*) with taxane and anthracycline in breast cancer patients from the GEO25066 dataset; (*D*) with taxane and anthracycline in breast cancer patients from the GEO20194 dataset; (*E*) with bortezomib in multiple myeloma patients from the GSE9782 dataset; (*F*) with immunotherapy in patients with lung adenocarcinoma from the GSE207422 dataset; (*G*) immunotherapy in patients with lung squamous cell carcinoma from the GSE207422 dataset; (*H*) immunotherapy in patients with lung cancer (all histological types) from the GSE207422 dataset. The results of the RECIST response analysis are presented as boxplots, where the horizontal line represents the median; the first and third quartiles are represented by the lower and upper boundaries of the rectangle; the minimum and maximum observed values are indicated by the ends of the vertical lines; and possible outliers are shown as individual points beyond them. Statistically significant differences are marked with * , indicating the exact *p*-value. "R" stands for treatment responders; "NR", for non-responders, and "PW", for pathway

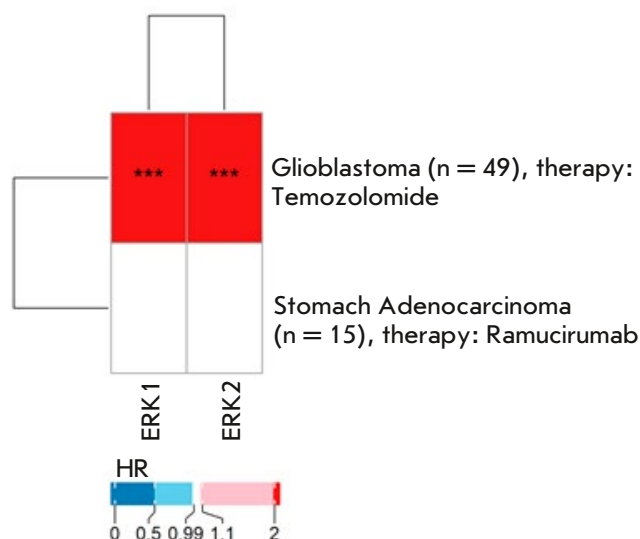Fig. 7. The heatmap of the hazard ratio values calculated for the activation of the molecular pathways ERK1 and ERK2 based on pathway activation levels in relation to the response to anticancer chemotherapy, as assessed by progression-free survival (PFS). HR – hazard ratio; *** $p < 0.001$

apy was assessed either according to the PFS alone (glioblastoma), the RECIST criteria alone (multiple myeloma), or both the PFS and the RECIST criteria (gastric cancer).

The PFS data results revealed a strongly negative prognosis for ERK1/2 activation in response to the temozolomide therapy in glioblastoma and no significant association for the treatment of stomach cancer patients with the targeted therapeutic ramucirumab (*Fig. 7*). No statistically significant difference could be observed for the ERK1/2 pathway activation for the RECIST responder and non-responder patient data.

In the multiple myeloma dataset, we also found no statistically significant difference in ERK1/2 PAL values for patients who responded or did not respond well to treatment with bortezomib-containing regimens.

DISCUSSION

In this study, we for the first time algorithmically reconstructed molecular pathways for the regulatory protein kinases ERK1 and ERK2 using a whole intractome model. We then examined the relationship between the activation levels of these pathways and the available data on patient survival and sensitivity

to different therapeutic regimens in different cancer types.

The results suggest that cancer types can be divided into three classes, in which ERK1/2 pathway activation may be either a negative or positive prognostic biomarker or may not be statistically significant at all. Specifically, the first class of such cancers includes gastric cancer, two different histologic types of lung cancer, glioblastoma, sarcomas, kidney cancer, and some other cancers (*Fig. 4*). Our results are also consistent with the literature: for example, an experimental association between ERK activation and a negative prognosis is known for gastric cancer [45, 46], kidney, bladder and lung adenocarcinoma [47]. For glioblastomas, angiogenic factors and receptors were shown to play one of the key roles in their development; in particular, activate the RAS-RAF-MEK-ERK axis and promote the proliferation, migration, and survival of malignant cells [48]. In our study, activation of the ERK pathway was associated with shorter PFS for glioblastoma patients after therapy with the alkylating drug temozolomide. Therefore, activation of the ERK1/2-pathway in glioblastoma may potentially be not only a prognostic biomarker of survival, but also a biomarker of the response to this type of therapy.

The second class includes cancers for which activation of the ERK1/2 pathway was a positive prognostic biomarker (HER2+, luminal A and luminal B breast and uterine corpus cancers). ERK1 activation has previously been shown to be associated with a better prognosis for breast cancer patients, because it leads to the blockage of the Hippo signaling pathway and one of its downstream targets, the YAP1 protein. However, in the same study, ERK2 activation proved to be associated with a negative prognosis [49]. On the other hand, it has recently been shown that HER2+ breast cancer is resistant to targeted therapy when ERK1/2 kinase activity is low, and that high kinase activity is a prognostic biomarker of tumor sensitivity to therapy [50]. It is consistent with our results, where positive associations were also shown for breast cancer sensitivity to taxanes and anthracyclines, whereas expression of the individual corresponding central genes of these pathways was a much less accurate biomarker.

Finally, for the third class, which includes basal breast cancer, hepatocellular carcinoma, melanoma, and some other cancers, no significant biomarker potential could be detected for activation of the ERK1/2 pathway. We believe that, taken together, these results may be useful for cataloging clinically relevant alterations in intracellular signaling in cancers, and for further developing combination cancer therapies

that may include targeted ERK1/2 inhibitors. It may also be useful to establish adequate models for testing such drug combinations, since activation of the ERK1/2 pathway may have opposite effects on the therapeutic success of treatments for different types of human cancers.

CONCLUSION

In this study, we showed that the level of activation of algorithmically reconstructed ERK1/2 signaling pathways may be an effective prognostic and predictive cancer biomarker, with its prognostic value and significance depending strongly on cancer type and the type of therapy. ●

REFERENCES

1. https://www.iarc.who.int/faq/latest-global-cancer-data-2020-qa. (Accessed June 13, 2024).
2. Wild C.P., Weiderpass E., Stewart B.W. World Cancer Report: Cancer Research for Cancer Prevention. // 2020 (Accessed June 15, 2024). https://publications.iarc.fr/Non-Series-Publications/World-Cancer-Reports/World-Cancer-Report-Cancer-Research-For-Cancer-Prevention-2020. (Accessed June 15, 2024).
3. Buzdin A., Sorokin M., Garazha A., Sekacheva M., Kim E., Zhukov N., Wang Y., Li X., Kar S., Hartmann C., et al. // Semin Cancer Biol. 2018. V. 53. P. 110–124.
4. Chappell W.H., Steelman L.S., Long J.M., Kempf R.C., Abrams S.L., Franklin R.A., Bäsecke J., Stivala F., Donia M., Fagone P., et al. // Oncotarget. 2011. V. 2. № 3. P. 135–164.
5. Steelman L.S., Chappell W.H., Abrams S.L., Kempf C.R., Long J., Laidler P., Mijatovic S., Maksimovic-Ivanic D., Stivala F., Mazzarino M.C., et al. // Aging (Albany NY). 2011. V. 3. № 3. P. 192–222.
6. Stefani C., Miricescu D., Stanescu-Spinu I.-I., Nica R.I., Greabu M., Totan A.R., Jinga M. // Int J Mol Sci. 2021. V. 22. № 19. P. 10260.
7. Sanchez-Vega F., Mina M., Armenia J., Chatila W.K., Luna A., La K.C., Dimitriadoy S., Liu D.L., Kantheti H.S., Saghafinia S., et al. // Cell. 2018. V. 173. № 2. P. 321–337. e10.
8. Liu F., Yang X., Geng M., Huang M. // Acta Pharmaceutica Sinica B. 2018. V. 8. № 4. P. 552–562.
9. Lebedev T., Buzdin A., Khabusheva E., Spirin P., Suntsova M., Sorokin M., Popenko V., Rubtsov P., Prassolov V. // International Journal of Molecular Sciences. 2022. V. 23. № 14. P. 7724.
10. Fu L., Chen S., He G., Chen Y., Liu B. // J Med Chem. 2022. V. 65. № 20. P. 13561–13573.
11. Mass R.D., Press M.F., Anderson S., Cobleigh M.A., Vogel C.L., Dybdal N., Leiberman G., Slamon D.J. // Clinical Breast Cancer. 2005. V. 6. № 3. P. 240–246.
12. Kamel H.F.M., Al-Amodi H.S.A.B. // Genomics, Proteomics & Bioinformatics. 2017. V. 15. № 4. P. 220–235.
13. Ozerov I.V., Lezhnina K.V., Izumchenko E., Artemov A.V., Medintsev S., Vanhaelen Q., Aliper A., Vijg J., Osipov A.N., Labat I., et al. // Nat Commun. 2016. V. 7. P. 13427.
14. Sorokin M., Borisov N., Kuzmin D., Gudkov A., Zolotovskaia M., Garazha A., Buzdin A. // Front Genet. 2021.

V. 12. P. 617059.
15. Borisov N., Suntsova M., Sorokin M., Garazha A., Kovalchuk O., Aliper A., Ilnitskaya E., Lezhnina K., Korzinkin M., Tkachev V., et al. // Cell Cycle. 2017. V. 16. № 19. P. 1810–1823.
16. Lezhnina K., Kovalchuk O., Zhavoronkov A.A., Korzinkin M.B., Zabolotneva A.A., Shegay P.V., Sokov D.G., Gaifullin N.M., Rusakov I.G., Aliper A.M., et al. // Oncotarget. 2014. V. 5. № 19. P. 9022–9032.
17. Gudkov A., Shirokorad V., Kashintsev K., Sokov D., Nikitin D., Anisenko A., Borisov N., Sekacheva M., Gaifullin N., Garazha A., et al. // Front Mol Biosci. 2022. V. 9. P. 753318.
18. Sorokin M., Poddubskaya E., Baranova M., Glusker A., Kogoniya L., Markarova E., Allina D., Suntsova M., Tkachev V., Garazha A., et al. // Cold Spring Harb Mol Case Stud. 2020. V. 6. № 2. P. a004945.
19. Sorokin M., Zolotovskaia M., Nikitin D., Suntsova M., Poddubskaya E., Glusker A., Garazha A., Moisseev A., Li X., Sekacheva M., et al. // BMC Cancer. 2022. V. 22. P. 1113.
20. Zhu Q., Izumchenko E., Aliper A.M., Makarev E., Paz K., Buzdin A.A., Zhavoronkov A.A., Sidransky D. // Hum Genome Var. 2015. V. 2. P. 15009.
21. Zolotovskaia M., Tkachev V., Sorokin M., Garazha A., Kim E., Kantelhardt S.R., Bikar S.-E., Zottel A., Šamec N., Kuzmin D., et al. // Cancers (Basel). 2021. V. 13. № 16. P. 4117.
22. Zolotovskaia M., Kovalenko M., Pugacheva P., Tkachev V., Simonov A., Sorokin M., Seryakov A., Garazha A., Gaifullin N., Sekacheva M., et al. // Proteomes. 2023. V. 11. № 3. P. 26.
23. https://portal.gdc.cancer.gov/. (Accessed June 4, 2024).
24. Tomczak K., Czerwińska P., Wiznerowicz M. // Contemp Oncol (Pozn). 2015. V. 19. № 1A. P. A68–77.
25. Zakharova G., Efimov V., Raevskiy M., Rumiantsev P., Gudkov A., Belogurova-Ovchinnikova O., Sorokin M., Buzdin A. // Int J Mol Sci. 2022. V. 24. № 1. P. 157.
26. Netanely D., Avraham A., Ben-Baruch A., Evron E., Shamir R. // Breast Cancer Research. 2016. V. 18. № 1. P. 74.
27. Eisenhauer E.A., Therasse P., Bogaerts J., Schwartz L.H., Sargent D., Ford R., Dancey J., Arbuck S., Gwyther S., Mooney M., et al. // European Journal of Cancer. 2009. V. 45. № 2. P. 228–247.

28. Borisov N., Sorokin M., Tkachev V., Garazha A., Buzdin A. // BMC Med Genomics. 2020. V. 13. № Suppl 8. P. 111.

29. Goldman M., Craft B., Swatloski T., Cline M., Morozova O., Diekhans M., Haussler D., Zhu J. // Nucleic Acids Res. 2015. V. 43. № Database issue. P. D812–D817.

30. https://www.ncbi.nlm.nih.gov/geo/. (Accessed June 5, 2024).

31. Edgar R., Domrachev M., Lash A.E. // Nucleic Acids Res. 2002. V. 30. № 1. P. 207–210.

32. Kim E.L., Sorokin M., Kantelhardt S.R., Kalasauskas D., Sprang B., Fauss J., Ringel F., Garazha A., Albert E., Gaifullin N., et al. // Cancers (Basel). 2020. V. 12. № 2. P. 520.

33. Sorokin M., Raevskiy M., Zottel A., Šamec N., Skoblar Vidmar M., Matjašič A., Zupan A., Mlakar J., Suntsova M., Kuzmin D.V., et al. // Cancers (Basel). 2021. V. 13. № 14. P. 3419.

34. Borisov N., Sergeeva A., Suntsova M., Raevskiy M., Gaifullin N., Mendeleeva L., Gudkov A., Nareiko M., Garazha A., Tkachev V., et al. // Front Oncol. 2021. V. 11. P. 652063.

35. Zolotovskaia M.A., Tkachev V.S., Guryanova A.A., Simonov A.M., Raevskiy M.M., Efimov V.V., Wang Y., Sekacheva M.I., Garazha A.V., Borisov N.M., et al. // Comput Struct Biotechnol J. 2022. V. 20. P. 2280–2291.

36. Buzdin A., Tkachev V., Zolotovskaia M., Garazha A., Moshkovskii S., Borisov N., Gaifullin N., Sorokin M., Suntsova M. // Adv Protein Chem Struct Biol. 2021. V. 127. P. 1–53.

37. Love M.I., Huber W., Anders S. // Genome Biology. 2014. V. 15. № 12. P. 550.

38. https://www.r-project.org/. (Accessed June 6, 2024).

39. Kassambara A., Kosinski M., Biecek P., Fabian S. 2021. https://cran.r-project.org/web/packages/survminer/index.html. (Accessed June 6, 2024).

40. Therneau T.M., Lumley T., Elizabeth A., Cynthia C. 2024. https://cran.r-project.org/web/packages/survival/index.html. (Accessed June 6, 2024).

41. Ogle DH, Doll JC, Wheeler AP, Dinno A. 2023. https://cran.r-project.org/web/packages/FSA/citation.html. (Accessed June 6, 2024).

42. Fox J, Weisberg S. 2019. https://cran.r-project.org/web/packages/car/citation.html. (Accessed June 6, 2024).

43. Wickham H. 2016. https://link.springer.com/book/10.1007/978-0-387-98141-3. (Accessed June 6, 2024).

44. Gu Z., Eils R., Schlesner M. // Bioinformatics. 2016. V. 32. № 18. P. 2847–2849.

45. Gao J., Pan H., Zhu Z., Yu T., Huang B., Zhou Y. // ABBS. 2020. V. 52. № 9. P. 975–987.

46. Tseng P.-C., Chen C.-L., Shan Y.-S., Chang W.-T., Liu H.-S., Hong T.-M., Hsieh C.-Y., Lin S.-H., Lin C.-F. // Cell Communication and Signaling. 2014. V. 12. № 1. P. 69.

47. Kawano T., Inokuchi J., Eto M., Murata M., Kang J.-H. // Cancers. 2022. V. 14. № 21. P. 5425.

48. Ahir B.K., Engelhard H.H., Lakka S.S. // Mol Neurobiol. 2020. V. 57. № 5. P. 2461–2478.

49. Yu S., Zhang M., Huang L., Ma Z., Gong X., Liu W., Zhang J., Chen L., Yu Z., Zhao W., et al. // Aging (Albany NY). 2019. V. 11. № 24. P. 12295–12314.

50. Debets D.O., Graaf E.L. de, Liefaard M.C., Sonke G.S., Lips E.H., Ressa A., Altelaar M. // iScience. 2024. V. 27. № 6. .https://www.cell.com/iscience/abstract/S2589-0042(24)01080-0. (Accessed June 11, 2024).

The Parameters of Long-Term Humoral Immunity Induced by a Single Injection of the Sputnik Light Vaccine Among Non-infected Volunteers and Those Infected with SARS-CoV-2

F. M. Izhaeva[1], A. I. Tukhvatulin[1*], A. S. Dzharullaeva[1], I. V. Dolzhikova[1], O. V. Zubkova[1], D. V. Shcheblyakov[1], N. L. Lubenets[1], E. A. Smolyarchuk[2], T. G. Zubkova[3], A. S. Erokhova[1], I. M. Cherenkova[1], K. M. Bukhtin[1], O. Popova[1], N. M. Tukhvatulina[1], B. S. Naroditsky[1], D. Y. Logunov[1,2], A. L. Gintsburg[1,2]

[1]N.F. Gamaleya National Research Center for Epidemiology and Microbiology, Ministry of Health of the Russian Federation, Moscow, 123098 Russian Federation
[2]I.M. Sechenov First Moscow State Medical University, Ministry of Health of the Russian Federation (Sechenov University), Moscow, 119991 Russian Federation
[3]Eco-Safety Medical Center, St. Petersburg, 191119 Russian Federation
*E-mail: Amir_tukhvatulin@gamaleya.org

ABSTRACT Although the immunogenicity of clinically approved COVID-19 vaccines remains under intensive investigation, little is still known about the parameters of long-term immune responses. In this paper, we present for the first time the parameters of humoral immunity studied in the phase 1–2 open-label clinical trial of the Sputnik Light vaccine, with a special focus on late follow-up time points (90 and 180 days). For the most accurate assessment of the parameters of humoral post-vaccination immunity (titer and avidity index of antigen-specific antibodies against the RBD domain of SARS-CoV-2), we conducted an additional analysis that allowed us to triage volunteers with immunity formed only in response to vaccination, as well as those with hybrid immunity (infected with SARS-CoV-2 before and after vaccination). The findings indicate that single-shot vaccination with the Sputnik Light vaccine induces a durable (seroconversion 73% on day 180) and mature humoral immunity. Natural immunization as a result of the SARS-CoV-2 infection leads to significant changes in the studied parameters of post-vaccination immunity.

KEYWORDS COVID-19, SARS-CoV-2, vaccines, Sputnik Light, vaccine-induced antibody response, serum maturation, hybrid immunity.

ABBREVIATIONS Ad26 – replication-defective recombinant human adenovirus serotype 26; CT – clinical trial; ELISA – enzyme-linked immunosorbent assay; GMT – geometric mean titer; HIV – human immunodeficiency virus; IgG – immunoglobulin G; IgG1 – isotype 1 immunoglobulin G; IgG4 – isotype 4 immunoglobulin G; IgM – immunoglobulin M; OD – optical density; PC – positivity coefficient; PCR – polymerase chain reaction; RBD – receptor-binding domain; TMB – tetramethylbenzidine; WHO – World Health Organization.

INTRODUCTION

The outbreak of the COVID-19 pandemic in 2019, caused by the sudden explosive spread of a novel coronavirus known as SARS-CoV-2, significantly affected the health care infrastructures of many countries around the globe [1]. A massive effort consisting of measures for the specific treatment and prevention of COVID-19 was promptly launched. According to the World Health Organization (WHO), over 180 clinical trials were conducted within three years, resulting in the approval of 50 vaccines in different countries [2].

Once the vaccines were cleared for clinical practice, studies aiming to assess their immunogenicity had to be continued. The findings of these studies are needed not only in order to detail the principles that underpin the general functioning of the human immune system, but also to assess and compare the short- and long-term immunogenicity profiles of the current COVID-19 vaccines. It is worth mentioning that conducting, and analyzing the results, of long-term clinical trials is very challenging. An example of such challenges is the inconsistency of the results of long-term clinical trials of the vaccine based on the replication-defective recombinant human adenovirus serotype 26 (Ad26), Ad26.COV2.S (Janssen Vaccines). After comparing the parameters of the humoral immune response between peak values at week 4 and eight months after single-shot administration of the Ad26.COV2.S vaccine, Collier et al. detected an increase in the virus-neutralizing antibody titer (the geometric mean titer (GMT) changed from 1 : 146 to 1 : 629) and a reduction in the titer of IgG antibodies against the receptor-binding domain (RBD) of the SARS-CoV-2 surface glycoprotein (from 1 : 1 361 to 1 : 843) [3]. Yet, another study reported an increase in the titer of anti-RBD IgG antibodies (from 1 : 645 on day 29 to 1 : 1 306 on day 239) and a reduction in the titer of neutralizing antibodies in pseudo-typed virus neutralization assay (from 1 : 272 to 1 : 192) eight months after single-shot immunization with Ad26.COV2.S [4]. Finally, the third long-term clinical trial revealed a decrease in the titer of neutralizing antibodies in pseudo-typed virus neutralization assay (from 1 : 105 to 1 : 41) and a statistically insignificant reduction in the titer of anti-RBD IgG antibodies (GMT, from 1 : 20 447 to 1 : 15 379) during the follow-up period, between 1.5 and 6 months in volunteers subjected to single-shot immunization with Ad26.COV2.S [5].

These inconsistencies in the results could have been caused by the effect of the unregistered COVID-19 infections during the post-vaccination period, which is known to be able to significantly alter the intensity of the immune response [6, 7]. Since all the approved vaccines do not ensure 100% protection against the SARS-CoV-2 infection, clinical trial duration is obviously proportional to the risk of being infected with the coronavirus [8]. In a long-term study, it is impossible to isolate volunteers for the entire follow-up period. Therefore, it is crucial to separate volunteers infected with SARS-CoV-2 during the post-vaccination period from non-infected ones when analyzing the results. Additional challenges may also arise if a small number of volunteers is included in the study. In this situation, the sample size of the group of individuals not infected with SARS-CoV-2 may be insufficient as relates to obtaining statistically significant results.

Previously, we have reported the results of an evaluation of the safety, reactogenicity, and immunogenicity of the Sputnik Light vaccine, which is based on the Ad26 vector carrying the gene encoding the full-length SARS-CoV-2 spike protein, until day 42 of the follow-up period [9]. The objective of this new study was to quantify the changes in the parameters of the post-vaccination humoral immunity in vaccinated volunteers at late follow-up time points (days 90 and 180). For the purpose of obtaining data on auto-immunogenicity of the vaccine, we additionally analyzed serum samples collected from the volunteers (measuring the titers of antibodies specific to the SARS-CoV-2 N protein throughout the study), by selecting a group comprising 59 individuals that had not been infected with the SARS-CoV-2 virus prior to vaccination and remained uninfected throughout the entire period of the clinical trial.

The reported results make it possible to determine the long-term self-immunogenicity of the Sputnik Light vaccine and compare the evolution of humoral post-vaccination immune responses with two groups of volunteers with hybrid immunity: infected with SARS-CoV-2 before (group 2) or after (group 3) vaccination.

EXPERIMENTAL

Clinical trial design and procedures

The phase 1–2 clinical trial designated "An open study on the safety, tolerability, and immunogenicity of the medicinal drug 'Sputnik Light' to help prevent the coronavirus infection caused by the SARS-CoV-2 virus" (Protocol No. 06-Sputnik Light-2020) was conducted in 2020 at the medical institution Eco-safety Medical Center (St. Petersburg, Russia). The study was approved by the Local Ethics Committee and authorized by the Ministry of Health of the Russian Federation. The ClinicalTrials.gov identifier is NCT04713488.

The screening procedure was started immediately after informed consent was secured, and it lasted no longer than seven days before study enrollment.

As a result of the screening, 110 out of 150 volunteers were enrolled in the study without prior randomization and stratification. All clinical trial participants met the following inclusion criteria: the volunteers had signed an informed consent to participate in the study; aged more than 18 years; had no chronic infectious diseases (HIV, hepatitis B and C, syphilis) or cancer; had not been vaccinated against COVID-19 with any other medicinal products; had

received no therapy with immunoglobulins or immunosuppressants within 30 days prior to enrollment; had no COVID-19 as confirmed by the negative PCR SARS-CoV-2 RNA test result at screening (Intifica Alkor Bio kit, Russia) and the negative result of semi-quantitative enzyme immunoassay for IgM and IgG antibodies against SARS-CoV-2 (Mindray kit, China); and had no past history of COVID-19.

After the screening procedure, six outpatient visits (days 1, 10, 28, 42, 90, and 180 post-vaccination) involving blood collection were arranged. At visit 1 (day 1), the volunteers received a single-dose intramuscular injection of the Sputnik Light vaccine in liquid formulation, developed and manufactured at the N.F. Gamaleya National Center of Epidemiology and Microbiology, Ministry of Health of the Russian Federation, in compliance with Good Manufacturing Practice regulations. The vaccine was based on the recombinant human adenovirus of serotype 26 carrying the gene encoding the full-length SARS-CoV-2 S protein (10^{11} viral particles per 0.5 mL/dose). A PCR test for SARS-CoV-2 RNA was additionally performed on study days 1, 10, and 28.

Measuring the titer of IgG total antibodies specific to the RBD of the SARS-CoV-2 S glycoprotein and their subclasses

Sera were isolated from blood samples by 15-min centrifugation at 4 000 rpm. The sera were subjected to twofold serial dilution, from 1 : 50 to 1 : 102 400. The titer of antigen-specific antibodies was quantified using a kit for enzyme-linked immunosorbent assay of anti-RBD IgG "SARS-COV-2-RBD-IFA-Gamaleya," manufactured at the N.F. Gamaleya National Center of Epidemiology and Microbiology, Ministry of Health of the Russian Federation (Marketing Authorization No. RZN 2020/10393). The serially diluted serum samples were pipetted onto an antigen-coated plate (100 ng RBD per well) and incubated under stirring (300 rpm, 37°C) for 1 h. After washing with phosphate-buffered saline supplemented with 0.05% Tween-20, HRP-conjugated antibodies specific to human total IgG (NA933-1ML, Cytiva, USA) or IgG1 and IgG4 subclasses (A10648 and A10654, Invitrogen, USA) were added to the plate, and incubation under stirring (300 rpm, 37°C) for 1 h was repeated. After a washing procedure, a tetramethylbenzidine hydrochloride (TMB) solution was added; the plate was incubated in the dark for 15 min, and the reaction was stopped by adding 1 M sulfuric acid. The optical density was measured at 450 nm (OD_{450}). The IgG titer was determined as the highest state of dilution of the serum where OD_{450} of the test sample exceeded that of the control serum at the same dilution more than

twofold (for each volunteer, his or her own pre-vaccination serum sample was used as their control). If OD_{450} in the serum sample (1 : 50 dilution) was not higher than that in the control serum, the sample was assigned a titer of 1 : 25. All the samples were analyzed in two replicates, and the mean values were determined.

Determining the avidity index of IgG antibodies specific to the RBD of SARS-CoV-2 S glycoprotein

Twofold dilutions of sera were pipetted onto plates for the detection of anti-RBD IgG "SARS-COV-2-RBD-IFA-Gamaleya". One hour later, an equal volume of phosphate-buffered saline or 8 M urea (100 μL) was added to the wells for 10 min. The next procedure was identical to that used when measuring the anti-RBD-IgG titer. The avidity index for each serum was calculated as the ratio between OD_{450} of the well containing the denaturing agent (in the next-to-the-last dilution, being twofold higher than OD_{450} of the control serum in the same dilution) and OD_{450} of the well containing phosphate-buffered saline in the same dilution [10]. All the samples were analyzed in two replicates; the result was determined as the mean value recorded in two replicates.

Detecting antibodies specific to the SARS-CoV-2 nucleoprotein (N protein)

Antibodies specific to the SARS-CoV-2 N protein were additionally detected using the *in vitro* ELISA diagnostic kit "K153NG" (XEMA, Russia) according to the manufacturer's instructions. Sera were diluted 100-fold in a dilution buffer and then added onto a 96-well antigen-coated plate (100 μL per well) in two replicates. The control samples (negative and positive, supplied as part of the kit) were also placed into three additional wells. The plate was incubated at 37°C for 30 min without stirring, rinsed with a wash solution five times, and 100 μL of conjugated secondary antibodies was added into the wells. After incubation and washing according to the procedure described above, 100 μL of the TMB solution was added and the plate was incubated in the dark at room temperature for 25 min. The reaction was then stopped by adding 100 μL of 1 M sulfuric acid per well, and the optical density was immediately measured at 450 nm. For the purpose of interpreting the results, the Cut-off value was found using the following formula: Cut off = X + 0.2, where X is the mean OD_{450} value obtained for Negative Controls 1 and 2. Next, for each sample, the positivity coefficient (PC) was determined using the formula PC = OD_{450} of the sample/cut-off. The result was interpreted as follows: PC > 0.9 is negative; PC > 1.1 is positive. For the samples with
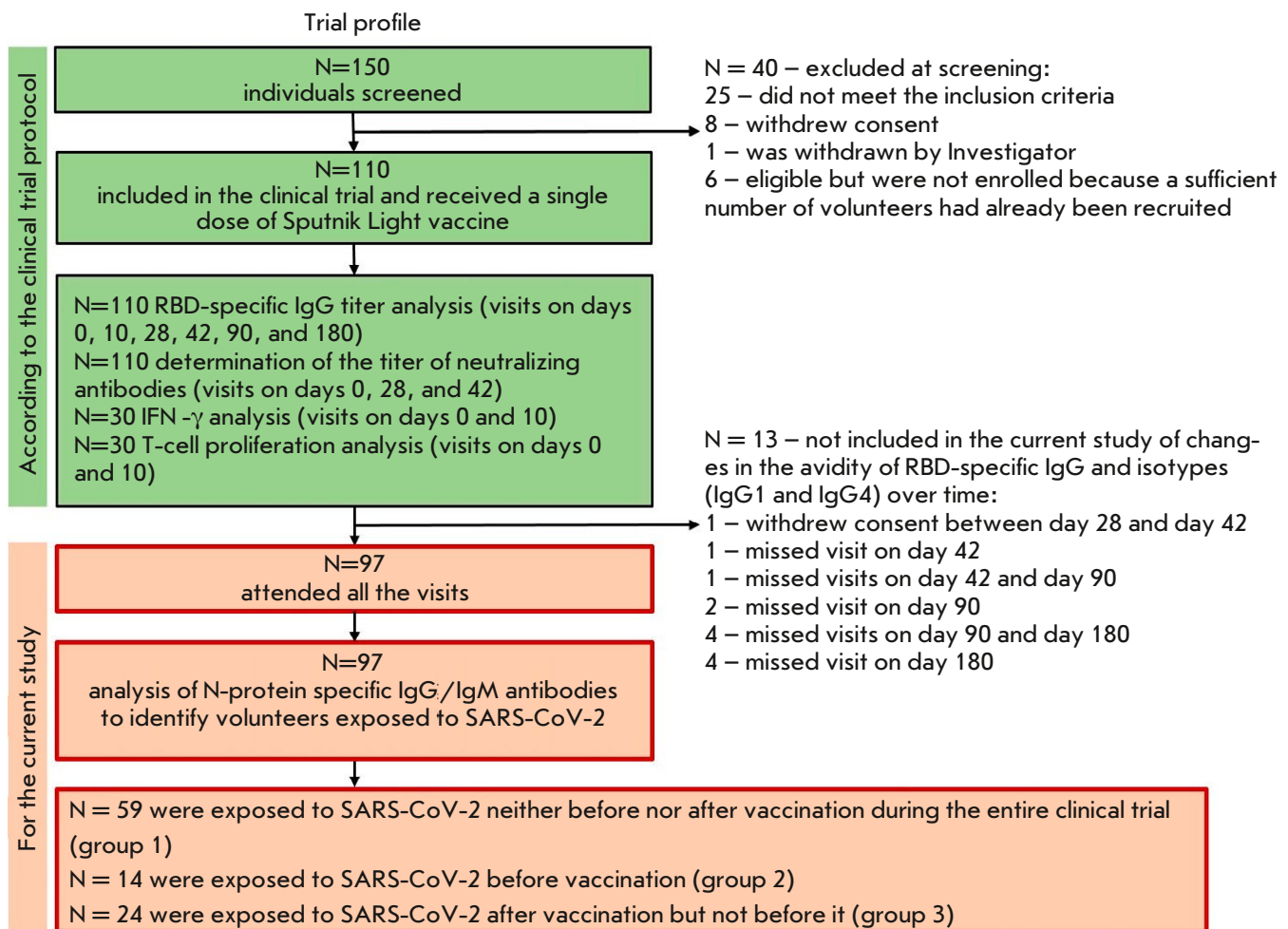
Fig. 1. Trial profile and stratification of volunteers into groups

0.9 < PC < 1.1, the assay was repeated using a smaller serum dilution.

Statistical analysis

The changes in the parameters within one group over time were compared using the Friedman test with Dunn's correction. The Kruskal–Wallis test with Dunn's correction was employed to compare parameters at the same time point between different groups. The correlation was assessed using the Pearson correlation coefficient. The analysis was conducted using the GraphPad 8 and Microsoft Office Excel 2019 software.

RESULTS

In order to determine the dynamics, including individual ones, of the development of post-vaccination immunity by follow-up day 180, 97 volunteers who had attended all the scheduled blood sampling visits

(on days 1, 42, 90, and 180 post-vaccination) were selected (*Fig. 1*).

The serum samples of the volunteers were used to quantify IgG antibodies specific to RBD and the SARS-CoV-2 N protein before and after vaccination. While all the volunteers had negative results in the test for SARS-CoV-2 RNA and ELISA assay for anti-SARS-CoV-2 IgM and IgG at the screening stage, in an earlier publication reporting the results obtained until study day 42, a group consisting of 14 seropositive volunteers with anti-RBD IgG antibodies before vaccination was identified [9]. In this study, antibodies specific to the SARS-CoV-2 N protein were detected in other volunteers using sera collected on days 90 and 180. Hence, to obtain data on the immunogenicity of the Sputnik Light vaccine in the current study, the 97 volunteers were allocated to three groups. The first group comprised volunteers exposed to SARS-CoV-2 neither before nor after vaccination (i.e., those whose
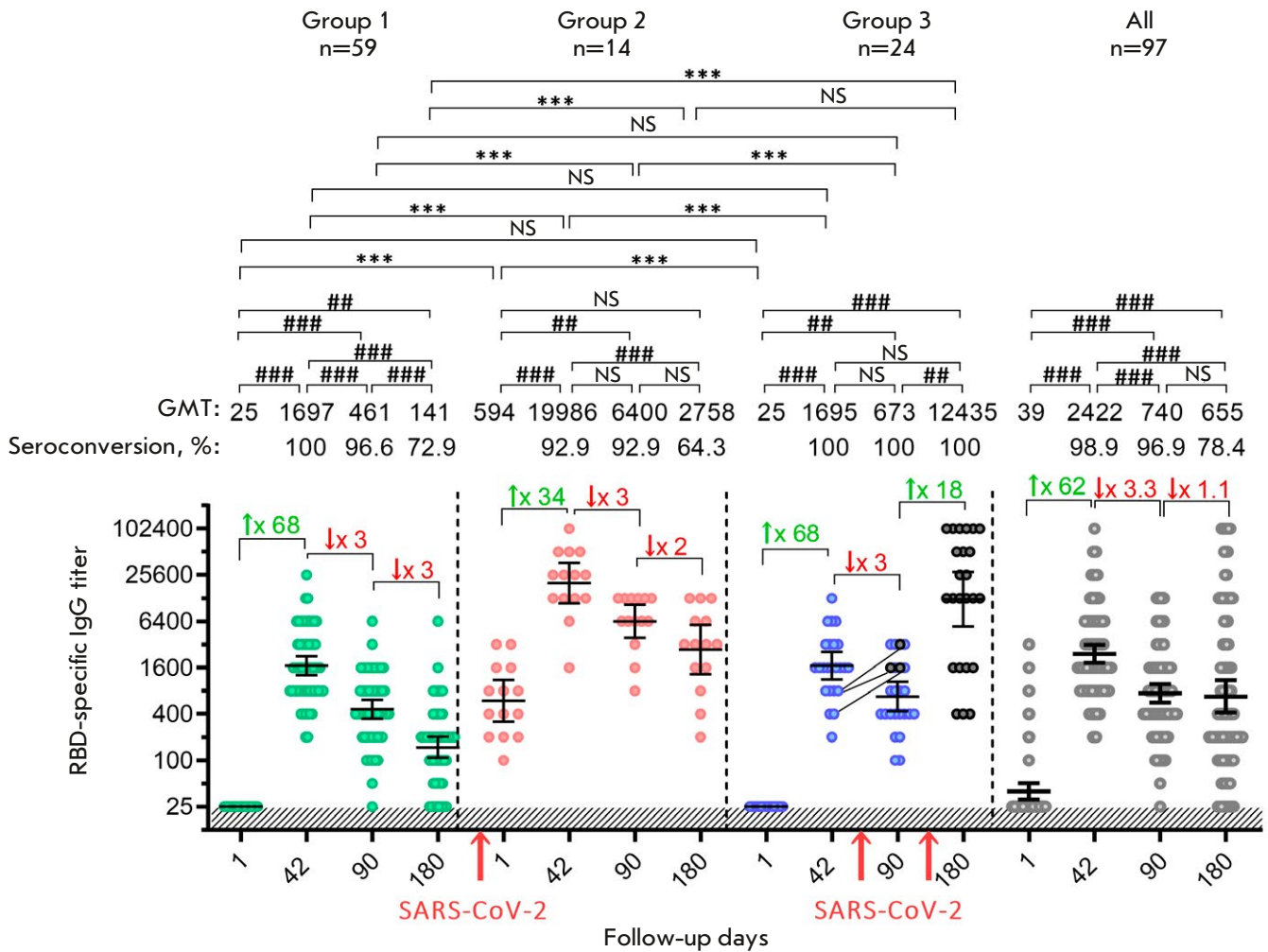
Fig. 2. Titer of RBD-specific IgG antibodies in volunteers vaccinated with the Sputnik Light vaccine. The data before (day 1) and on days 42, 90, and 180 post-vaccination for all the analyzed participants (gray dots), as well as those stratified depending on the presence/absence of a SARS-CoV-2 infection, are presented: group 1 – individuals non-infected with SARS-CoV-2 (green dots); group 2 – individuals with SARS-CoV-2 before vaccination (red dots); and group 3 – individuals infected with SARS-CoV-2 post-vaccination (blue dots). Black dots indicate participants infected with SARS-CoV-2 in group 3. The lines between the dots connect the values in the same participant before (day 42) and after infection (day 90). N denotes the number of volunteers in each stratum. Dots show individual data points. Horizontal lines represent geometric mean titers (GMTs); the values are shown above the graph. The percentage of participants (%) who had seroconversion at different time points was defined as a statistically significant, at least fourfold, increase in post-vaccination titer compared to the baseline (day 1). The whiskers represent a 95% confidence interval (CI). The colored numbers with arrows above the square brackets indicate the fold increase or decrease in the GMT compared to the previous time point. The red arrows below the horizontal axis indicate the time of infection with the SARS-CoV-2 virus. Significant differences between different time points within the same group are indicated with hashes: ## $p < 0.05$; ### $p < 0.005$; ### $p < 0.0001$ (calculated using the Friedman test with Dunn's correction). Statistically significant intergroup differences are indicated with asterisks: * $p < 0.05$; ** $p < 0.005$; or *** $p < 0.0001$ (Kruskal–Wallis test with Dunn's correction). NS – non-significant difference

humoral immunity parameters depended exclusively on vaccination, n = 59). The immunity of group 2 volunteers was primed with a SARS-CoV-2 infection (n =14) prior to the administration of the Sputnik Light vaccine. Group 3 volunteers (n = 24) had no im-

munity against SARS-CoV-2 before vaccination but acquired hybrid immunity following a SARS-CoV-2 infection between days 42 and 180 (three participants were exposed to the virus between days 42 and 90; the remaining 21 participants, between days 90 and 180).
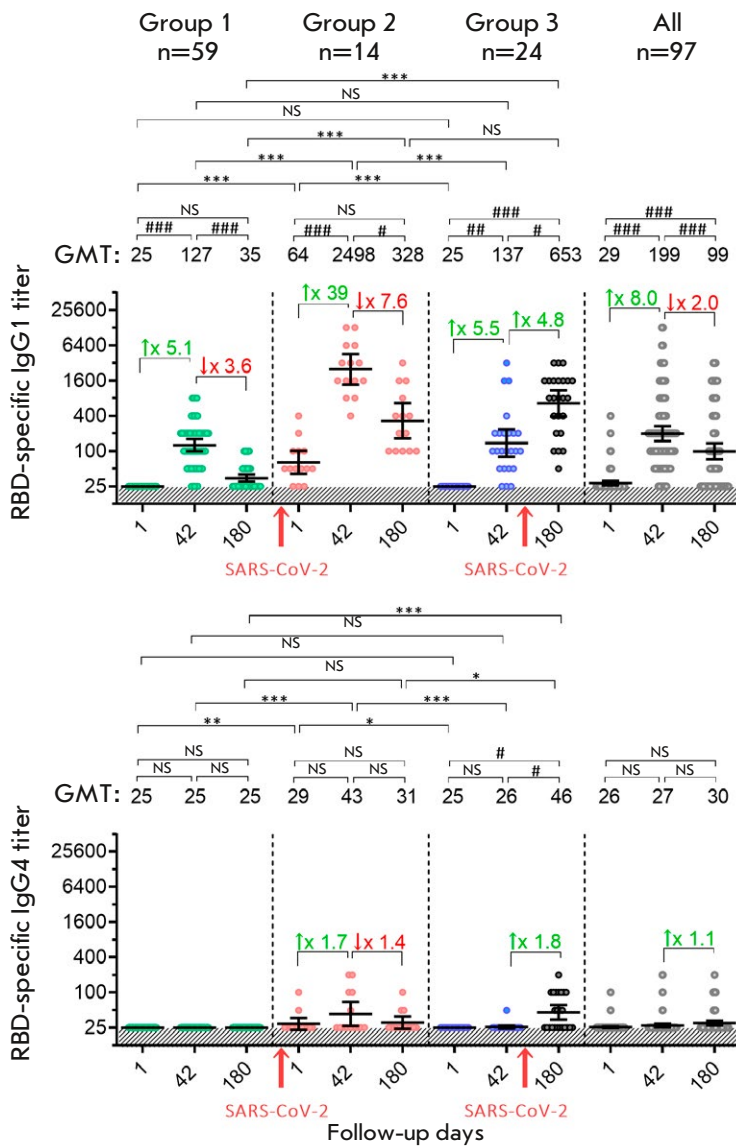
Fig. 3. Titer of RBD-specific IgG1 and IgG4 antibodies in volunteers vaccinated with Sputnik Light. The data before (day 1) and on days 42 and 180 after vaccination for all the participants (gray dots), as well as ones stratified depending on the presence/absence SARS-CoV-2 infection: group 1 – individuals not infected with SARS-CoV-2 (green dots); group 2 – individuals infected with SARS-CoV-2 before vaccination (red dots); and group 3 – individuals infected with SARS-CoV-2 after vaccination (blue dots). Black dots indicate participants infected with SARS-CoV-2 in group 3. N denotes the number of volunteers in each stratum. Dots show individual data points. Horizontal lines refer to the geometric mean titers (GMT); whiskers represent a 95% confidence interval (CI). The values are shown above the graph. The colored numbers with arrows above the square brackets indicate the fold increase or decrease in the GMT compared to the previous time point. The red arrows below the horizontal axis indicate the time of infection with the SARS-CoV-2 virus. Significant differences between different time points within the same group are indicated by hashes: # $p < 0.05$; ## $p < 0.005$; ### $p < 0.0001$ (calculated using the Friedman test with Dunn's correction). Statistically significant intergroup differences are indicated by asterisks: * $p < 0.05$; ** $p < 0.005$ or *** $p < 0.0001$ (the Kruskal–Wallis test with Dunn's correction). NS indicates non-significant difference

The titer dynamics of RBD-specific IgG antibodies in the serum of non-infected volunteers and those with hybrid immunity

An analysis of the titers of RBD-specific IgG antibodies demonstrated that in volunteers with no prior immunity (group 1), vaccination with the Sputnik Light vaccine elicited an abrupt rise in the geometric mean titer (GMT) to 1 : 1 697 on day 42, which then started to prominently decrease, reaching 1 : 461 by day 90 and 1 : 141 by day 180 (*Fig. 2*). In group 2 volunteers with prior immunity against SARS-CoV-2, the GMT at the instant of vaccination was 1 : 594. In this group, immunization triggered the largest increase in the titer of antigen-specific antibodies on day 42 (GMT 1 : 19 986), which then started to decrease at a pace close to that for group 1 (GMT 1 : 6 400 on day

90; GMT 1 : 2 758 on day 180). Group 3 volunteers without prior SARS-CoV-2 immunity (the pre-threshold GMT being 1 : 25 on day 1) exhibited an increase in the humoral immune response on day 42 (GMT 1 : 1 695) similar to that observed in group 1. However, after GMT statistically significantly dropped to 1 : 673 on day 90, it abruptly increased to 1 : 12 435 on day 180. The rise observed on day 180 is attributed to an immunity boost from a prior SARS-CoV-2 infection in all the volunteers in this group (as evidenced by the detection of antibodies specific to the SARS-CoV-2 N protein), whereas on day 90, reduction in the titer of post-vaccination antibodies was not accompanied by significant changes in the GMT of anti-RBD IgG in 3 out of the 24 vaccinated participants (between days 42 and 90). When assessing the results obtained for the

entire cohort of 97 volunteers, one can see that the antibody response curve is similar to the response in group 1, where the strongest immunity was observed on day 42 after vaccination, followed by a decline. However, the antibody titers in the overall group were higher than those in group 1 at all the blood collection points, reaching statistically significant differences on day 180 ($p < 0.002$). Furthermore, at later time points, the titer in the overall group decreased more smoothly compared to group 1. In total, the reported results vividly illustrate the effect of the SARS-CoV-2 infection on the intensity of humoral immunity.

Having detected a prominent rise in total IgG titers after vaccination with the Sputnik Light vaccine, we characterized the changes in the titers of IgG1 and IgG4 antibody subclasses in the analyzed groups. Serum samples were collected at the beginning of the clinical trial (day 1), when the humoral immunity was the strongest in group 1 (day 42), and at the latest follow-up point (day 180) (*Fig. 3*). The IgG1 and IgG4 subclasses were selected because of the differences in their functions and predictive power. IgG1 are the main components in the post-vaccination titer of total IgG antibodies with several defensive functions: antibody-dependent cytotoxicity, phagocytosis, complement activation, and virus neutralization [11, 12]. Meanwhile, the individuals infected with SARS-CoV-2 demonstrated a pronounced rise in the titer of poorly functional IgG4, which allows the virus to evade the defensive responses of adaptive immunity [13]. An analysis of IgG1 antibody titers revealed similar kinetics for total IgG antibodies. Group 1 volunteers with IgG1 titers undetectable on day 1 had a prominent peak (GMT 1 : 127) on day 42 post-vaccination, followed by a reduction on day 180 (GMT 1 : 35). The curve of IgG1 response in group 2 individuals was similar to that of group 1 individuals; the IgG1 titer was maximal on day 42 (GMT 1 : 2 498) and further decreased by day 180 (GMT 1 : 328). In group 3 volunteers, the IgG1 titer was on a gradual increase: it was undetectable on day 1, it increased on day 42 to a level close to that in group 1 (GMT 1 : 137), but it rose to GMT 1 : 653 on day 180, after the hybrid immunity had kicked in. In the overall sample, IgG1 antibody titers on days 42 (GMT 1 : 199) and 180 (GMT 1 : 99) were higher than those in group 1, indicating that inclusion of participants with hybrid immunity can significantly change resulting values. When interpreting the values of IgG4 titers, it is worth noting that this class of antibodies was not detected in group 1. Meanwhile, IgG4 antibodies formed in participants with hybrid immunity (groups 2 and 3) but a statistically significant increase in the IgG4 titer was observed only in group 3 on study day 180. The results

support the conclusions that SARS-CoV-2 can trigger the formation of IgG4 antibodies and characterize the inability of the single-shot Sputnik Light vaccine to induce an increase in the IgG4 titer.

The dynamics of the avidity index of RBD-specific IgG antibodies in the serum of not infected volunteers and those with hybrid immunity

The measurement of the avidity index of RBD-specific IgG antibodies demonstrated that this parameter continued to gradually increase throughout the entire follow-up period in group 1 volunteers from the minimal values (0.06) on day 1 to 0.61 on day 180 (*Fig. 4*). Group 2 volunteers with prior immunity were characterized by a prominent avidity index of RBD-specific IgG antibodies on day 1 (0.47), which did not show an increase on day 42, but began to noticeably rise starting on day 90 and by day 180 had reached a higher value compared to that for group 1 (0.74). Regardless of exposure to the SARS-CoV-2 infection during the period between day 42 and day 180 of the follow-up period, volunteers in groups 3 and 1 showed similar avidity indices of RBD-specific IgG antibodies. This fact may be indication that the time between the priming immunization and exposure to the boosting coronavirus infection was insufficient [14]. Interestingly, the median avidity index of antibodies for the entire sample did not significantly differ from that in group 1 (unlike for the titers of RBD-specific IgG antibodies) because of the oppositely directed changes in groups 2 and 3. Meanwhile, the overall sample was characterized by significant dispersion of individual data.

The correlation between the titer and the avidity index of RBD-specific IgG antibodies in the serum of not infected volunteers and those with hybrid immunity

After assessing the changes in the quantitative (the titer) and qualitative (the avidity) parameters of antigen-specific antibodies in volunteers post vaccination with Sputnik Light, we conducted a correlation analysis in groups with indication of the day of blood sample withdrawal (*Fig. 5*). The correlation between the analyzed parameters was found to differ in the course of blood sampling time in all three study groups. Thus, a weak overall correlation between the titer and the avidity index of RBD-specific IgG antibodies ($r = 0.34$) was observed in group 1. It is worth mentioning that the avidity index of serum continued to increase over time, while the titer of antigen-specific antibodies was declining. Interestingly, no correlation between the titer and the avidity index of antibodies ($r = -0.05$, $p = 0.7102$) was observed in vol-
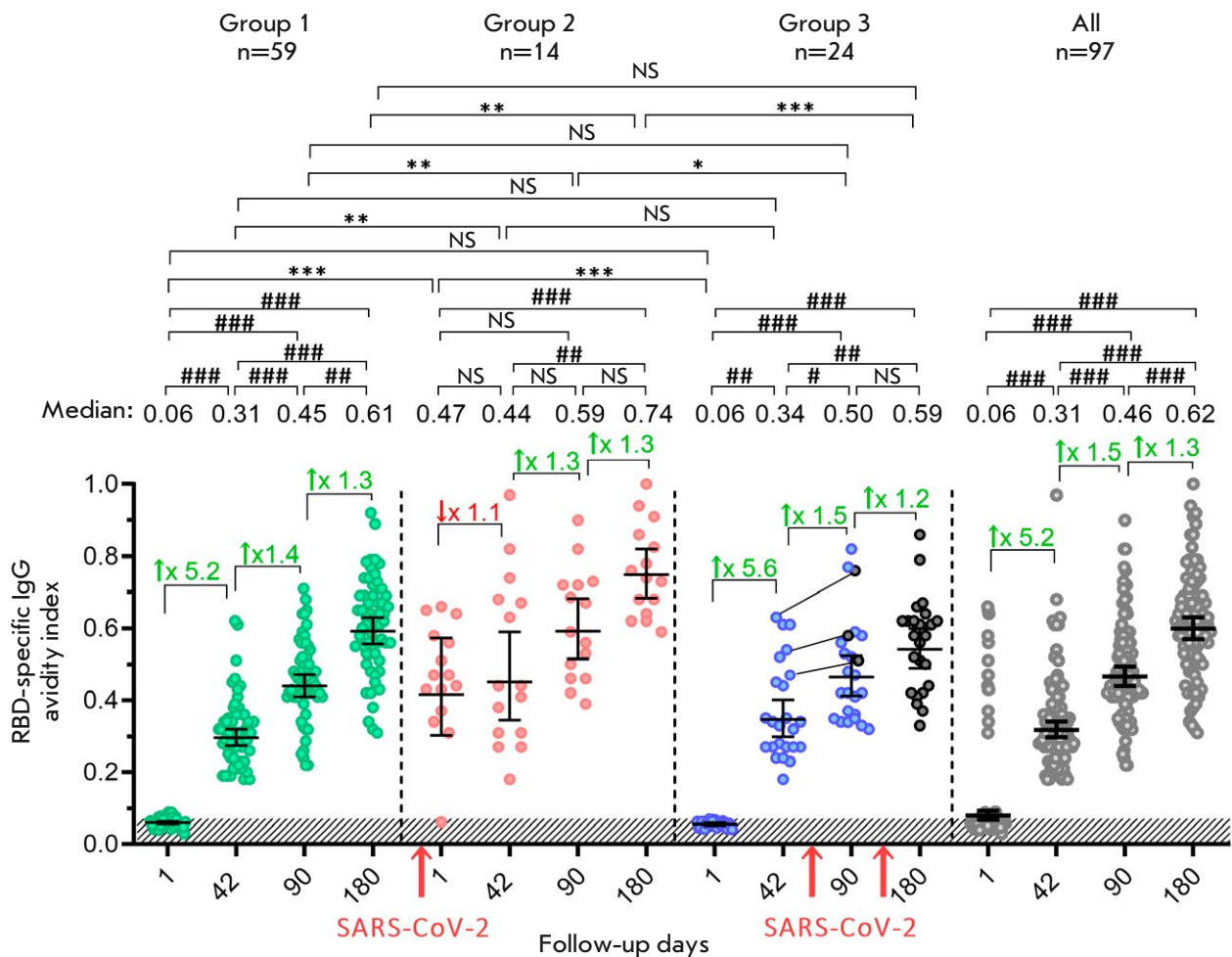
Fig. 4. The avidity index of RBD-specific IgG antibodies in volunteers vaccinated with Sputnik Light. Avidity indices are shown before (day 1) and on days 42, 90, and 180 after vaccination for all the participants (gray dots), as well as the ones stratified depending on the presence/absence of the SARS-CoV-2 infection: group 1 – individuals not -infected with SARS-CoV-2 (green dots); group 2 – individuals infected with SARS-CoV-2 before vaccination (red dots); and group 3 – individuals infected with SARS-CoV-2 after vaccination (blue dots). Black dots indicate participants infected with SARS-CoV-2 in group 3. The lines between the dots connect the values of the same participant before (day 42) and after infection (day 90). N denotes the number of participants in each stratum. Dots show individual data points. Horizontal lines represent the geometric mean titers (GMT); the values are shown as black numbers above the graph. Whiskers represent a 95% confidence interval (CI). The colored numbers and arrows above the square brackets indicate the fold increase or decrease in avidity indices compared to the previous time point. The red arrows below the horizontal axis indicate the time of SARS-CoV-2 infection of the volunteers. Significant differences between different time points within the same group are indicated with hashes: # $p < 0.05$; ## $p < 0.005$; ### $p < 0.0001$ (Friedman test with Dunn's correction). Significant intergroup differences between groups are indicated with asterisks: *$p < 0.05$; ** $p < 0.005$ or *** $p < 0.0001$ (Kruskal–Wallis test with Dunn's correction). NS indicates non-significant difference

unteers with prior immunity (group 2). The previous COVID-19 infection in group 2 volunteers, which had not increased antibody avidity, apparently, also has a negative impact on serum maturation in the post-vaccination period [15]. The increase in the avidity index by day 180 in group 2 was accompanied by a less prominent decrease in antibody titer compared to group 1. A strong correlation between the titer and the avidity index of RBD-specific IgG antibodies ($r = 0.65$) was revealed in group 3 volunteers infected with SARS-CoV-2 after vaccination, which was reflected in the simultaneous rise in both parameters with time elapsed since vaccination. It is worth emphasizing that the SARS-CoV-2 infection, as well
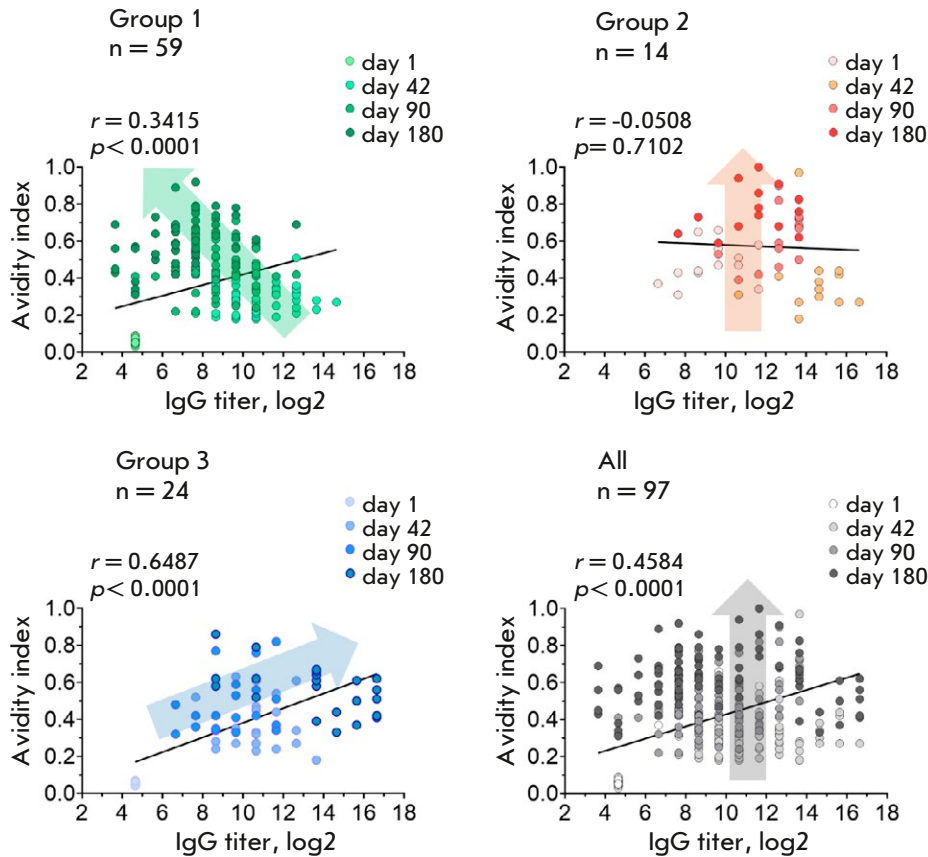
Fig. 5. Correlation between the titer and the avidity index of RBD-specific IgG antibodies. Each graph shows the summary data before (day 1) and on days 42, 90, and 180 post-vaccination for all study participants (gray), as well as after stratification depending on the presence/absence of additional immunization due to a SARS-CoV-2 infection: group 1 – individuals not-infected with SARS-CoV-2 (green dots); group 2 – individuals infected with SARS-CoV-2 before vaccination (red dots); group 3 – individuals infected with SARS-CoV-2 after vaccination (blue dots). N is the number of volunteers in each group. Dots represent individual data. Color intensity refers to the study day. Arrows on each graph show the general trend of parameters changing over time. The Pearson correlation coefficient (r) and statistical significance (p), as well as linear trend line, are shown for each graph

as the time of the event with respect to vaccination, fundamentally alters the evolution of humoral immunity parameters over time. Since the avidity index of total anti-RBD IgG antibodies was increased, all three groups were characterized by different dynamics of anti-RBD IgG titers (shown with arrows in *Fig. 5*). An analysis of the overall sample of volunteers revealed the resulting moderate correlation ($r = 0.46$) between the two parameters, demonstrating that the avidity index of antibodies increased with time, while no noticeable changes in their titer took place.

Hence, our findings demonstrate that natural immunization has a substantial impact on the intensity of the humoral immune response and its maturation with time; thus, it interferes with the self-immunogenicity of the analyzed vaccine product.

DISCUSSION

The COVID-19 pandemic has set a number of precedents in global science and medicine. A range of vaccines based on different platforms (mRNA, recombinant viral vectors, inactivated or subunit ones,

etc.) effectively defending humans against COVID-19-associated mortality has promptly been developed [16]. Because of the novelty of the pathogen and vaccine products, studies aiming to refine the immune responses that play a crucial role in the development and maintenance of protective immunity in vaccinated individuals need to be continued. In particular, the gained knowledge allows to (1) conduct a comparative analysis of the immunogenicity of vaccines based on different platforms; (2) identify the optimal revaccination time intervals for different population groups, as relates to the new SARS-CoV-2 variants; (3) promptly adapt the antigenic composition of vaccine products in accordance with currently circulating SARS-CoV-2 variants; (4) determine how the developed immune response changes with time after vaccination; and (5) determine the features of the developed immunity in different population groups, etc. The solutions to the aforementioned problems are further complicated by the fact that SARS-CoV-2 remains pervasive in the human population. Undetected exposure to the pathogen can significantly alter the immuno-

genicity parameters of studied vaccine products [17]. Therefore, particular accuracy is warranted when analyzing the results of clinical trials aiming to assess the immunogenicity of the vaccines, especially those with a long-term follow-up period.

In this paper, we present the results of the phase 1–2 clinical trial to assess the immunogenicity of the Sputnik Light vaccine up to day 180 in the follow-up period. After the clinical trial was completed, we additionally determined whether the participants presented IgG antibodies specific to the SARS-CoV-2 N protein at all time points during the study, by separating the group of volunteers who had been exposed to the SARS-CoV-2 virus neither before vaccination nor throughout the study (group 1), as well as those who had been exposed to the SARS-CoV-2 virus before (group 2) or after vaccination (group 3). Importantly, a small percentage (~ 0.5%) of the Russian population was infected with SARS-CoV-2 at the time the study was initiated (June 17, 2020), which was reflected in our study as a predominance of the percentage of non-infected volunteers (group 1) with respect to the total number of participants (60%) [18]. Therefore, the applied criteria and sample size make it possible to quantify the self-immunogenicity of the Sputnik Light vaccine by a statistical analysis.

The statistically significant drop in the titer of RBD-specific antibodies in group 1 by study day 180 is apparently related to the objective kinetics of the development of the antibody response after a single injection of Ad26-S-based vaccines, which has also been observed by other authors [3, 19]. The titers of antigen-binding antibodies that had been shown in other studies to persist after vaccination with single-dose Ad26.COV2.S at late time points may be a result of the influence of some additional stimuli [20, 21]. For example, a dramatic increase in anti-RBD IgG titers, along with a slowly declining titer of total IgG, was clearly demonstrated in volunteers infected with SARS-CoV-2 after vaccination with Ad26.COV2.S [4]. Hence, the lack of a careful selection of volunteers when analyzing the immunogenicity of SARS-CoV-2 vaccines may lead to significant overestimation of the parameters being analyzed.

Like a number of other authors, we have demonstrated that individuals with hybrid immunity (groups 2 and 3) display significantly higher titers of antigen-binding antibodies compared to those in vaccinated volunteers who had not been exposed to SARS-CoV-2 [22]. In the context of persistent population exposure to SARS-CoV-2, the Sputnik Light vaccine appears to be an effective agent for priming and eventually maintaining immunity intensity in individuals that have recovered from COVID-19. Furthermore, the prime-boost revaccination strategy has no advantage in terms of immunogenicity over single-dose administration of the vaccine [23].

The dynamics of antigen-binding antibody titers in volunteers with hybrid immunity indicate that the moment of SARS-CoV-2 infection is important. Thus, in the group of volunteers (group 2) who had been infected before vaccination (according to the titers of antibodies specific to N- and S protein on day 1), the anti-RBD IgG titer increased dramatically, from 594 on day 1 to 19 985 (34-fold) as early as on day 42. Group 3 volunteers infected after vaccination had a less robust rise in anti-RBD IgG titer within the period between days 90 and 180 (18-fold). These results indicate that the interval and/or sequence of vaccination and infection play a pivotal role in the intensity of humoral immunity. Indeed, several studies have confirmed that the efficacy of the boosting stimulus increases with time between immunizations [6, 24]. However, adding a third vaccination within the interval between the first and final vaccination does not significantly increase immunity intensity [25]. The effect of the sequence of exposure to infection and vaccination on immunity intensity has not been identified in detail yet. More convincing data can be provided by clinical studies of the immunogenicity of SARS-CoV-2 vaccines, where the exact time of infection of SARS-CoV-2 volunteers before or after vaccination would be confirmed by laboratory methods (e.g. by PCR tests).

The analysis of IgG antibody subclasses showed that volunteers who had received the single-dose Sputnik Light vaccine lacked IgG4 antibodies until day 180 in the follow-up period, whereas IgG4 antibodies were detected in individuals with hybrid immunity, especially in group 3. This might be caused by differences in immunity against COVID-19 that had developed in response to vaccination and exposure to the SARS-CoV-2 infection. Interestingly, reimmunization with mRNA vaccines (BNT162b2 and mRNA-1273) can trigger the development of IgG4 antibodies, in contrast to the use of the simian adenovirus-vectored AZD1222 vaccine [26]. Therefore, it seems important to determine whether the detected effect applies to vaccines based on other adenovirus platforms. An analysis of the IgG4 titers in volunteers who had undergone multi-dose vaccination with the Sputnik Light or Sputnik V vaccines would provide an answer to this question.

The avidity of antibodies is an important indicator of the maturation of anti-infection immunity. The avidity of antibodies increases because of the emergence of B-cells with higher affinity antibodies as a result of somatic hypermutation if antigen presentation has sufficient duration and intensity [27].

The SARS-CoV-2 infection is known to slightly increase the avidity of antigen-binding antibodies [28]. Meanwhile, the present study demonstrates that single-shot vaccination with the Sputnik Light vaccine results in a notable rise in the avidity index after immunization.

Along with the increased intensity of humoral post-vaccination immunity, exposure to a SARS-CoV-2 infection also significantly affects immune maturation. According to earlier publications, the hybrid immunity in individuals infected with SARS-CoV-2 long before vaccination is characterized by a higher avidity index compared to that in vaccinated volunteers [29]. However, if the SARS-CoV-2 infection occurs shortly after vaccination (group 3), serum maturation is slowed down. This phenomenon can be attributed to the recruitment of new clones of naïve B cells in the proliferative response post-infection (with increasing titers of antigen-specific antibodies), which thus leads to a reduction in the contribution of high-affinity B cells that have already passed the somatic hypermutation stage to the total avidity index (*Fig. 4*). This assumption is reflected in the differing correlations between the titer and the avidity index of RBD-specific IgG antibodies in different groups of volunteers.

CONCLUSION

This study has for the first time demonstrated the auto-immunogenicity of the Sputnik Light vaccine during a 180-day follow-up period in a clinical trial and assessed the effect of exposure to the SARS-CoV-2 infection before and after vaccination on the parameters of humoral post-vaccination immunity. The findings more accurately characterize the immunogenic properties of the Sputnik Light vaccine, which has been in use in clinical practice since 2020. ●

REFERENCES

1. WHO Director-General's opening remarks at the media briefing on COVID-19 – March 2020 // Official website of the World Health Organization. 2020. https://www.who.int/director-general/speeches/detail/who-director-general-s-opening-remarks-at-the-media-briefing-on-covid-19---21-august-2020 (Accessed September 25, 2024).
2. «COVID19 Vaccine Tracker» // «COVID19 Vaccine Tracker» (USA). 2022. https://covid19.trackvaccines.org/vaccines/approved/ (Accessed September 25, 2024).
3. Collier A.Y., Yu J., McMahan K., Liu J., Chandrashekar A., Maron J.S., Atyeo C., Martinez D.R., Ansel J.L., Aguayo R., Rowe M., Jacob-Dolan C., et al. // N. Engl. J. Med. 2021. V. 385. № 21. P. 2010–2012. doi:10.1056/NEJMc2115596.
4. Barouch D.H., Stephenson K.E., Sadoff J., Yu J., Chang A., Gebre M., McMahan K., Liu J., Chandrashekar A., Patel S., et al. // N. Engl. J. Med. 2021. V. 385. № 10. P. 951–953. doi: 10.1056/NEJMc2108829.
5. Cho A., Muecksch F., Wang Z., Ben Tanfous T., DaSilva J., Raspe R., Johnson B., Bednarski E., Ramos V., Schaefer-Babajew D., et al. // J. Exp. Med. 2022. V. 219. № 8. P. e20220732. doi: 10.1084/jem.20220732.
6. Bates T.A., Leier H.C., McBride S.K., Schoen D., Lyski Z.L., Lee D.X., Messer W.B., Curlin M.E., Tafesse F.G. // JCI Insight. 2023. V. 8. № 5. P. e165265. doi: 10.1172/jci.insight.165265.
7. Edelstein M., Wiegler Beiruti K., Ben-Amram H., Beer N., Sussan C., Batya P., Zarka S., Abu Jabal K. // Int. J. Infect. Dis. 2023. V. 135. P. 57–62. doi: 10.1016/j.ijid.2023.08.009.
8. Wu N., Joyal-Desmarais K., Ribeiro P.A.B., Vieira A.M., Stojanovic J., Sanuade C., Yip D., Bacon S.L. // Lancet. Respir. Med. 2023. V. 11. P. 439–452. doi: 0.1016/S2213-2600(23)00015-2.
9. Tukhvatulin A.I., Dolzhikova I.V., Shcheblyakov D.V., Zubkova O.V., Dzharullaeva A.S., Kovyrshina A.V., Lubenets N.L., Grousova D.M., Erokhova A.S., Botikov A.G., et al. // Lancet Reg. Health Eur. 2021. V. 11. P. 100241. doi: 10.1016/j.lanepe.2021.100241.
10. Nurmi V., Hedman L., Perdomo M.F., Weselindtner L., Hedman K. // Int. J. Infect. Dis. 2021. V. 110. P. 479–487. doi: 10.1016/j.ijid.2021.05.047.
11. Klingler J., Weiss S., Itri V., Liu X., Oguntuyo K.Y., Stevens C., Ikegame S., Hung C.T., Enyindah-Asonye G., Amanat F. // J. Infect. Dis. 2021. V. 223. P. 957–970. doi: 10.1093/infdis/jiaa784.
12. Lapuente D., Winkler T.H., Tenbusch M. // Cell Mol. Immunol. 2024. V. 21. P. 144–158. doi: 10.1038/s41423-023-01095-w.
13. Rubio-Casillas A., Redwan E.M., Uversky V.N. // Biomolecules. 2023. V. 13. P. 1338. doi: 10.3390/biom13091338.
14. Tauzin A., Gong S.Y., Beaudoin-Bussières G., Vézina D., Gasser R., Nault L., Marchitto L., Benlarbi M., Chatterjee D., Nayrac M., Laumaea A., et al. // Cell Host Microbe. 2022. V. 30. № 1. P. 97–109. doi: 10.1016/j.chom.2021.12.004.
15. Chia W.N., Zhu F., Ong S.W.X., Young B.E., Fong S.W., Le Bert N., Tan C.W., Tiu C., Zhang J., Tan S.Y., et al. // Lancet Microbe. 2021. V. 2. № 6. P. e240–e249. doi: 10.1016/S2666-5247(21)00025-2.
16. Rahman M.M., Masum M.H.U., Wajed S., Talukder A. // Virusdisease. 2022. V. 33. № 1. P. 1–22. doi: 10.1007/s13337-022-00755-1.
17. Bates T.A., McBride S.K., Leier H.C, Guzman G., Lyski Z.L., Schoen D., Winders B., Lee J.Y., Lee D.X., Messer W.B., et al. // Sci. Immunol. 2022. V. 7. № 68. P. eabn8014.

doi: 10.1126/sciimmunol.abn8014.

18. Mathieu E., Ritchie H., Rodés-Guirao L., Appel C., Giattino C., Hasell J., Macdonald B., Dattani S., Beltekian D., Ortiz-Ospina E., et al. // Our World in Data (Great Britain). 2020. https://ourworldindata.org/covid-deaths (date of request: 25.09.2024).

19. Sheikh-Mohamed S., Isho B., Chao G.Y.C., Zuo M., Cohen C., Lustig Y., Nahass G.R., Salomon-Shulman R.E., Blacker G., Fazel-Zarandi M., et al. // Mucosal. Immunol. 2022 V. 15. № 5. P. 799–808. doi: 10.1038/s41385-022-00511-0.

20. Liu J., Chandrashekar A., Sellers D., Barrett J., Jacob-Dolan C., Lifton M., McMahan K., Sciacca M., VanWyk H., Wu C., et al. // Nature. 2022. V. 603. № 7901. P. 493–496. doi: 10.1038/s41586-022-04465-y.

21. Sadoff J., Le Gars M., Brandenburg B., Cárdenas V., Shukarev G., Vaissiere N., Heerwegh D., Truyers C., de Groot A.M., Jongeneelen M., et al. // Vaccine. 2022. V. 40. № 32. P. 4403–4411. doi: 10.1016/j.vaccine.2022.05.047.

22. Andreano E., Paciello I., Piccini G., Manganaro N., Pileri P., Hyseni I., Leonardi M., Pantano E., Abbiento V., Benincasa L., et al. // Nature. 2021. V. 600. № 7889. P. 530–535. doi: 10.1038/s41586-021-04117-7.

23. Focosi D., Baj A., Maggi F. // Hum. Vaccin. Immunother. 2021. V. 17. № 9. P. 2959–2961. doi: 10.1080/21645515.2021.1917238.

24. Le Gars M., Hendriks J., Sadoff J., Ryser M., Struyf F., Douoguih M., Schuitemaker H. // Immunol. Rev. 2022. V. 310. № 1. P. 47–60. doi: 10.1111/imr.13088.

25. Cárdenas V., Le Gars M., Truyers C., Ruiz-Guiñazú J., Struyf F., Colfer A., Bonten M., Borobia A., Reisinger E.C., Kamerling I.M.C., et al. // Vaccine. 2024. V. 42. № 16. P. 3536–3546. doi: 10.1016/j.vaccine.2024.04.059.

26. Buhre J.S., Pongracz T., Künsting I., Lixenfeld A.S., Wang W., Nouta J., Lehrian S., Schmelter F., Lunding H.B., Dühring L. // Front. Immunol. 2023. V. 13. P. 1020844. doi: 10.3389/fimmu.2022.1020844.

27. Victora G.D., Nussenzweig M.C. // Annu. Rev. Immunol. 2022. V. 40. P. 413–442. doi: 10.1146/annurev-immunol-020711-075032.

28. Struck F., Schreiner P., Staschik E., Wochinz-Richter K., Schulz S., Soutschek E., Motz M., Bauer G. // J. Med. Virol. 2021. V. 93. № 12. P. 6765–6777. doi: 10.1002/jmv.27270.

29. Bellusci L., Grubbs G., Zahra F.T., Forgacs D., Golding H., Ross T.M., Khurana S. // Nat. Commun. 2022. V. 13. № 1. P. 4617. doi: 10.1038/s41467-022-32298-w.

Alterations in the Expression of Proprotein Convertase Genes in Human Esophagus Squamous Cell Carcinomas

A. A. Komissarov[1], M. V. Zinovyeva[2], A. V. Sass[2], T. V. Vinogradova[2], S. I. Koshechkin[1], V. V. Demkin[1], I. B. Zborovskaya[3], S. V. Kostrov[1], I. V. Demidyuk[1*]

[1]National Research Centre "Kurchatov Institute", Moscow, 123182 Russian Federation
[2]Shemyakin-Ovchinnikov Institute of Bioorganic Chemistry of the Russian Academy of Sciences, Moscow, 117997 Russian Federation
[3]N.N. Blokhin National Medical Research Center of Oncology, Moscow, 115478 Russian Federation
*E-mail: ilyaduk@yandex.ru

ABSTRACT Proprotein convertases (PCs) constitute an enzyme family that includes nine highly specific human subtilisin-like serine proteases. It is known that the PCs mRNA levels vary in tumors, and that these proteases are involved in carcinogenesis. Thus, PCs may be considered as potential markers for typing and predicting the course of the disease, as well as potential targets for therapy. We used quantitative real-time PCR to evaluate the expression levels of PC genes in the paired samples of tumor and adjacent normal tissues derived from 19 patients with esophageal squamous cell carcinomas. We observed a significant enrichment of *PCSK6*, *PCSK9*, *MBTPS1*, and *FURIN* mRNAs in the tumor tissue, which may be indication of the involvement of these PCs in the development and progression of esophageal cancers. Additionally, cluster analysis of PC expression alteration patterns in tumor compared to normal adjacent tissues (esophageal and previously analyzed lung tissue samples) revealed a limited set of scenarios for the changes in PC expression. These scenarios are implemented during malignant transformation of lung and esophagus cells, as well as, probably, the cells of other organs. These findings indicate that PC genes may be important markers of human cancers.
KEYWORDS proprotein convertase, serine protease, cancer, gene expression, quantitative real-time PCR.
ABBREVIATIONS IGF-1R – insulin-like growth factor 1 receptor; PC – proprotein convertase.

INTRODUCTION

Proprotein convertases (PCs) are a family of highly specific mammalian subtilisin-like serine endopeptidases whose key function is processing various proteins and peptides [1, 2]. In humans, nine PC genes have been identified; the endogenous substrates of these proteases come in the form of numerous proteins and peptides, such as neuropeptide precursors, peptide hormones, growth and differentiation factors, receptors, and enzymes. It flows from this that PCs regulate a wide range of physiological processes, both in health and in disease. In particular, there is extensive evidence of an association between PCs and the development and progression of cancer.

PC substrates encompass a number of proteins involved in the progression of malignancies: cytokines, growth factors and their receptors, matrix metalloproteinases, and adhesion molecules (discussed in detail in [3–5]). There is ample evidence pointing to the

fundamental role of PCs in tumor progression and metastasis, as well as the relationship between PC expression levels and patient survival [6–12]. All this suggests that data on PC expression levels may be used for typing and predicting the course of cancers, and that PCs themselves may serve as therapeutic targets.

Previously, we used quantitative PCR to demonstrate that PC expression in human lung malignancies was altered compared with that in the adjacent normal tissue. In this case, we, for the first time, found that the alterations in the expression occurred in a few scenarios: 80% of the analyzed samples formed three groups, each of which displayed a significantly altered expression of one of the three genes – *FURIN*, *PCSK1*, or *PCSK6* (hereinafter, we use the Human Gene Nomenclature Committee (HGNC) guidelines for gene names, https://www.genenames.org, *Table 1*). We did not find any correlations between the identi-

Table 1. Genes and PCR kits used in the study

Protein	Gene (HGNC*)	Alternative protein names	PCR assay ID
Proprotein convertase subtilisin/kexin type 1	PCSK1	PC1/3, NEC1	Rn00567266_m1
Proprotein convertase subtilisin/kexin type 2	PCSK2	PC2, NEC2	Rn00562543_m1
Proprotein convertase subtilisin/kexin type 4	PCSK4	PC4	Rn00592006_m1
Proprotein convertase subtilisin/kexin type 5	PCSK5	PC5/6	Rn01450819_m1
Proprotein convertase subtilisin/kexin type 6	PCSK6	PACE4, SPC4	Rn00564475_m1
Proprotein convertase subtilisin/kexin type 7	PCSK7	PC7	Rn00570376_m1
Proprotein convertase subtilisin/kexin type 9	PCSK9	PC9, NARC-1	Rn01416753_m1
Membrane-bound transcription factor peptidase, site 1	MBTPS1	SKI-1/S1P	Rn00585707_m1
Furin	FURIN	PACE	Rn00570970_m1
Glyceraldehyde-3-phosphate dehydrogenase	GAPDH	G3PD	Rn01775763_g1

*HGNC – Human Gene Nomenclature Committee, https://www.genenames.org

fied groups and the available clinical data of patients [13]. However, the data we obtained may be indication that there exist unidentified properties of human lung tumors which are associated with one of the three identified scenarios of alterations in the PC expression.

In this work, we studied esophageal malignancies in a way similar to that described above. Quantitative real-time PCR was used to analyze mRNA levels in tumor and adjacent normal tissues in samples obtained from 19 patients with esophageal squamous cell carcinoma. We found significantly increased expressions of the PCSK6, PCSK9, MBTPS1, and FURIN genes in tumor tissue, which may indicate the involvement of these PCs in the formation and progression of esophageal malignancies. We also performed a cluster analysis of PC expression alteration patterns in esophageal cancer samples and the previously analyzed lung cancer samples. As a result, a limited set of scenarios for PC expression alterations during malignant transformation of lung and esophageal cells and, probably, the cells of other organs, were identified.

EXPERIMENTAL
Samples were collected in accordance with Federal Law No. 180 "On Biomedical Cell Products" (Order of the Ministry of Health of the Russian Federation No. 517n, Appendix 2, of August 11, 2017). The study protocol was approved by the Ethics Committee of the N.N. Blokhin National Medical Research Center of Oncology of the Ministry of Health of the Russian Federation (N.N. Blokhin NMRCO).

Esophageal tumor and adjacent normal tissue samples were obtained during surgery on patients with esophageal squamous cell carcinoma (stage II or III) at N.N. Blokhin NMRCO. Every patient provided written informed consent. The patients had not undergone chemotherapy or radiotherapy before surgery. Part of the samples was frozen in liquid nitrogen for subsequent RNA extraction; the other part was used for histological verification in the Department of Pathological Anatomy of Human Tumors of N.N. Blokhin NMRCO and graded in accordance with the TNM classification of the International Union Against Cancer [14]. According to the results of our histological examination, all malignant tumor tissue samples contained at least 70–80% of tumor cells. The tissue samples of the affected organ taken outside the pathological growth in each patient during surgery were used as control samples (conditional normal tissue).

Total RNA was isolated from the normal and tumor tissue samples that were frozen earlier and homogenized in liquid nitrogen. RNA was purified using guanidine isothiocyanate and phenol [15] and, then, an RNeasy Mini Kit (Qiagen, USA) according to the manufacturer's protocol, followed by treatment with DNase I (Promega, USA). The concentration of isolated RNA was quantified by measuring absorption at 260 nm. The first cDNA strands were synthesized using a hexanucleotide primer (Promega, USA) and Powerscript reverse transcriptase (Clontech, USA).

Quantitative real-time PCR was performed on a CFX96 Touch device (Bio-Rad, USA) using predesigned primer and probe kits (Applied Biosystems, USA) (Table 1). The PCR program was as follows: 50°C for 2 min; 95°C for 10 min; then, 40 cycles: 95°C for 15 s and 60°C for 60 s. The reaction mixture volume was 20 μL (6 μL of deionized water, 4 μL of a 5X qPCRmix-HS PCR master mix (Eurogen,

Russia), 5 µL of a primer and probe solution, and 5 µL of a sample). Each sample was analyzed in two independent experiments with duplicates. The Bio-Rad CFX Manager 3.1 software (Bio-Rad, USA) was used to process the PCR data and determine the cycle threshold (Ct) value.

PC mRNA levels were normalized to the mRNA levels of the reference gene *GAPDH* using the formula:

$$\text{normalized\_expression\_of\_a\_PC\_gene} = 2^{\text{Ct(GAPDH)}-\text{Ct(PC)}}.$$

If expression of a PC gene was detected only in tumor or normal tissue, the normalized gene expression was calculated using the Ct value set to 42 for the missing sample.

Statistical data were processed using the R programming language (R Core Team (2023). R: A Language and Environment for Statistical Computing. R Foundation for Statistical Computing, Vienna, Austria. https://www.R-project.org/) and RStudio software (Posit team (2023). RStudio: Integrated Development Environment for R. Posit Software, PBC, Boston, MA. URL http://www.posit. co/). The differences in PC expression levels were evaluated using the paired Wilcoxon test. Cluster analysis of the samples was performed using Ward's method with the Euclidean distance as a measure of the difference.

Sample	Gender	Age	Stage	T	N	M	Keratinization	Localization
E1	M	76	2	3	0	0	No	Mid
E2	M	77	2	3	0	0	No	Low
E3	M	72	3	3	1	0	No	Low
E4	M	70	3	3	1	0	Yes	Mid
E5	M	59	2	2	0	0	Yes	Low
E6	M	71	2	3	0	0	Yes	Mid
E7	M	74	3	2	1	0	No	Low
E8	M	65	2	-	-	-	Yes	Mid
E9	M	68	3	3	1	0	No	Mid
E10	M	71	2	3	0	0	No	Mid
E11	F	85	2	3	0	0	No	Mid
E12	M	72	2	3	0	0	Yes	Low
E13	F	81	3	4	1	0	Yes	Low
E14	M	76	3	3	1	0	No	Mid
E15	M	76	2	3	0	0	Yes	Low
E16	M	91	3	4	1	0	No	Low
E17	M	87	3	3	1	0	Yes	Mid
E18	M	74	3	-	-	-	Yes	Mid
E19	F	82	3	3	1	0	Yes	Mid

Heatmap columns (left to right): PCSK9, PCSK2, PCSK6, PCSK5, PCSK7, MBTPS1, FURIN, PCSK1, PCSK4. Expression ratio: −12 to 12.
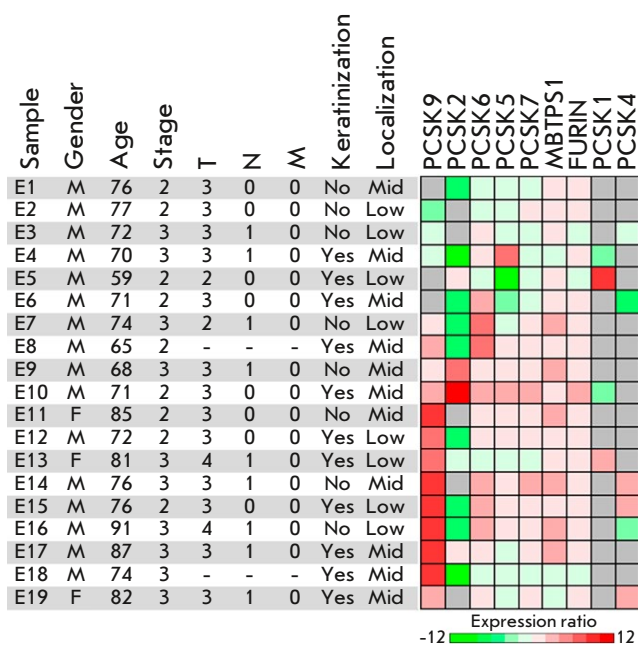
Fig. 1. Sample characterization and heatmap representation of PC expression ratios in tumor compared to adjacent normal esophageal tissues. The heatmap is shown in the log2 scale. Gray cells indicate samples with undetectable gene expression in both tumor and normal tissues. Tumor localization is designated as the middle (mid) or lower (low) third of the esophagus. "−", data are not available. T, N, and M denote tumor staging according to the TNM classification

RESULTS AND DISCUSSION

In this study, the mRNA levels of all nine proprotein convertase (PC) genes in the 19 paired samples of human esophageal malignant and normal adjacent tissues were analyzed by quantitative real-time PCR (*Fig. 1*, Appendix *Table A1*). As expected, we detected expression of the *FURIN*, *PCSK5*, *PCSK6*, *PCSK7*, and *MBTPS1* genes encoding ubiquitous enzymes in all or the vast majority of both tumor and normal tissue samples. *PCSK1*, *PCSK2*, *PCSK4*, and *PCSK9* expression is considered tissue-specific and atypical of esophageal tissues [16–18]. Indeed, *PCSK1* mRNA was detected only in two tumor and two normal tissue samples and *PCSK4* mRNA was identified in four tumor and two normal tissue samples. At the same time, *PCSK2* expression, typical of neuroendocrine cells, was detected in 5 tumor and 11 normal tissue samples. The causes behind the atypical *PCSK2* expression in esophageal tissues are unclear. We also detected *PCSK9* expression, which is normally observed mainly in liver, kidney, cerebellum, and small intestine cells, in 15 tumor and 9 normal esophageal tissue samples. However, this result was not unexpected, because *PCSK9* expression in esophageal tumors was

detected previously [19]. The possible causes of this phenomenon will be discussed below.

Comparison of PC expression levels revealed that *PCSK6*, *PCSK9*, *MBTPS1*, and *FURIN* expressions in the esophageal tumor tissue were statistically significantly higher than those in the normal adjacent tissue (*Fig. 2*). In this case, expressions of the *PCSK9* and *PCSK6* genes proved upregulated most significantly, approximately 175- and 10-fold higher, respectively, on average. Expressions of the *MBTPS1* and *FURIN* genes were upregulated moderately, approximately 4- and 3-fold higher, respectively, on average. A significant increase in PCSK9 expression at the protein level in the esophageal tumor tissue compared with that in normal tissue was previously detected in a study by Wang et al.; in that case, patients with high PCSK9 expression levels in tumors had a lower survival likelihood [19]. A study by Ito et al. revealed that a high anti-PCSK9 antibody titer in the blood of esophageal cancer patients correlated with a higher survival likelihood in the postoperative period [20]. We could not find any studies that reported increased *MBTPS1* ex-
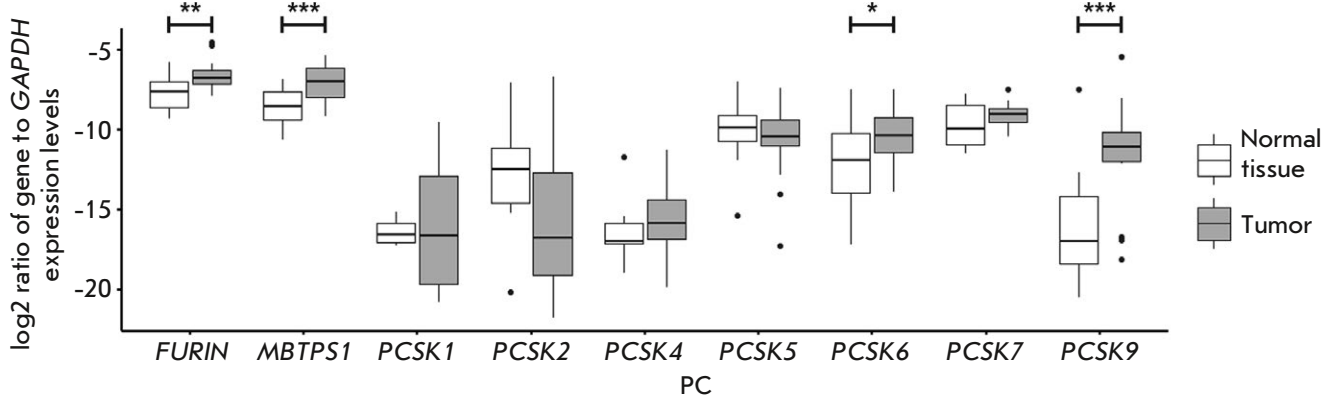
Fig. 2. PC expression levels in esophageal tumor and normal samples. PC mRNA levels were analyzed using quantitative real-time PCR as indicated in the Experimental section and then normalized to the mRNA levels of the *GAPDH* reference gene. The significance of the differences in normalized PC mRNA levels between tumor and adjacent normal tissues was analyzed using the Wilcoxon paired test. *, $p < 0.05$; **, $p < 0.01$; ***, $p < 0.001$

pression in esophageal tumors. Regarding the *PCSK6* and *FURIN* genes, their association with oncological diseases has been established in many studies [3, 7–9, 11, 21–26].

It is noteworthy that two PC genes with upregulated expression in esophageal cancer cells are involved in lipid homeostasis. Thus, *PCSK9* encodes a key regulator of blood low-density lipoprotein–cholesterol complex levels and the product of the *MBTPS1* gene plays an important role in the regulation of cholesterol, lipid, and fatty acid synthesis. To date, a substantial amount of data has been gathered indicating the fundamental role of lipid metabolism and biosynthesis in the development and progression of cancers [27]. In this context, our findings suggest that PCSK9 and MBTPS1 may be involved in the progression of human esophageal cancer through the regulation of lipid homeostasis in the tumor.

Recently, the role of PCSK9 in immune response evasion by tumor cells has begun to be actively studied. For example, PCSK9 inhibition was shown to increase the effectiveness of immunotherapy against a number of cancers (for details, see [28]). However, the first line of treatment for stage II and III esophageal cancer is chemoradiotherapy without additional immune drugs. However, a recent study, CheckMate 577, reported that the combination of chemoradiotherapy and the neoadjuvant drug Nivolumab approximately doubled the median relapse-free survival time compared with chemoradiotherapy alone [29]. Nivolumab is a monoclonal antibody from the group of immune checkpoint inhibitors; it specifically inactivates the PD-1 protein on the cell surface. The PD-1 protein plays an important role in the inhibition of immune responses through suppression of T cell activity, in-

ducing apoptosis of activated antigen-specific T cells and, conversely, inhibition of apoptosis of anti-inflammatory regulatory T cells [30]. Recently, mouse models were used to show an inverse relationship between the efficacy of anti-PD-1 therapy and PCSK9 expression levels, as well as a significant increase in the antitumor effect by combined inhibition of PD-1 and PCSK9 [31]. These data, along with the significantly increased PCSK9 expression in tumor tissue, found in our study, indicate that simultaneous blockade of PD-1/PCSK9 may be considered a promising approach to improve the efficacy of human esophageal tumor therapy.

Cluster analysis of PC expression alteration patterns in esophageal tumor compared to normal tissue samples revealed two groups of samples (*Fig. 3*). The first group included 9 (47%) samples with significantly upregulated *PCSK9* expression (*Fig. 3*, cluster EC1). The second group was less homogeneous (*Fig. 3*, cluster EC2) and included samples with significantly increased expressions of the *PCSK6* (three samples, 16%), *PCSK2* (two samples, 10%), *PCSK1* (one sample, 5%), and *PCSK5* (one sample, 5%) genes, or no significant changes in any individual gene (three samples, 16%). The PC expression alteration patterns identified in esophageal tumors differed from those we had identified previously in lung tumors [13]. For example, esophageal tumors lacked clusters with predominant alterations in the *FURIN* and *PCSK1* expressions, which included most of the lung tumor samples (18 of 30, 60%), whereas lung tumors lacked the cluster with predominant alteration in *PCSK9* expression, which was the most abundant in esophageal tumors. Meanwhile, samples with altered *PCSK6* expression were detected in both nosologies. Our findings indi-
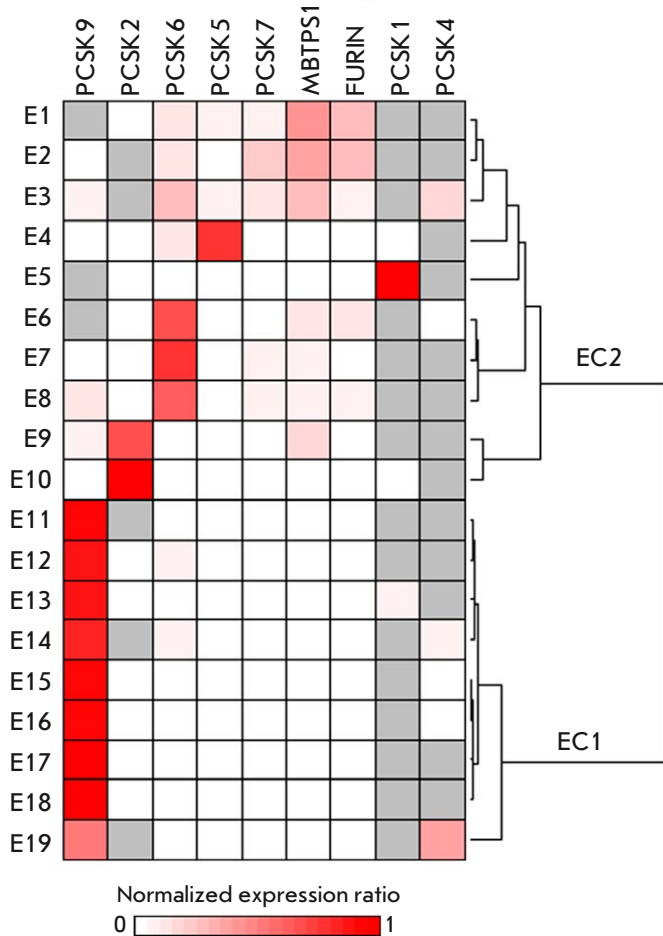
Fig. 3. Cluster analysis of PC expression patterns in esophageal samples. Normalized PC mRNA level ratios in tumor compared to normal tissues were additionally row-normalized and presented as a heatmap in fractions of one. Gray cells indicate samples with undetectable gene expression in both tumor and normal tissues. Row-normalized data were clustered as indicated in the Experimental section. The dendrogram indicates the distance between samples. The identified clusters are designated as EC1 and EC2
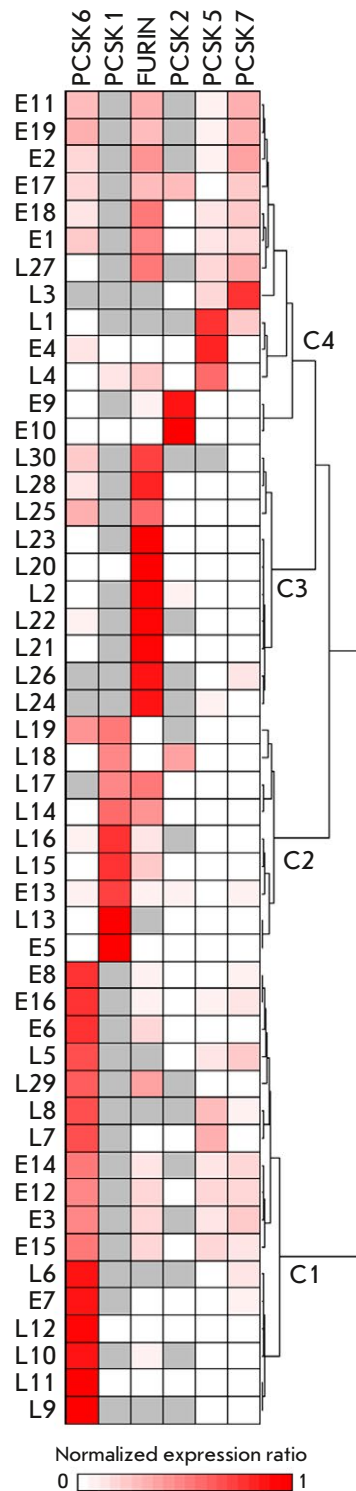

Fig. 4. Cluster analysis of the expression patterns of the six key PC genes in esophageal and lung tumors. Normalized PC mRNA level ratios in tumor compared to normal tissues were additionally row-normalized and presented as a heatmap in fractions of one. Gray cells indicate samples with undetectable gene expression in both tumor and normal tissues. Lung tumors are designated as L1–L30, and esophageal samples are designated as E1–E19. Row-normalized data were clustered as indicated in the Experimental section. The dendrogram indicates the distance between samples. The identified clusters are designated as C1–C4

cate that the PC expression alterations in tumor tissue compared to adjacent normal tissue differ across tumor types, but that there is a limited set of scenarios for PC expression alterations in each case.

Investigation of PC functions, in particular using gene knockout rodents, has revealed that most of these enzymes have overlapping substrate specificity. PCSK1 and PCSK2 were shown to act on common substrates, and the substrate specificity overlap of the FURIN, PCSK5, PCSK6, and PCSK7 proteins is so broad that they are able to partially compensate for each other's lack in tissues [32, 33]. At the same time, the PCSK4, PCSK9, and MBTPS1 enzymes act on a narrow range of quite specific substrates. In this regard, the functioning of six PCs (PCSK1, PCSK2, PCSK5, PCSK6, PCSK7, and FURIN) may potentially be considered as a single protein processing sys-

tem. Cluster analysis of the expression alteration patterns of these six PCs in the total sample of lung and esophageal tumors revealed four sample groups (*Fig. 4*). Three groups included almost three quarters of the samples ($n = 36$, 73.5%) and were characterized by a predominant change in the expression of one PC gene: *PCSK6*, *PCSK1*, or *FURIN* (the groups correspond to clusters C1, C2, and C3, respectively, in *Fig. 4*). Group C3 consisted exclusively of lung tumor samples, whereas groups C1 and C2 included samples of both nosologies. The fourth group that corresponded to cluster C4 in *Fig. 4* was more heterogeneous and included the remaining quarter of the samples ($n = 13$, 26.5%). In this group, three subgroups may be distinguished; of these, two include five samples with significantly altered expression of the *PCSK2* or *PCSK5* gene. However, most samples (8 out of 13) belong in the third subgroup, characterized by increased expression of the *PCSK6*, *PCSK7*, and *FURIN* genes with a lack of *PCSK1* expression. We did not find statistically significant correlations between the identified sample groups and available clinical data from the patients. Nevertheless, the obtained data may be indication that there is a limited number of scenarios for PC expression alterations during the malignant transformation of cells and the genesis of lung and esophageal tumors, as well as, possibly, tumors of other nosologies.

Unfortunately, the available information may only be suggestive of the nature of the differences between the identified sample groups. For example, high *PCSK6* expression in group C1 may indicate active restructuring of the tumor microenvironment and, thus, correlate with the invasiveness and/or metastatic activity of the tumor [25, 26]. Increased *PCSK1* expression in group C2 may be related to the possible origin of the tumor from neuroendocrine cells [34, 35]. Increased levels of *FURIN* mRNA in group C3 may be associated with active expression and processing of the insulin-like growth factor 1 receptor (IGF-1R) in tumors, indicating their increased aggressiveness [36]. Obviously, further research is required to elu-cidate the causes underlying the identified scenarios of PC expression alterations. Probably, more detailed investigation of a larger batch of samples from different nosologies is required, including analysis of additional clinical characteristics, in particular, patients' resistance to drugs, relapse rates, and patients' survival time.

It should also be noted that this study was conducted on a relatively small number of samples. Therefore, the changes in the expression of PC genes and the groups identified during cluster analysis need confirmation with a larger sample size. Nevertheless, the samples analyzed here include lung and esophageal tumors, representing two independent and quite heterogeneous groups, which, however, are characterized by similar patterns in PC expression alterations. In this regard, these patterns are likely to be quite pronounced and, thus, can be detected even on a small sample size, which makes mRNAs of PC genes potentially important tumor markers.

CONCLUSION

Our analysis revealed increased *PCSK6*, *PCSK9*, *MBTPS1*, and *FURIN* expressions in human esophageal tumors. This indicates the potential involvement of these PCs in the development and progression of esophageal malignancies. In this case, the role of *PCSK9* and *MBTPS1* in the pathological process is probably associated with the involvement of the protein products of these genes in lipid metabolism and/or immune response evasion by tumor cells. We found that alterations in PC expression in esophageal and lung tumors follow a limited set of similar scenarios. This may be indicative of common mechanisms of malignant transformation of lung and esophageal cells and, possibly, tumors of other localizations. ●

REFERENCES
1. Seidah N.G., Prat A. // Nat. Rev. Drug Discov. 2012. V. 11. № 5. P. 367–383.
2. Garten W. Characterization of Proprotein Convertases and Their Involvement in Virus Propagation. Cham.: Springer Internat. Publ., 2018. P. 205–248.
3. He Z., Khatib A.M., Creemers J.W.M. // Oncogene. 2022. V. 41. № 9. P. 1252–1262.
4. Khatib A.M., Siegfried G., Chretien M., Metrakos P., Seidah N.G. // Am. J. Pathol. 2002. V. 160. № 6. P. 1921–1935.
5. Cendron L., Rothenberger S., Cassari L., Dettin M., Pasquato A. // Adv. Protein Chem. Struct. Biol. 2023. V. 133. P. 1–54.
6. Zaafour A., Seeneevassen L., Nguyen T.L., Genevois C., Nicolas N., Sifre E., Giese A., Porcheron C., Descarpentrie J., Dubus P., et al. // Gastric Cancer. 2024. V. 27. № 2. P. 292–307.
7. Poyil P.K., Siraj A.K., Padmaja D., Parvathareddy S.K., Diaz R., Thangavel S., Begum R., Haqawi W., Al-Mohanna F.H., Al-Sobhi S.S., et al. // Mol. Oncol. 2023. V. 17. № 7.

P. 1324–1342.

8. Lin Y., Long H., Tan X., Zhang D., Jiang L. // Cancer Manag. Res. 2020. V. 12. P. 8623–8629.

9. Page R.E., Klein-Szanto A.J., Litwin S., Nicolas E., Al-Jumaily R., Alexander P., Godwin A.K., Ross E.A., Schilder R.J., Bassi D.E. // Cell Oncol. 2007. V. 29. № 4. P. 289–299.

10. Lopez de Cicco R., Watson J.C., Bassi D.E., Litwin S., Klein-Szanto A.J. // Clin. Cancer Res. 2004. V. 10. № 13. P. 4480–4488.

11. Bassi D.E., Mahloogi H., Al-Saleem L., Lopez De Cicco R., Ridge J.A., Klein-Szanto A.J. // Mol–Carcinog. 2001. V. 31. № 4. P. 224–232.

12. Righi A., Faustini-Fustini M., Morandi L., Monti V., Asioli S., Mazzatenta D., Bacci A., Foschini M.P. // Endocrine. 2017. V. 56. № 2. P. 286–297.

13. Demidyuk I.V., Shubin A.V., Gasanov E.V., Kurinov A.M., Demkin V.V., Vinogradova T.V., Zinovyeva M.V., Sass A.V., Zborovskaya I.B., Kostrov S.V. // PLoS One. 2013. V. 8. № 2. P. e55752.

14. O'Sullivan B., Brierley J., Byrd D., Bosman F., Kehoe S., Kossary C., Pineros M., van Eycken E., Weir H.K., Gospodarowicz M. // Lancet Oncol. 2017. V. 18. № 7. P. 849–851.

15. Sambrook J., Fritsch E.F., Maniatis T. Molecular Cloning: A Laboratory Manual. NY.: Cold Spring Harbor Lab., 1989. 1659 p.

16. Hoshino A., Lindberg I. Peptide Biosynthesis: Prohormone Convertases 1/3 and 2. CA.: Morgan & Claypool Life Sciences, 2012. 112 p.

17. Gyamera-Acheampong C., Mbikay M. // Hum. Reprod. Update. 2009. V. 15. № 2. P. 237–247.

18. Seidah N.G., Benjannet S., Wickham L., Marcinkiewicz J., Jasmin S.B., Stifani S., Basak A., Prat A., Chretien M. // Proc. Natl. Acad. Sci. USA. 2003. V. 100. № 3. P. 928–933.

19. Wang H., Guo Q., Wang M., Liu C., Tian Z. // Oncol. Lett. 2023. V. 26. № 5. P. 500.

20. Ito M., Hiwasa T., Oshima Y., Yajima S., Suzuki T., Nanami T., Sumazaki M., Shiratori F., Funahashi K., Li S.Y., et al. // Front. Oncol. 2021. V. 11. P. 708039.

21. Panet F., Couture F., Kwiatkowska A., Desjardins R., Guerin B., Day R. // Eur. J. Cell. Biol. 2017. V. 96. № 5.

P. 469–475.

22. Lin Y.E., Wu Q.N., Lin X.D., Li G.Q., Zhang Y.J. // J. Thorac. Dis. 2015. V. 7. № 5. P. 850–860.

23. Couture F., Wang L., Dufour F., Chabot-Maheux K., Ekindi Ndongo N., Sabbagh R., Day R. // Sci. Rep. 2022. V. 12. № 1. P. 6066.

24. Weishaupt C., Mastrofrancesco A., Metze D., Kemper B., Stegemann A., Picardo M., Klein-Szanto A.J.P., Bohm M. // Acta Derm. Venereol. 2020. V. 100. № 10. P. adv00157.

25. Rykaczewska U., Suur B.E., Rohl S., Razuvaev A., Lengquist M., Sabater-Lleal M., van der Laan S.W., Miller C.L., Wirka R.C., Kronqvist M., et al. // Circ. Res. 2020. V. 126. № 5. P. 571–585.

26. Jiang H., Wang L., Wang F., Pan J. // Mol. Med. Rep. 2017. V. 16. № 6. P. 8477–8484.

27. Fu Y., Zou T., Shen X., Nelson P.J., Li J., Wu C., Yang J., Zheng Y., Bruns C., Zhao Y., et al. // MedComm. 2021. V. 2. № 1. P. 27–59.

28. Bao X., Liang Y., Chang H., Cai T., Feng B., Gordon K., Zhu Y., Shi H., He Y., Xie L. // Signal Transduct. Target Ther. 2024. V. 9. № 1. P. 13.

29. Kelly R.J., Ajani J.A., Kuzdzal J., Zander T., Van Cutsem E., Piessen G., Mendez G., Feliciano J., Motoyama S., Lievre A., et al. // N. Engl. J. Med. 2021. V. 384. № 13. P. 1191–1203.

30. Han Y., Liu D., Li L. // Am. J. Cancer Res. 2020. V. 10. № 3. P. 727–742.

31. Wang R., Liu H., He P., An D., Guo X., Zhang X., Feng M. // Front Immunol. 2022. V. 13. P. 947756.

32. Seidah N.G., Sadr M.S., Chretien M., Mbikay M. // J. Biol. Chem. 2013. V. 288. № 30. P. 21473–21481.

33. Creemers J.W., Khatib A.M. // Front. Biosci. 2008. V. 13. P. 4960–4971.

34. Segawa Y., Takata S., Fujii M., Oze I., Fujiwara Y., Kato Y., Ogino A., Komori E., Sawada S., Yamashita M., et al. // J. Cancer Res. Clin. Oncol. 2009. V. 135. № 8. P. 1055–1059.

35. Geng Z.-H., Liu Y.-L., Xu C., Zhu Y., Zhou P.-H., Cai M.-Y. // Clin. Cancer Bull. 2023. V. 2. № 1. P. 5.

36. Bassi D.E., Zhang J., Renner C., Klein-Szanto A.J. // Mol. Carcinog. 2017. V. 56. № 3. P. 1182–1188.

Heterologous Production of Antimicrobial Peptides in Yeast Allows for Massive Assessment of the Activity of DNA-Encoded Antimicrobials *In Situ*

S. O. Pipiya[1], A. O. Ivanova[1], Yu. A. Mokrushina[1,2], I. E. Eliseev[1], A. G. Gabibov[1,2], I. V. Smirnov[1,2], S. S. Terekhov[1*]

[1]Shemyakin–Ovchinnikov Institute of Bioorganic Chemistry of the Russian Academy of Sciences, Moscow, 117997 Russian Federation
[2]Faculty of Chemistry, Lomonosov Moscow State University, Moscow, 119991 Russian Federation
*E-mail: sterekhoff@mail.ru

ABSTRACT Antibiotic resistance threatens global healthcare. In clinical practice, conventional antibiotics are becoming gradually less effective. Moreover, the introduction of new antimicrobial agents into clinical practice leads to the emergence of resistant pathogenic strains within just a few years. Hence, the development of platforms for massive creation and screening of new antimicrobial agents is of particular importance. Massive parallel screening will greatly reduce the time required to identify the most promising drug candidates. Meanwhile, DNA-encoded antimicrobial agents offer unique opportunities for the high-throughput development of new antibiotics. Here, the yeast *Pichia pastoris* was engineered to produce a panel of antimicrobial peptides (AMPs), followed by high-throughput screening of AMP producers that inhibit bacterial growth *in situ*. Yeast clones producing thanatin and protegrin-1 exhibited the highest level of antimicrobial activity among the panel of AMPs under investigation. The production level of recombinant thanatin was significantly higher than that of protegrin-1, which correlates with its low toxicity. The designed technique of massive assessment of the activity of DNA-encoded antimicrobial agents enables the identification of drug candidates with an increased therapeutic index. Further development of methods for a rational design of artificial diversity in AMPs, followed by deep functional profiling of antimicrobial activity, will yield new AMPs with improved therapeutic characteristics.

KEYWORDS antimicrobial peptides (AMPs), yeast *Pichia pastoris*, heterologous production, template search, protegrin-1, thanatin.

ABBREVIATIONS AMP – antimicrobial peptide; GAP – glyceraldehyde 3-phosphate dehydrogenase; GFP – green fluorescent protein; NGS – next-generation sequencing.

INTRODUCTION

The spread of antibiotic resistance renders conventional broad-spectrum antibiotics less effective, thus limiting treatment options for bacterial infections [1]. Furthermore, there is growing concern over the development of cross-resistance [2, 3]. Therefore, in order to tackle the rapid pace of microbial adaptation to drugs, it is necessary to expand the spectrum of potential antibiotics and increase their screening scale [4, 5].

Natural sources are a vast reservoir of compounds exhibiting antimicrobial activity; however, the search for and production of these compounds is often con-fined to culturable and highly abundant microbial strains [6]. In turn, this raises the problem of rediscovering already known antibiotics. This problem can be addressed by ultra-high throughput screening of samples from various sources [7], which allows one to identify compounds of different chemical nature. However, chemical synthesis or cultivation of the antibiotic producer and production of the target substance for subsequent experiments related to its modification is required to further fine tune the properties of these antibiotics.

Antimicrobial peptides (AMPs) are a promising class of alternative antibiotics [8]. Natural antimicro-
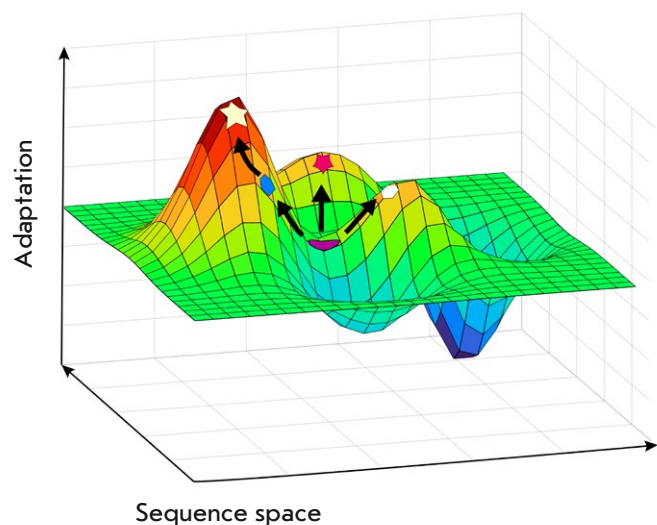
Fig. 1. Schematic representation of directed evolution in the adaptation vs. sequence space coordinates

bial peptides active against Gram-negative bacteria are of exceptional interest in the context of combating the spread of hospital-acquired infections and antibiotic resistance [9]. The advantages of AMPs are that they are genetically encoded and have a simple biosynthetic pathway, which can be adapted for heterologous protein production. This makes it possible to easily make structural modifications and simplifies the procedure for screening and improving the pharmacological properties of AMPs. Analysis of peptide databases allows one to search across natural sources for new AMPs [10]. The metagenomic and proteomic data can also be analyzed for this purpose to identify potential AMPs and then test their antimicrobial activity [11, 12].

Another approach is to utilize artificial molecular diversity based on a rational design and *de novo* approaches. The libraries of AMP variants are constructed and tested using the chemical synthesis [13], phage display [14], or yeast display technologies [15]. *De novo* design of AMPs using artificial intelligence and neural networks have recently witnessed extensive development [16]. Many of these approaches rely on directed evolution methods, which mimic the natural process in designing novel molecules. Choosing the starting point for generating a novel molecule is crucial in navigating the surface of the evolutionary landscape (*Fig. 1*). This will make it possible to analyze various directed evolutionary paths and identify the optimal variants. This setting of initial experimen-

tal conditions reduces the risk of following an evolutionary path that leads to a dead end.

Cytotoxicity and the mechanisms of action of AMPs are currently being assessed in artificial systems using vesicles, liposomes, and synthetic membranes as model membranes [17]. These methods allow one to roughly estimate how peptides interact with bacterial or eukaryotic membranes; however, they are conducted after the initial steps of antimicrobial activity screening and active peptide selection. AMP production in eukaryotic cells can be employed, and the antimicrobial activity of the producer strain can be assessed directly to reduce the number of screening steps and increase the throughput in research. Potentially cytotoxic peptides will not have a high yield in this heterologous system or will significantly affect the growth of the antibiotic-producer population. Hence, the number of variants can be minimized and allow one space to further investigate the properties of the selected AMPs more thoroughly. This approach can significantly accelerate the analysis.

The yeast *Pichia pastoris* is an interesting heterologous producer host in this regard, as it exhibits all the features of a eukaryotic cell, an affords the ability to introduce post-translational modifications, with a growth rate comparable to that of bacteria and a high level of recombinant protein production. [18].

The present study aims to investigate the features of heterologous AMP production in yeast and the application of recombinant technologies to template search for engineering novel antimicrobial peptides.

EXPERIMENTAL

Bacterial and yeast strains
The methylotrophic yeast *P. pastoris* GS115 (Invitrogen, USA) was used; *Escherichia coli* XL-Blue cells (Evrogen, Russia) were utilized in plasmid cloning and production; *E. coli* Δ*lptD* (kindly provided by I.A. Osterman) was used as the target bacteria.

Cloning the AMP genes
The expression vector pGAP4 was constructed by replacing the P_{AOX1} promoter in the pPIC9k vector (Invitrogen) with the promoter P_{GAP} sequence from vector pGAPZa (Thermo Fisher Scientific Inc., USA) using the HiFi DNA assembly kit (New England Biolabs, UK).

The nucleotide sequences of the AMP genes were optimized for production in *P. pastoris* cells using the GeneArt GeneOptimizer software (Thermo Fisher Scientific Inc.). The genes were synthesized by overlapping PCR and cloned into the expression vector pGAP4 using a HiFi DNA assembly kit (New England

Biolabs). The cloned AMP genes and the gene encoding the yeast alpha-mating factor, which ensures the secretion of peptide molecules in the growth medium, lay within the same reading frame. During transport, the alpha-mating factor sequence was processed by KEX2 endopeptidase and the active peptide was released into the growth medium. The AMP library in the vector pGAP_AMP was linearized at the AvrII restriction site to be further transformed into yeast cells.

Transformation of yeast cells

The *P. pastoris* GS115 cells were transformed with the linearized plasmid library pGAP_AMP in accordance with the protocol reported in [19]. The transformed yeast cells were harvested from an RDB agar medium (1 M sorbitol, 20 g/L glucose, 13.4 g/L YNB, 0.4 mg/L biotin, 0.005 g/L of essential amino acids (L-glutamic acid, L-methionine, L-lysine, L-leucine, and L-isoleucine)) and cultured in an incubator at 30°C for 72 h.

Evaluation of antimicrobial activity

The transformed yeast library clones were seeded into cell culture dishes with a YPD agar medium (2% peptone, 1% yeast extract, 2% glucose, 100 mM potassium phosphate buffer pH 6.0, and 1.8% agar) and incubated at 30°C for 48 h. The target bacteria, *E. coli ΔlptD* GFP, were cultured overnight. Soft agar (0.8% tryptone, 0.5% yeast extract, 0.25% NaCl, and 0.5% agarose) was inoculated with the overnight culture of the target bacteria to a final concentration of 10^5 CFU/mL; the yeast colonies were overlaid with it and incubated at 37°C for 18 h until bacterial growth inhibition zones were formed.

Analysis of the AMP production level in the liquid culture

AMP-producing yeast strains were cultured in the YPD growth medium (2% peptone, 1% yeast extract, 2% glucose, and 100 mM potassium phosphate buffer pH 6.0) in shake-flasks at 30°C and 180 rpm overnight. Aliquots of the growth medium were sampled after 24, 48, and 72 h and analyzed by Tricine-SDS-polyacrylamide gel electrophoresis (PAGE), in accordance with the protocol described in ref. [20]. The AMP production level was assessed according to the intensity of protein bands after Coomassie staining.

Peptide identification in clones exhibiting an antimicrobial activity

Active yeast clones were grown on the selective RDB medium. The genomic DNA was extracted using lithium acetate and SDS according to the protocol reported in ref. [21]. The AMP genes were amplified by PCR using flanking primers: Forw 5'-TGCTAAAGAAGA-AGGGGTATCTCTGGAGAAAAG-3' and Rev 5'-GA-ACTGAGGAACAGTCATGTCTAAGGCTACAAA-3'. The PCR products were sequenced using the Sanger sequencing method; the peptide gene was identified by aligning the resulting nucleotide sequence to the sequence of the AMP genes in the panel.

Extraction of yeast genomic DNA and sample preparation for next-generation sequencing

The genomic DNA was extracted from the merged pool of transformed yeast clones according to the protocol described in ref. [21]. The AMP genes were amplified by emulsion PCR (ePCR) according to the protocol in [22] using the aforelisted primers. The resulting pool of PCR products was subjected to additional purification using VAHTS DNA Clean Beads (Vazyme, China).

Next-generation sequencing

The prepared PCR products were amplified using the REPLI-g Single Cell Kit (Qiagen, Germany). Sequencing was conducted using a HiSeq 2500 system, HiSeq PE Cluster Kit v4 cBot, and HiSeq SBSKit v4 (250 cycles) (Illumina, USA) in accordance with the manufacturer's instructions.

RESULTS

Choosing the panel of antimicrobial peptides from the AMP databases

Based on AMP databases such as APD3 [23] and DBAASP [24], we constructed a panel of AMPs exhibiting a prominent antimicrobial activity (*Table 1*).

Validation using a panel of AMPs exhibiting different physicochemical characteristics is required to verify the ubiquity of the use of yeasts as a heterologous AMP producer. Based on this criterion, we chose AMP sequences with allowance for a relatively high antimicrobial activity, structural versatility, and length of the amino acid sequence. Hence, an AMP panel covering a broad range of structural templates was compiled.

Creation of genetic constructs of the AMP panel and transformation of yeast cells

The nucleotide sequences of the genes encoding antimicrobial peptides were optimized using the GeneArt GeneOptimizer software (Thermo Fisher Scientific Inc.). The synthesized fragments were cloned into a yeast vector for secretory production of pGAP4_AMP (*Fig. 2*). There was no need to add an inducer for target peptide production due to the presence of

Table 1. The panel of AMPs exhibiting a prominent antimicrobial activity

Antimicrobial peptide	Amino acid sequence[*]	Length, aa	Structure type
TP4	FIHHIIGGLFSAGKAIHRLIRRRRR	25	β-sheet
Protegrin-1	RGGRLCYCRRRFCVCVGR	18	β-sheet
Magainin 1	GIGKFLHSAGKFGKAFVGEIMKS	23	α-helix
Melittin	GIGAVLKVLTTGLPALISWIKRKRQQ	26	α-helix
Mastoparan	INLKAIAALAKKLF	14	α-helix
Thanatin	GSKKPVPIIYCNRRTGKCQRM	21	β-sheet
HNP-1	ACYCRIPACIAGERRYGTCIYQGRLWAFCC	30	β-sheet
Tachyplesin-1	KWCFRVCYRGICYRRCR	17	β-sheet
Indolicidin	ILPWKWPWWPWRR	13	α-helix
Arminin 1a	KPWRFRRAIRRVRWRKVAPYIPFVVKTVGKK	31	α-helix

[*]The amino acid sequence, length, and structure data were acquired from the APD3 [23] and DBAASP databases [24].

a strong constitutive promoter for the glyceraldehyde 3-phosphate dehydrogenase (GAP) gene. The resulting genetic constructs were transformed into yeast cells as a single pool. The yield of yeast clones produced using 1 µg of the plasmid library was 10⁴; they were pooled together into a single library for further functional studies.

Analysis of the representativity of the AMP genes from the panel

The quantity of produced yeast clones was three orders of magnitude larger than the number of variants of the analyzed AMP genes, thus indicating that representativity of this library was sufficient. Extraction of total genomic DNA and next-generation sequencing were used to verify the presence of all the AMP genes from the panel in the library and establish their ratios. The sequencing data demonstrated that the library contained all the AMP genes from the panel (*Fig. 3*).

Analysis of the antimicrobial activity of the library of AMP-producing yeasts

Antimicrobial activity was tested by analyzing the formation of zones of growth inhibition of the target *E. coli* Δ*lptD* bacteria on the nutrient medium in Petri dishes (*Fig. 4*).

A total of ~ 3 000 clones were analyzed, covering the studied AMP library by more than two orders of magnitude. Thereby, the risk of overlooking a clone carrying the gene encoding any of the selected AMPs because of an insufficient number of analyzed clones was minimized. Genomic DNA was extracted in 55 clones. The region carrying the AMP gene was ampli-

fied and analyzed by Sanger sequencing. The analysis revealed that 37 clones carried the thanatin gene, while 18 clones carried the protegrin-1 gene.

Large zones of growth inhibition of the target bacteria were detected for active yeast clones, which could potentially overlap with the growth inhibition zones from other peptides. In order to rule out the potential loss of active clones, we additionally cloned a new pool of AMP genes, with the protegrin-1 and thanatin genes excluded. An analysis of clone activity in the shortened library revealed no new active candidates.

The level of AMP production by active clones was also assessed according to band intensity in the SDS-PAGE analysis (*Fig. 5*).
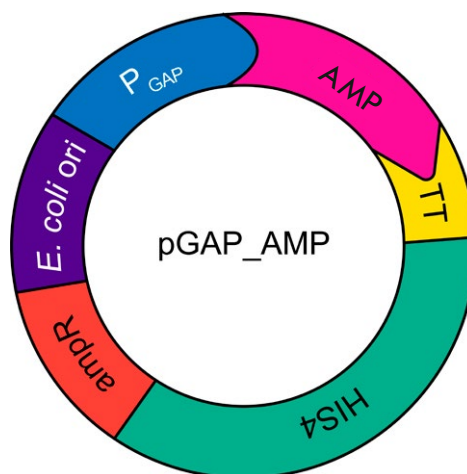

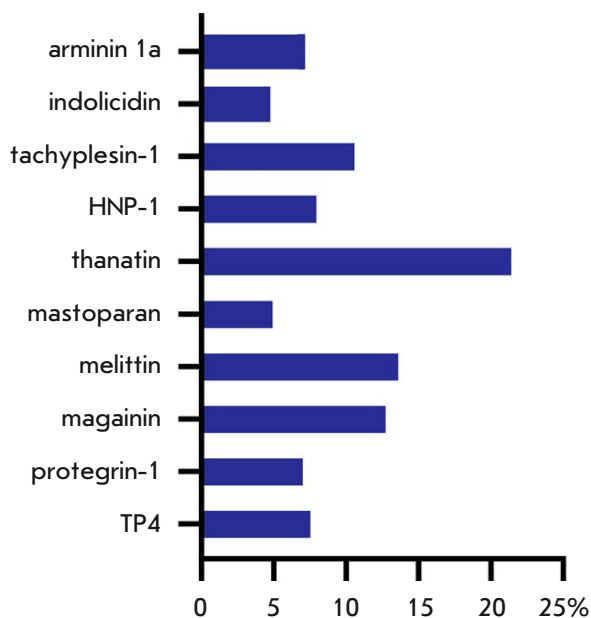Fig. 2. The scheme of the genetic construct for constitutive production of AMP

Fig. 3. Analysis of AMP gene representation in a yeast library. The shares of the total number of sequences are displayed as a percentage on the X axis

Fig. 4. An assay of inhibition of the growth zones of the target bacteria *Escherichia coli ΔlptD* by yeast clones transfected with pGAP_AMP

The growth medium samples were characterized by a high level of recombinant thanatin production, as indicated by the presence of a clear band in the low-molecular-weight region of the electrophoregram. Meanwhile, the absence of respective bands in the culture media from protegrin-1 producers was demonstration that the production level of this peptide was low. However, despite the low level of protegrin-1 production, recombinant AMP-producing yeast clones exhibited a detectable level of antimicrobial activity, since this AMP *per se* has significant antimicrobial properties.

Our findings are indication that AMPs can be detected in this system both due to their high production level and according to their antimicrobial activity.

DISCUSSION

Antimicrobial peptides (AMPs) are naturally abundant as defense and signaling molecules [25]. They mainly consist of 5–50 amino acid residues; positively charged and hydrophobic side chains are often predominant. A large group of AMPs has no specific protein target in bacterial cells, because they target the membrane or cause oxidative stress, thus suppressing the development of resistance to AMPs by bacteria [26]. Antimicrobial-resistant bacteria are also known to be substantially sensitive to AMPs [27]. Hence, AMPs are promising candidates for the role of alter-
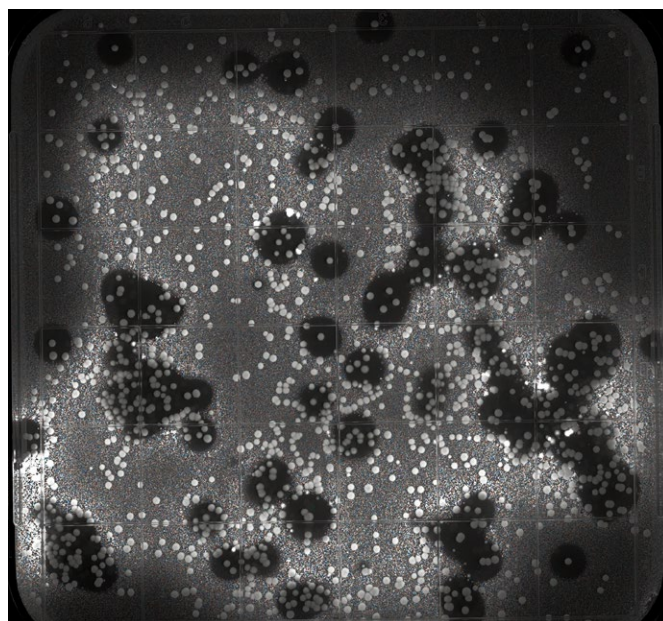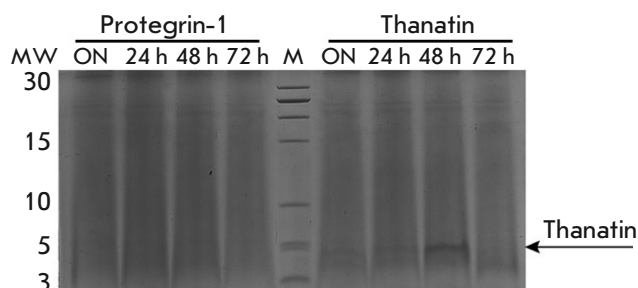

Fig. 5. Tricine-SDS-PAGE electrophoregram. 24 h, 48 h, 72 h — culture media from protegrin-1 and thanatin producers taken at respective time points; ON — the overnight time point; M — protein molecular weight marker

native antimicrobial compounds for combating multidrug resistance.

The methylotrophic yeast *P. pastoris* is a convenient and cost-effective heterologous producer thanks to the availability of a vast pool of tools used in genetic engineering to produce a broad spectrum of protein molecules, as well as the low net cost of the required components of the growth medium. The cost of AMP synthesis and primary activity screening can be significantly reduced by detecting antimicrobial activity in a heterologous AMP producer. A library of yeast

clones producing a panel of antimicrobial peptides was engineered in our study. Simultaneous activity assays of the yeast clones allowed us to compare the potential cytotoxicity of the selected peptides against eukaryotic cells and their specific activity. The protegrin-1 and thanatin-producing clones were shown to exhibit a prominent antimicrobial activity.

Protegrin-1 is known to be characterized by high hemolytic activity and cytotoxicity [28], whereas thanatin, while specifically targeting bacteria, causes no marked hemolysis [29] and exhibits low cytotoxicity in mammals [30]. That can be one of the reasons behind the differences in the production levels of these AMPs observed in our study. The other peptide-producing strains from the panel exhibited no prominent antimicrobial effect against the target bacterium. The reason behind this can be the potential fungicidal activity of the respective AMPs against *P. pastoris* yeast cells. On the other hand, yeasts are eukaryotic organisms; therefore, AMPs targeting eukaryotic cell membranes via a nonspecific mechanism of action would be cytotoxic to yeast cells. In turn, this may reduce the production levels, thus leading to the lack of antimicrobial activity in the AMP-producing yeast. However, this effect can be used to exclude AMPs characterized by low selectivity against bacterial membranes and cytotoxic to eukaryotic cells. To be successfully detected by such screening, the potentially cytotoxic variants must be characterized by high specific activity.

Hence, it can be inferred that screening of active AMP variants by recombinant production in yeast cells allows one to select peptides with different characteristics. This system can be used to search for new templates for generating artificial diversity in AMPs and improving their pharmacokinetic properties.

CONCLUSIONS

An AMP panel for generating a pool of recombinant antimicrobial producers was engineered in this study. The methylotrophic yeast *P. pastoris* was genetically modified to ensure secreted production of antimicrobial peptides. An analysis of the zones of growth inhibition of yeast clones demonstrated that producers of protegrin-1 and thanatin peptides exhibited the most prominent activity. An analysis of the production levels of protegrin-1 and thanatin revealed that thanatin content in the growth medium was higher than that of protegrin-1, thus indicating that there were different reasons for the manifested high activity of the yeast clones. For thanatin, this occurs due to its high production level, while being caused by high specific activity in the case of protegrin-1. Hence, by using yeast cells as AMP producers and generating a pool of cells exhibiting antimicrobial activity based on them, one can simultaneously analyze the antimicrobial properties of substances under the same conditions, thus reducing the time and cost of such research. This study demonstrated the potential of recombinant technologies in the development of strategies for massive screening of antimicrobial compounds. ●

REFERENCES
1. Murray C.J.L., Ikuta K.S., Sharara F., Swetschinski L., Robles Aguilar G., Gray A., Han C., Bisignano C., Rao P., Wool E., et al. // The Lancet. 2022. V. 399. № 10325. P. 629–655.
2. Cherny S.S., Nevo D., Baraz A., Baruch S., Lewin-Epstein O., Stein G.Y., Obolski U. // J. Antimicrob. Chemother. 2021. V. 76. № 1. P. 239–248.
3. Nichol D., Rutter J., Bryant C., Hujer A.M., Lek S., Adams M.D., Jeavons P., Anderson A.R.A., Bonomo R.A., Scott J.G. // Nat. Commun. 2019. V. 10. № 1. P. 334.
4. Itoh H., Tokumoto K., Kaji T., Paudel A., Panthee S., Hamamoto H., Sekimizu K., Inoue M. // Nat. Commun. 2019. V. 10. № 1. P. 2992.
5. Li S., She P., Zhou L., Zeng X., Xu L., Liu Y., Chen L., Wu Y. // Front. Microbiol. 2020. V. 11. P. 591426.
6. Lewis K. // Cell. 2020. V. 181. № 1. P. 29–45.
7. Terekhov S.S., Smirnov I.V., Malakhova M.V., Samoilov A.E., Manolov A.I., Nazarov A.S., Danilov D.V., Dubiley S.A., Osterman I.A., Rubtsova M.P., et al. // Proc. Natl. Acad. Sci. USA. 2018. V. 115. № 38. P. 9551–9556.
8. Magana M., Pushpanathan M., Santos A.L., Leanse L., Fernandez M., Ioannidis A., Giulianotti M.A., Apidianakis

Y., Bradfute S., Ferguson A.L., et al. // Lancet Infect. Dis. 2020. V. 20. № 9. P. e216–e230.
9. Barreto-Santamaría A., Arévalo-Pinzón G., Patarroyo M.A., Patarroyo M.E. // Antibiotics. 2021. V. 10. № 12. P. 1499.
10. Porto W.F., Pires A.S., Franco O.L. // Biotechnol. Adv. 2017. V. 35. № 3. P. 337–349.
11. Jhong J.-H., Yao L., Pang Y., Li Z., Chung C.-R., Wang R., Li S., Li W., Luo M., Ma R., et al. // Nucl. Acids Res. 2022. V. 50. № D1. P. D460–D470.
12. Ma Y., Guo Z., Xia B., Zhang Y., Liu X., Yu Y., Tang N., Tong X., Wang M., Ye X., et al. // Nat. Biotechnol. 2022. V. 40. № 6. P. 921–931.
13. Mourtada R., Herce H.D., Yin D.J., Moroco J.A., Wales T.E., Engen J.R., Walensky L.D. // Nat. Biotechnol. 2019. V. 37. № 10. P. 1186–1197.
14. Kim H., Jang J.H., Kim S.C., Cho J.H. // Eur. J. Med. Chem. 2020. V. 185. P. 111814.
15. Chun J., Bai J., Ryu S. // ACS Synth. Biol. 2020. V. 9. № 3. P. 508–516.
16. Kazmirchuk T.D.D., Bradbury-Jost C., Withey T.A., Gessese T., Azad T., Samanfar B., Dehne F., Golshani A. // Genes. 2023. V. 14. № 6. P. 1194.

17. Hollmann A., Martinez M., Maturana P., Semorile L.C., Maffia P.C. // Front. Chem. 2018. V. 6. P. 204.
18. Karbalaei M., Rezaee S.A., Farsiani H. // J. Cell Physiol. 2020. V. 235. № 9. P. 5867–5881.
19. Wu S., Letchworth G.J. // Biotechniques. 2004. V. 36. № 1. P. 152–154.
20. Schägger H. // Nat. Protoc. 2006. V. 1. № 1. P. 16–22.
21. Lõoke M., Kristjuhan K., Kristjuhan A. // BioTechniques. 2011. V. 50. № 5. P. 325–328.
22. Terekhov S.S., Eliseev I.E., Ovchinnikova L.A., Kabilov M.R., Prjibelski A.D., Tupikin A.E., Smirnov I.V., Belogurov A.A., Severinov K.V., Lomakin Y.A., et al. // Proc. Natl. Acad. Sci. USA. 2020. V. 117. № 44. P. 27300–27306.
23. Wang G., Li X., Wang Z. // Nucl. Acids Res. 2016. V. 44. № D1. P. D1087–D1093.
24. Pirtskhalava M., Amstrong A.A., Grigolava M., Chubinidze M., Alimbarashvili E., Vishnepolsky B., Gabrielian A., Rosenthal A., Hurt D.E., Tartakovsky M. // Nucl. Acids Res. 2021. V. 49. № D1. P. D288–D297.
25. Koczulla A.R., Bals R. // Drugs. 2003. V. 63. № 4. P. 389–406.
26. Bahar A.A., Ren D. // Pharmaceuticals. 2013. V. 6. № 12. P. 1543–1575.
27. Lázár V., Martins A., Spohn R., Daruka L., Grézal G., Fekete G., Számel M., Jangir P.K., Kintses B., Csörgő B., et al. // Nat. Microbiol. 2018. V. 3. № 6. P. 718–731.
28. Edwards I.A., Elliott A.G., Kavanagh A.M., Zuegg J., Blaskovich M.A.T., Cooper M.A. // ACS Infect. Dis. 2016. V. 2. № 6. P. 442–450.
29. Hou Z., Lu J., Fang C., Zhou Y., Bai H., Zhang X., Xue X., Chen Y., Luo X. // J. Infect. Dis. 2011. V. 203. № 2. P. 273–282.
30. Tanhaeian A., Azghandi M., Mousavi Z., Javadmanesh A. // Protein Pept. Lett. 2020. V. 27. № 1. P. 41–47.

Galanin Reduces Myocardial Ischemia/ Reperfusion Injury in Rats with Streptozotocin Diabetes

I. M. Studneva, L. I. Serebryakova, O. M. Veselova, I. V. Dobrokhotov, M. E. Palkeeva, D. V. Avdeev, A. S. Molokoedov, M. V. Sidorova, O. I. Pisarenko[*]
Chazov National Medical Research Center of Cardiology, Moscow 121552 Russian Federation
[*]E-mail: olpi@live.ru

ABSTRACT Most clinical studies confirm the negative impact diabetes mellitus (DM) has on the course and outcome of cardiovascular complications caused by a myocardial ischemia–reperfusion injury (IRI). In this regard, the search for new approaches to IRI treatment in diabetic myocardium is of undeniable value. The aim of this work was to study the effect of galanin (G) on the size of myocardial infarct (MI), on mitochondrial functions, and on the energy state in the area at risk (AAR) in rats with type 1 diabetes mellitus (DM1) subjected to regional myocardial ischemia and reperfusion. Rat G was obtained by solid-phase synthesis using the Fmoc strategy and purified by HPLC. DM1 was induced by streptozotocin administration. Myocardial IRI was modeled by occlusion of the left anterior descending coronary artery and subsequent reperfusion. G at a dose of 1 mg/kg was administered intravenously before reperfusion. G decreased MI size and plasma creatine kinase MB (CK–MB) activity in DM rats by 40 and 28%, respectively. G injection improved mitochondrial respiration in saponin-skinned fibers in the AAR: namely, the maximal ADP-stimulated state 3, respiratory control, and the functional relationship between the mitochondrial CK–MB and oxidative phosphorylation. G provided significantly higher ATP levels, total adenine nucleotide pool, and adenylate energy charge of cardiomyocytes. It also reduced total creatine loss in myocardial AAR in DM rats. The results suggest there is a possibility of therapeutic use of G in myocardial IRI complicated by DM1.

KEYWORDS galanin, rat, streptozotocin diabetes, myocardial ischemia and reperfusion, mitochondrial dysfunction, myocardial energy state, cell membrane damage.

ABBREVIATIONS ROS – reactive oxygen species; AEC – adenylate energy charge; RC – respiratory control; AAR – area at risk; MI – myocardial infarction; IRI – ischemia/reperfusion injury; CK–MB – creatine kinase MB; LDH – lactate dehydrogenase; LV – left ventricle; mt-CK – mitochondrial creatine kinase; OP – oxidative phosphorylation; LAD – left anterior descending coronary artery; LPP – lipid peroxidation; DM – diabetes mellitus, STZ – streptozotocin; CK – creatine kinase; Cr – creatine; G – galanin; PCr – phosphocreatine; ΣAN – total adenine nucleotide pool; ΣCr – total creatine; TTC – 2,3,5-triphenyltetrazolium chloride.

INTRODUCTION

If we consider the mutually reinforcing negative impact of diabetes mellitus (DM) and myocardial ischemia as two common pathologies on prognosis and a patient's life quality, this comorbidity presents one of the most vexing challenges in modern experimental and clinical cardiology. DM patients are more likely to suffer from coronary artery occlusions, and their myocardium is more prone to ischemia–reperfusion injury (IRI) compared to non-DM individuals [1]. As a rule, cardioprotection from IRI is ineffective in DM [2]. This has to do with the defects in the PI3K/Akt and JAK2/STAT3 signaling cascades, which play the key role in cardioprotection [3]. Diabetic hyperglycemia can cause mitochondrial dysfunction by increasing the expression of the dynamin-1-like protein [4], inhibiting mitochondrial ATP-dependent K^+ channels [5], and inactivating hypoxia-inducible factor 1α (HIF-1α) [6]. These metabolic changes contribute to the desensitization of the diabetic myocardium to therapeutic interventions against IRI. In this regard, the search for new pharmacological targets for preventing and treating myocardial IRI in DM is of undeniable value.

An important role in cardiovascular regulation in diseases has recently been attributed to the galanin-

ergic system [7]. The neuropeptide galanin (G; GWTLNSAGYLLGPHAIDNHRSFSDKHGLT-NH2) is widely found in the central and peripheral nervous systems and other tissues [8]. In peripheral organs, including the heart, G acts not only through neuronal mechanisms, but it also activates the galanin receptor GalR1-3 [9]. We recently showed that intravenous injection of G to rats after regional myocardial ischemia significantly reduced cardiomyocyte necrosis [10]. This effect was mediated by GalR2 activation and significantly reduced in the presence of M871, a GalR2 antagonist [11]. Reduced myocardial infarction (MI) in the presence of G was accompanied by a decreased formation of the hydroxyl radical adduct 5,5-dimethyl-pyrroline-N-oxide-OH and lipid peroxidation products (LPP) in the area at risk (AAR) upon blood flow restoration. G can also inhibit the free radical oxidation of low-density lipoproteins in human plasma [12]. It is important to note that G prevented hyperglycemia in streptozotocin (STZ)-induced DM in rats, improved the metabolic state of DM animals thanks to an increase in the mitochondrial respiratory function, and reduced LPP formation in plasma [13]. We hypothesized that this peptide, which improves energy production in cardiac mitochondria and reduces oxidative stress, is a promising agent for reducing IRI in type 1 DM (DM1). The G effect on ischemic myocardium exposed to DM has never been studied before. To test this hypothesis, we used G during the reperfusion period after regional myocardial ischemia in rats with STZ-induced hyperglycemia. We used the following cardiac damage criteria: MI size and plasma activity of the necrosis markers creatine kinase-MB (CK–MB) and lactate dehydrogenase (LDH). To understand the mechanisms of G action, we placed the main focus on the energy state in the AAR and mitochondrial function, which was characterized by respiration in saponin-skinned myocardial fibers.

EXPERIMENTAL

Reagents
Fmoc-protected amino acid derivatives were purchased from Novabiochem and Bachem (Switzerland); reagents for peptide synthesis were obtained from Fluka Chemie GmbH (Switzerland). Enzymes and the chemicals used to determine metabolites and evalu-ate myocardial fiber respiration were purchased from Merck Life Science LLC (Russia). Solutions were prepared using deionized water (Millipore Corp., USA).

Peptide G synthesis and chromatography
Peptide G was obtained by convergent solid-phase synthesis through condensation of peptide segments, which, in turn, were obtained either on a polymer surface or in solution. Peptide G was purified by preparative HPLC to 98% purity on a Knauer chromatograph (Germany) using a Kromasil 100-10 ODS column (Sweden) (30 × 250 mm) [14]. Analytical HPLC was performed on a Kromasil 100-5 C18 column (4.6 × 250 mm) with a 5-μm sorbent particle size. The following eluents were used: 0.1% TFA as buffer A and 80% acetonitrile in buffer A as buffer B. The elution was carried out in a linear buffer B gradient ranging from 20 to 80% for 30 min at a rate of 1 ml/min. Detection was performed at λ = 220 nm (Supplementary materials; *Fig. S1*). The peptide structure was confirmed by MALDI-TOF/TOF mass spectrometry on an UltrafleXtreme Bruker Daltonics GmbH mass spectrometer (Germany) equipped with a UV laser (Nd) (Supplementary materials, *Fig. S2*). Peptide G characteristics are provided in *Table 1*.

Experimental design
Male Wistar rats weighing 280–290 g were used in the study. The animals were procured from the Stolbovaya Animal Nursery of the Scientific Center for Biomedical Technologies (Moscow, Russia). The rats were kept in individual cages at 20–25°C in the natural light–dark cycle with free access to a standard pelleted diet and water. All the animals were weighed prior to the study. After a 24-h fasting period, the rats were taken in for blood collection. Blood was collected from the tail vein of 10 rats to determine the glucose plasma level and CK–MB and LDH activities in the animal plasma. The rats were then anesthetized with 2,2,2-tribromoethanol (avertin, 1 mg/kg intraperitoneally; Merck, Russia); their hearts were excised to assess energy metabolism parameters ($n = 5$) and mitochondrial respiration parameters in left ventricular (LV) fibers ($n = 5$) (initial state group; IS). The remaining animals were randomly divided into 5 groups of 15 rats, each: control (C), cardiac IRI (IR); diabetes mellitus (D), diabetes

Table 1. Characteristics of peptide G

Amino acid sequence	Molecular weight, g/mol	MALDI-TOF, m/z	Solubility in water, mg/ml	Purity, HPLC, %
GWTLNSAGYLLGPHAIDNHRSFSDKHGLT-NH$_2$	3164.45	3163.474 [$M + H$]$^+$	> 40	98.10

mellitus followed by cardiac IRI (D + IR), and diabetes mellitus with cardiac IRI and G administration at the onset of reperfusion (D + IRG). In the IR group, cardiac injury was modeled by occlusion of the left anterior descending coronary artery (LAD), followed by reperfusion [11]. Acute DM1 was induced by a single STZ injection (60 mg/kg intravenously) [15]. DM was confirmed based on an increase in the blood glucose level to ⩾12 mM two days after STZ injection. The glucose level did not decrease during 16 days of experiment in all STZ-receiving animals. The D + IR group received a single STZ injection (60 mg/kg intravenously). After a 16-day experiment, the D + IR animals were subjected to LAD occlusion and reperfusion for the same period of time as the IR group. The D + IRG group received a single STZ administration (60 mg/kg intravenously); IRI was modeled after 16 days. Peptide G in saline was administered intravenously at a bolus dose of 1 mg/kg at the beginning of reperfusion. The G dose was selected based on our previous results [11]. The control rats received a single intravenous injection of 0.1 M citrate buffer (pH 4.5; STZ solvent). Body weight and the blood glucose level in the experimental animals were determined on a weekly basis. After a 16-day study, blood samples were collected from the tail vein of the rats of all groups to determine the plasma activities of CK–MB and LDH. The AAR and MI sizes were assessed in the hearts of five animals from the IR, D + IR, and D + IRG groups by histochemical analysis. The hearts of five rats from the experimental groups were isolated after anesthesia with avertin (1 mg/k intraperitoneally) and frozen in liquid nitrogen using Wollenberger forceps for subsequent metabolite analysis. The remaining five animals from the same groups were used to evaluate the mitochondrial respiration parameters in LV fibers. The experimental protocol is represented schematically in *Fig. 1*.

Rat model of regional myocardial ischemia and reperfusion

The IR, D + IR, and D + IRG groups of animals were anesthetized with 20% urethane (1 200 mg/kg of body weight, intraperitoneally) and artificially ventilated with room air through thoracotomy using the KTR-5 system (Hugo Sacks Electronik, Germany). Mean arterial pressure and heart rate were monitored. Parameters were recorded during the experiment using a USB-6210 analog-to-digital converter (National Instruments, USA) and the LabView 7 system software (National Instruments). The preparation period was followed by a period of hemodynamic parameter stabilization (30 min). The animals were then subjected to 40-min LAD occlusion, followed by 60-min
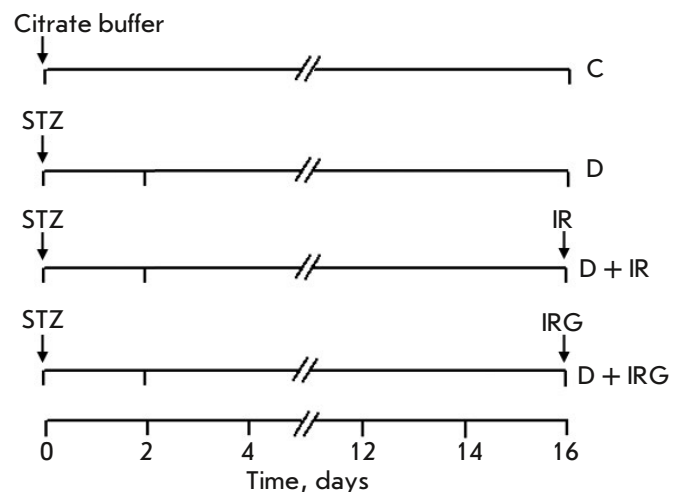

Fig. 1. Experimental protocol scheme. D – rats receiving STZ (60 mg/kg in 0.1 M citrate buffer; pH 4.5; intravenously); D + IR – DM rats (STZ, 60 mg/kg; intravenously) subjected to regional myocardial IRI; D + IRG – DM rats (STZ, 60 mg/kg; intravenously) subjected to regional myocardial IRI, receiving G (1 mg/kg, bolus intravenous administration at the onset of reperfusion). Cit. buffer – 0.1 M citrate buffer (pH 4.5); STZ – streptozotocin

reperfusion. In the D + IRG group, simultaneously with the beginning of reperfusion, peptide G was injected intravenously at a bolus dose of 1.0 mg/kg body weight. In the IR and D + IR groups, the same volume of a physiological solution was administered intravenously as a bolus after a period of regional ischemia. At the end of the experiment, the LAD was reoccluded and 2 ml of a 2% Evans solution were injected into the jugular vein to determine the AAR and the intact myocardial region. The heart was then excised, and LV was isolated to determine the MI size.

Determination of the MI size

The frozen LV was incised perpendicular to the long cardiac axis into 4- to 5- ~1.5- to 2.0-mm-thick sections. The sections were incubated for 10 min in a 1% solution of 2,3,5-triphenyltetrazolium chloride (TTC) in 0.1 M potassium phosphate buffer (pH 7.4 at 37℃). The resulting samples were scanned; MI and AAR were determined by computer planimetry using the ImageJ software (NIH, USA). Sections were then weighed to determine the LV mass. The AAR/LV and MI/AAR ratios were calculated and expressed in % for each group [11].

Assessment of cardiomyocyte membrane damage

Damage to cardiomyocyte membranes was assessed based on the increase in plasma LDH and CK–MB

activities. Approximately 0.5 ml of blood was collected into heparin tubes from a venous catheter at the baseline (prior to LAD occlusion) and 1 h after reperfusion. Enzyme activity was evaluated in plasma using BioSystems kits on a Shimadzu UV-1800 spectrophotometer (Japan) at $\lambda = 340$ nm.

Respiration in permeabilized myocardial fibers

Saponin-permeabilized fibers from rat LV were prepared using a modified approach [16]. LV fiber respiration parameters were assessed using complex I substrates: 10 mM glutamate and 5 mM malate. An Oxygraph plus system (HansaTech Instruments, UK) was used for analysis. The resulting values were expressed as nmol O_2/min/mg dry weight. The respiration rate in state 3 (V_3) was achieved by adding 2 mM ADP. Fiber dry weight was determined after overnight drying at 95°C. The respiration parameters of each LV fiber sample were measured twice. The respiration rate in state 2 (V_2) was evaluated base on the oxygen consumption rate after the addition of 10 mM glutamate and 5 mM malate in the absence of ADP. Mitochondrial function was assessed based on a measurement of the respiratory control (RC) value, which was calculated as the V_3/V_2 ratio. The integrity of the outer mitochondrial membrane was determined by adding 10 μM cytochrome *c* after maximal respiration stimulation using 2 mM ADP; the obtained values were expressed as the $V_{cyt\ c}/V_{ADP}$ ratio in %. The degree of functional coupling between mitochondrial creatine kinase (mt-CK) and oxidative phosphorylation (OP) was assessed by adding 30 mM Cr to fibers in the presence of ADP at a submaximal concentration (0.1 mM) and calculated as the $(V_{Cr} - V_{ADP})/V_{ADP}$ ratio (%) [17].

Assessment of metabolite content in the AAR

After reperfusion, the AAR was quickly isolated from the LV and frozen using a Wollenberger clamp cooled in liquid nitrogen. The frozen tissue was homogenized in cold 6% $HClO_4$ (10 ml/g of tissue) in an Ultra-Turrax T-25 homogenizer (IKA-Labortechnik, Germany). Proteins were precipitated by centrifugation (Sorvall RT1 centrifuge, Thermo Fisher Scientific, USA) at 2 800 *g* at 4°C for 10 min. Supernatants were neutralized with 5M K_2CO_3 to pH 7.4. The $KClO_4$ precipitate was separated by centrifugation under the same conditions. Protein-free extracts were stored at −70°C prior to metabolite determination. The dry weight of homogenized tissue was determined after drying samples at 110°C for 24 h. The ATP, ADP, AMP, PCr, and Cr levels in tissue extracts were determined by modified enzymatic methods [18] using a Shimadzu UV-1800 spectrophotometer (Japan).

Table 2. Changes in body weight and blood glucose level in the studied animal groups

Group	Body mass, g		
	Day 1	Day 9	Day 16
C	326.2 ± 11.7	344.2 ± 3.5	379.2 ± 4.5*
D	335.2 ± 2.5	348.7 ± 3.3*	295.5 ± 14.5*$@
IR	340.6 ± 3.6	–	–
D + IR	338.2 ± 1.7	376.5 ± 2.6*@	291.3 ± 4.6*$@
D + IRG	336.2 ± 2.3	380.0 ± 4.3*@#	321.2 ± 13.0$@+
Blood glucose level, mM			
C	6.1 ± 0.2	–	6.3 ± 0.2
D	5.3 ± 0.5	22.4 ± 0.8*	23.8 ± 1.7*@
IR	5.1 ± 0.4	–	–
D + IR	4.9 ± 0.6	26.8 ± 3.3*	21.3 ± 5.1*@
D + IRG	5.0 ± 0.2	25.0 ± 2.0*	21.5 ± 3.3*@

Data are presented as M ± m (*n* = 15). *p* < 0.05 vs: * – value on day 1, $ – value on day 9, @ – control, # – D, + – D + IR.

Statistical analysis

The SigmaPlot 11.2 software package (SysStat, USA) was used for the statistical analysis. Values are presented as a mean ± standard error of the mean (M ± m). Differences between the groups were statistically confirmed using the analysis of variance (ANOVA). Student's t-test with Bonferroni correction was used to compare several groups with the control. Differences were considered statistically significant at *p* < 0.05.

RESULTS

Body weight and the blood glucose level

At baseline (day 1 of the experiment), animal weight did not differ significantly between the groups (*Table 2*). A progressive increase in body weight was noted during the observation period in the control group. In the diabetic group, no weight gain was observed until day 9 of the study (one week after an increase in the blood glucose level higher than 12 mM in the presence of STZ). At the end of the study, the body weight in this group was, on average, 11.8 and 22.1% lower than that in the initial state and in the control (*p* < 0.02 and *p* < 0.001, respectively). A similar change in the body weight was noted in the D + IR and D + IRG groups. No differences in the body weight were found in DM animals on the last day prior to IR heart damage modeling and G injection.

At baseline, no significant difference between the blood glucose levels in the groups of animals were found. STZ administration increased the glucose level

Fig. 2. The sizes of the AAR (*A*), MI (*B*), and LV sections (*C*) stained with 2,3,5-triphenyltetrazolium chloride at the end of reperfusion in groups with regional myocardial IRI. M ± m for groups of 5 animals are shown. $p < 0.05$ compared to: ^ − IR, + − D + IR
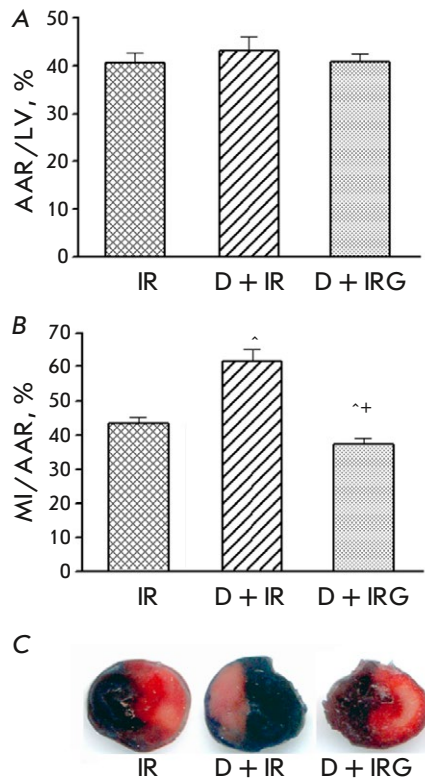
compared to the control throughout the entire experiment. After 16 days, the blood glucose level in group D rats was 4.5 times higher compared to the baseline ($p < 0.001$) and 3.8 times higher compared to the control group ($p < 0.001$). Similar changes were observed in the groups D + IR and D + IRG. No statistically significant differences in the glucose levels were found in either of the DM groups prior to IRI modeling.

The effect of DM and peptide G on the size of the myocardial infarction

Histochemical analysis of LV sections at the end of reperfusion revealed no differences in AAR sizes between the IR, D + IR, and D + IRG groups (*Fig. 2*). AAR/LV values were similar in these groups: 41.3 ± 1.3% on average. This means that IRI modeling was standard in all the animals. In the IR group, the MI size, expressed as the MI/AAR ratio, was 43.4 ± 1.6%. In the presence of STZ, the MI size had increased 1.4-fold compared to the IR group by the end of the experiment ($p = 0.002$). Reperfusion with G significantly decreased the MI/AAR in the DM rats: this value was 40% lower in the D + IRG animals compared to the D + IR group. *Figure 2B* shows the localization of the necrotic zone in LV sections after staining with TTC. An increase in the formation of red formazan crystals due to TTC reduction by
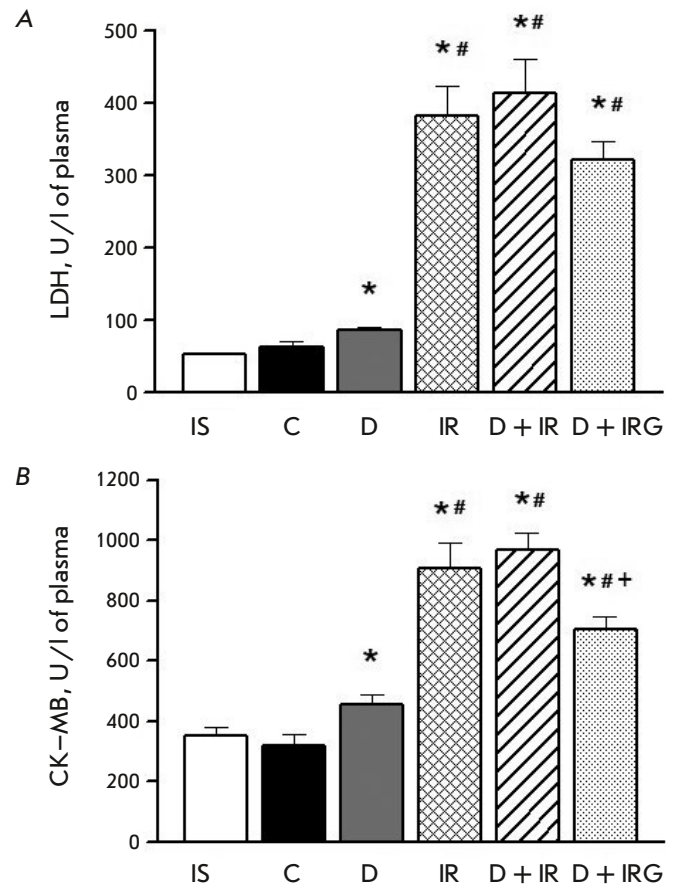

Fig. 3. Lactate dehydrogenase (LDH, *A*) and creatine kinase-MB (CK-MB, *B*) activities in rat plasma. Values represent M ± m for groups of 5 animals. $p < 0.05$ compared to: * − C, # − D, + − D + IR. IS − initial state

NAD⁺ and NADP⁺-dependent dehydrogenases in the D + IRG group indicates a decrease in the MI intensity in the presence of G.

Plasma activities of CK−MB and LDH

The CK−MB and LDH activities in the control rats did not differ from those at baseline (*Fig. 3A,B*). STZ-induced DM development resulted in a significant increase in the CK−MB and LDH activities by the end of the experiment compared to the control ($p = 0.027$ and $p = 0.046$, respectively). IRI modeling had significantly increased the CK−MB and LDH activities by the end of reperfusion compared to the control ($p < 0.001$). The CK−MB and LDH values were 2.0- and 4.4-fold higher, respectively, compared to the DM group ($p < 0.001$). Regional IRI in the DM animals of the D + IR group did not cause a significant increase in the activity of necrosis markers compared to the IR group. Bolus intravenous administration of G at the onset of reperfusion reduced the CK−MB activi-
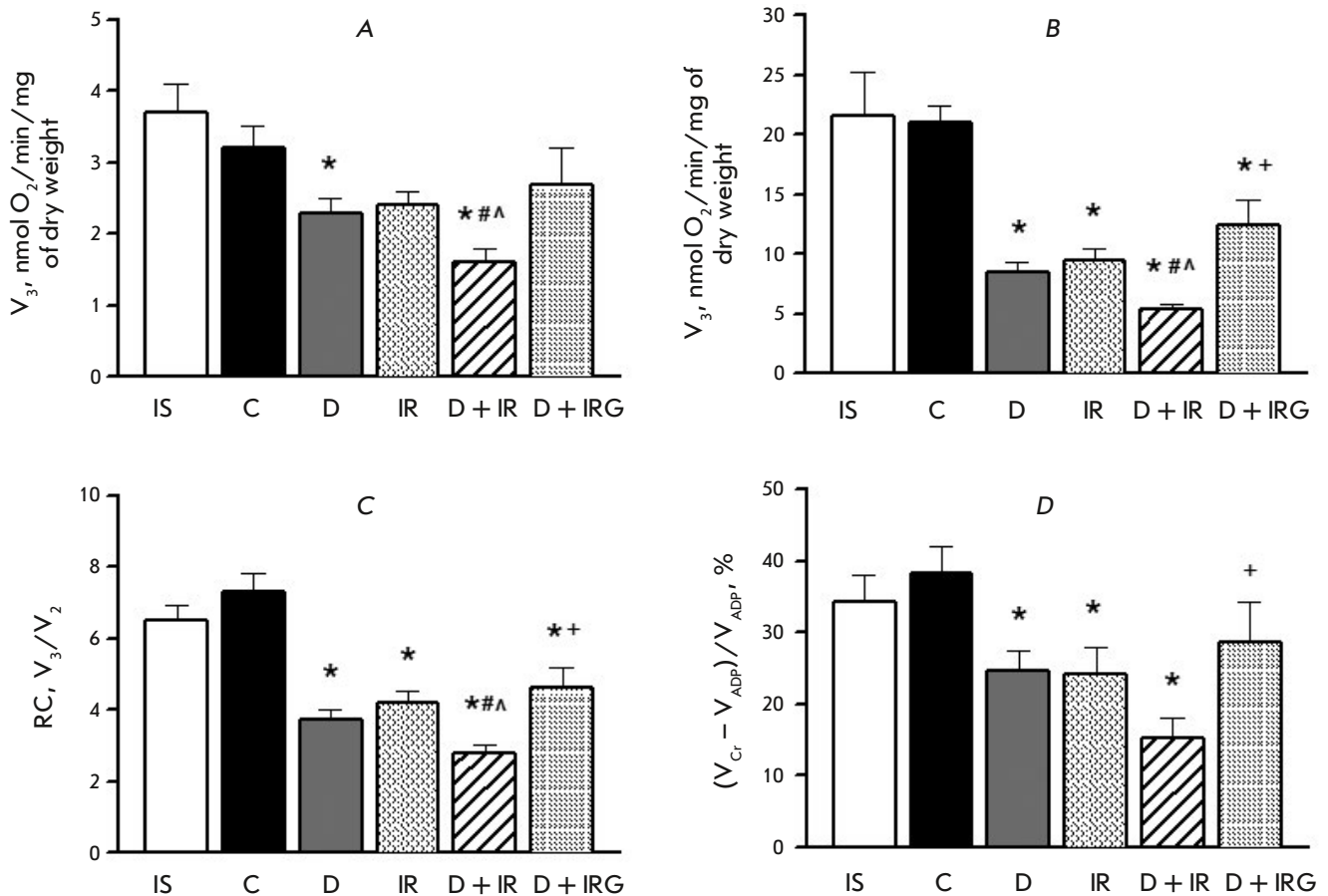
Fig. 4. Mitochondrial respiration parameters in saponin-skinned LV fibers in the presence of 10 mM glutamate and 5 mM malate. (*A*) – oxygen consumption rate in state 2 (V_2); (*B*) – oxygen consumption rate in state 3 (V_3); (*C*) – respiratory control index = V_3/V_2; (*D*) – rate of functional coupling between mt-CK and OP ($V_{Cr} - V_{ADP}$)/V_{ADP}, %. Values represent $M \pm m$ for groups of 5 animals. $p < 0.05$ compared to: * – C, # – D, ^ – IR, and + – D + IR. IS – initial state

ty 1.4-fold compared to the D + IR group ($p = 0.006$). The LDH activity in the D + IR group in the presence of G decreased insignificantly compared to D + IR rats ($p = 0.085$).

Respiration in saponin-skinned fibers

After 16 days into the experiment, no differences in the respiratory rate in states 2 and 3, the RC value, or the degree of functional relationship between mt-CK and OP were observed compared to the control group and the baseline (*Fig. 4*). A decrease in both V_2 and V_3 was observed in rats receiving STZ: by 28 and 60% compared to the control, respectively ($p < 0.05$ and $p < 0.001$, respectively). This resulted in a two-fold decrease in RC ($p < 0.001$). The degree of mt-CK functional activity in the DM animals, evaluated in the Cr test, decreased 1.6-fold compared to the control ($p < 0.001$). Similar changes in the mitochondrial respiratory function in the AAR were caused by

myocardial IRI. Average respiratory values did not differ significantly from those in the D group. The combined effect of STZ and IRI worsened respiration in states 2 and 3 compared to the DM rats ($p = 0.038$ and $p < 0.01$, respectively) and IRI animals ($p = 0.022$ and 0.004, respectively). This led to a decrease in RC compared to the groups D and IR ($p = 0.037$ and $p = 0.05$, respectively). The functional activity of mt-CK in the D + IR group was noticeably lower compared to the groups D and IR; however, the differences between the groups were statistically insignificant. Administration of peptide G to DM animals after regional myocardial ischemia increased the maximum ADP-stimulated state 3 and RC 2.3- and 1.6-fold, respectively, compared to the D + IR group ($p = 0.011$ and $p = 0.022$, respectively). The functional relationship between mt-CK and OP in the D + IRG group increased 2.4-fold compared to the D + IRG group. Representative respiratory protocols demonstrating

Table 3. Energy state of rat myocardium in the studied groups

Parameter	IS	C	D	IR	D + IR	D + IRG
ATP	20.16 ± 1.27	19.16 ± 1.56	14.53 ± 1.21*	10.34 ± 1.45*	8.11 ± 0.44*#	11.27 ± 1.04*+
ADP	5.47 ± 0.43	5.36 ± 0.53	4.93 ± 0.68	4.54 ± 0.51	4.98 ± 0.27	5.69 ± 0.34
AMP	1.03 ± 0.14	1.13 ± 0.24	1.02 ± 0.27	0.97 ± 0.14	1.75 ± 0.28^	2.20 ± 0.15*#^
ΣAN	26.66 ± 1.87	25.68 ± 1.90	20.43 ± 1.24*	15.86 ± 1.12*#	14.83 ± 1.02*#	18.68 ± 1.35*+
AEC	0.85 ± 0.01	0.85 ± 0.02	0.82 ± 0.01	0.79 ± 0.02	0.71 ± 0.01*#^	0.75 ± 0.01*#+
PCr	25.34 ± 1.98	25.29 ± 1.39	15.62 ± 0.95*	13.86 ± 2.02*	17.06 ± 1.54*	18.89 ± 1.25*
Cr	37.21 ± 2.77	34.98 ± 1.36	32.54 ± 2.77	31.54 ± 2.67	30.57 ± 1.47	34.42 ± 2.41
ΣCr	62.55 ± 2.15	60.27 ± 1.37	48.16 ± 2.03*	45.40 ± 2.33*	47.63 ± 0.74*	52.86 ± 1.26+^

Data are presented as M ± m ($n = 15$) and expressed for metabolites in μmol/g of dry weight.
IS – initial state. ΣAN = ATP + ADP + AMP; AEC = (ATP + 0.5ADP)/ΣAN; ΣCr = PCr + Cr.
$p < 0.05$ vs: * – C and IS, # – D, ^ – IR, + – D + IR.

changes in state 3 in the studied groups are presented in the Supplementary material (*Fig. S3*). The addition of 10 μM cytochrome *c* did not affect ADP-stimulated respiration in the D, D + IR, and D + IRG groups at the end of the experiment as compared to the control. The percentage ratio of $V_{cyt\ c}/V_{ADP}$ in these groups averaged 103.5 ± 1.9%, indicating the absence of damage to the outer mitochondrial membrane in the presence of STZ and under IR conditions.

Myocardium energy state
On day 16 of the experiment, the ATP, ADP, AMP, PCr, and Cr levels in LV in the control did not differ statistically significantly from their initial values (*Table 3*). A reliable decrease in the ATP, ΣAN, PCr, and SCr levels was noted in the DM animals compared to the controls ($p < 0.05$–0.001). Myocardial IRI had a stronger effect on ATP and ΣAN in the AAR: these parameters were decreased on average 1.3-fold compared to the controls ($p < 0.003$ and $p < 0.002$, respectively). STZ injection and subsequent regional IRI increased the loss of ATP and ΣAN in the AAR compared to the DM animals ($p = 0.001$ and $p = 0.008$, respectively). These changes in the adenine nucleotides content led to a decrease in the adenylate energy charge (AEC) of cardiomyocytes compared to the groups D and IR ($p < 0.01$ and $p < 0.001$, respectively). There were no significant changes in the PCr–Cr system in the AAR of the animals in the D + IR group compared to the groups D and IR. Administration of peptide G to DM animals at the beginning of reperfusion improved the energy state in the AAR by the end of reperfusion. This manifested itself in maintenance of higher ATP and ΣAN levels compared to the D + IR group (1.4- and 1.25-fold; $p = 0.023$ and $p = 0.04$, respectively) and a significantly higher cardiomyocyte adenylate energy charge (AEC) ($p = 0.022$). In the presence of peptide G, the ΣCr level in the AAR was higher than that in the D + IR group ($p = 0.007$) and did not differ significantly from the controls.

DISCUSSION
In addition to hyperglycemia and a lack of body weight gain, STZ-induced DM1 modeling was accompanied by depletion of high-energy phosphate reserves and a subsequent decrease in the myocardial ΣAN and ΣCr levels in the rats. The detected impairments of the myocardial energy supply were accompanied by a slump in the maximum ADP-stimulated oxygen consumption rate in state 3 and a decrease in mt-CK functional activity, as estimated in the Cr test. These changes in mitochondrial respiration are usually associated with a lower ATP production [19] and increased ROS generation [20]. The effect of STZ-induced DM was accompanied by an increase in the circulating levels of CK–MB and LDH, which indicates myocardial injury. Increased CK–MB and LDH activities in plasma were previously detected in STZ-induced diabetic cardiomyopathy models in laboratory animals [21] and DM patients [22]. Subsequent myocardial IRI in STZ-receiving rats exacerbated the necrotic damage to the LV (up to 25.6%) and significantly elevated the activity of both necrosis markers in the plasma compared to the DM animals. Necrotic death of cardiomyocytes in the AAR was accompanied by a deterioration of the mitochondrial respiratory function, greater losses of ATP and ΣAN compared to the DM rats, and a decrease in cardiomyocyte AEC by the end of reperfusion. It should be noted that the combined effect of STZ and IRI significantly increased the MI size, expressed as the MI/AAR ratio (%), compared to IRI alone.

In the present work, we demonstrated for the first time the protective effect of G administration at the beginning of reperfusion after a regional ischemia period in rats with DM1. G significantly reduced the MI size and plasma CK–MB activity in these rats compared to the D + IR animals. These effects can be also due to a reduction in mitochondrial dysfunction, as indicated by an increase in ADP-stimulated respiration in state 3, RC, and an improvement in functional coupling between mt-CK with OP. This resulted in an increase in the ATP, ΣAN and AAR of cardiomyocytes and improved ΣCr preservation in the AAR. Previously, we established the ability of G to reduce the myocardial reperfusion injury in rats *in situ*, which manifested itself in MI size reduction and a decrease in damage to the cardiomyocyte membrane [23]. This was due to a decreased production of ROS and LPP in reperfused myocardium. In the present study, excessive ROS and LPP production induced by diabetic hyperglycemia and subsequent regional myocardial IRI could have been the leading cause of mitochondrial dysfunction and necrotic cell death [24]. It is possible that the protective effect of G may have to do with its antioxidant properties: increased expression of the *SOD*, *CAT*, and *GSH-Px* genes encoding enzymes of the myocardial antioxidant defense system and/or the ability to intercept ROS and inhibit LPP [12, 23].

In addition to the regulation of free radical processes, activation of various G signaling pathways upon binding to GalR1-3 receptors can contribute to a reduction in cell damage [10]. This knowledge is of fundamental importance, since DM disrupts the intracellular signaling cascades that are activated by RISK kinases. These kinases are responsible for increased cell resistance to damage, primarily the PI3K/Akt signaling pathway [2, 3]. The main factors of G-activated intracellular signaling are presented in the Supplementary material (*Fig. S4*). The most physiologically significant factors induce a stimulation of the glucose uptake by cardiomyocytes, an inhibition of the proapoptotic proteins BAD/BAX, caspase-3, and caspase-9, inhibition of mitochondrial permeability transition pore (mPTP) opening, and an increase in the expression of peroxisome proliferator-activated receptors (PPAR). These adaptive mechanisms play a crucial role in reducing ATP production in DM and myocardial reperfusion [25]. A decrease in cardiomyocyte apoptosis in *in vivo* models is known to be accompanied by a reduction in the MI size and an improvement in cardiac contractile function [26]. Inhibition of mPTP opening promotes cell survival and motility [27], while PPARγ expression stimulates glucose uptake and oxidation by cardiomyocytes [28].
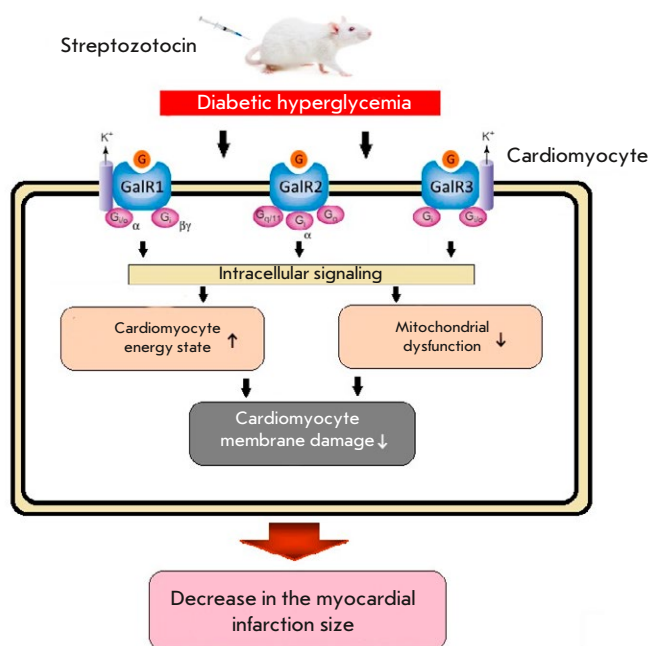

Fig. 5. Activation of intracellular G signaling during streptozotocin-induced hyperglycemia in rats reduces mitochondrial dysfunction, improves the myocardial energy state and reduces damage to cell membranes in the AAR of reperfused myocardium, thus reducing the MI size

The receptor nature of the action of G is also evidenced by the fact that GalR2 blockade with the selective antagonist M871 in myocardial IRI significantly weakens the G protective potential, increasing MI size and the plasma activity of necrosis markers [11]. It is important to note that the effect of full-length galanin, which binds to all GalR1-3 receptor subtypes, is reproduced by native and modified N-terminal G fragments, which possess a high affinity for GalR2 [10]. This suggests a potential role for GalR2 activation in the treatment and prevention of myocardial IRI in DM patients.

CONCLUSION

The present study confirms the effect of STZ-induced DM on myocardial susceptibility to IRI in rats. We showed that G administration significantly reduces MI upon reperfusion restoration. This benefit is due to the induction of intracellular signaling through the G-protein-coupled transmembrane receptors GalR1, GalR2, and GalR3 (*Fig. 5*). The protective effect of G manifested itself in less mitochondrial dysfunction, resulting in an improved energy state of the reperfused myocardial region. These positive shifts in the myocardial energy state were accompanied by a reduction in damage to the cell membrane. Taken to-

gether, the obtained results indicate that it is possible to use G as an accompanying therapy in DM1 complicated by myocardial IRI. In this regard, further study into the molecular mechanisms that reduce reperfusion stress in the diabetic myocardium using native and modified galanin peptides seems an important direction. ●

REFERENCES

1. Dia M., Paccalet A., Pillot B., Leon Ch., Ovize M., Claire C., Bochaton Th., Paillard M. // Front. Cardiovasc. Med. 2021. V. 8. P. 660698.
2. Lejay A., Fang F., John R., Thaveau F., Chakfe N., Geny B., Scholey J. // J. Mol. Cell. Cardiol. 2016. V. 91. P. 11–22.
3. Gao S., Wang R., Dong S., Wu J., Perek B., Xia Z., Yao Sh., Wang T. // Oxid. Med. Cell. Longev. 2021. P. 6657529.
4. Ding M., Lei J., Han H., Li W., Qu Y., Fu E., Fu F., Wang X. // Cardiovasc. Diabetol. 2015. V. 14. P. 143.
5. Li D., Huang B., Liu J., Li L., Li X. // PLoS One. 2013. V. 8. P. e73334.
6. Riquelme J.A., Westermeier F., Hall A.R., Vicencio J.M., Pedrozo Z., Ibacache M., Fuenzalida B., Sobrevia L., Davidson S.M., Yellon D.M., et al. // Pharmacol. Res. 2016. V. 103. P. 318–327.
7. Díaz-Cabiale Z., Parrado C., Narváez M., Millón C., Puigcerver A., Fuxe K., Narváez J.A. // EXS. 2010. V. 102. P. 113–131.
8. Lang R., Gundlach A.L., Holmes F.E., Hobson S.A., Wynick D., Hökfelt T., Kofler B. // Pharmacol. Rev. 2015. V. 67. P. 118–175.
9. Webling K.E., Runesson J., Bartfai T., Langel U. // Front. Endocrinol. 2012. V. 3. P. 146.
10. Pisarenko O.I., Studneva I.M., Veselova O.M. // Biochemistry (Moscow). 2021. V. 86. № 10. P. 1342–1351.
11. Serebryakova L., Veselova O., Studneva I., Dobrokhotov I., Palkeeva M., Avdeev D., Molokoedov A., Ovchinnikov M., Sidorova M., Pisarenko O. // Fundam. Clin. Pharmacol. 2022. V. 37. № 6. P. 1109–1118.
12. Pisarenko O.I., Studneva I.M., Serebryakova L.I., Timoshin A.A., Konovalova G.G., Lankin V.Z., Tihaze A.K., Veselova O.M., Dobrokhotov I.V., Sidorova M.V., et al. // Biochemistry (Moscow). 2021. V. 86. № 4. P. 496–505.
13. Veselova O., Studneva I., Dobrokhotov I., Pal'keeva M., Molokoedov A., Sidorova M., Pisarenko O. // Int. J. Peptide Res. Therap. 2022. V. 28. P. 103.
14. Sidorova M.V., Palkeev M.E., Avdeev D.V., Molokoedov A.S., Ovchinnikov M.V., Azmuko A.A., Serebryakova L.I., Veselova O.M., Studneva I.M., Pisarenko O.I. // Rus. J. Bioorg. Chem. 2020. V. 46. P. 32–42.
15. Chen H., Brahmbhatt S., Gupta A., Sharma A. // Cardiovasc. Diabetol. 2005. V. 4. P. 3.
16. Saks V.A., Veksler V.I., Kuznetsov A.V., Kay L., Sikk P., Tiivel T., Tranqui L., Olivares J., Winkler K., Wiedemann F., et al. // Mol. Cell. Biochem. 1998. V. 184. № 1–2. P. 81–100.
17. Kuznetsov A.V., Veksler V., Gellerich F.N., Saks V., Margreiter R., Kunz W.S. // Nat. Prot. 2008. V. 3. № 6. P. 965–976.
18. Bergmeyer H.U. Methods of enzymatic analysis. 4th edn. N.Y.: Acad. Press, 1974. pp. 1196–1200, 1475–1478, 1772–1776, 1777–1781, 2101–2110.
19. Avram V.F., Merce A.P., Hâncu I.M., Bătrân A.D., Kennedy G., Rosca M.G., Muntean D.M. // Int. J. Mol. Sci. 2022. V. 23. P. 8852.
20. Dominiak K., Jarmuszkiewicz W. // Antioxidants. 2021. V. 10. № 3. P. 533.
21. Huang E.J., Kuo W.W., Chen Y.J., Chen T.H., Chang M.H., Lu M.C., Tzang B.S., Hsu H.H., Huang C.Y., Lee S.D. // Clin. Chim. Acta. 2006. V. 366. P. 293–298.
22. Fuleshwor M., Pratik A., Deepak K. // Sciences. 2013. V. 3. P. 51–54.
23. Serebryakova L., Studneva I., Timoshin A., Veselova O., Pal'keeva M., Ovchinnikov M., Az'muko A., Molokoedov A., Sidorova M., Pisarenko O. // Inter. J. Pept. Res. Ther. 2021. V. 27. P. 2039–2048.
24. Münzel T., Camici G.G., Maack C., Bonetti N., Fuster V., Kovacic J.// J. Am. Coll. Cardiol. 2017. V. 70. P. 212–229.
25. Tian R., Abel E.D. // Circulation. 2001. V. 103. P. 2961–2966.
26. Krijnen P.A., Nijmeijer R., Meijer C.J., Visser C.A., Hack C.E., Niessen H.W.M. // J. Clin. Pathol. 2002. V. 55. P. 801–811.
27. Hausenloy D.J., Yellon D.M. // J. Clin. Invest. 2013. V. 203. P. 123.
28. Jay M.A., Ren J. // Curr. Diab. Rev. 2007. V. 3. P. 33–39.

Combination with a Low Dose of Doxorubicin Further Boosts the Antitumor Effect of SLURP-1 *In Vivo* and Associates with EGFR Down-Regulation

O. V. Shlepova[1], M. L. Bychkov[1], V. O. Shipunova[1,2], E. I. Shramova[1], M. A. Shulepko[3], T. Y. Gornostaeva[1,2], E. A. Kiseleva[1,2], I. D. Kukushkin[1,2], V. A. Kazakov[4], E. A. Tukhovskaya[4], I. A. Dyachenko[4], A. N. Murashev[4], Z. O. Shenkarev[1,2], S. M. Deyev[1,5,6], M. P. Kirpichnikov[1,7], E. N. Lyukmanova[1,2,3,7*]

[1]Shemyakin-Ovchinnikov Institute of Bioorganic Chemistry, Russian Academy of Sciences, Moscow, 117997 Russian Federation
[2]Moscow Center for Advanced Studies, Moscow, 123592 Russian Federation
[3]Faculty of Biology, MSU-BIT Shenzhen University, Shenzhen, 518172 China
[4]Branch of Shemyakin-Ovchinnikov Institute of Bioorganic Chemistry RAS, Pushchino, 142290 Russian Federation
[5]Biomarker Research Laboratory, Institute of Fundamental Medicine and Biology, Kazan Federal University, Kazan, 420008 Russian Federation
[6]National Research Ogarev Mordovia State University, Republic of Mordovia, Saransk, 430005 Russian Federation
[7]Interdisciplinary Scientific and Educational School of Moscow University "Molecular Technologies of the Living Systems and Synthetic Biology", Faculty of Biology, Lomonosov Moscow State University, Moscow, 119234 Russian Federation
*E-mail: lyukmanova_ekaterina@smbu.edu.cn

ABSTRACT Skin cancers such as squamous cell carcinoma (SCC) are among the most aggressive types of tumors. They come with a high rate of growth, metastasis, and frequently occurring chemoresistance. Smoking is one of the risk factors for SCC progression, and the α7 nicotinic acetylcholine receptor (α7-nAChR) is a promising target for SCC therapy. Human secreted protein SLURP-1 is an auto/paracrine regulator of epithelial homeostasis and a selective negative allosteric modulator of α7-nAChR. Recently, we demonstrated the high efficiency of the therapy based on the recombinant SLURP-1 in controlling SCC cell growth and metastasis *in vivo*. The anti-tumor effect of SLURP-1 was mediated through interaction with both α7-nAChR and the epidermal growth factor receptor (EGFR). Cytotoxic antibiotic doxorubicin has been proposed for the SCC therapy; however, its use is limited due to the high toxicity. In this study we investigated the use of an enhanced SLURP-1 dose and of a combination of SLURP-1 with low-dozen doxorubicin for SCC treatment of mice xenografted with squamous cell carcinoma A431 cells. An increased SLURP-1 dose didn't significantly enhance the efficiency of the therapy. However, the combination with doxorubicin further enhanced the anti-tumor activity of SLURP-1 and dramatically suppressed metastasis. The effect from the combined therapy was accompanied by down-regulation of EGFR expression in tumors. Direct inhibition of EGFR activation by SLURP-1 was shown. No toxicity of the combined therapy was encountered. Our data indicate that the combination of SLURP-1 with chemotherapy in lower doses is a promising approach in SCC treatment and should be further studied.

KEYWORDS cancer, chemotherapy, SLURP-1, Ly6/uPAR, α7-nAChR, EGFR.

ABBREVIATIONS AKT – protein kinase B; EGF – epidermal growth factor; EGFR – epidermal growth factor receptor; nAChR – nicotinic acetylcholine receptors; PI3K – phosphoinositide 3-kinase; SCC – squamous cell carcinoma; Src – non-receptor tyrosine kinase Src; STAT3 – signal transducer and activator of transcription 3.

INTRODUCTION

Skin cancer, particularly squamous cell carcinoma (SCC), is one of the most aggressive types of tumors, as its incidence, morbidity, and mortality rates continue to increase worldwide [1]. The major obstacles in the treatment of SCC are the inability to achieve a complete surgical removal of the tumor, tumor metastasis, and the development of resistance to chemotherapeutic agents [1–4]. Smoking is one of the risk factors for SCC progression [5], and nicotinic acetylcholine receptors (nAChRs) activated upon tobacco consumption are promising targets for SCC therapy. nAChR of α7 type (α7-nAChR) is well known as a tumor growth promoter [6–9]. The expression of α7-nAChR is increased in cancer cells compared to normal cells [10], and it correlates with a poor prognosis [11, 12]. Activation of α7-nAChR promotes the proliferation, angiogenesis, migration, and invasion of carcinoma and glioma cells [8, 12–19]. In cancer cells, α7-nAChR can form heteromeric complexes with another prooncogenic receptor: the epidermal growth factor receptor (EGFR) [20–23]. Moreover, activation of α7-nAChR in SCC by nicotine promotes chemoresistance and metastasis via the transactivation of EGFR [24].

Some endogenous human proteins of the Ly6/uPAR family [25] modulate the α7-nAChR activity and can be considered prototypes for tumor-selective and nontoxic targeted anticancer drugs. The human secreted protein SLURP-1 is one of such α7-nAChR modulators [26] and an auto/paracrine regulator of epithelial homeostasis [27]. SLURP-1 expression is down-regulated in primary and metastatic melanoma compared to normal cells [28, 29], while an elevated plasma level of SLURP-1 correlates with a better chance of survival for patients with pancreatic cancer [30]. A recombinant analogue of SLURP-1 inhibits cancer cell growth *in vitro* and *in vivo* [21, 22, 30–35], as well as abolishes nicotine-induced cell proliferation [36]. Its anti-tumor effect *in vivo* in the SCC model (A431 xenografts) is mediated by an interaction with both α7-nAChR and EGFR [22].

Doxorubicin (a DNA-intercalating anthracycline antibiotic that also inhibits EGFR signaling [37, 38]) has been proposed for SCC therapy [39], because it appears to exert a complex, antiproliferative effect by inhibiting the transcription of oncogenes and generating free radicals [40]. However, its use in therapy is severely limited by its high toxicity [41]. Thus, a reduced dose of doxorubicin can be a good way to counteract its possible side effects.

Here, we propose using lowered concentrations of doxorubicin in combination with SLURP-1. We investigated whether a combination of low-dose SLURP-1 and doxorubicin could be used to control the growth and metastasis of SCC cells *in vivo*. Beside the high efficiency of the proposed therapy, a decreased EGFR expression in tumors of mice treated with SLURP-1 and doxorubicin was revealed. The data obtained indicate the high potential of the proposed approach.

EXPERIMENTAL

Materials and animals

Recombinant SLURP-1 was produced in *E. coli* as previously described [31, 42].

Doxorubicin was provided by TEVA (Tel Aviv-Yafo, Israel).

The animals were bred and housed under the standard conditions of the Animal Breeding Facility, BIBCh, RAS, accredited at the international level by AAALACi. All procedures were performed in accordance with the ethical recommendations of Rus-LASA approved by the Institutional Animal Care and Use Committee of IBCh, RAS (protocol # 318/2021).

Cell cultivation and migration analysis by scratch assay

Human squamous cell carcinoma A431 cells (ATCC, Manassas, VA, USA) were grown (37°C, 5% CO_2) in a DME medium (PanEco, Russia), 10% fetal calf serum (Thermo Fisher Scientific, USA), abbreviated as the complete medium. The cells were subcultured at least twice per week.

Cell migration was measured by a scratch assay as described earlier [21, 43]. Images were obtained using CloneSelect Imager (Molecular Devices, United States), and the scratch area occupied by migrating cells was quantified using ImageJ (NIH, United States). Data were normalized to the average area occupied by migrated cells in the control wells and approximated with a Hill equation.

Tumor xenograft model, treatment strategy, and living mice imaging

To obtain the luminescent A431/NanoLuc cells, the parental A431 cells were transfected with the NanoLuc plasmid as described in [44] using the FuGENE HD transfection reagent (Promega, USA).

Male BALB/c Nu/Nu mice (22–25 g) were engrafted subcutaneously on the back with 10^7 A431/NanoLuc cells in 100 μL of 30% Matrigel (Corning, USA) in the complete medium. On the 3rd day after A431/NanoLuc cells engraftment, the mice were randomly divided into five groups (initially n = 8–10, *Table S1*), and i.v. injected once a day for the ten subsequent days with 100 μL of a 0.9% NaCl solution (saline) containing: 1) no additives – control, 2) 100 μg of SLURP-1 (final body concentration 5 mg/kg), 3) 10 μg of SLURP-1 (final

body concentration 0.5 mg/kg), 4) 50 μg of doxorubicin (2.5 mg/kg), 5) 5 μg of doxorubicin (final body concentration 0.25 mg/kg) with 10 μg of SLURP-1 (final body concentration 0.5 mg/kg) (*Fig. 1A*). Some animals died during the experiment (*Table S1* and *Fig. S1*) and were excluded from the analysis.

The primary tumor volume was measured with a caliper and calculated using the formula

$$V = 0.52 \times A \times B^2$$

(*A* is the largest diameter and *B* is the smallest diameter).

On the 3rd, 13th, and 23rd days after tumor engraftment, tumors were visualized with the IVIS Spectrum CT imaging system (Perkin Elmer, USA) as described earlier [22]. Bioluminescence images were acquired using a IS1803N7357 iKon camera (Andor, Belfast, UK) and normalized to photons per second per cm² per steradian (p/sec/cm²/sr) and analyzed using the Living Image 4.5.5.19626 software (Xenogen, USA).

On the 24th day after tumor engraftment, the mice were euthanized by cervical dislocation, and the tumors were isolated with a scalpel and forceps and immediately frozen at −150°C for further analysis. The lungs, liver, kidneys, spleen, and heart were removed from the euthanized mice with a scalpel and forceps and placed in a 4% paraformaldehyde solution (Applichem, Spain).

Western blotting
To assess the influence of SLURP-1 and doxorubicin on EGFR expression, the tumors (0.05 mg per sample) were homogenized, solubilized in 2% Triton X-100, and diluted in non-reducing PAGE buffer. Western blotting was performed with primary antibodies (sc-120, Santa Cruz, USA, 1 : 1 000) and secondary antibodies (715-035-150, Jackson Immoresearch, USA, 1 : 5 000) for EGFR detection. The HRP signal was detected with the ECL substrate (Bio-Rad, USA) using an ImageQuant LAS 500 chemidocumenter (GE Healthcare, USA). Data were processed using the ImageJ 1.53t software (NIH, USA).

In-cell ELISA
To study the effect of SLURP-1 on EGFR activation, A431 cells were seeded in 96-well culture plates (1×10^4 cells/well). After 24 h the culture medium was replaced with a serum-free medium, and after another 24 h the culture medium was changed to ones containing SLURP-1 at various concentrations. Preincubation with SLURP-1 was performed for 30 min. After that, EGFR activation was stimulated by the addition of 25 nM EGF to the cells, which

were incubated for another 3 h at 37°C, 5% CO_2. The cells were fixed with a 4% paraformaldehyde solution in PBS, blocked with PBS buffer containing 2% BSA and 0.1% Triton X-100, and incubated with primary antibodies against p-EGFR(Y1173) (ABIN343717, antibodies-online, 1 : 1 000) and with secondary antibodies (715-035-150, Jackson Immunoresearch, West Grove, PA, USA, 1 : 5 000). Next, 50 μL of a TMB solution was added to the wells. The reaction was stopped with a 2M H_2SO_4 solution, and the absorbance in the wells was determined at 450 nm using a AMR-100 plate reader (Allsheng, China).

Histochemistry
For the histochemical analysis, samples of the lung, liver, kidney, spleen, and heart from three randomly selected mice from each group that had received saline (control), SLURP-1 (5 mg/kg), doxorubicin (2.5 mg/kg), or SLURP-1 (0.5 mg/kg) + doxorubicin (0.25 mg/kg) were fixed in a 10% neutral formaldehyde solution in PBS buffer, washed in running tap water, dehydrated in graded alcohols, and embedded in paraffin. The 4- to 5-μm-thick Paraffin sections stained with hematoxylin and eosin were examined with a conventional light AxioScope.A1 microscope (Carl Zeiss, Germany). Microphotographs of the histologic preparations were taken with the high-resolution camera Axiocam 305 color (Carl Zeiss) equipped with the ZEN 2.6 lite software (Carl Zeiss) at ×200 magnification.

Statistical Analysis
Data are presented as a mean ± SEM. The number of samples (n) is indicated in the figure legends. The statistical analysis was performed using the GraphPad Prism 9.5.0 software (Graphpad software, USA). The data were analyzed for a normal distribution using the Shapiro-Wilk omnibus normality test. For nonparametric data, the Kruskal-Wallis test was used, instead of the one-way ANOVA test. The analysis was performed using the unpaired t-test; the Kruskal-Wallis test, followed by Dunn's post hoc test; one-way ANOVA, followed by Dunnett's or Tukey's post hoc test; one-way Welch ANOVA, followed by Dunnet's post hoc test; and two-way ANOVA, followed by Dunnett's post hoc test as indicated in the figure legends. Differences between groups were considered statistically significant at $p < 0.05$.

RESULTS

An increased dose of SLURP-1 doesn't increase the therapeutic efficiency *in vivo*
In this work we compared two doses of the protein: we used the 0.5 mg/kg used in [22] and the ten
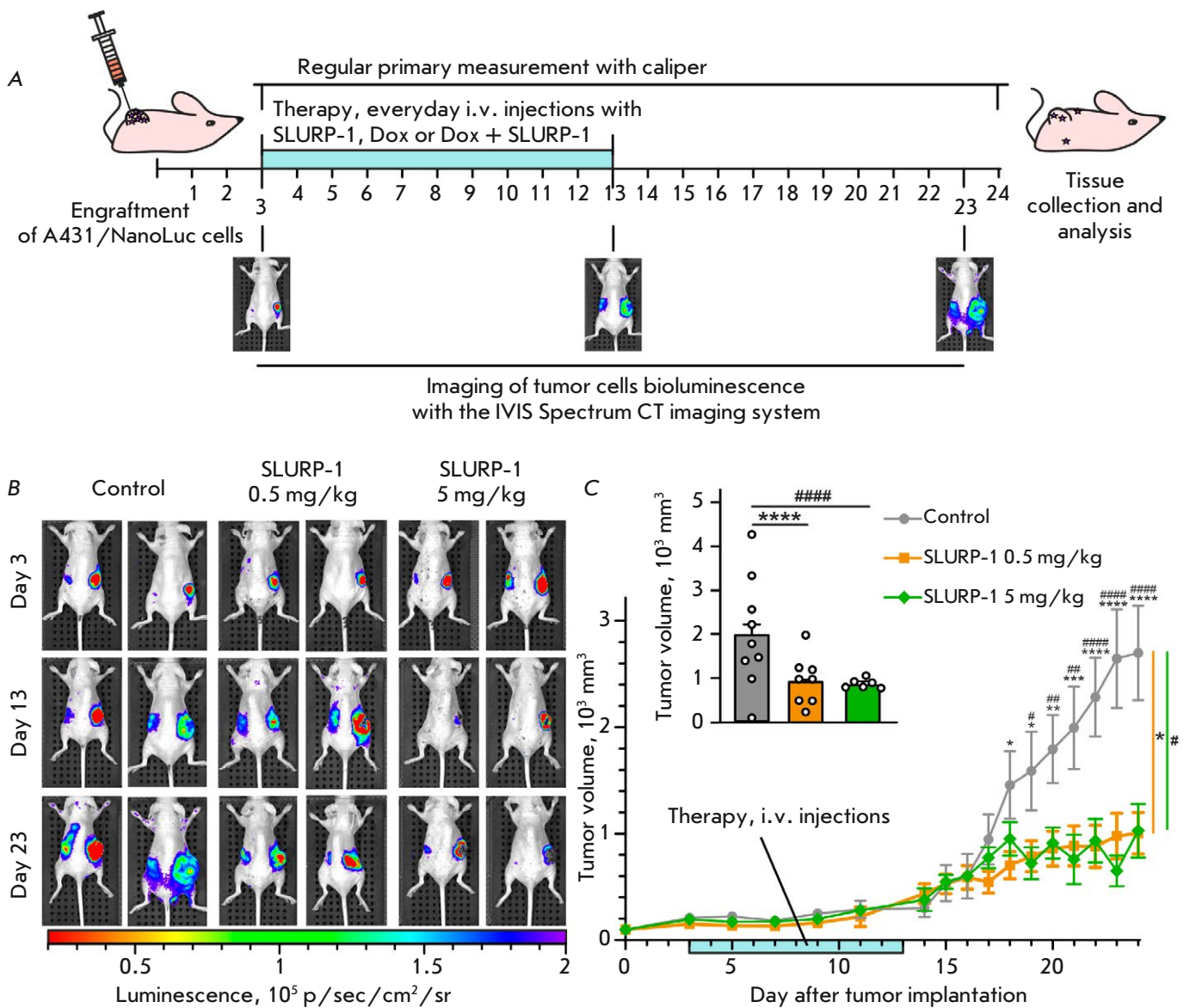
Fig. 1. The influence of different SLURP-1 doses on tumor growth in the A431/NanoLuc mice xenograft model.
(*A*) Scheme of drugs administration and tumor growth measurements.
(*B*) Representative images of tumor bioluminescence (A431/NanoLuc cells) before treatment (the 3rd day after tumor engraftment, the 1st day of the therapy), after treatment (the 13th day after tumor engraftment, the next day after end of the 10-day therapy course), and before sacrification (the 23rd day after tumor engraftment). See *Fig. S1* for all mice images.
(*C*) The primary tumor volume measurements with a caliper. Data presented as mm³ ± SEM. *($p < 0.05$),
($p < 0.01$), *($p < 0.001$), and ****($p < 0.0001$) indicate a significant difference between the Control (saline) and
(0.5 mg/kg SLURP-1) groups; #($p < 0.05$), ##($p < 0.01$), and ####($p < 0.0001$) indicate a significant difference
between the Control and (5 mg/kg SLURP-1) groups according to the two-way ANOVA, followed by Dunnett's post
hoc test. The days of treatment are marked with a light blue bar; (*C*, insert). The average primary tumor volume measured with a caliper for each mouse in the last 5 days (20–24 days after tumor engraftment). Data are presented as mm³
± SEM. ****($p < 0.0001$) and #### ($p < 0.0001$) indicate the significant difference between the Control and groups
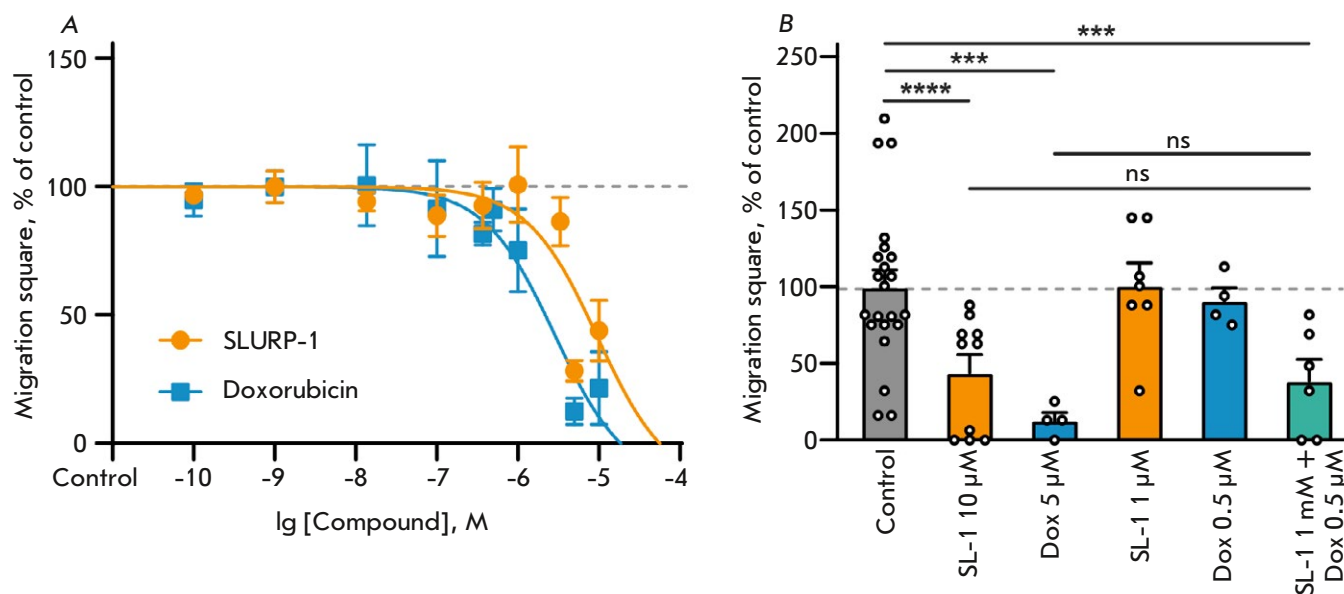according to one-way ANOVA followed by Tukey's post hoc test

Fig. 2. The influence of different SLURP-1 and doxorubicin doses on A431 cells migration.
(*A*) Effect of different SLURP-1 and doxorubicin concentrations on cell migration. Data are presented as the mean scratch surface occupied by migrating cells (% normalized to the control), ± SEM, $n = 3$–22. The data obtained was approximated using a Hill equation. The Control level (100%) is shown with a dashed line.
(*B*) Effect of SLURP-1 (SL-1) and doxorubicin (Dox) and their combination on cell migration. Data are presented as the mean scratch surface occupied by migrating cells (% normalized to control), ± SEM, $n = 3$–22; Control level (100%) is shown by dashed line. ***($p < 0.001$), and ****($p < 0.0001$) indicate a significant difference from the control group (untreated cells) by one-way ANOVA followed by Dunnett's post hoc test, "ns" means no significant difference between the groups

times higher 5 mg/kg dose in the same xenograft mouse model of human epidermoid carcinoma used as described previously [22]. Surprisingly, the effect of the higher dose of SLURP-1 did not differ from that achieved with the lower dose (*Fig. 1B,C*). The 0.5 mg/kg and 5 mg/kg doses of SLURP-1 both inhibited primary tumor growth (*Fig. 1A–C, S1*) with similar efficacy, with a ~ 3-fold reduction in the primary tumor volume compared to the control (*Fig. 1C*, insert). Thus, the experiment demonstrated that the effect of SLURP-1 hit a ceiling and could not be enhanced by increasing the dose.

Low doses of the SLURP-1 /doxorubicin combination have an additive antimigratory effect *in vitro*
Previously, using multicellular spheroids reconstituted from A549 and A431 cells, we observed the additive antiproliferative effect of doxorubicin (a widely used cancer chemotherapy drug [45]) and SLURP-1 *in vitro* [46]. Here, we observed a strong dose-dependent reduction of cell migration after 24 h incubation with SLURP-1 or doxorubicin with EC_{50} 9.4 ± 7.8 μM and 2.3 ± 1.7 μM, respectively (*Fig. 2A,B,*

Table S2). Notably, 10 μM of SLURP-1 is equivalent to the 5 mg/kg dose used *in vivo*, and 5 μM of doxorubicin is equivalent to 2.5 mg/kg (equivalent to the 25 mg/kg cumulative dose (75 mg/m²) recommended for one cycle of solid tumor therapy (60 mg/m²) [47]). The combination of 1 μM SLURP-1 and 0.5 μM doxorubicin resulted in robust cell migration inhibition compared to the effects of 10 μM of SLURP-1 or 5 μM doxorubicin taken alone (*Fig. 1B*). Thus, the combination of low doses of SLURP-1 and doxorubicin has an additive effect on A431 cell migration.

Combination with low-dose doxorubicin increases the antitumor activity of SLURP-1 *in vivo*
Next, we showed that the combination of 0.5 mg/kg SLURP-1 (1 μM *in vitro*) with 0.25 mg/kg of doxorubicin (0.5 μM *in vitro*) reduced primary tumor growth more efficiently than the application of a high dose of SLURP-1 taken alone (*Fig. 3A,B,C*). Moreover, combined usage of SLURP-1 with low-dose doxorubicin significantly suppressed metastasis, while treatment with SLURP-1 (5 mg/kg) or doxorubicin (2.5 mg/kg) alone failed to have any impact on metastasis (*Fig. 3A,B,D* and *Fig. S1*). Thus, it's reasonable
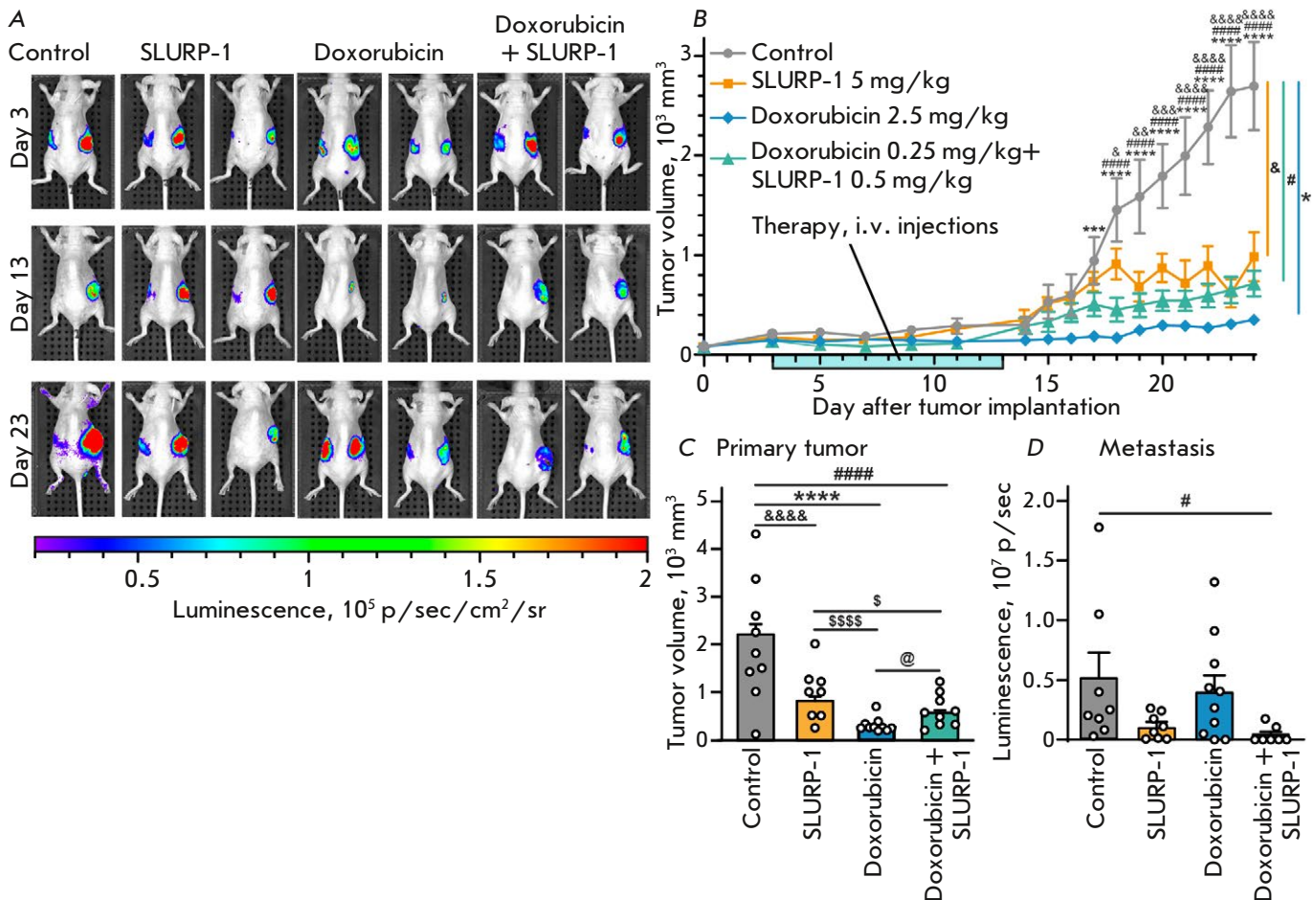
Fig. 3. The influence of SLURP-1, doxorubicin, and their combination on tumor growth and metastasis in a A431/NanoLuc mice xenograft model.
(*A*) Representative images of tumor bioluminescence (A431/NanoLuc cells) before treatment (the 3rd day after tumor engraftment, the 1st day of therapy), after treatment (the 13th day after tumor engraftment, the next day after conclusion of the 10-day therapy), and before sacrifice (the 23rd day after tumor engraftment). See *Fig. S1* for all mice images.
(*B*) The primary tumor volume measurements with a caliper. Data are presented as mm³ ± SEM. **(*p* < 0.01) and ****(*p* < 0.0001) indicate a significant difference between the Control (saline) and (2.5 mg/kg doxorubicin) groups; #### (*p* < 0.0001) indicates a significant difference between the Control and (0.5 mg/kg SLURP-1 + 0.25 mg/kg doxorubicin) groups; &(*p* < 0.05), &&(*p* < 0.01), &&&(*p* < 0.001), and &&&&(*p* < 0.0001) indicate a significant difference between the Control and (5 mg/kg SLURP-1) groups according to two-way ANOVA followed by Dunnett's post hoc test. The days of treatment are marked with a light blue bar.
(*C*) The average primary tumor volume measured with a caliper for each mouse for the last 5 days (20–24 days after tumor engraftment). Data presented as mm³ ± SEM. ****(*p* < 0.0001) indicates a significant difference between the Control and (2.5 mg/kg doxorubicin) groups; #### (*p* < 0.0001) indicates a significant difference between the Control and (0.5 mg/kg SLURP-1 + 0.25 mg/kg doxorubicin) groups; &&&&(*p* < 0.001) indicates a significant difference between the Control and (5 mg/kg SLURP-1) groups; $(*p* < 0.05) indicates a significant difference from the (5 mg/kg SLURP-1) group; and @(*p* < 0.05) indicates a significant difference between the (2.5 mg/kg doxorubicin) and (0.5 mg/kg SLURP-1 + 0.25 mg/kg doxorubicin) groups according to one-way ANOVA followed by Tukey's post hoc test.
(*D*) Total luminescence measured in the areas outside of the primary tumor. Data are presented as photons per second (p/sec) ± SEM. #(*p* < 0.05) indicates a significant difference from the Control (saline) group according to the Kruskal-Wallis followed by Dunn's post hoc test
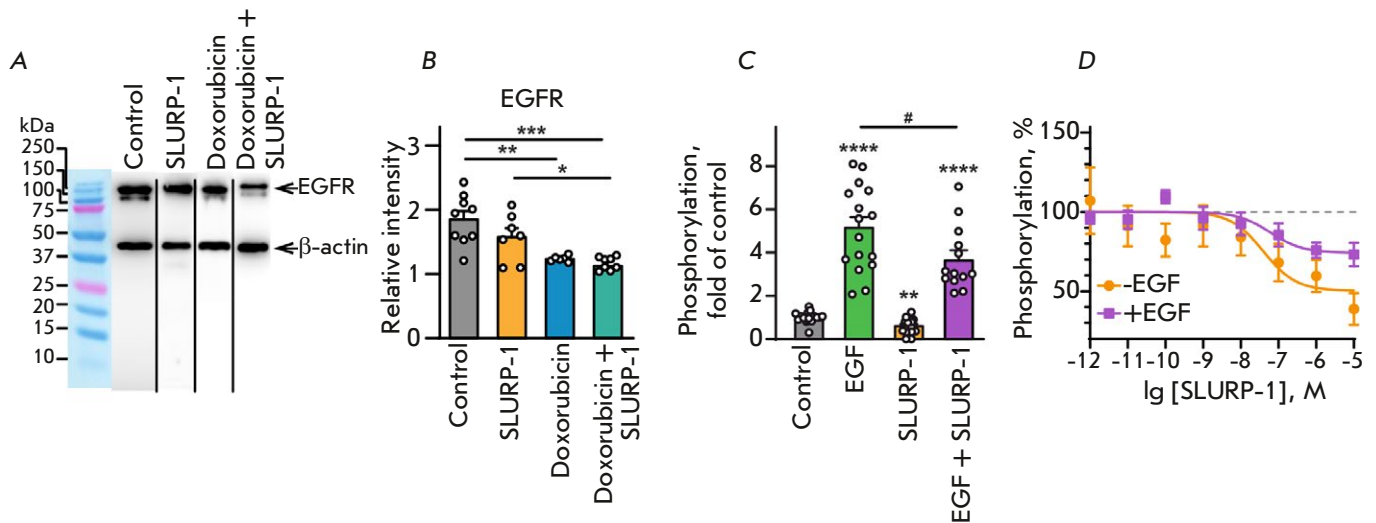
Fig. 4. The effect of SLURP-1 on EGFR expression and activation.
(*A*) Representative Western blot membrane analysis of the EGFR expression in tumors after treatment with saline (control), SLURP-1 (5 mg/kg), doxorubicin (2.5 mg/kg), or SLURP-1 (0.5 mg/kg) + doxorubicin (0.25 mg/kg). Whole membranes are shown in Fig. S2. The samples shown were run on different membranes in parallel.
(*B*) The expression level of EGFR was normalized to the β-actin expression level. Data are presented as the relative intensity ± SEM ($n = 6–9$). **($p < 0.01$), ***($p < 0.001$), and ****($p < 0.0001$) indicate significant differences between the groups per one-way ANOVA followed by Tukey's post hoc test.
(*C*) The effect of 1 μM SLURP-1, 25 nM EGF alone, and their mix on EGFR activation by autophosphorylation at Y1173 in A431 cells. Data are presented as fold of control (untreated cells) ± SEM ($n = 13–17$). **($p < 0.01$) and ****($p < 0.0001$) indicate significant differences from Control according to one-way Welch ANOVA followed by Dunnet's post hoc test. # ($p < 0.05$) indicates significant differences between the groups per the unpaired t-test.
(*D*) The effect of different concentrations of SLURP-1 on EGFR activation in the absence and presence of EGF ($n = 10–14$). Data are presented as % of the Control ± SEM. The data obtained was approximated using a Hill equation

to conclude that SLURP-1 is a perspective anticancer agent for combination therapy in which the dose of the toxic chemotherapeutic agent can be reduced.

The combination of SLURP-1 with doxorubicin suppresses EGFR expression in tumors *in vivo*
EGFR, the best known pro-oncogenic receptor [23], is overexpressed in squamous cell carcinoma A431 cells [48]. In this work, we showed that therapy with either doxorubicin alone (2.5 mg/kg) or in combination with SLURP-1 and doxorubicin (0.25 mg/kg doxorubicin + 0.5 mg/kg SLURP-1) results in a significant decrease in the EGFR expression in xenografted A431 tumors (*Fig. 4A,B*).

SLURP-1 affects the activation of EGFR
SLURP-1 dampened the Y1173 autophosphorylation of EGFR expressed in A431 cells. Moreover, a decreased EGF-induced phosphorylation of EGFR was observed in the presence of SLURP-1 (*Fig. 4C,D, Table S3*). These effects demonstrated a dose-concentration dependence with similar $EC_{50} \sim 40 \pm 11$ nM

and 60 ± 17 nM, respectively, with a significant difference in the maximum effect ($50 \pm 9\%$ and $74 \pm 5\%$, respectively). The same efficiency in the inhibition of EGFR activation with a changed amplitude of the effect (*Fig. 4D, Table S3*) points to the rather different binding sites of EGF and SLURP-1 on the surface of the EGFR molecule.

Combined SLURP-1 and doxorubicin administration showed no toxicity *in vivo*
To study the potential toxicity of the investigated drugs, organs from mice (three randomly selected mice from each group) were harvested and tests were run for pathological changes. No lung, liver, spleen, kidney, or liver of any animals from any of the groups showed any significant abnormalities that could be attributed to toxicity (*Fig. S3*). At the same time, foci of cardiomyocyte necrosis were found in the hearts of two animals that had received 2.5 mg/kg doxorubicin (*Fig. 5*). Thus, we could conclude that combined therapy with low doses of SLURP-1 and doxorubicin is safer than the use of high doses of doxorubicin alone.
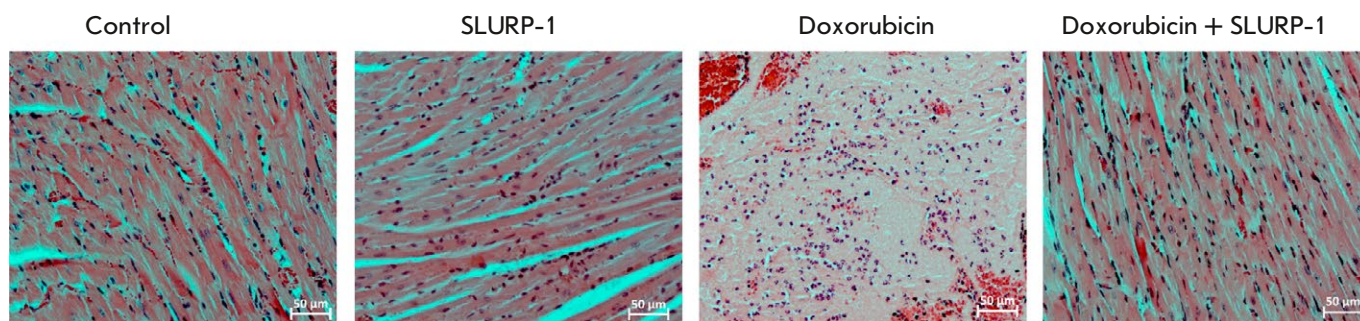
Fig. 5. Cardiotoxicity of the SLURP-1 and doxorubicin treatment. Heart fragments of mice treated with saline (control), SLURP-1 (5 mg/kg), doxorubicin (2.5 mg/kg), and SLURP-1 (0.5 mg/kg) + doxorubicin (0.25 mg/kg). Extensive focus of cardiomyocyte necrosis with neutrophil infiltration in the heart of mouse from the doxorubicin group was revealed. Hematoxylin and eosin staining, magnification ×200

DISCUSSION

Despite its severe adverse effects, chemotherapy remains the main choice for cancer treatment [49]. One of the most popular chemotherapeutic agents is doxorubicin, which exhibits high antitumor efficacy but also is highly toxic [40, 50]. The toxicity increases with cumulative doses and patient age, which limits the scope of use of the drug [41, 50–54]. Several studies have proposed therapies featuring a combination of chemotherapy with other approaches to lower the dose of chemotherapy and ease its side effects [55, 56]. Inhibition of α7-nAChR can be considered a promising approach on the road to combined cancer therapy, as it can help reduce tumor progression, metastasis, chemoresistance, and the side effects of chemotherapy [19, 25, 57–61]. The human secreted protein SLURP-1 negatively modulates the α7-nAChR function [26] and exhibits antitumor activity *in vivo* [22]. Here, we proposed two approaches to improve the efficacy of SLURP-1-based therapy: (1) increasing the dose of SLURP-1 as a monotherapy and (2) a combination of SLURP-1 with doxorubicin.

In keeping with our previous data, SLURP-1 alone was shown to inhibit tumor growth *in vivo*, while a 10-fold increase in the SLURP-1 dose failed to improve the outcome (*Fig. 1*). By testing the second approach, it was shown that low concentrations of SLURP-1 and doxorubicin have an additive antimigratory effect *in vitro* (*Fig. 2B*), as well as anti-tumor and anti-metastastatic effects *in vivo* (*Fig. 3E,F*). Previously, it had been shown through immunogenicity and toxicity tests that SLURP-1 upon intravenous treatment was highly safe [22]. In contrast to SLURP-1, doxorubicin demonstrated elevated cardiotoxicity in mice (*Fig. 5*) at the concentration usu-

ally used in clinics [47]. At the same time, a 10-time decrease in the doxorubicin concentration, in combination with SLURP-1, showed no cardiotoxic effects (*Fig. 5*). Thus, the use of low doses of doxorubicin, in combination with SLURP-1 or other inhibitors of α7-nAChR, could be a positive development in antitumor therapy.

The exact molecular mechanisms underlying the combined effect of SLURP-1 and doxorubicin on A431 tumor growth remain unknown. One of the explanations can be a joint inactivation of the EGFR overexpressed in A431 cells [62] by both agents. Indeed, doxorubicin alone, and in combination with SLURP-1, suppresses the expression of this receptor in tumors (*Fig. 4A,B*). EGFR mediates the growth, migration and survival of cancer cells [63]. SLURP-1 cancels the EGF-induced activation of the receptor (*Fig. 4C,D*) by interacting with the α7-nAChR/EGFR complex in A549 and A431 cells [21, 22], and doxorubicin likewise affects the EGFR signaling pathways [38]. On the other hand, the observed orchestra-like interaction between SLURP-1 and doxorubicin can be a result of the inhibition of the complementary intracellular signaling mechanisms. Indeed, overexpression of Src [64], activation of the STAT3 [65] and PI3K/AKT [66] pathways all lead to the stimulation of EGFR activity and expression in cancer cells. In line, incubation with SLURP-1 leads to inhibition of these signaling pathways in A431 cells [22]. On the other hand, the anti-tumor effect of doxorubicin is mediated by the reorganization of lipid rafts via the EGFR/Src signaling [38]. Thus, the enhanced combined effect of SLURP-1 and doxorubicin could be a result of synergy between the effects of each compound on the signaling pathways regulating the EGFR expression and activation.

CONCLUSION

Combination with low-dose doxorubicin enhances the SLURP-1 anti-tumor activity and dramatically suppresses tumor metastasis. The enhanced effect could be associated with down-regulation of EGFR in tumors at the expression and activation levels by both drugs. Thus, combined therapy of tumors, in particularly SCC, by SLURP-1 with low doses of chemotherapeutic agents looks promising and requires further study. ●

REFERENCES
1. Khan N.H., Mir M., Qian L., Baloch M., Ali Khan M.F., Rehman A.-U., Ngowi E.E., Wu D-D., Ji X.-Y. // J. Adv. Res. 2022. V. 36. P. 223–247.
2. Burns C., Kubicki S., Nguyen Q.-B., Aboul-Fettouh N., Wilmas K.M., Chen O.M., Doan H.Q., Silapunt S., Migden M.R. // Cancers. 2022. V. 14. № 15. P. 3653.
3. Winge M.C.G., Kellman L.N., Guo K., Tang J.Y., Swetter S.M., Aasi S.Z., Sarin K.Y., Chang A.L.S., Khavari P.A. // Nat. Rev. Cancer. 2023. V. 23. № 7. P. 430–449.
4. Sharma A., Sharma U., Jagannathan N.R., Ray R., Rajeswari M.R. // Cancer Invest. 2019. V. 37. № 8. P. 339–354.
5. Arafa A., Mostafa A., Navarini A.A., Dong J.-Y. // Cancer Causes Control CCC. 2020. V. 31. № 8. P. 787–794.
6. Grando S.A. // Nat. Rev. Cancer. 2014. V. 14. № 6. P. 419–429.
7. Schaal C., Chellappan S.P. // Mol. Cancer Res. 2014. V. 12. № 1. P. 14–23.
8. Wang S., Hu Y. // Oncol. Lett. 2018. V. 16. № 2. P. 1375–1382.
9. Hollenhorst M.I., Krasteva-Christ G. // Mol. Basel Switz. 2021. V. 26. № 20. P. 6097.
10. Li L., Chen H., Chang H. // J. Clin. Med. 2019. V. 8. № 9. P. 1391.
11. Bordas A., Cedillo J.L., Arnalich F., Esteban-Rodriguez I., Guerra-Pastrián L., de Castro J., Martín-Sánchez C., Atienza G., Fernández-Capitan C., Rios J.J., et al. // Oncotarget. 2017. V. 8. № 40. P. 67878–67890.
12. Cheng W.-L., Chen K.-Y., Lee K.-Y., Feng P.-H., Wu S.-M. // J. Cancer. 2020. V. 11. № 5. P. 1125–1140.
13. Dasgupta P., Rizwani W., Pillai S., Kinkade R., Kovacs M., Rastogi S., Banerjee S., Carless M., Kim E., Coppola D., et al. // Int. J. Cancer. 2009. V. 124. № 1. P. 36–45.
14. Li C.-L., Lin Y.-K., Chen H.-A., Huang C.-Y., Huang M.-T., Chang Y.-J. // J. Clin. Med. 2019. V. 8. № 9.P. 1391.
15. Tu C.-C., Huang C.-Y., Cheng W.-L., Hung C.-S., Uyanga B., Wei P.-L., Chang Y.-J. // Tumor Biol. 2016. V. 37. № 4. P. 4421–4428.
16. Davis R., Rizwani W., Banerjee S., Kovacs M., Haura E., Coppola D., Chellappan S. // PLoS One. 2009. V. 4. № 10. P. e7524.
17. Pucci S., Fasoli F., Moretti M., Benfante R., Di Lascio S., Viani P., Daga A., Gordon T.J., McIntosh M., Zoli M., et al. // Pharmacol. Res. 2021. V. 163. P. 105336.
18. Schaal C., Padmanabhan J., Chellappan S. // Cancers. 2015. V. 7. № 3. P. 1447–1471.
19. Afrashteh Nour M., Hajiasgharzadeh K., Kheradmand F., Asadzadeh Z., Bolandi N., Baradaran B. // Life Sci. 2021. V. 278. P. 119557.
20. Chernyavsky A.I., Shchepotin I.B., Grando S.A. // Int. Immunopharmacol. 2015. V. 29. № 1. P. 36–44.
21. Bychkov M.L., Shulepko M.A., Shlepova O.V., Kulbatskii D.S., Chulina I.A., Paramonov A.S., Baidakova L.K., Azev V.N., Koshelev S.G., Kirpichnikov M.P., et al. // Front. Cell Dev. Biol. 2021. V. 9. P. 739391.
22. Shlepova O.V., Shulepko M.A., Shipunova V.O., Bychkov M.L., Kukushkin I.D., Chulina I.A., Azev V.N., Shramova E.I., Kazakov V.A., Ismailova A.M., et al. // Front. Cell Dev. Biol. 2023. V. 11. P. 1256716.
23. Sigismund S., Avanzato D., Lanzetti L. // Mol. Oncol. 2018. V. 12. № 1. P. 3–20.
24. Shimizu R., Ibaragi S., Eguchi T., Kuwajima D., Kodama S., Nishioka T., Okui T., Obata K., Takabatake K., Kawai H., et al. // Int. J. Oncol. 2019. V. 54. № 1. P. 283–294.
25. Vasilyeva N.A., Loktyushov E.V., Bychkov M.L., Shenkarev Z.O., Lyukmanova E.N. // Biochem. (Moscow). 2017. V. 82. № 13. P. 1702–1715.
26. Lyukmanova E., Shulepko M., Kudryavtsev D., Bychkov M., Kulbatskii D.S., Kasheverov I., Astapova M., Feofanov A., Thomsen M., Mikkelsen J., et al. // PLoS One. 2016. V. 11. № 2. P. e0149733.
27. Arredondo J., Chernyavsky A.I., Grando S.A. // Life Sci. 2007. V. 80. № 24–25. P. 2243–2247.
28. Bergqvist C., Kadara H., Hamie L., Nemer G., Safi R., Karouni M., Marrouche N., Abbas O., Hasbani D.J., Kibbi A.G., et al. // Int. J. Dermatol. 2018. V. 57. № 2. P. 162–170.
29. Arousse A., Mokni S., H'mida Ben Brahim D., Bdioui A., Aounallah A., Gammoudi R., Saidi W., Boussofara L., Ghariani N., Denguezli M., et al. // Int. J. Dermatol. 2019. V. 58. № 8. P. 966–968.
30. Throm V.M., Männle D., Giese T., Bauer A.S., Gaida M.M., Kopitz J., Bruckner T., Plaschke K., Grekova S.P., Felix K., et al. // Oncotarget. 2018. V. 9. № 14. P. 11734–11751.
31. Lyukmanova E.N., Shulepko M.A., Bychkov M.L., Shenkarev Z.O., Paramonov A.S., Chugunov A.O., Arseniev A.S., Dolgikh D.A., Kirpichnikov M.P. // Acta Naturae. 2014. V. 6. № 4. P. 60–66.
32. Lyukmanova E., Bychkov M., Sharonov G., Efremenko A., Shulepko M., Kulbatskii D., Shenkarev Z., Feofanov A., Dolgikh D., Kirpichnikov M. // Br. J. Pharmacol. 2018. V. 175. № 11. P. 1973–1986.
33. Bychkov M.L., Shulepko M.A., Shlepova O.V., Lyukmanova E.N., Kirpichnikov M.P. // Dokl. Biochem. Biophys. 2019. V. 489. № 1. P. 392–395.
34. Shulepko M.A., Bychkov M.L., Lyukmanova E.N., Kirpichnikov M.P. // Dokl. Biochem. Biophys. 2020. V. 493. № 1. P. 211–214.

35. Shulepko M.A., Bychkov M.L., Kirpichnikov M.P., Lyukmanova E.N. // Rus. J. Bioorg. Chem. 2023. V. 49. № 4. P. 403–410.

36. Shulepko M.A., Bychkov M.L., Shlepova O.V., Shenkarev Z.O., Kirpichnikov M.P., Lyukmanova E.N. // Int. Immunopharmacol. 2020. V. 82. P. 106303.

37. Tortora G., Gelardi T., Ciardiello F., Bianco R. // Int. J. Biol. Markers. 2007. V. 22. № 1 Suppl 4. P. S47–52.

38. Yun U.-J., Lee J.-H., Shim J., Yoon K., Goh S.-H., Yi E.H., Ye S.-K., Lee J.-S., Lee H., Park J., et al. // Lab. Invest. 2019. V. 99. № 8. P. 1157–1172.

39. Mendez B.M., Thornton J.F. // Plast. Reconstr. Surg. 2018. V. 142. № 3. P. 373e–387e.

40. van der Zanden S.Y., Qiao X., Neefjes J. // FEBS J. 2021. V. 288. № 21. P. 6095–6111.

41. Swain S.M., Whaley F.S., Ewer M.S. // Cancer. 2003. V. 97. № 11. P. 2869–2879.

42. Shulepko M., Lyukmanova E., Paramonov A., Lobas A., Shenkarev Z., Kasheverov I., Dolgikh D., Tsetlin V., Arseniev A., Kirpichnikov M. // Biochem. (Moscow). 2013. V. 78. № 2. P. 204–211.

43. Varankar S.S., Bapat S.A. // Front. Oncol. 2018. V. 8. P. 633.

44. Shipunova V.O., Komedchikova E.N., Kotelnikova P.A., Zelepukin I.V., Schulga A.A., Proshkina G.M., Shramova E.I., Kutscher H.L., Telegin G.B., Kabashin A.V., et al. // ACS Nano. 2020. V. 14. № 10. P. 12781–12795.

45. Sritharan S., Sivalingam N. // Life Sci. 2021. V. 278. P. 119527.

46. Bychkov M.L., Shulepko M.A., Shlepova O.V., Lyukmanova E.N., Kirpichnikov M.P. // Dokl. Biochem. Biophys. 2019. V. 489. № 1. P. 392–395.

47. Johnson-Arbor K., Dubey R. Doxorubicin // StatPearls. Treasure Island (FL): StatPearls Publishing, 2023.

48. Cuan X., Yang X., Zhu W., Zhao Y., Luo R., Huang Y., Wang X., Sheng J. // BMC Pharmacol. Toxicol. 2023. V. 24. № 1. P. 29.

49. Miller K.D., Nogueira L., Devasia T., Mariotto A.B., Yabroff K.R., Jemal A., Kramer J., Siegel R.L. // CA. Cancer J. Clin. 2022. V. 72. № 5. P. 409–436.

50. Kamińska K., Cudnoch-Jędrzejewska A. // Neurotox. Res. 2023. V. 41. № 5. P. 383–397.

51. Tian Z., Yang Y., Yang Y., Zhang F., Li P., Wang J., Yang J., Zhang P., Yao W., Wang X. // BMC Cancer. 2020. V. 20. № 1. P. 1139.

52. Upshaw J.N. // Curr. Oncol. Rep. 2020. V. 22. № 7. P. 72.

53. El-Agamy S.E., Abdel-Aziz A.K., Esmat A., Azab S.S. // Cancer Chemother. Pharmacol. 2019. V. 84. № 1. P. 1–14.

54. Du J., Zhang A., Li J., Liu X., Wu S., Wang B., Wang Y., Jia H. // Front. Oncol. 2021. V. 11. P. 673340.

55. Qin S.-Y., Cheng Y.-J., Lei Q., Zhang A.-Q., Zhang X.-Z. // Biomaterials. 2018. V. 171. P. 178–197.

56. Bello L., Carrabba G., Giussani C., Lucini V., Cerutti F., Scaglione F., Landré J., Pluderi M., Tomei G., Villani R., et al. // Cancer Res. 2001. V. 61. № 20. P. 7501–7506.

57. Yan Y., Su C., Hang M., Huang H., Zhao Y., Shao X., Bu X. // Virol. J. 2017. V. 14. № 1. P. 190.

58. Bu X., Zhang A., Chen Z., Zhang X., Zhang R., Yin C., Zhang J., Zhang Y., Yan Y. // BMC Cancer. 2019. V. 19. № 1. P. 976.

59. Brown K.C., Lau J.K., Dom A.M., Witte T.R., Luo H., Crabtree C.M., Shah Y.H., Shiflett B.S., Marcelo A.J., Proper N.A., et al. // Angiogenesis. 2012. V. 15. № 1. P. 99–114.

60. Grozio A., Paleari L., Catassi A., Servent D., Cilli M., Piccardi F., Paganuzzi M., Cesario A., Granone P., Mourier G., et al. // Int. J. Cancer. 2008. V. 122. № 8. P. 1911–1915.

61. Shulepko M.A., Kulbatskii D.S., Bychkov M.L., Lyukmanova E.N. // Rus. J. Bioorg. Chem. 2019. V. 45. № 2. P. 66–75.

62. Xu Y.H., Richert N., Ito S., Merlino G.T., Pastan I. // Proc. Natl. Acad. Sci. USA. 1984. V. 81. № 23. P. 7308–7312.

63. Uribe M.L., Marrocco I., Yarden Y. // Cancers. 2021. V. 13. № 11. P. 2748.

64. Bao J., Gur G., Yarden Y. // Proc. Natl. Acad. Sci. USA. 2003. V. 100. № 5. P. 2438–2443.

65. Zhao C., Yang L., Zhou F., Yu Y., Du X., Xiang Y., Li C., Huang X., Xie C., Liu Z., et al. // Oncogene. 2020. V. 39. № 20. P. 3997–4013.

66. Wang D., Su L., Huang D., Zhang H., Shin D.M., Chen Z.G. // Mol. Cancer. 2011. V. 10. P. 116.

Inhibition of HBV Replication by a Fully Humanized Neutralizing Antibody *In Vivo* and *In Vitro*

Zhipeng Zhang[1,2*], Yanqin Ma[2], Yan He[2], Dong Wang[2], Huaien Song[2], Kun Yue[2], Xiaomei Zhang[1]
[1]Laboratory of Pharmaceutical Engineering, School of Life Science and Health Engineering, Jiangnan University, Wuxi, 214122 China
[2]Suzhou Hepa Thera Biopharmaceutical Co., Ltd., Shanghai, 200120 China
*E-mail: zhipengzhang2009@163.com

ABSTRACT Neutralizing antibodies are capable of specifically binding to the HBsAg virus, thereby preventing HBV infection and subsequently reducing viral antigen load in both the liver and systemic circulation. This has significant implications for restoring the postnatal immune function. By utilizing the phage antibody library technology, we successfully screened a fully humanized neutralizing antibody targeting the hepatitis B surface antigen. The antiviral activity was assessed in primary human hepatocytes (PHHs) by determining the EC_{50} values for HBeAg and HBsAg biomarkers in HBV types B, C, and D; no cytotoxicity was observed within the tested concentration range. Furthermore, HT-102 exhibited no ADCC effect but displayed a weak CDC effect along with a dose-dependent response. We established an AAV/HBV mouse model and observed significant dose-dependent reduction in HBsAg and HBV DNA levels for both the medium-dose and high-dose groups. The immunohistochemical staining data showed dose-dependent reduction in HBsAg expression in the liver, with high-dose group exhibiting minimal positive expression. Finally, a mild immune response was induced, while reducing the burden of antigen–antibody complexes circulating within the system. Consequently, strain on the patient's immune system was alleviated by effectively slowing down $CD8^+T$ lymphocyte depletion, and functional cure was ultimately achieved as intended.
KEYWORDS Neutralizing antibody, CDC effect, HBsAg.

INTRODUCTION

Hepatitis B virus (HBV) infection is a common public health problem worldwide; 5–10% of persistent HBV infections following acute hepatitis B develop into chronic liver disease, including chronic active hepatitis, cirrhosis, and primary liver cell carcinoma [1]. Although nucleic acid analogs effectively prevent the risk of HBV reactivation and completely eliminate the possibility of hepatitis outbreak, the probability of functional cure is extremely low, and it still causes serious damage to the liver and even the occurrence of liver cancer [2].

Currently, prevention of hepatitis B virus infection primarily involves active and passive immunization [3]. Active immunization entails administering the hepatitis B vaccine, making it one of effective measures for preventing hepatitis B transmission [4]. Passive immunization involves administering hepatitis B immune globulin (HBIG), which is mainly used to prevent mother-to-child transmission (in combina-

tion with the hepatitis B vaccine) [5]. Research has demonstrated that a combination of both HBIG and the hepatitis B vaccine is more effective in reducing the chronic infection rate [6]. Most HBIG is derived from positive serum containing anti-HBsAg, which limits its large-scale production and poses a risk for blood-borne infectious diseases because it is originating from serum sources. Despite the transition from blood-derived vaccines to genetically engineered ones, there is an urgent need to develop genetically engineered antibodies against anti-HBs as a replacement for HBIG [7]. The phage antibody library technology offers an alternative solution to address this issue.

The present study mainly introduced a new fully humanized neutralizing antibody (HT-102), which was in phase 1 clinical stage (Chinese Clinical Trial Registry No. ChiCTR2200072837). The phage display Fab libraries were constructed using the established methods [8, 9] based on targeted genes isolated from PBMCs of 18 donors who had received

hepatitis B virus vaccination. Total cellular mRNAs were extracted using an RNeasy Mini Kit (Qiagen), and cDNA synthesis was primed with oligo (dT) using a Transcriptor High Fidelity cDNA Synthesis Kit (Roche). The light and heavy chain genes were amplified from the cDNA by PCR and sequentially cloned into the pComb 3H vector using a standard protocol [10]. Fab antibody preparations were tested and screened by indirect ELISA using 96-well plates coated with 0.5–1 µg of purified S protein, with horseradish peroxidase (HRP)-conjugated anti-human Fab used as a secondary antibody. Following the evaluation of the clones, HT-102 was selected as the final monoclonal antibody due to its superior performance in terms of anti-HBsAg titer, Fab expression levels, and binding affinity [11]. The primary mechanism involves specific binding to the S antigen on the surface of the HBV virus [12], which prevents its interaction with cell receptors and subsequent entry into cells, consequently impeding HBV infection in uninfected cells [13].

MATERIALS AND METHODS

In vitro

The following commercial cell lines were used for *in vitro* efficacy assays: PHHs (Wuxi Apptec, cat. # LGI, China), Myrcludex B (Wuxi AppTec, cat. # P1214012, China), Cell PBMC (HemaCare, cat. # 20063062, USA), HepG2-HBsAg and Raji cells (Wuxi AppTec, China). Detailed information regarding the HBV virus is provided in *Table 1* (see Appendix). The following commercial test kits were utilized in this experiment: LDH assay kit (Promega, cat. # G1780, USA), CCK-8 (Li Ji Biochemicals, cat. # AC11L057, China), HBsAg ELISA kit (Autobio Inc., cat. # CL-0310, China), and HBeAg ELISA kit (Autobio Inc., cat. # CL-0312, China). The main instruments used in this experiment include an enzyme-linked immunosorbent assay (ELISA) reader (Molecular Devices, USA), a centrifuge (Beckman Coulter, USA), and a cell counter (Countstar, China).

Anti-HBV efficacy. On day 0, PHH cells were recovered and adjusted to a suitable density of 1.32×10^5 cells/well before being seeded into 48-well cell plates at a concentration of 20 µg/ml. On day 1, HT-102 was prepared at starting concentrations of 20, 5, 1.250, 0.313, 0.078, 0.020, and 0.005 µg/ml to be mixed with type B, type C, and type D HBV viruses for 1 h before being added to the cells. Similarly, Myrcludex B was prepared at starting concentrations of 100, 25, 6.250, 1.563, 0.391, 0.098, and 0.024 nM. On day 8, the cell culture supernatants were collected for CCK-8 assay to determine cell viability as well

as ELISA analysis for HBeAg and HBsAg detection. The HBsAg inhibition rate (%) and HBeAg inhibition rate (%) were calculated as (1 – [HBsAg or HBeAg test sample concentration / HBsAg or HBeAg medium control concentration]) × 100%, respectively. Cell viability% was determined as (test sample absorbance – blank average absorbance)/ (medium control average absorbance – blank average absorbance) × 100%. The data were analyzed using the log(inhibitor) vs response-variable slope method in the GraphPad Prism software to obtain the EC_{50} and CC_{50} values of the compound against HBV.

The antibody-dependent cellular cytotoxicity (ADCC) and complement-dependent cytotoxicity (CDC) effects. The binding rate of the tested antibody to the target cell was verified as follows. Different concentrations of HT-102 (0.1, 1, 10, and 100 µg/ml) were prepared and incubated with HepG2-HBsAg stably transfected cells at 4°C for a specified duration. A negative control was included simultaneously. Fluorescent secondary antibody APC-anti-human IgG Fc (Jackson ImmunoResearch, cat. # 109-605-098, USA) was added and incubated. Finally, flow cytometry was employed to determine the binding rate.

ADCC: On day 1, PBMC cells were adjusted to a density of 2×10^6 cells/ml. Raji and HepG2-HBsAg stable transfection cell lines were also adjusted to a density of 4×10^5 cells/ml. The antibodies, including positive control Rituximab (MedChemExpress, cat. # HY-P9913, USA) and negative control IgG1 (Genenode, cat. # 91001B, China), were then prepared at concentrations ranging from 100 to 0 µg/ml. The LDH test was performed in strict accordance with the manufacturer's instructions provided in the LDH assay kit. Killing rate = (Test sample absorbance – Low control absorbance – PBMC absorbance) / (High control absorbance – Low control absorbance) × 100%. ADCC% = (killing rate of test sample – killing rate of no-antibody control) × 100%.

CDC: The cell density of Raji and HepG2 cells was separately adjusted to 4×10^5 cells/ml. HT-102 antibody, positive control Rituximab, and negative control IgG1 were prepared at concentrations ranging from 100 to 0 µg/ml. Next, the lysis solution was introduced into each well for lysing the cells thereby releasing LDH (lactate dehydrogenase). The instructions provided in the LDH kit were followed meticulously to conduct the LDH test. Complement-Mediated Cytotoxicity of Target Cells: Killing rate = (Test sample absorbance – Low control absorbance) / (High control absorbance – Low control absorbance) × 100%. CDC% = (killing rate of test sample – killing rate of no-antibody control) × 100%.
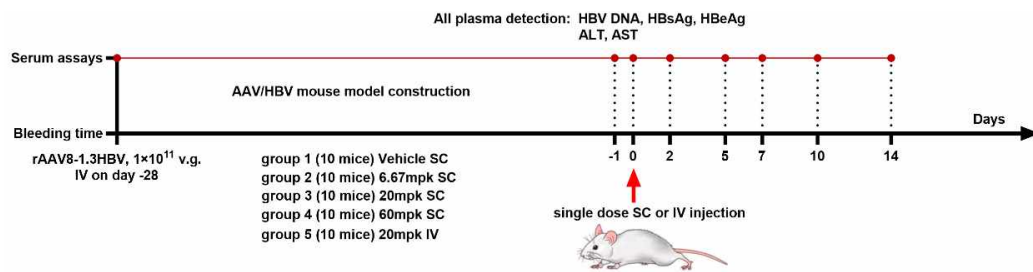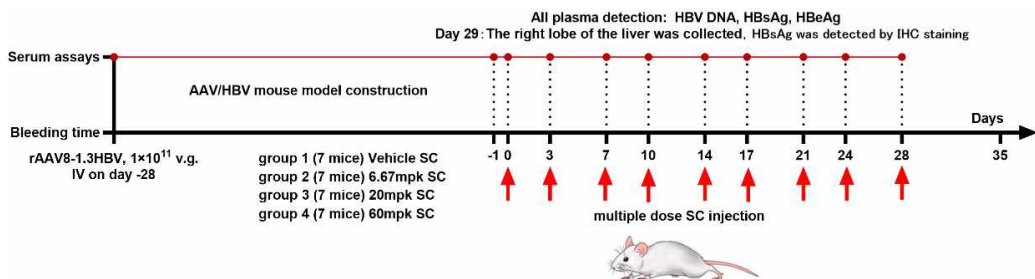
Fig. 1. Experimental design

Fig. 2. Experimental design

In vivo

The recombinant rAAV8-1.3HBV (type D, ayw; batch number: awy1-P4-220301) was procured from Shanghai Wuxi AppTec. The primary reagents and instruments used are detailed in *Tables 2* and *3* (see Appendix).

Evaluation of the anti-HBV activity by a single dose injection. Before injection, rAAV8-1.3HBV was prepared in sterile PBS at a concentration of 1×10^{11} v.g./200 μl. Injections were administered to 60 mice via the tail vein. After screening, 50 mice were divided into five groups and designated as group 1 through group 5. Blood plasma was collected before detecting HBV DNA, HBsAg, and HBeAg on days 14 and 21 after virus injection. On day 0 (28 days after virus injection), four groups of mice were subcutaneously injected with a blank vehicle or a test compound solution, while the fifth group of mice was injected with the test compound solution via the tail vein. Blood plasma samples were collected from all mice via the submandibular vein on days -1, 2, 5, 7, 10, and 14, and used to detect HBV DNA, HBsAg, and HBeAg. These blood plasma samples were also used to detect ALT and AST on days -1, 7, and 14 (Appendix, *Fig. S1*). The experimental protocol is shown in *Fig. 1*. Data are presented as mean ± standard deviation of each group of mouse samples, unless otherwise specified.

Evaluation of the anti-HBV activity by multiple dose injection. All 35 mice successfully received 200 μl of the rAAV8-1.3HBV solution via the tail vein. After

screening, 28 mice were selected into groups and labeled as group 1 through group 4. Blood samples were collected from infected mice via the subclavian vein on days 24 and 44 post-infection and stored at −80°C for detecting HBV DNA, HBsAg, and HBeAg [14]. On day 0, mice in groups 1–4 received subcutaneous injections of either a vehicle or a test compound. Blood samples were collected from all mice through the subclavian vein on days -1, 1, 5, 8, 12, 15, 19, 22, 26, and 29 post-infection for detecting HBV DNA, HBsAg, and HBeAg. All mice were sacrificed by CO_2 inhalation on day 29, and the right lobe of the liver was harvested and preserved in formaldehyde, transferred to PBS, and embedded into paraffin blocks to conduct IHC staining for detecting HBsAg. *Figure 2* illustrates the experimental protocol design. The results of HBV DNA, HBsAg, HBeAg analysis are presented as the mean value ± standard deviation per group of mouse samples, unless otherwise specified.

RESULTS

In vitro anti-HBV efficacy

The experimental protocol was designed to validate the *in vitro* antiviral activity within the PHHs system. Myrcludex B exhibited expected inhibition against HBeAg subtypes B, C, and D with EC_{50} values of 8.583, 11.180, and 0.853 nM, respectively, as well as against HBsAg subtypes B, C, and D with EC_{50} values of 3.358, 7.545, and 0.908 nM, respectively [15, 16]. HT-102 (batch number: C19455-YY2022001(C)) demonstrated EC_{50} values of 0.083, 0.057, and 0.117 μg/ml for inhibition of HBeAg subtypes B, C
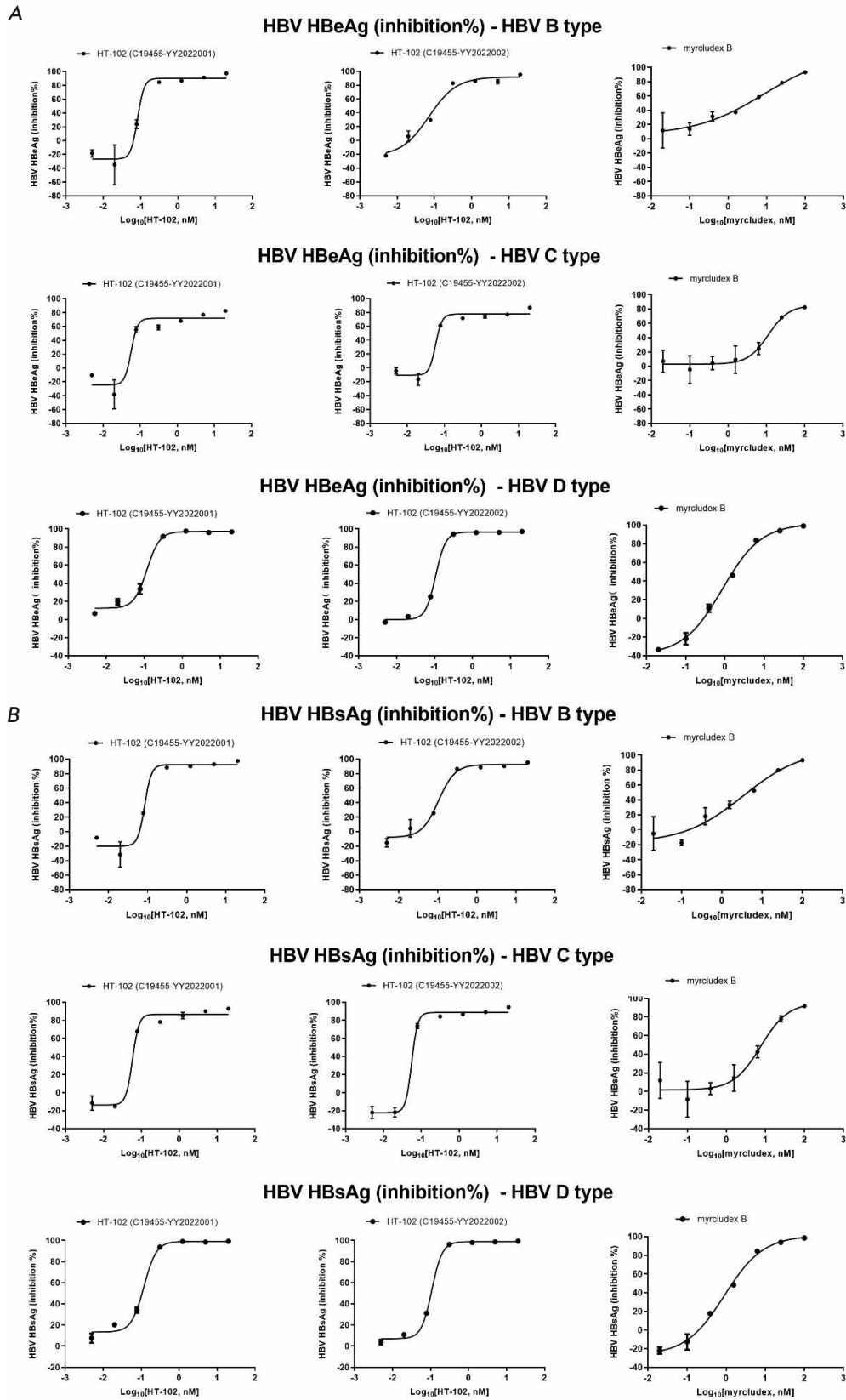
A

B

Fig. 3. (*A*) The fit curve for the inhibition of HBeAg by neutralizing antibody. (*B*) The fitting curve for the inhibition of HBsAg by neutralizing antibody targeting HBV surface antigens. Error bars represent standard errors
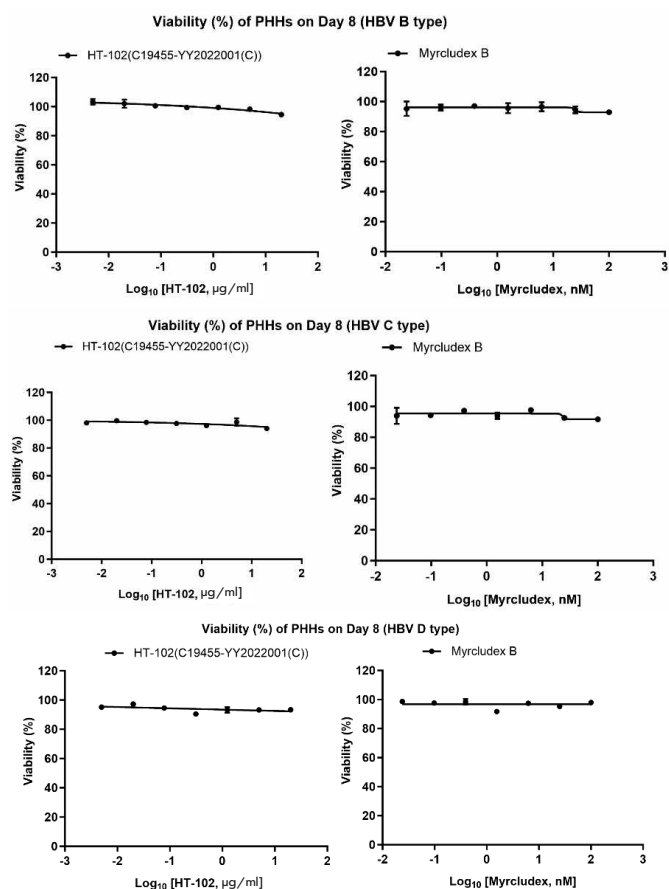
Fig. 4. The fit curves for cell viability. Error bars represent standard errors

and D, and EC_{50} values of 0.084, 0.058, and 0.119 µg/ml for inhibition of HBsAg subtypes B, C, and D. HT-102 (batch number: C19455-YY2022002) showed EC_{50} values of 0.072, 0.058, and 0.107 µg/ml for inhibition of HBeAg subtypes B, C, and D, and EC_{50} values of 0.104, 0.055, and 0.108 µg/ml for inhibition of HBsAg subtypes B, C, and D. The fit curves are shown in *Fig. 3*.

A microscopy study revealed that neither HT-102 (batch number: C19455-YY2022001(C)) nor myrcludex B exhibited an apparent toxicity against PHHs cells. This finding was further supported by the results obtained from CCK-8 detection. *Figure 4* shows the cell viability curve.

The antibody-dependent cellular cytotoxicity (ADCC) and complement-dependent cytotoxicity (CDC) effects

HepG2 cells stably expressing HBsAg protein were used as target cells. When evaluating the binding efficiency of the neutralizing antibody to these target cells [17], flow cytometry results demonstrated a con-

centration-dependent increase in binding rates between the target cells and various concentrations (0.1, 1, 10, and 100 µg/ml) of HT-102(BM012). The highest binding rate, 37.9% at a concentration of 100 µg/ml, was observed with HepG2-HBsAg stably transfected cells. In contrast, the binding rates of the negative control antibody were significantly lower than those of HT-102(BM012) at the same concentrations. However, it is worth noting that at a concentration of 100 µg/ml, the binding rate was elevated (48.2%) for the negative control antibody, suggesting potential non-specific staining due to excessive concentration. These findings shown in *Fig. 5*.

Evaluation of the ADCC activity revealed that Rituximab exhibited a significant dose-dependent ADCC activity within its specified range (13.57–53.03%) [18, 19]. The negative control antibody, human IgG1, exhibited an ADCC activity of -7.35%. Concentrations of the positive and negative controls used in the test are listed in *Table 4* (see Appendix). The test antibody HT-102(BM012) displayed no detectable ADCC activity within its specified range (0.0064–100 µg/ml) (*Table 5*, see Appendix).

During further assessment of the CDC effect of the test antibody, it was observed that Rituximab exhibited a CDC effect ranging from 0.68 to 15.59% within its tested concentration range (0.0064–100 µg/ml). The HT-102 (BM012) showed a CDC effect ranging from -0.71 to 5.23% within its tested concentration range (0.0064–100 µg/ml), while the negative control human IgG antibody had a CDC effect value of -0.13%. These findings indicated that HT-102 (BM012) exhibited a weak but dose-dependent CDC effect. The detailed results are available in *Tables 6* and *7* (see Appendix).

Evaluation of the *in vivo* anti-HBV activity by a single dose injection

The levels of HBeAg, HBsAg, and HBV DNA in mice in the vehicle group remained relatively stable throughout the experiment, fluctuating within the ranges of 3.30–3.70 log10 PEIU/ml for HBeAg, 5.10–5.72 log10 IU/ml for HBsAg, and 5.47–6.02 log10 copy/µL for HBV DNA during the experimental period [20]. Low-dose group (6.67 mpk, SC): on day 0, mice in group 2 were compared to the vehicle group. No significant reduction was observed in plasma levels of HBeAg, HBsAg, and HBV DNA. Medium-dose group (20 mpk, SC): mice in group 3 were compared to the vehicle group; on day 2, a slight decrease was observed in plasma levels of HBeAg (-0.15 log10 PEIU/ml; $p < 0.01$), HBsAg (-0.60 log10 IU/ml; $p < 0.01$), and HBV DNA (-0.47 log10 copy/µL; $p < 0.05$), but these levels rebounded by day 10 after treatment. High-dose group (60mpk, SC):
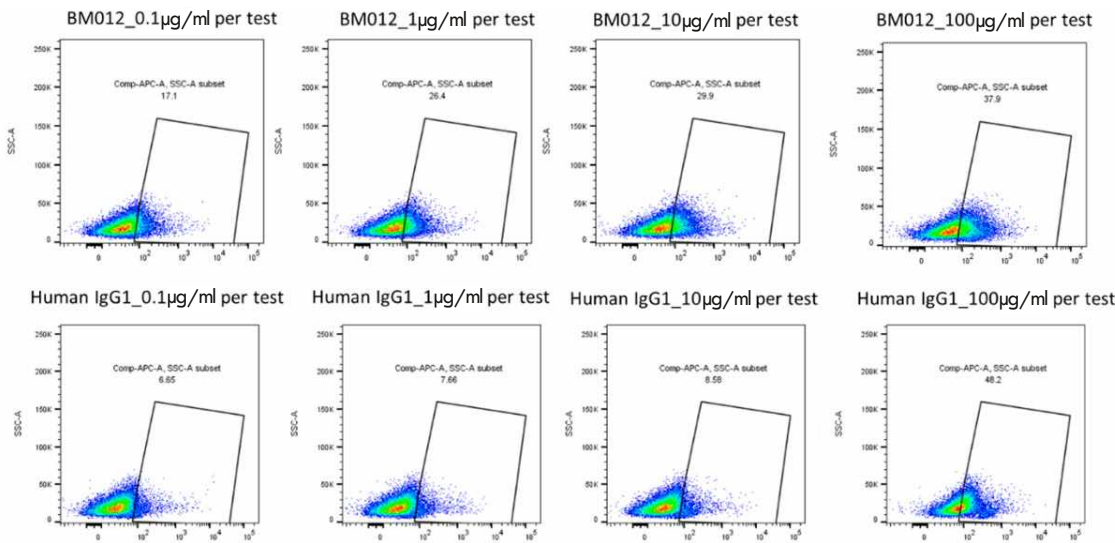
Fig. 5. The efficacy of the neutralizing antibody and negative control antibody in their binding to the target cells

mice in group 4 were compared to those in the vehicle group; on day 2, there was a slight decline in plasma level of HBeAg (-0.18 log10 PEIU/ml; $p < 0.01$), and significant decrease in both HBsAg (-3.26 log10 IU/ml; $p < 0.01$) and HBV DNA levels (-2.47 log10 copy/µL; $p < 0.01$). However, identically to the observations in the medium-dose group, the levels of HBeAg, HBsAg, and HBV DNA returned to the baseline. In the medium-dose group (20 mg/kg, IV), mice in group 5 were injected via the tail vein. Compared to the vehicle group, there was slight reduction in plasma HBeAg and HBV DNA levels on day 2 (0.12 log10 PEIU/ml ($p < 0.01$) and 0.41 log10 copies/µL ($p < 0.01$), respectively). However, by day 10 post-dose, the HBsAg levels returned to the level of the vehicle group. The results of the entire experiment are presented in *Fig. 6*.

Evaluation of the *in vivo* anti-HBV activity by multiple dose injection

Group 2 (6.67 mg/kg, SC): HT-102 was administered subcutaneously at a dose of 6.67 mg/kg every three days. Compared to the vehicle group, the plasma HBeAg level in mice slightly decreased from day 8 to day 19 post-dose; the mean decrease ranged from 0.09 to 0.19 log10 PEIU/ml ($p < 0.05$). The other time points were similar to those in the vehicle group. The plasma HBsAg level in mice was significantly reduced on day 1 after the first administration and decreased to the lower limit of quantification (LLOQ); the plasma level of HBsAg fluctuated between day 5 and day 29. A significant decline was observed on days 8, 15, 22, and 29; the mean decrease was 4.67, 4.84, 3.33, and 3.26 log10 IU/ml ($p < 0.01$), respectively. Compared with the vehicle group, the plasma level of HBV DNA

in mice was significantly lower after the first administration of HT-102; subsequently, on days 5 through 29, there were fluctuations in the plasma levels of HBV DNA related to the administration time, with a significant decrease observed on days 8, 15, 22, and 29 (the mean decrease being 2.20, 2.12, 1.78, and 1.43 log10 copies/µL ($p < 0.01$), respectively). Plasma levels of HBeAg in group 3 mice were slightly decreased (20 mg/kg) compared to the vehicle group on days 5 and day12 through day 19 post-dose. The plasma levels of HBsAg in mice were significantly reduced on days 1 through 29, reaching the LLOQ value. The mean decrease in the HBsAg level was between -4.42 and -4.97 log10 IU/ml ($p < 0.01$). In a similar manner, the plasma levels of HBV DNA in mice were significantly decreased at all time points between day 1 and day 29 compared to those in the vehicle group and slightly reduced, approaching the LLOQ value. The mean decrease in HBV DNA was between -1.92 and -2.32 log10 copy/µl ($p < 0.01$). In group 4 mice, the serum levels of HBeAg were slightly decreased on days 12 through 19 compared to those in the vehicle group; the mean reduction range was -0.15 to -0.23 log10 PEIU/ml ($p < 0.05$), while results similar to those in the vehicle group were observed for other time points. Furthermore, the serum HBsAg levels were significantly reduced on days 1 through 29, reaching the LLOQ value, the mean reduction range being -4.40 to -4.97 log10 IU/ml ($p < 0.01$). In a similar manner, the serum levels of HBV DNA significantly decreased from day 1 to 29 and approached the LLOQ value, with mean reduction range of -1.81 to -2.20 log10 copy/µl ($p < 0.01$). Detailed graphs are shown in *Fig. 7*.
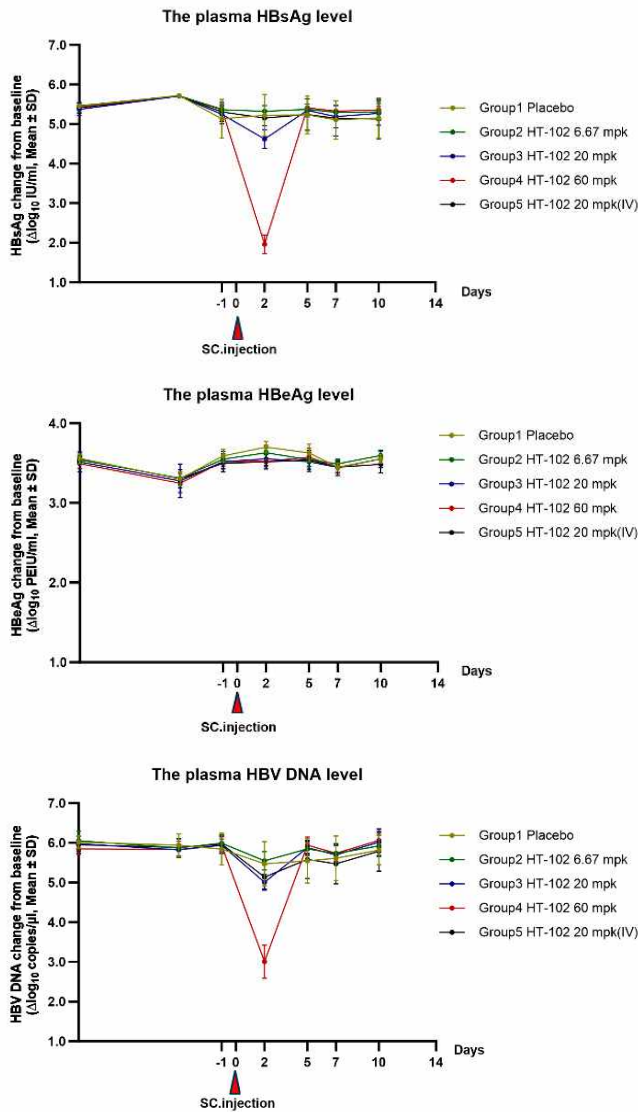
Fig. 6. The effects of the test compound on HBsAg, HBeAg, and HBV DNA in the plasma of AAV/HBV mice. The plasma levels of HBsAg and HBeAg in mice were quantified by ELISA, while the HBV DNA level was determined by quantitative PCR analysis. Error bars represent standard errors

Fig. 7. The effects of the test compound on plasma levels of HBsAg, HBeAg, and HBV DNA in AAV/HBV mice. The plasma levels of HBsAg and HBeAg in mice were quantified by ELISA, while the HBV DNA level was determined by quantitative PCR analysis. Error bars represent standard errors

Figure 8 shows HBsAg expression in the liver for each mouse group. All the liver tissue sections harvested from AAV/HBV-infected mice were characterized by specific localization of HBsAg. Moreover, equine anti-HBsAg polyclonal antibody was used to stain brown for the positive control in IHC staining. Positive HBsAg expression was predominantly concentrated within the hepatic sinusoidal region and exhibited a radial distribution [21, 22]. Microscopic examination r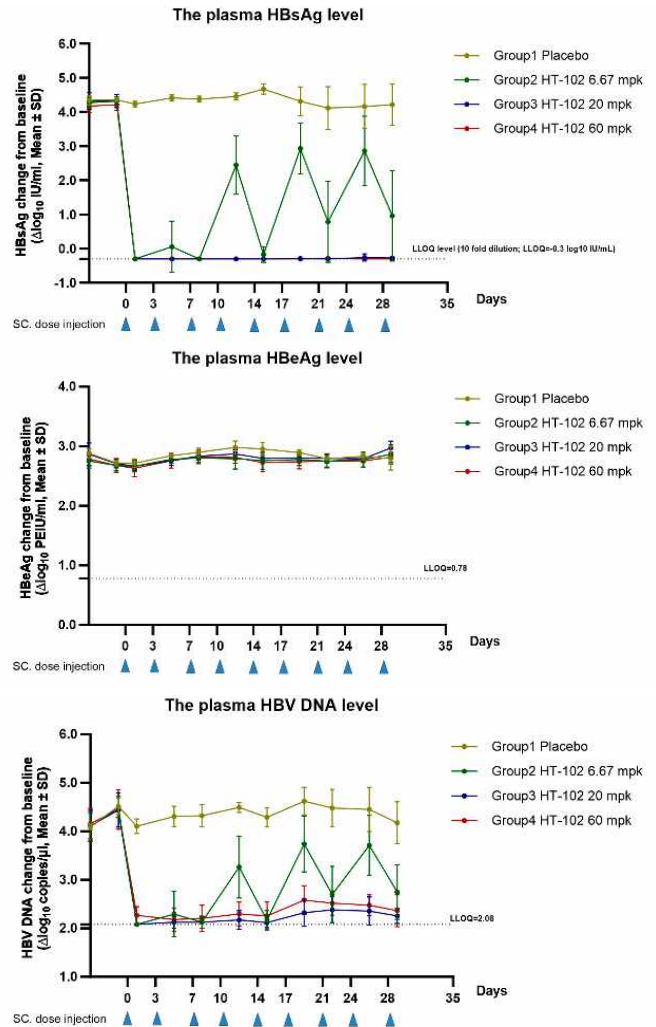evealed a significant dose-dependent reduction in HBsAg expression in liver tissue samples from the low-dose, medium-dose, and high-dose groups compared to the placebo group. Notably, the lowest level of HBsAg positive expression was observed for mice in the high-dose group.

DISCUSSION

The excessive release of HBsAg in chronic HBV patients leads to tolerance to antibodies and cell-mediated immune responses, which currently is a major
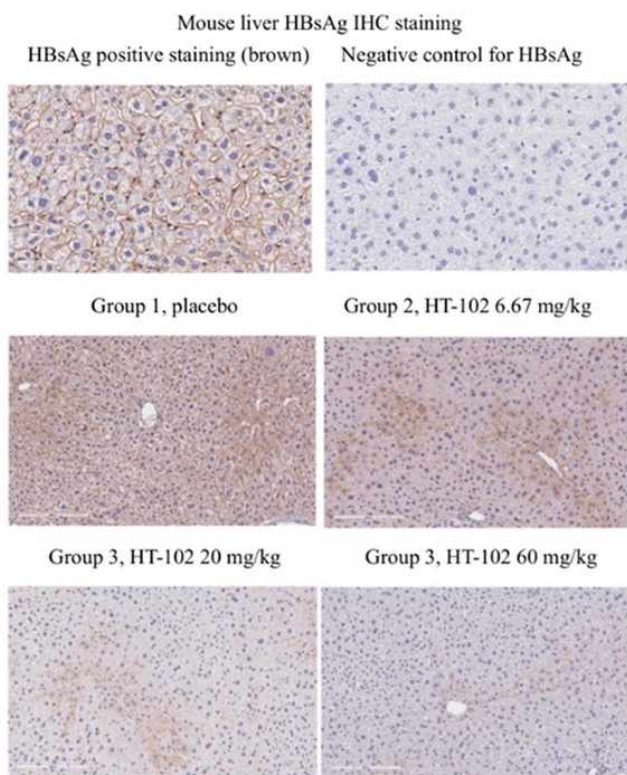
Mouse liver HBsAg IHC staining

HBsAg positive staining (brown)   Negative control for HBsAg

Group 1, placebo   Group 2, HT-102 6.67 mg/kg

Group 3, HT-102 20 mg/kg   Group 3, HT-102 60 mg/kg

Fig. 8. Immunohistochemical staining of HBsAg was performed in mouse liver samples to evaluate the anti-HBV activity in the AAV/HBV mouse model through multiple dose injections. The HBsAg levels in the mouse liver were determined by IHC staining, compared with positive and negative controls; groups 1 to 3 were sampled for liver tissue staining on day 29

obstacle to eradication of the virus [23, 24]. Therefore, it is crucial to identify approaches that can overcome immune tolerance and enable hosts to generate effective immune responses capable of clearing the virus and preventing further HBV infection [25, 26].

We conducted *in vitro* assays to evaluate the antiviral activity of the compound against hepatitis B virus (HBV) types B, C, and D. The HBeAg and HBsAg levels were quantified by ELISA, while human primary hepatocytes (PHHs) were employed for assessing the efficacy of the compound. Furthermore, no cytotoxic effects were observed within the tested concentration range. This study revealed no ADCC effect; however, HT-102 exhibited a weak and dose-dependent CDC effect. Subcutaneous administration of the test antibody at medium and high doses effectively reduced the HBeAg, HBsAg, and HBV DNA levels, being indicative of a significant dose-dependent response. Analysis of the ALT and AST levels in blood samples

revealed no significant elevation in the mean post-dose levels among the treatment groups, indicating that there was no adverse impact on liver function. Furthermore, repeated subcutaneous low-dose, medium-dose, and high-dose injections effectively reduced the HBeAg, HBsAg, and HBV DNA levels, while exhibiting a favorable dose-dependent effect across all dosage groups. The immunohistochemical staining data revealed significant decline in HBsAg expression in the liver tissue samples; mice in the high-dose group exhibited the lowest HBsAg positive expression.

The results of both *in vivo* and *in vitro* pharmacological experiments indicate that the *in vivo* studies yielded some unexpected outcomes. Specifically, single medium- and high-dose administration led to a rapid rebound in HBsAg levels. After multiple low-dose administrations, HBsAg biomarkers exhibited cross-correlation between rebound and inhibition. However, after administration of multiple medium and high doses, HBsAg biomarkers remained at or below the lower limit of detection. The low-dose group exhibited unsatisfactory findings, two fundamental reasons underlying this observation. First, immunogenicity played a crucial role. Although neutralizing antibodies had shown promising clinical effects, fully humanized antibodies may elicit immune responses in mice, resulting in production of antidrug antibodies (ADAs). ADAs could neutralize activity of the antibody drug, affect drug clearance and bioavailability, alter the pharmacokinetic characteristics of drugs, as well as interfere with or impede therapeutic efficacy [27–29]. A fluctuating rebound effect was observed in the medium-dose group. It was possible to detect the presence of antidrug antibody (ADA) in the blood serum of mice and assess changes in its pharmacokinetic properties, as well as conduct research on constructing a humanized liver chimeric mouse model infected with HBV. Second, the initial administration of neutralizing antibodies may induce a negative feedback regulation, thereby further stimulating the release of viral particles from infected hepatocytes, leading to the inefficacy observed in the low-dose group, while the medium-dose group exhibited a fluctuating rebound in the mouse model of HBV infection. However, the high-dose group directly neutralized both extracellular circulating HBV viral particles and newly secreted ones from infected hepatocytes, consistently maintaining them below the limit of quantification (LLOQ). This finding provided valuable insights for subsequent clinical dosing regimens [30]. ●

Appendix is available on the website
https://doi.org/10.32607/actanaturae.27457.

REFERENCES

1. Liang T.J. // Hepatology. 2009. V. 49. P. S13–S21.
2. Papatheodoridi M., Tampaki M., Lok A.S., Papatheodoridis G.V. // Hepatology. 2022. V. 75. № 5. P. 1257–1274. doi: 10.1002/hep.32241
3. Orlando R., Foggia M., Maraolo A.E., Mascolo S., Palmiero G., Tambaro O. // Eur. J. Clin. Microbiol. Infect. Dis. 2015. V. 34. № 6. P. 1059–1070.
4. Kato T., Akari H. // Uirusu. 2023. V. 72. № 2. P. 149–158.
5. Veronese P., Dodi I., Esposito S., Indolfi G. // World J. Gastroenterol. 2021. V. 27. № 26. P. 4182–4193.
6. Hsu Y.C., Huang D.Q., Nguyen M.H. // Nat. Rev. Gastroenterol. Hepatol. 2023. V. 20. № 8. P. 524–537.
7. Wu C.R., Kim H.J., Sun C.P., Chung C.Y., Lin Y.Y., Tao M.H., Kim J.H., Chen D.S., Chen P.J. // Hepatology. 2022. V. 76. P. 207–219.
8. Sun L., Lu X., Li Ch., Wang M., Liu Q., Li Z., Hu X., Li J., Liu F., Li Q., et al. // PLoS One. 2009. V. 4. https://doi.org/10.1371/journal.pone.0005476
9. Kashyap A.K., Steel J., Oner A.F., Dillon M.A., Swale R.E., Wall K.M., Perry K.J., Faynboym A., Ilhan M., Horowitz M., et al. // Proc. Natl. Acad. Sci. USA. 2008. V. 105. P. 5986–5991.
10. Barbas C.F. 3rd, Kang A.S., Lerner R.A., Benkovic S.J. // Proc. Natl. Acad. Sci. USA. 1991. V. 88. P. 7978–7982.
11. Burm R., van Houtte F., Verhoye L., Mesalam A.A., Ciesek S., Roingeard P., Wedemeyer H., Leroux-Roels G., Meuleman P. // JHEP Rep. 2022. V. 5. № 3. P. 100646. doi: 10.1016/j.jhepr.2022.100646
12. Zhang H., Itoh Y., Suzuki T., Ihara K., Tanaka T., Haga S., Enatsu H., Yumiya M., Kimura M., Takada A., et al. // Microbiol. Immunol. 2022. V. 66. P. 179–192. https://onlinelibrary.wiley.com/doi/full/10.1111/1348-0421.12964
13. Yue M., Nie M., Huang X., Zhang T., Zhao Q. // Chin. J. Microbiol. Immunol. 2021. V. 41. P. 805–810. https://rs.yiigle.com/CN115399202004/1340647.htm
14. Yang D., Liu L., Zhu D., Peng H., Su L., Fu Y.X., Zhang L. // Cell. Mol. Immunol. 2013. V. 11. P. 71–78.
15. Donkers J.M., Appelman M.D., van de Graaf S.F.J. // JHEP Rep. 2019. V. 1. № 4. P. 278–285.
16. Guo H., Urban S., Wang W. // Front. Microbiol. 2023. V. 14. P. 1169770.
17. Hehle V., Beretta M., Bourgine M., Ait-Goughoulte M., Planchais C., Morisse S., Vesin B., Lorin V., Hieu T., Stauffer A., et al. // J. Exp. Med. 2020 V. 217. № 10. e20200840. doi: 10.1084/jem.20200840
18. Golay J., Manganini M., Facchinetti V., Gramigna R., Broady R., Borleri G., Rambaldi A., Introna M. // Haematologica. 2003. V. 88. № 9. P. 1002–1012.
19. Smith M.R. // Oncogene. 2003. V. 22. № 47. P. 7359–7368.
20. Yang D., Liu L., Zhu D., Peng H., Su L., Fu Y.X., Zhang L. // Cell. Mol. Immunol. 2014. V. 11. № 1. P. 71–78.
21. He Z., Chen J., Wang J., Xu L., Zhou Z., Chen M., Zhang Y., Shi M. // Eur. J. Gastroenterol. Hepatol. 2021. V. 33. № 1. P. 76–82.
22. Song Z., Lin S., Wu X., Ren X., Wu Y., Wen H., Qian B., Lin H., Huang Y., Zhao C., et al. // Hepatol Int. 2023. V. 17. № 5. P. 1300–1317. https://pubmed.ncbi.nlm.nih.gov/37368186/
23. Qi R., Fu R., Lei X., He J., Jiang Y., Zhang L., Wu Y., Wang S., Guo X., Chen F., et al. // J. Hepatol. 2024. V. 80. № 5. P. 714–729. https://pubmed.ncbi.nlm.nih.gov/38336348/
24. Zhang Y.M., Yang Y.D., Jia H.Y., Zeng L.Y., Yu W., Zhou N., Li L.J. // World J. Gastroenterol. 2014. V. 20. № 15. P. 4407–4413.
25. Burm R., van Houtte F., Verhoye L., Mesalam A.A., Ciesek S., Roingeard P., Wedemeyer H., Leroux-Roels G., Meuleman P. // JHEP Reports. 2023. V. 5. № 3. 100646. doi: 10.1016/j.jhepr.2022.100646
26. Lempp F.A., Vincenzetti L., Volz T., Guarino B., Benigni F., Rosen L.E., Zatta F., Bianchi S., Lombardo G., Jaconi S., et al. // American Association for the Study of Liver Diseases (AASLD). Hepatology. 2021. V. 74. P. 513A–514A.
27. Dingman R., Balu-Iyer S.V. // J. Pharm. Sci. 2019. V. 108. № 5. P. 1637–1654. https://pubmed.ncbi.nlm.nih.gov/30599169/
28. Vaisman-Mentesh A., Gutierrez-Gonzalez M., DeKosky B.J., Wine Y. // Front. Immunol. 2020. V. 11. P. 1951. doi: 10.3389/fimmu.2020.01951
29. Lazar G.A., Desjarlais J.R., Jacinto J., Karki S., Hammond P.W. // Mol. Immunol. 2007. V. 44. № 8. P. 1986–1998.
30. Agarwal K., Yuen M.F., Wedemeyer H., Cloutier D., Shen L., Arizpe A., Pang P.S., Tay C., Gupta S.V., Cathcart A.L., et al. // EASL International Liver Congress. 2021. https://www.natap.org/2021/EASL/EASL_43.htm

Rhodobacter capsulatus PG Lipopolysaccharide As a Potential Blocker of Toll-like Receptor 2 and 4 Activation

S. V. Zubova[1*], Ya. V. Radzyukevich[2], N. I. Kosyakova[3], I. R. Prokhorenko[2]

[1]Institute for Biological Instrumentation, Federal Research Center Pushchino Scientific Center for Biological Research of the Russian Academy of Sciences, Pushchino, 142290 Russian Federation
[2]Institute of Basic Biological Problems, Federal Research Center Pushchino Scientific Center for Biological Research of the Russian Academy of Sciences, Pushchino, 142290 Russian Federation
[3]Clinical Hospital at the Pushchino Scientific Center of the Russian Academy of Sciences, Pushchino, 142290 Russian Federation
*E-mail: zusvet@rambler.ru

ABSTRACT TLR2 and TLR4 play a key role in the development of an inflammation in response to a bacterial infection. We studied the effect of *Rhodobacter capsulatus* PG lipopolysaccharide (LPS) on proinflammatory cytokine synthesis activation by the TLR2 and TLR4 agonists *E. coli* LPS, *Streptococcus pyogenes* lipoteichoic acid (LTA), and Pam3CSK4 (a synthetic bacterial lipopeptide) in human whole blood cells. *Rhodobacter capsulatus* PG LPS was shown to exhibit antagonistic properties against the studied TLR4 and TLR2 agonists, blocking the synthesis of the cytokines TNF-α, IL-6, and IL-8. Possible mechanisms behind the suppressing effect of *Rhodobacter capsulatus* PG LPS are proposed. *Rhodobacter capsulatus* PG LPS can serve as a prototype for drugs against both gram-negative and gram-positive bacteria.
KEYWORDS lipopolysaccharides, *Rhodobacter capsulatus*, lipoteichoic acids, Pam3CSK4, TLR, CD14, cytokines.
ABBREVIATIONS KDO – 3-deoxy-d-manno-octulosonic acid; LPS – lipopolysaccharide; LTA – lipoteichoic acid; IL – interleukin; MD-2 – myeloid differentiation protein 2; Pam3CSK4 – synthetic triacylated lipopeptide; PAMP – pathogen-associated molecular patterns; TLR – Toll-like receptor; TNF-α – tumor necrosis factor α.

INTRODUCTION

Pathogen recognition by blood cells is the most important stage of an adequate immune response to infection. TLR2 and TLR4 play a key role in inflammation thanks to their ability to identify certain pathogen-associated molecular patterns (PAMPs) [1]. These receptors also form and interconnect innate and adaptive immune responses. The study of the mechanisms of the functional responses of innate immune cells to different PAMPs is important in developing effective methods against bacterial and viral infections. TLR4 is a receptor specific to lipopolysaccharides (LPSs), which are the basic components of the gram-negative bacterial cell wall [2]. Ligand-specific recognition of TLR2 occurs via its heterodimerization with TLR1 and TLR6. Triacylated lipopeptides induce heterodimerization of TLR2 and TLR1, while TLR2 interacts with TLR6 and CD36 in response to diacylated lipopeptides [3]. Two of the three lipid chains of the triacylated ligand (in par-

ticular, Pam3CSK4) interact with TLR2, while the third chain occupies the TLR1 hydrophobic pocket [4]. Since the TLR6 molecule lacks a hydrophobic pocket, the TLR2/TLR6 heterodimer cannot recognize triacylated lipopeptides [5]. The ability of TLR2 to form a complex with either TLR1 or TLR6 opens the door for blood cells to interact with a wider range of microbial products. It also increases the production of proinflammatory cytokines and complicates the pathogenesis of sepsis.

LPS from the phototrophic bacterium *Rhodobacter capsulatus* PG exhibits low endotoxic activity and acts as an endotoxin antagonist [6]. A synthetic analogue of the lipid A of *R. capsulatus*, namely the drug E5531, is capable of blocking the immunobiological activity of LPSs and lipoteichoic acid (LTA) [7].

The aim of this work is to study the ability of *R. capsulatus* PG LPS to suppress the activation of innate immune cells by different TLR2 and TLR4 ligands.

EXPERIMENTAL

The studies were carried out using whole blood of conditionally healthy volunteers aged 25 to 30 years. All volunteers provided a written consent to participate in the study. The study protocol complies with the World Medical Association Declaration of Helsinki (2013); it was approved by the Local Ethics Committee of the Hospital Pushchino Scientific Center of the Russian Academy of Sciences (No. 2 dated 10.04.2014). Peripheral blood was collected using vacutainers (Becton, Dickinson and Company, UK) treated with sodium heparin (17 u/ml) in the clinical setting.

Blood cell activation by LPS, LTA, and Pam3CSK4

To study the effect of LPS, LTA, and Pam3CSK4 on cytokine synthesis, whole blood was diluted in a RPMI 1640 medium at a ratio of 1 : 10 and incubated in various combinations with *E. coli* O55:B5 LPS (100 ng/ml), *Streptococcus pyogenes* LTA (1 000 ng/ml), synthetic lipopeptide Pam3CSK4 (300 ng/ml) (Sigma-Aldrich, USA), and *R. capsulatus* PG LPS (1 000 ng/ml) for 6 h at 37°C and 5% CO_2. *R. capsulatus* PG LPS was obtained according to the previously described method [8]. To determine the antagonistic effect of *R. capsulatus* PG LPS on agonists, blood was preincubated with *R. capsulatus* PG LPS for 30 min. After incubation, either LPS, LTA, or Pam3CSK4 was added. Blood cells were then pelleted by centrifugation at 300 *g* for 10 min. Supernatants were collected and stored at −20°C prior to cytokine assessment.

Cytokine assessment

The cytokine level was evaluated using TNF-α, IL-6, and IL-8 ELISA kits (Vector-Best, Russia) according to the manufacturer's protocol. The optical density of the samples was determined at 450 nm on a Stat Fax 3200 microplate reader (Awareness Technology Inc., USA).

Statistical analysis

The statistical analysis and graphical presentation of the results were conducted using nonparametric statistics methods in Origin Pro 7.5 and Microsoft Office Excel 2010 (AtteStat plugin). The results are presented as median values with upper and lower quartiles (IQR). The statistical significance of differences between median values was determined using the Mann–Whitney test ($p < 0.05$).

RESULTS

The specific receptors TLR2 and TLR4, which provide an adequate immune response to various pathogens, are the most important elements in cytokine synthesis activation. We analyzed the activation of the synthesis of the cytokines TNF-α and IL-6 and chemokine IL-8 by the following TLR2 and TLR4 ligands in human whole blood cells in a single series of experiments: *E. coli* LPS, *S. pyogenes* LTA, and Pam3CSK4. Activating ligands stimulated the production of TNF-α, IL-6, and IL-8 by blood cells at levels significantly above those in the control (*Fig. 1*).

An increase in TNF-α and IL-8 synthesis was observed in response to *S. pyogenes* LTA activation; the TNF-α and IL-8 levels were higher compared to those in the cells exposed to *E. coli* LPS and Pam3CSK4. In other words, the level of cytokines synthesized by the cells decreased in the following order: *S. pyogenes* LTA > *E. coli* LPS > Pam3CSK4. *R. capsulatus* PG LPS at a concentration exceeding that of the *E. coli* endotoxin and Pam3CSK4 by ten times and thrice, respectively, and at the same concentration as for *S. pyogenes* LTA did not stimulate TNF-α production in the cells (*Fig. 1*).

The blood levels of IL-8 and IL-6 increased insignificantly in response to *R. capsulatus* PG LPS, compared to the control; however, the levels were significantly lower than those in blood cells activated by other ligands.

The study of the ability of *R. capsulatus* PG LPS to protect cells against the action of *E. coli* LPS, *S. pyogenes* LTA, and Pam3CSK4 showed that *R. capsulatus* PG LPS suppresses TNF-α and IL-6 synthesis in the blood. The suppression of the response decreased in the same order as in the case of blood cell activation by the studied ligands: *S. pyogenes* LTA > *E. coli* LPS > Pam3CSK4. In contrast to activation by *S. pyogenes* LTA and Pam3CSK4, where a significant protective effect of *R. capsulatus* PG LPS was observed, *R. capsulatus* PG LPS did not protect blood cells from the activation of IL-8 synthesis by LPS *E. coli*.

DISCUSSION

In this work, we studied the potential antagonistic activity of LPS from the non-pathogenic bacterium *R. capsulatus* PG not only against LPS of the gram-negative bacterium *E. coli*, which is a typical TLR4 agonist, but also against di- and triacylated lipopeptides such as LTA of the gram-positive bacterium *S. pyogenes* and the synthetic analogue of triacylated lipopeptides Pam3CSK4.

The endotoxic activity of LPSs is determined by the lipid A structure. The number of lipid chains in the structure of lipid A is the most significant factor determining LPS toxicity. It has been previously shown that E5531, a synthetic analogue of lipid A from the phototrophic bacterium *R. capsulatus* 37b4, blocks the immunobiological activity of *E. coli* LPS and *Staphylococcus faecalis* LTA [7]. Unlike E5531, *R. capsulatus* PG LPS contains not only the atypi-
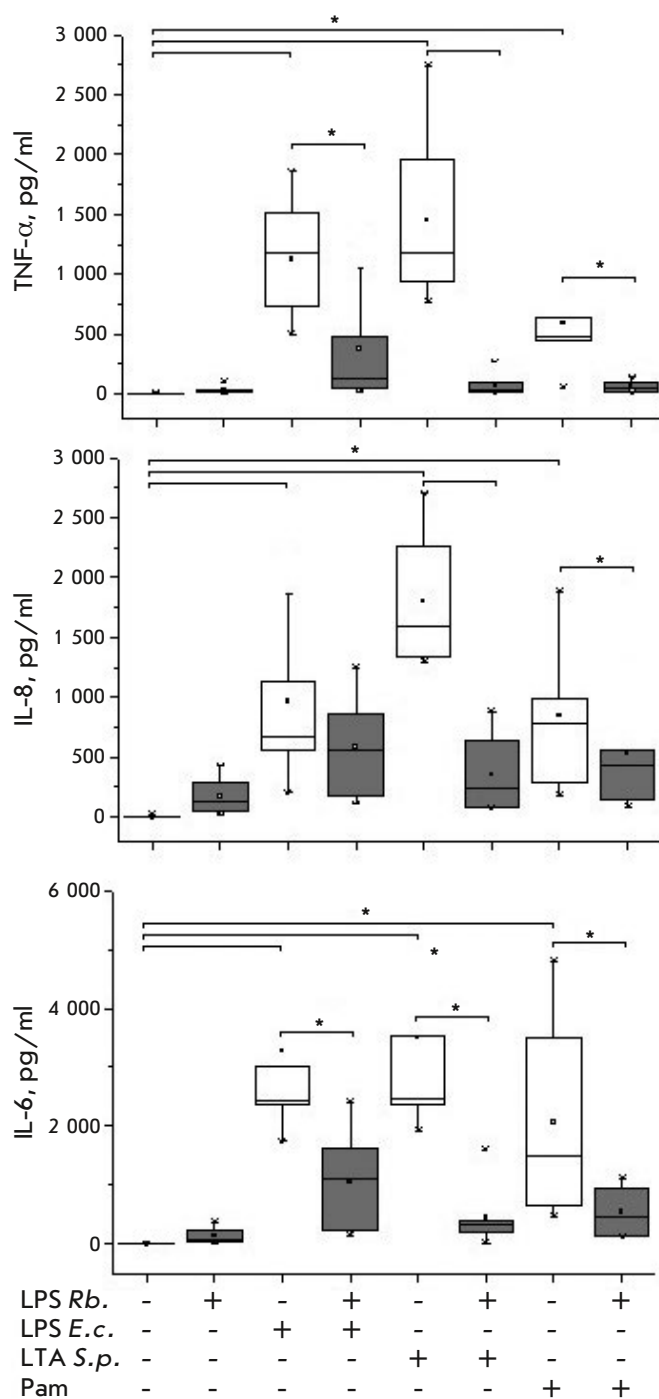
Fig. 1. Effect of *R. capsulatus* PG LPS on TNF-α, IL-8, and IL-6 synthesis upon activation of whole blood cells by *E. coli* LPS, *S. pyogenes* LTA, and Pam3CSK4, n = 7. *p < 0.05

cal lipid A with five truncated fatty acids, including an unsaturated one, but also 3-deoxy-d-manno-octulosonic acid (KDO), an outer core, and O-antigen. The LPS inner core determines not only the LPS biological activity but also the nature of its interaction with the MD-2 protein and TLR4 [9]. For LPS recognition, TLR4 forms a dimer with the membrane protein MD-2, which binds to LPS, forming a complex capable of activating TLR4-positive cells [2]. The *R. sphaeroides* lipid was shown to occupy the entire MD-2 hydrophobic pocket, thus forming the MD-2/lipid A complex, whose stability mainly owes to the hydrophobic interaction between the lipid A tails and the amino acids of the MD-2 binding groove. Tyr102 may be responsible for the antagonist activity of lipid A due to its inverted position in the MD-2/lipid A complex [10]. MD-2 is also involved in the TLR2-mediated responses of blood cells to the wall components of gram-positive bacterial cells. MD-2 binds to TLR2; however, this binding is weaker than that to TLR4 [11].

To recognize tri- or diacylated lipopeptides, TLR2 forms receptor heterodimers with TLR1 and TLR6 [12]. Atypical LPSs of *Legionella pneumophila* and *Rhizobium spp.* induce an inflammatory response most likely via TLR2 than via TLR4 signaling [13]. In our research, we established that *R. capsulatus* PG LPS blocks the activation of cytokine synthesis in blood cells by not only TLR4 agonists, but also TLR2/6 and TLR2/1 agonists. This seems to indicate that, because of the specific composition and structure of lipid A, *R. capsulatus* PG LPS can bind not only to TLR4, but also to TLR2. Apparently, in contrast to classical agonists, the lipid A structure of *R. capsulatus* PG does not stimulate the formation of the $(TLR4)_2$ homodimer or the complexes TLR2/TLR1 and TLR2/TLR6 required for cell activation and subsequent proinflammatory cytokine synthesis. It is possible that *R. capsulatus* PG LPS forms a TLR2/MD-2/LPS_{Rb} complex. This complex then suppresses the formation of the TLR2/6 and TLR2/1 heterocomplexes and the subsequent TLR2-mediated cell activation via LTA and Pam3CSK4, thereby increasing the production of the TNF-α, IL-6, and IL-8 cytokines.

Since *R. capsulatus* PG LPS blocks the activation of TLR4 and TLR2, we cannot exclude the mechanism of antagonistic activity proposed for *Ochrobactrum intermedium* LPS [14]. This atypical, low-toxicity LPS induces interaction of the TLR4 and TLR2 receptors and formation of the TLR4/TLR2 heterodimer upon blood cell activation. The bacteria *R. capsulatus* PG and *O. intermedium* belong to the alpha subgroup of Proteobacteria [15]. LPS from both bacteria show low endotoxic activity. The LPSs of these bacteria are comprised of lipid A containing an un-

saturated fatty acid residue, an inner core, an outer core, and the O-antigen. Core saccharides are known to participate in the formation of the low-reactivity TLR2/TLR4/MD-2 complex in response to *O. intermedium* LPS [14]. It cannot be excluded that an excess of *R. capsulatus* PG LPS also induces the formation of a low-reactivity TLR4/MD-2/TLR2 complex, which blocks TNF-α, IL-6, and IL-8 production in response to *E. coli* LPS, *S. pyogenes* LTA, and Pam3CSK4.

CONCLUSION

The results obtained here show that *R. capsulatus* PG LPS exhibits antagonistic activity against the TLR4 ligands and various TLR2 ligands, including tri- and diacylated lipopeptides. In this work, we proposed possible mechanisms behind the suppressing effect of *R. capsulatus* PG LPS on TLR2 and TLR4 activation.

R. capsulatus PG LPS can serve as a prototype of drugs against both gram-negative and gram-positive bacteria. ●

REFERENCES

1. Mukherjee S., Karmakar S., Babu S.P.S. // Braz. J. Infect. Dis. 2016. V. 20. № 2. P. 193–204.
2. Park B.S., Song D.H., Kim H.M., Choi B.-S., Lee H., Lee J.-O. // Nature. 2009. V. 458. № 7242. P. 1191–1195.
3. Hoebe K., Georgel P., Rutschmann S., Du X., Mudd S., Crozat K., Sovath S., Shamel L., Hartung T., Zähringer U., et al. // Nature. 2005. V. 433. № 7025. P. 523–527.
4. Triantafilou M., Gamper F.G.J., Haston R.M., Mouratis M.A., Morath S., Hartung T., Triantafilou K. // J. Biol. Chem. 2006. V. 281. № 41. P. 31002–31011.
5. Maeshima N., Fernandez R.C. // Front. Cell. Infect. Microbiol. 2013. V. 3. № 3. P. 1–13.
6. Prokhorenko I.R., Grachev S.V., Zubova S.V. Patent for invention RU № 2392309 of 20.06.2010.
7. Kawata T., Bristol J.R., Rossignol D.P., Rose J.R., Kobayashi S., Yokohama H., Ishibashi A., Christ W.J., Katayama K., Yamatsu I., et al. // Br. J. Pharmacol. 1999. V. 127. № 4. P. 853–862.
8. Makhneva Z.K., Vishnevetskaya T.A., Prokhorenko I.R. // Pric. Biochim. Microbe. 1996. V. 32. № 4. P. 444–447.
9. Prokhorenko I., Zubova S., Kabanov D., Grachev S. // Crit. Care. 2014. V. 18. № 2. P. 7–8.
10. Anwar M.F., Panneerselvam S., Shah M., Choi S. // Sci. Rep. 2015. V. 5. № 7657. P. 1–11.
11. Dziarski R., Wang Q., Miyake K., Gupta D. // J. Immun. 2001. V. 166. № 3. P. 1938–1944.
12. Takeuchi O., Sato S., Horiuchi T., Hoshino K., Takeda K., Dong Z., Modlin R.L., Akira S. // J. Immunol. 2002. V. 169. № 1. P. 10–14.
13. Girard R., Pedron T., Uematsu S., Balloy V., Chignard M., Akira S., Chaby R. // J. Cell Sci. 2003. V. 116. Pt 2. P. 93–302.
14. Francisco S., Billod J.-M., Merino J., Punzon C., Gallego A., Arranz A., Martin-Santamaria S., Fresno M. // Front. Immunol. 2022. V. 12. № 748303. P. 1–12.
15. Velasco J., Romero C., López-Goñi I., Leiva J., Díaz R., Moriyón I. // Int. J. Syst. Bacteriol. 1998. V. 48. Pt 3. P. 759–768.

Intergeneric Introgression Enhances the Adaptive Potential of Nine-Spined Stickleback (*Pungitius pungitius*)

A. V. Nedoluzhko[1*], F. S. Sharko[1,2], S. M. Rastorguev[3**]
[1]European University at St. Petersburg, St. Petersburg, 191187 Russian Federation
[2]National Research Center "Kurchatov Institute", Moscow, 123182 Russian Federation
[3]Pirogov Russian National Research Medical University of the Ministry of Health of the Russian Federation, Moscow, 117997 Russian Federation
*E-mail: nedoluzhko@gmail.com
**E-mail: rastorgueff@gmail.com

ABSTRACT Over the past decades, number of evidences has accumulated that demonstrates the importance of genomic introgression between relatively distant eukaryote species, including the introgression of teleost fish species; the three-spined stickleback (*Gasterosteus aculeatus*) and the nine-spined stickleback (*Pungitius pungitius*). The whole-genome datasets of both teleost species give reasons for suggesting that the marine population of nine-spined stickleback increases its adaptive potential to the marine environment through introgression with the anadromous three-spined stickleback. These findings demand a reinterpreting of the mechanisms of evolution towards a process in which organisms acquire new traits not only through long-term accumulation and selection of spontaneous mutations, but also via introgression from other species and ecological forms.

KEYWORDS introgression, hybridization, nine-spined stickleback, *Pungitius pungitius*, adaptation, three-spined stickleback, *Gasterosteus aculeatus*.

INTRODUCTION

Natural interspecific hybridization giving rise to viable and fertile offspring occurs relatively frequently, even between genetically distant plant [1–3] and animal [4–8] species. In most cases, it remains unclear whether this genetic exchange is a result of random processes or whether it plays a crucial role in the species' adaptation to changing environmental conditions or to the conquering of new ecological niches [9, 10].

In some cases, it has been demonstrated that introgressive hybridization can be adaptive, leading to the emergence of morphologically and physiologically distinct forms that contain the genetic material of both parental species. Such adaptive mechanisms have been demonstrated to exist only in hybrid forms with a significant level of introgression from both parents [11–14]. Meanwhile, it still remains unclear whether interspecific introgression causing no noticeable morphological changes is adaptive or occurs occasionly, with its traces in the gene pool of a species eventually fading over time.

Previously, we detected introgressive hybridization in White Sea populations of the three-spine (*Gasterosteus aculeatus*) and nine-spine (*Pungitius pungitius*) sticklebacks [15, 16]. It was suggested that this introgression contributes to the emergence of phenotypes of nine-spine stickleback adapted to salinity. This level of introgression caused no significant morphological changes and could only be identified by whole-genome sequencing. In that case, it also was unclear whether the emergence of introgressed loci in the nine-spined stickleback was the result of random hybridization or was adaptive [16].

In this study, we detected traces of introgression of the three-spined stickleback into the genotypes of Holarctic populations of the nine-spined stickleback based on previously reported genomic datasets of marine and freshwater nine-spined stickleback specimens [17] and using D-statistics analysis, also known as the ABBA-BABA test [18]. Furthermore, the observed level of introgression was much higher for marine populations of the nine-spined stick-
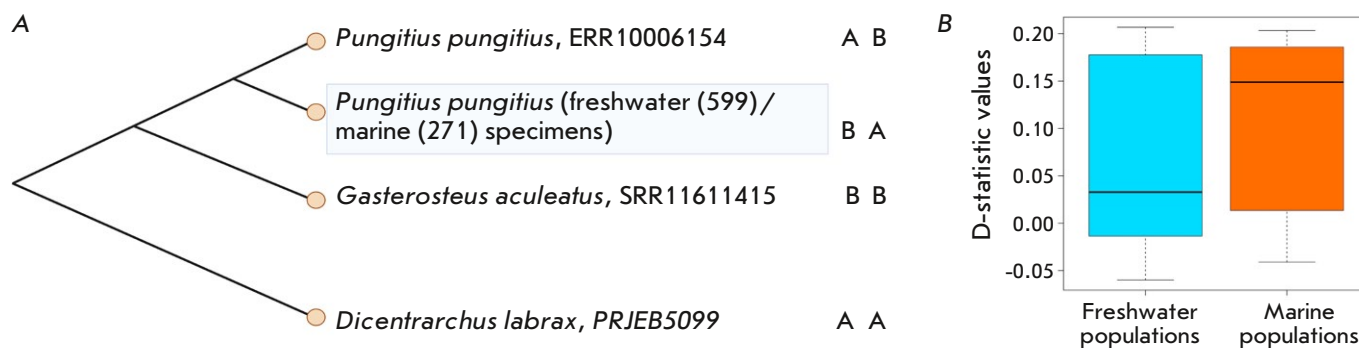
Fig. 1. The ABBA-BABA test. (*A*) Schematic interpretation of the four-taxon ABBA-BABA test used to detect introgression between freshwater and marine populations of the nine-spined stickleback and three-spined stickleback. AB — randomly selected freshwater nine-spined stickleback specimens from the dataset obtained by Feng et al. [17]. BA — the marine and freshwater nine-spined stickleback specimens investigated by Feng et al. [17]. BB — the marine three-spined stickleback specimen genomic data obtained earlier by Nedoluzhko et al. [16], AA — European seabass (*Dicentrarchus labrax*), the outgroup. (*B*) D-statistic values distributions among freshwater and marine populations of nine-spined stickleback

leback than it was for freshwater ones, suggesting that introgression between these two species is adaptive.

EXPERIMENTAL

Bioinformatics analysis
In this study, we used whole-genome sequencing data from 870 nine-spined stickleback specimens that had been obtained by Feng et al. and deposited in the European Nucleotide Archive (ENA; PRJEB39599) to reconstruct the phylogeographic history of Holarctic nine-spined stickleback populations [17].

We classified the genomic datasets of the nine-spined stickleback specimens in accordance with their ecotype into marine (271 specimens) and freshwater (599 specimens) groups. Next, we performed a comparative analysis aiming to assess the level of introgression of the three-spined stickleback into the genotypes of specimens belonging to the marine and freshwater ecotypes of the nine-spined stickleback (*Fig. 1A*).

The introgressive hybridization between the two stickleback species was detected using the ABBA-BABA test [18]; the genome of the European seabass (*Dicentrarchus labrax*, diclab1, PRJEB5099) was used as the outgroup for this test. Initially, the sequencing data for each nine-spined stickleback specimen were mapped to a reference genome of *D. labrax* using the bowtie2 software package (v. 2.3.4.1), with the *very-sensitive-local* parameter [19] (Appendix 1). The mapped data, in SAM format, were then converted to the BAM format, sorted, and indexed using the SAMtools package (v. 0.1.19) [20]. The resulting BAM files were analyzed using the ANGSD software package [21] to evaluate the introgression between the anadromous three-spined stickleback and two ecotypes of the nine-spined stickleback. The statistical significance of the results of the tests for introgression were assessed using the nonparametric Wilcoxon test.

The introgressed loci were revealed using the SNP genotyping chart obtained by mapping the genomic sequencing data to the reference genome of *D. labrax*. A freshwater ERR9997510 specimen, with the minimal D-statistic value, was chosen as the reference genome of *P. pungitius*. The genomic data of the SRR11611426 specimen reported by Nedoluzhko et al. [16] were used as the reference for the genome of *G. aculeatus*. Only the loci homozygous, with respect to the reference allele for the ERR9997510 specimen, and homozygous, with respect to the alternative allele for the SRR11611426 specimen, were analyzed. The alternative allele frequency in all the specimens of the marine ecotype of the nine-spined stickleback was determined in all the filtered loci. In the loci where the alternative allele frequency was > 0.5, the genes were identified by mapping to the reference database of the zebrafish (*Danio rerio*) GRCz11 (https://www.ncbi.nlm.nih.gov/datasets/genome/GCF_000002035.6/), and the blastx software v2.12.0+ [22]. Gene ontology analysis was conducted using the ShinyGO v0.81 web tool [23].

RESULTS

We have assessed the level of introgressive hybridization of the three-spined stickleback into the genotypes of the nine-spined sticklebacks corresponding to the marine and freshwater genotypes using the ABBA–BABA test. The introgression was evaluated by calculating the D-statistics value for each specimen within each sample (Appendix 1). The mean distribution of the D-statistic values in marine populations of the nine-spined stickleback was 0.1488593, while it was 0.03277605 (near-zero) in the freshwater populations (*Fig. 1B*).

Hence, the level of genomic introgression from the three-spined stickleback to the nine-spined one was significantly higher in the group of marine specimens compared to the group of freshwatetr ones (Appendix 1; *Fig. 1B*). This finding proves the hypothesis that genomic introgression from the three-spined to the nine-spined stickleback, which has largely evolved in fresh water [24] and presumably is not well-adapted to marine water, has an adaptive effect [16].

The nonparametric Wilcoxon test allowed us to assess the statistical significance of the difference in D-statistic values between the marine and freshwater nine-spined stickleback populations (*p-value* = 1.004e-07), revealing a high statistical significance of the differences in the level of introgression in the genomes of marine as compared to freshwater nine-spined stickleback specimens.

The higher level of introgressive hybridization in marine populations can presumably be attributed to the presence of alleles of the anadromous three-spined stickleback in their genomes, which have been fixed in marine populations of the nine-spined stickleback, thus facilitating the adaptation of their carriers to higher salinity.

An analysis of the introgressed regions revealed 715 loci where the frequency of the allele specific to the three-spined stickleback is > 0.5 in marine nine-spined stickleback populations. These loci reside in 432 genes. The list of the genes is provided in Appendix 2. Gene ontology (GO) enrichment analysis demonstrated that the list of introgressed genes is enriched in groups of categories related to organism development processes and regulation of transcription, cell adhesion, and transmembrane ion transport (Appendices 3–5). These gene groups, primarily those functionally related to cell adhesion and ion transport, can potentially be associated with salinity adaptation.

CONCLUSIONS

The progress and cheapening of deep DNA sequencing technologies, as well as the development of fundamentally new bioinformatics analysis methods, make it possible to assess the reasons for the explosive speciation, adaptive radiation, and rapid ecological adaptation, or identify the traces, of ancient genomic hybridization [12, 14, 25].

The fact that introgressive hybridization between the three-spined and nine-spined stickleback in the White Sea basin was possible had previously been demonstrated [15, 16]. Interestingly, distinct signals of introgression from the three-spined stickleback were had been observed in most of the genomes of the studied nine-spined stickleback specimens [16]. However, in the absence of marine nine-spined stickleback specimens, it was impossible to confirm the adaptive potential of such intergeneric introgression. This study has clearly demonstrated, using genomic data on marine and freshwater populations of the nine-spined stickleback and statistical tests, that the marine populations of this species enhance adaptivity to water salinity due to introgression from the three-spined stickleback, a mostly marine species.

Our findings indicate that the available genomic data need reinterpreting from the position that the destruction of reproductive barriers between species, including evolutionarily distant ones, is a much more frequent phenomenon than previously thought. Furthermore, it appears that introgressive hybridization can have a significant adaptive potential during periods of environmental changes, global cataclysms, and mass species extinction [11]. Another conclusion flowing from our results is that genomic introgression events require a more careful consideration as one of the significant factors in evolution. Moreover, introgression should be taken into account when conducting phylogenetic studies and when assessing the demographic history of species, since introgressive hybridization events substantially contribute to them. ●

REFERENCES

1. Hu L., Yang R., Wang Y.-H., Gong X. // AoB PLANTS. 2021. V. 13. № 2. P. plab012. doi: 10.1093/aobpla/plab012.
2. Martin G., Cottin A., Baurens F.C., Labadie K., Hervouet C., Salmon F., Paulo-de-la-Reberdiere N., Van den Houwe I., Sardos J., Aury J.M., et al. // Plant J. 2022. V. 113. № 4. P. 802–818. doi: 10.1111/tpj.16086.
3. Zhang H., Zhang X., Wu G., Dong C., Liu J., Li M. // Mol. Phylogenet. Evol. 2022. V. 180. P. 107686. doi: 10.1016/j.ympev.2022.107686.
4. Chiba S. // Evolution. 2005. V. 59. P. 1712−1720.
5. Nichols P., Genner M.J., van Oosterhout C., Smith A., Parsons P., Sungani H., Swanstrom J., Joyce D.A. // Proc. Biol. Sci. 2015. V. 282. P. 20142272. doi: 10.1098/rspb.2014.2272.
6. Pereira R.J., Barreto F.S., Burton R.S. // Evolution. 2014. V. 68. P. 204−215. doi: 10.1111/evo.12254.
7. Korniienko Y., Nzimora K.C., Vater M., Tiedemann R., Kirschbaum F. // J. Comp. Physiol. A Neuroethol. Sens Neural Behav. Physiol. 2022. V. 208. P. 355−371. doi: 10.1007/s00359-022-01542-5.
8. Wang Y., Wang Y., Cheng X., Ding Y., Wang C., Merila J., Guo B. // Mol. Biol. Evolution. 2023. V. 40. № 2. P. msad026. doi: 10.1093/molbev/msad026.
9. Frei D., Reichlin P., Seehausen O., Feulner P.G.D. // Mol. Ecol. 2022. V. 32. P. 841–853. doi: 10.1111/mec.16791.
10. Heliconius Genome C. // Nature. 2012. V. 487. P. 94−98. doi: 10.1038/nature11041.
11. Brauer C.J., Sandoval-Castillo J., Gates K., Hammer M.P., Unmack P.J., Bernatchez L., Beheregaray L.B. // Nat. Climate Change. 2023. V. 13. P. 282−289 doi: 10.1038/s41558-022-01585-1.
12. Lamichhaney S., Han F., Webster M.T., Andersson L., Grant B.R., Grant P.R. // Science. 2018. V. 359. P. 224−228. doi: 10.1126/science.aao4593.
13. Levin B., Simonov E., Gabrielyan B.K., Mayden R.L., Rastorguev S.M., Roubenyan H.R., Sharko F.S., Nedolu-zhko A.V. // Mol. Phylogenet. Evol. 2022. V. 167. P. 107346. doi: 10.1016/j.ympev.2021.107346.
14. Meier J.I., Marques D.A., Mwaiko S., Wagner C.E., Excoffier L., Seehausen O. // Nat. Commun. 2017. V. 8. P. 14363. doi: 10.1038/ncomms14363.
15. Nedoluzhko A., Sharko F., Tsygankova S., Boulygina E., Ibragimova A., Teslyuk A., Galindo-Villegas J., Rastorguev S. // Heliyon. 2021. V. 7. № 2. P. e06160. doi: 10.1016/j.heliyon.2021.e06160.
16. Nedoluzhko A., Sharko F., Tsygankova S., Boulygina E., Slobodova N., Teslyuk A., Galindo-Villegas J., Rastorguev S. // Front Genet. 2022. V. 13. P. 863547. doi: 10.3389/fgene.2022.863547.
17. Feng X., Merila J., Loytynoja A. // Mol. Ecol. 2022. V. 31. P. 5386−5401. doi: 10.1111/mec.16651.
18. Green R.E., Krause J., Briggs A.W., Maricic T., Stenzel U., Kircher M., Patterson N., Li H., Zhai W., Fritz M.H., et al. // Science. 2010. V. 328. P. 710−722. doi: 10.1126/science.1188021.
19. Langmead B., Salzberg S.L. // Nat. Meth. 2012. V. 9. P. 357−359. doi: 10.1038/nmeth.1923.
20. Li H. // Bioinformatics. 2011. V. 27. P. 2987−2993. doi: 10.1093/bioinformatics/btr509.
21. Korneliussen T.S., Albrechtsen A., Nielsen R. // BMC Bioinformatics. 2014. V. 15. P. 356. doi: 10.1186/s12859-014-0356-4.
22. Camacho C., Coulouris G., Avagyan V., Ma N., Papadopoulos J., Bealer K., Madden T.L. // BMC Bioinformatics. 2009. V. 10. P. 421. doi: 10.1186/1471-2105-10-421.
23. Ge S.X., Jung D., Yao R. // Bioinformatics. 2020. V. 36. P. 2628−2629. doi: 10.1093/bioinformatics/btz931.
24. Wang C., Shikano T., Persat H., Merilä J. // J. Biogeography. 2015. V. 42. P. 2334−2348. doi: https://doi.org/10.1111/jbi.12591.
25. Brawand D., Wagner C.E., Li Y.I., Malinsky M., Keller I., Fan S., Simakov O., Ng A.Y., Lim Z.W., Bezault E., et al. // Nature. 2014. V. 513. P. 375−381. doi: 10.1038/nature13726.

GENERAL RULES

Acta Naturae publishes experimental articles and reviews, as well as articles on topical issues, short reviews, and reports on the subjects of basic and applied life sciences and biotechnology.

The journal *Acta Naturae* is on the list of the leading periodicals of the Higher Attestation Commission of the Russian Ministry of Education and Science. The journal Acta Naturae is indexed in PubMed, Web of Science, Scopus and RCSI databases.

The editors of *Acta Naturae* ask of the authors that they follow certain guidelines listed below. Articles which fail to conform to these guidelines will be rejected without review. The editors will not consider articles whose results have already been published or are being considered by other publications.

The maximum length of a review, together with tables and references, cannot exceed 50 000 characters with spaces (approximately 30 pages, A4 format, 1.5 spacing, Times New Roman font, size 12) and cannot contain more than 16 figures.

Experimental articles should not exceed 30 000 symbols (approximately 15 pages in A4 format, including tables and references). They should contain no more than ten figures.

A short report must include the study's rationale, experimental material, and conclusions. A short report should not exceed 12 000 symbols (5−6 pages in A4 format including no more than 12 references). It should contain no more than three figures.

The manuscript and all necessary files should be uploaded to www.actanaturae.ru:

1) text in Word 2003 for Windows format;
2) the figures in TIFF format;
3) the text of the article and figures in one pdf file;
4) the article's title, the names and initials of the authors, the full name of the organizations, the abstract, keywords, abbreviations, figure captions, and Russian references should be translated to English;
5) the cover letter stating that the submitted manuscript has not been published elsewhere and is not under consideration for publication;
6) the license agreement (the agreement form can be downloaded from the website www.actanaturae.ru).

MANUSCRIPT FORMATTING

The manuscript should be formatted in the following manner:

· Article title. Bold font. The title should not be too long or too short and must be informative. The title should not exceed 100 characters. It should reflect the major result, the essence, and uniqueness of the work, names and initials of the authors.
· The corresponding author, who will also be working with the proofs, should be marked with a footnote *.
· Full name of the scientific organization and its departmental affiliation. If there are two or more scientific organizations involved, they should be linked by digital superscripts with the authors' names. Abstract. The structure of the abstract should be very clear and must reflect the following: it should introduce the reader to the main issue and describe the experimental approach, the possibility of practical use, and the possibility of further research in the field. The average length of an abstract is 20 lines (1 500 characters).
· Keywords (3 − 6). These should include the field of research, methods, experimental subject, and the specifics of the work. List of abbreviations.
· INTRODUCTION
· EXPERIMENTAL PROCEDURES
· RESULTS AND DISCUSSION
· CONCLUSION
The organizations that funded the work should be listed at the end of this section with grant numbers in parenthesis.
· REFERENCES
The in-text references should be in brackets, such as [1].

RECOMMENDATIONS ON THE TYPING AND FORMATTING OF THE TEXT

· We recommend the use of Microsoft Word 2003 for Windows text editing software.
· The Times New Roman font should be used. Standard font size is 12.
· The space between the lines is 1.5.
· Using more than one whole space between words is not recommended.
· We do not accept articles with automatic referencing; automatic word hyphenation; or automatic prohibition of hyphenation, listing, automatic indentation, etc.
· We recommend that tables be created using Word software options (Table → Insert Table) or MS Excel. Tables that were created manually (using lots of spaces without boxes) cannot be accepted.
· Initials and last names should always be separated by a whole space; for example, A. A. Ivanov.
· Throughout the text, all dates should appear in the "day.month.year" format, for example 02.05.1991, 26.12.1874, etc.
· There should be no periods after the title of the article, the authors' names, headings and subheadings, figure captions, units (s − second, g − gram, min − minute, h − hour, d − day, deg − degree).
· Periods should be used after footnotes (including those in tables), table comments, abstracts, and abbreviations (mon. − months, y. − years, m. temp. − melting temperature); however, they should not be used in subscripted indexes (T_m − melting temperature; $T_{p.t}$ − temperature of phase transition). One exception is mln − million, which should be used without a period.
· Decimal numbers should always contain a period and not a comma (0.25 and not 0,25).
· The hyphen ("-") is surrounded by two whole spaces, while the "minus," "interval," or "chemical bond" symbols do not require a space.
· The only symbol used for multiplication is "×"; the "×" symbol can only be used if it has a number to its

right. The "·" symbol is used for denoting complex compounds in chemical formulas and also noncovalent complexes (such as DNA·RNA, etc.).

· Formulas must use the letter of the Latin and Greek alphabets.

· Latin genera and species' names should be in italics, while the taxa of higher orders should be in regular font.

· Gene names (except for yeast genes) should be italicized, while names of proteins should be in regular font.

· Names of nucleotides (A, T, G, C, U), amino acids (Arg, Ile, Val, etc.), and phosphonucleotides (ATP, AMP, etc.) should be written with Latin letters in regular font.

· Numeration of bases in nucleic acids and amino acid residues should not be hyphenated (T34, Ala89).

· When choosing units of measurement, SI units are to be used.

· Molecular mass should be in Daltons (Da, KDa, MDa).

· The number of nucleotide pairs should be abbreviated (bp, kbp).

· The number of amino acids should be abbreviated to aa.

· Biochemical terms, such as the names of enzymes, should conform to IUPAC standards.

· The number of term and name abbreviations in the text should be kept to a minimum.

· Repeating the same data in the text, tables, and graphs is not allowed.

GUIDENESS FOR ILLUSTRATIONS

· Figures should be supplied in separate files. Only TIFF is accepted.

· Figures should have a resolution of no less than 300 dpi for color and half-tone images and no less than 600 dpi.

· Files should not have any additional layers.

REVIEW AND PREPARATION OF THE MANUSCRIPT FOR PRINT AND PUBLICATION

Articles are published on a first-come, first-served basis. The members of the editorial board have the right to recommend the expedited publishing of articles which are deemed to be a priority and have received good reviews.

Articles which have been received by the editorial board are assessed by the board members and then sent for external review, if needed. The choice of reviewers is up to the editorial board. The manuscript is sent on to reviewers who are experts in this field of research, and the editorial board makes its decisions based on the reviews of these experts. The article may be accepted as is, sent back for improvements, or rejected.

The editorial board can decide to reject an article if it does not conform to the guidelines set above.

The return of an article to the authors for improvement does not mean that the article has been accepted for publication. After the revised text has been received, a decision is made by the editorial board. The author must return the improved text, together with the responses to all comments. The date of acceptance is the day on which the final version of the article was received by the publisher.

A revised manuscript must be sent back to the publisher a week after the authors have received the comments; if not, the article is considered a resubmission.

E-mail is used at all the stages of communication between the author, editors, publishers, and reviewers, so it is of vital importance that the authors monitor the address that they list in the article and inform the publisher of any changes in due time.

After the layout for the relevant issue of the journal is ready, the publisher sends out PDF files to the authors for a final review.

Changes other than simple corrections in the text, figures, or tables are not allowed at the final review stage. If this is necessary, the issue is resolved by the editorial board.

FORMAT OF REFERENCES

The journal uses a numeric reference system, which means that references are denoted as numbers in the text (in brackets) which refer to the number in the reference list.

For books: the last name and initials of the author, full title of the book, location of publisher, publisher, year in which the work was published, and the volume or issue and the number of pages in the book.

For periodicals: the last name and initials of the author, title of the journal, year in which the work was published, volume, issue, first and last page of the article, doi. Must specify the name of the first 10 authors. Ross M.T., Grafham D.V., Coffey A.J., Scherer S., McLay K., Muzny D., Platzer M., Howell G.R., Burrows C., Bird C.P., et al. // Nature. 2005. V. 434. № 7031. P. 325–337. doi: 10.1038/nature03440.

References to books which have Russian translations should be accompanied with references to the original material listing the required data.

References to doctoral thesis abstracts must include the last name and initials of the author, the title of the thesis, the location in which the work was performed, and the year of completion.

References to patents must include the last names and initials of the authors, the type of the patent document (the author's rights or patent), the patent number, the name of the country that issued the document, the international invention classification index, and the year of patent issue.

The list of references should be on a separate page. The tables should be on a separate page, and figure captions should also be on a separate page.

The following e-mail addresses can be used to contact the editorial staff: actanaturae@gmail.com, tel.: (495) 727-38-60.